Chair of Ferrous Metallurgy

Doctoral Thesis

Tracing of Non-Metallic Inclusions in Steel by Applying Modern Analytical Techniques

Dipl.-Ing. Kathrin Thiele, BSc

June 2024

AFFIDAVIT

I declare on oath that I wrote this thesis independently, did not use any sources and aids other than those specified, have fully and truthfully reported the use of generative methods and models of artificial intelligence, and did not otherwise use any other unauthorized aids.

I declare that I have read, understood and complied with the "Good Scientific Practice" of the Montanuniversität Leoben.

Furthermore, I declare that the electronic and printed versions of the submitted thesis are identical in form and content.

Date 26.06.2024

Signature Author
Kathrin Thiele

"You cannot hope to build a better world without improving the individuals. To that end each of us must work for his own improvement, and at the same time share a general responsibility for all humanity, our particular duty being to aid those to whom we think can be most useful."

Marie Curie

Acknowledgments

First and foremost, I would like to express my special thanks to my supervisor, Univ.-Prof. Dipl.-Ing. Dr.mont. Susanne Michelic. She gave me the opportunity to write my thesis in the Christian Doppler Laboratory for Inclusion Metallurgy in Advanced Steelmaking. The joint discussions with her, as well as her expertise, guidance, and support accompanied me throughout my PhD journey. I am grateful for her constructive advice and motivation, which kept me going even in tough times.

Secondly, I would also like to thank Univ.-Prof. Dipl.-Ing. Dr.techn. Thomas Prohaska for his inspiration, thoughtful insights, and continuous support as well as his team at the Chair of General and Analytical Chemistry. Especially, I would like to thank assoc. Prof. Dipl.-Ing. Dr.nat.techn. Johanna Irrgeher, Dipl.-Ing. Dr.techn. Christoph Walkner, Univ.-Prof. Ao. Univ.-Prof. Mag.rer.nat. Dr.mont. Thomas C. Meisel, and Dr.nat.techn. Stefan Wagner, MSc for their expertise in isotope analysis and elemental analysis.

This thesis would not have been possible without my company partners from voestalpine Stahl GmbH, in particular, Dr. Sergiu Ilie and Dr. Roman Rössler. Thank for providing me with materials and opportunities to conduct my research. Especially, I want to mention Christoph Truschner who I have shared many fruitful discussions and equally delightful conversations with.

I would like to extend my heartfelt thanks to my colleagues of the Chair of Ferrous Metallurgy who have become close friends throughout the past few years. Special thanks to the team of the Christian Doppler Laboratory for Inclusion Metallurgy in Advanced Steelmaking, namely Julian Cejka, Manuel Schickbichler, Nikolaus Preißer, Robert Musi, Bernhard Sammer, Isabell Gruber and Jannik Wiesel. Together we have spent countless hours laughing and occasionally

sharing our grievances with each other over a nice little cold drink. Furthermore, I would like to thank Alexander Mayerhofer who supported me in the beginning of my thesis.

My friends who I met over the course of many years in Leoben have always supported me and made my life exciting and I surely will be looking back at this time with a smile.

Lastly but probably most importantly, I want to express my gratitude to my family for their endless support and for enabling the great path I am currently walking on. My parents are the reason I was able to reach my goals, they helped me through difficult times and stayed patient with me even when I grew impatient at times during the completion of this work. Thank you Mum and Dad.

Abstract

Non-metallic inclusions (NMI) are formed during the steelmaking process and have different origins, such as chemical reactions in the process, slag entrapments or outbreaks from refractory. The negative impact of NMIs on production and product quality leads to the necessity of understanding their behavior in the process to apply countermeasures if required. Tracing methods are used to identify the source of NMIs and track their modification. Tracing also represents an important tool in the future, considering the transformation of the iron- and steel industry to a CO_2-neutral and perhaps CO_2-free production and the associated impact on steel cleanness and secondary metallurgy treatments. For example, the transformation is connected to an increased use of scrap leading to higher concentrations of trace and tramp elements in the steel whose influence on the steel quality needs to be investigated.

With the state-of-the-art method, an active tracing method, NMIs are marked due to a partial reduction by rare earth elements (REEs), such as La and Ce. Using automated scanning electron microscopy with energy dispersive spectroscopy (SEM/EDS) analysis, REE-modified NMIs are clearly visible and distinguishable from common deoxidation products. One problem of REEs is their high oxygen affinity, leading to reoxidation and thereby affecting the alloying process. Another difficulty occurs in the characterization of REE-containing NMIs. Therefore, the aim of this thesis concerning this technique is to minimize the losses caused by reoxidation on a laboratory scale and develop suitable methods for the characterization of traced NMIs.

The conducted tracing trials on a laboratory scale show that the reoxidation losses of REEs can be reduced by applying specific alloying methods, such as adding them wrapped in Al-foil or as ferroalloy. REE-containing multiphase NMIs are erroneously split into single particles in the characterization with automated SEM/EDS. A self-developed tool improved the evaluation by recombining falsely split NMIs. Consequently, the occurring errors regarding the size,

chemical composition, and spatial distribution of NMIs were reduced. Another important issue is the analysis of the morphology of REE-traced NMIs which was done by applying the sequential chemical extraction technique since their stability in acids was not yet known.

For a faster classification of traced and untraced NMIs with a subsequent overview of the tracing success, artificial intelligence (AI) was applied to support automated SEM/EDS analysis. The AI model distinguishing between NMIs and artifacts (binary classification) achieved an accuracy above 95 %. Also, the trained 4-class model showed promising results classifying into traced, untraced, homogeneous and heterogeneous NMIs.

In addition to the active tracing experiments with REEs on a laboratory scale, industrial trials were performed to compare the findings regarding micro-cleanness. In both setups, similar NMI types and modifications occurred. Slag analysis and investigations of the clogging layer showed that REE-traced NMIs have the tendency to separate into the slag and also contribute to the clogging layer formation.

The major disadvantage of applying REEs as tracers is their influence on the properties of NMIs. Consequently, this research deals with the feasibility of alternative tracing techniques to identify the source of NMIs. Therefore, a passive and another active tracing method were applied. The elemental fingerprint, a passive approach, is based on the natural concentration of REEs in materials. The novel active approach is the isotopic spiking, where the isotopic ratio of one possible source is changed by the addition of enriched stable isotopes. These two tracing approaches have great potential to investigate the origin and modification of NMIs during steel production without influencing the properties of NMIs.

By applying the REE-Fingerprint, it is possible to determine the contributing auxiliaries to the clogging layer or NMIs formation by measuring the natural concentration of REEs in the materials. The first results show that sliding gate sand and Al granules affect clogging of Ti-stabilized interstitial free (IF) steels. The implementation of the isotopic spiking technique allows to distinguish whether a NMI was formed or influenced by the isotopically modified source or a source with natural isotopic composition. The first experiments dealt with the investigation of the impact of a ^{26}Mg-enriched slag on NMIs. Measuring the isotopic composition of NMIs with inductively coupled plasma–mass spectrometers confirmed a modification by the ^{26}Mg-enriched slag. While REE-traced NMIs appear brighter in the SEM/EDS analysis, isotopically traced NMIs are optically not distinguishable from untraced ones.

Kurzfassung

Nichtmetallische Einschlüsse (NME) entstehen bei der Stahlherstellung und können dabei diverse Ursachen haben, wie chemische Reaktionen im Prozess, Schlackeneinzüge oder Ausbrüche des Feuerfestmaterials. Da NME sich meist negativ auf die Produktion und die Produktqualität auswirken, ist es erforderlich deren Entstehung und Veränderung zu verstehen, um gegebenenfalls Gegenmaßnahmen zu treffen. Die Verwendung von Tracingmethoden ermöglicht die Bestimmung von NME-Quellen, sowie deren Nachverfolgung im Prozess. Aufgrund der Transformation der Eisen- und Stahlindustrie hin zu CO_2-neutraler und künftig sogar CO_2-freier Produktion bleibt das Tracen weiterhin ein wesentliches Forschungsthema, da sich die Umstellung auf die Stahlreinheit und folglich auf die Sekundärmetallurgie auswirkt. Beispielsweise ist die Transformation mit einem erhöhten Schrotteinsatz verbunden, wodurch es zu höheren Konzentrationen an Spurenelementen in den Stählen kommt, deren Auswirkung auf die Qualität es noch zu erforschen gilt.

Beim gängigen Tracingverfahren, einer aktiven Methode, werden NME durch Seltene Erden (SE) partiell reduziert und markiert. Somit sind diese NME in der automatisieren Rasterelektronenmikroskopie mit energiedispersiver Röntgenspektroskopie (REM/EDX)-Messung deutlich unterscheidbar. Jedoch treten Problematiken durch die Reoxidation der verwendeten Tracer (La/Ce), wie auch bei der anschließenden Charakterisierung SE-haltiger NME bei diesem Verfahren auf. Ein Ziel dieser Arbeit ist die Minimierung von Reoxidationsverlusten im Labormaßstab und Etablierung geeigneter Charakterisierungsmethoden.

Die aktiven Tracerversuche im Labor zeigen, dass die Verluste an SE durch spezifische Legierungstechniken, wie das Einwickeln in Aluminiumfolie oder die Zugabe als Ferrolegierung, reduziert werden können. Bei der nachfolgenden Charakterisierung der SE-

getracten NME kommt es bei den mehrphasigen NME zur fälschlichen Aufspaltung in einzelne Partikel. Eine korrekte Auswertung erfordert eine Rekombination dieser NME. Das dafür entwickelte Tool führt fälschlich aufgespaltene NME wieder zusammen und verringert somit Fehler in der Auswertung hinsichtlich Größe, chemischer Zusammensetzung und räumlicher Verteilung von NME. Ein weiterer Punkt ist die Morphologieuntersuchung SE-getracter NME. Nachdem die Stabilität der SE-haltigen Phasen in Säuren bisher nicht bekannt war, kam die sequenzielle, chemische Extraktion zum Einsatz zur Morphologiebestimmung.

Da es sich bei der automatisierten REM/EDX-Analyse um eine zeitintensive Charakterisierungsmethode handelt, soll die Implementierung von künstlicher Intelligenz zu einer schnelleren Klassifizierung von getracten und ungetracten NME beitragen. Die Kategorisierung zur Unterteilung in NME und Artefakt liefert Ergebnisse mit einer Richtigkeit über 95 %. Das eigenentwickelte 4-Klassen-Modell weist aussichtsreiche Resultate für die Unterscheidung in getracte, ungetracte, homogene und heterogene NME auf.

Neben aktiven Tracingexperimenten im Labormaßstab fanden auch Vergleiche mit Industrieversuchen statt. Beide Setups führten zu ähnlichen NME-Typen und Modifikationen. Schlackenanalysen und Untersuchungen der Cloggingschichten zeigten, dass SE-getracte NME sich in der Schlacke abscheiden sowie zur Cloggingbildung beitragen.

Der Einsatz von SE als Tracer hat den Nachteil, dass diese die NME-Eigenschaften beeinflussen. Um dieser Problematik entgegenzuwirken, beschäftigt sich diese Arbeit mit der Entwicklung neuer Tracingansätze, die keine Veränderung der NME-Eigenschaften mit sich bringen. Dies ist einerseits der elementare Fingerprint, basierend auf der natürlichen SE-Konzentration in Materialien, sowie das isotopische Spiking bei dem das Isotopenverhältnis einer möglichen Quelle mittels angereicherter stabiler Isotope verändert wird.

Der SE-Fingerprint ermöglicht die Bestimmung, welche Einsatzstoffe zur Bildung von Clogging oder NME beigetragen haben, anhand der Messung der natürlichen Konzentrationen an SE in den Ausgangs- und Zuschlagsstoffen. Erste Ergebnisse zeigen, dass vor allem Schiebersand und Aluminium zur Bildung von Clogging in Ti-stabilisierten Interstitial Free (IF) Stählen beitrugen. Das Isotopentracing basiert auf der Veränderung des Isotopenverhältnisses durch angereicherte stabile Isotope in einer möglichen Quelle. Durch die Bestimmung des Isotopenverhältnisses ist es möglich zu ermitteln, ob NME durch die Quelle mit modifizierter Isotopenzusammensetzung entstanden bzw. verändert wurden. Bei ersten Versuchen mit einer ^{26}Mg-angereicherten Schlacke im Labormaßstab stellte sich durch die Messung der Isotopenzusammensetzung einzelner NME heraus, dass es zu einer Modifikation der untersuchten NME durch die Schlacke kam. Während SE-getracte NME in

der REM/EDX-Analyse heller erscheinen, sind NME, die durch eine isotopisch modifizierte Quelle entstanden bzw. verändert wurden optisch nicht von unmarkierten NME unterscheidbar.

List of publications

Peer-reviewed publications included in this thesis[1]

Paper I: <u>K. Thiele</u>, P. Presoly, D. Ernst, S.R. Babu and S.K. Michelic, Evaluation of different alloying concepts to trace non-metallic inclusions by adding rare earths on a laboratory scale. Ironmaking and Steelmaking 50 (2023), 5, pp. 507–516. doi:10.1080/03019233.2022.2124816.

Paper II: <u>K. Thiele</u>, R. Musi, S. Ramesh Babu and S.K. Michelic, Optimization of the Two- and Three-Dimensional Characterization of Rare Earth-Traced Deoxidation Products. Adv Eng Mater 25 (2023), 11, pp. 2201748. doi:10.1002/adem.202201748.

Paper III: <u>K. Thiele</u>, R. Musi, T. Prohaska, J. Irrgeher and S.K. Michelic, AI assisted steel cleanness evaluation: Predicting the morphology of La-traced non-metallic inclusions using backscattered-electron images. J. Mater. Res. Technol. 28 (2024), pp. 2247–2257. doi:10.1016/j.jmrt.2023.12.172.

Paper IV: C. Truschner, <u>K. Thiele</u>, S. Ilie, R. Rössler, A. Jungreithmeier and S.K. Michelic, Tracing of Deoxidation Products in Ti-Stabilized Interstitial Free Steels by La and Ce on an Industrial and Laboratory Scale. Steel Res. Int. 95 (2023), 3, pp. 2300665. doi:10.1002/srin.202300665.

Paper V: <u>K. Thiele</u>, S. Ilie, R. Rössler, C. Walkner, T. Meisel, T. Prohaska and S.K. Michelic, Different Approaches to Trace the Source of Non-Metallic Inclusions in Steel. Iron & Steel Technology 20 (2023), 7. doi:10.33313/TR/0723.

Paper VI: <u>K. Thiele</u>, C. Truschner, C. Walkner, T.C. Meisel, S. Ilie, R. Rössler and S.K. Michelic, Investigating the Origin of Non-Metallic Inclusions in Ti-Stabilized ULC Steels Using Different Tracing Techniques. Metals 14 (2024), 1, pp. 103. doi:10.3390/met14010103.

Paper VII: <u>K. Thiele,</u> S. Wagner, J. Irrgeher, T. Prohaska and S.K. Michelic, Tracing Non-metallic Inclusions in Steel with Low Levels of Enriched Magnesium Stable Isotopes: A Novel Approach, under review in Metallurgical and Materials Transactions B

Table of contents

1 Significance of the study

In recent years, steel cleanness has come to the fore in metallurgy and relates thereto to microscopic particles, so-called NMIs. NMIs have a different chemical composition from the surrounding steel matrix and are inevitably formed during the steel production process [1]. Steel cleanness itself is not only characterized by the chemical composition of NMIs but also by their morphology, size, number per square millimeter, and their spatial distribution [2]. As the occurrence of NMIs in steel remains unavoidable, the steel industry has redirected its efforts toward targeted modification and optimization of NMIs within the product [3]. NMIs have a significant impact on the mechanical, physical, and chemical properties of the final product [4 – 8]. The studies of Li et al. [9], Velázquez et al. [10], and Chen et al. [11] showed, for example, that the chemical composition and the NMI size play an important role in the corrosion resistance of steel. Another crucial point is that NMIs have a different forming behavior than the surrounding steel matrix leading to higher crack initiation tendency at their phase boundaries. Subsequently, NMIs reduce the fatigue strength as the high cycle fatigue tests in the study of Schickbichler et al. [12] showed. Furthermore, NMIs are undesirable in automotive sheets as they influence the optical appearance [13]. Hence, it is important to focus on the formation and modification of NMIs to adjust them for the respective requirements of the final product. By understanding the origin and evolution of NMIs during the steelmaking process, possible countermeasures can be taken to influence steel cleanness. **Figure 1-1** illustrates the cycle between the NMI formation and their influence on steel properties. Due to the investigation of the behavior of various NMIs during steel production, possible measures to prevent the formation as well as the modification of NMIs can be implemented. As a result, new NMI types are formed, or existing NMIs are influenced leading, again, to unknown effects

on steel properties. The focus of the present thesis is on tracing NMIs throughout the process to identify their sources and track their modifications.
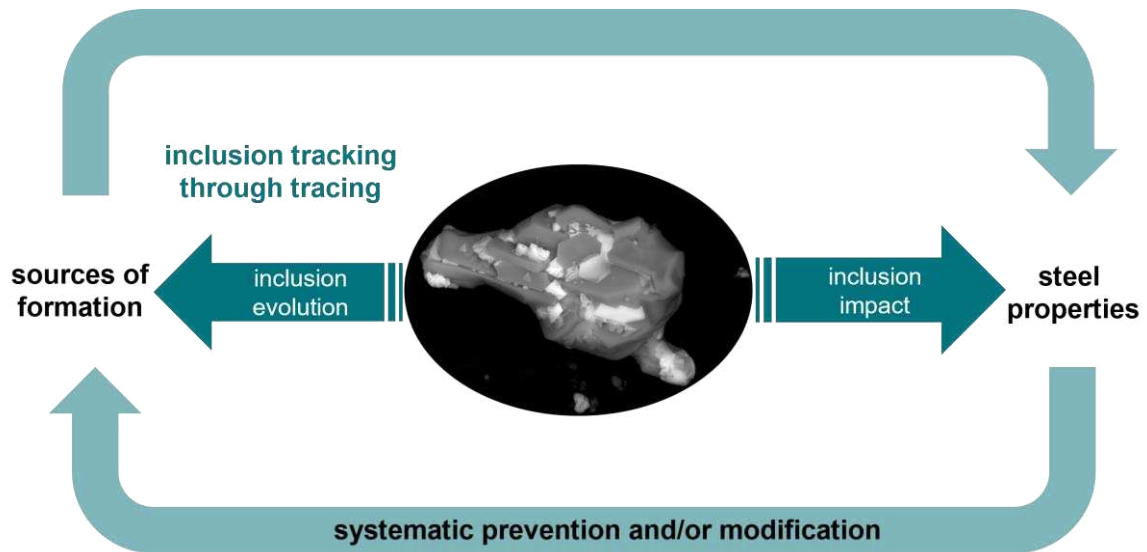

Figure 1-1: Cycle of NMI formation and their influence on steel properties.

Besides their influence on the final product properties, NMIs can cause problems during production. One major topic in connection with NMIs in steelmaking is the phenomenon of clogging. Clogging means the formation of a buildup of solid particles on the inner wall of the submerged entry nozzle (SEN) during the continuous casting process. In many cases, the resulting clogging layer also consists of entrapped and solidified steel droplets. The entrapment occurs due to a change in wettability caused by the formed NMIs [14]. The NMI deposition on the SEN wall causes the clogging layer to grow during the process [15].

2 Industrial focus

As a consequence of asymmetric flow or irregular temperature distribution in the mold caused by the formed clogging layer, slag entrapments, breakouts, or even interruptions of the casting sequence can arise [16, 17]. The reason behind the occurrence of the clogging phenomenon is not entirely clarified by today. With reference to several previous studies [18 – 21] four main mechanisms for the clogging layer formation can appear concurrently. A definition of the main mechanisms as well as an order of their incidence and occurrence was done by Rackers and Thomas [22]. Those are as follows:

1. The agglomeration of deoxidation products at the steel/refractory interface [23 – 25].
2. The buildup of reaction products due to interactions between the refractory and the steel [26, 27].
3. The reoxidation due to air aspiration of atmospheric oxygen into the nozzle [25, 28, 29].
4. The buildup of solid steel at the start of the casting sequence [30].

Depending on the predominant formation mechanisms, different parameters influence the origin and growth of the clogging layer. The influencing factors can be divided into metallurgical, refractory related, thermodynamic, and hydrodynamic key elements. The study of Bernhard et al. [18] lists possible countermeasures against clogging as well as the significance of the respective influencing parameters.

A schematic illustration of clogged material on the inner wall of the SEN and an exemplary picture of a clogging layer fragment are shown in **Figure 2-1**.
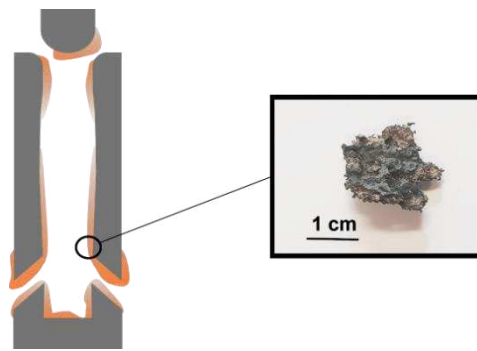
Figure 2-1: Clogging layer formation in SEN [31].

Ti-stabilized ultra-low carbon (ULC) and interstitial free (IF) steels are of particular interest due to their clogging sensitivity. There are several risk factors simultaneously influencing the clogging layer formation. The following conditions were found to increase the tendency for nozzle clogging for Ti-stabilized ULC steels [19, 32 – 37]:

- Increased Ti content
- Increased Ti/Al ratio
- Too little lapse time between Al deoxidation and FeTi addition
- Too little time between the FeTi addition and the start of the casting sequence
- FeTi quality, concerning yielded oxygen content

According to Diéguez Salgado et al. [38], FeTi addition leads to reoxidation and subsequently to the formation of a large number of smaller particles with an increased clogging tendency. Concerning all these factors, FeTi seems to be the main reason for the clogging sensitivity of Ti-stabilized ULC steels. By applying tracing techniques, the impact of FeTi on the clogging layer formation can be clarified with regard to possible reoxidation concerning the additional oxygen insertion. In addition, a distinction between the occurring clogging mechanisms is possible.

Furthermore, approaches using numerical models for the clogging layer formation and growth prediction exist [16, 39]. For example, Barati et al. [15] considered for their mathematical description the influence of FeTi on nozzle clogging. In their study, a two-stage model is implemented in which the clogging layer formation is divided into an early stage with focus on the initial layer formation and a later stage with focus on the growth of the layer. The mathematical description of the early stage model is based on the findings of Lee et al. [40]. Concerning their findings, an initial oxide layer is formed in Ti-stabilized ULC steels on the interface between SEN and steel melt caused by chemical reactions between CO gas coming from the SEN refractory and the liquid steel. The deposits of NMIs on the formed oxide layer

then lead to the growth of the clogging layer. A schematic illustration of the two-stage clogging model is shown in **Figure 2-2**.
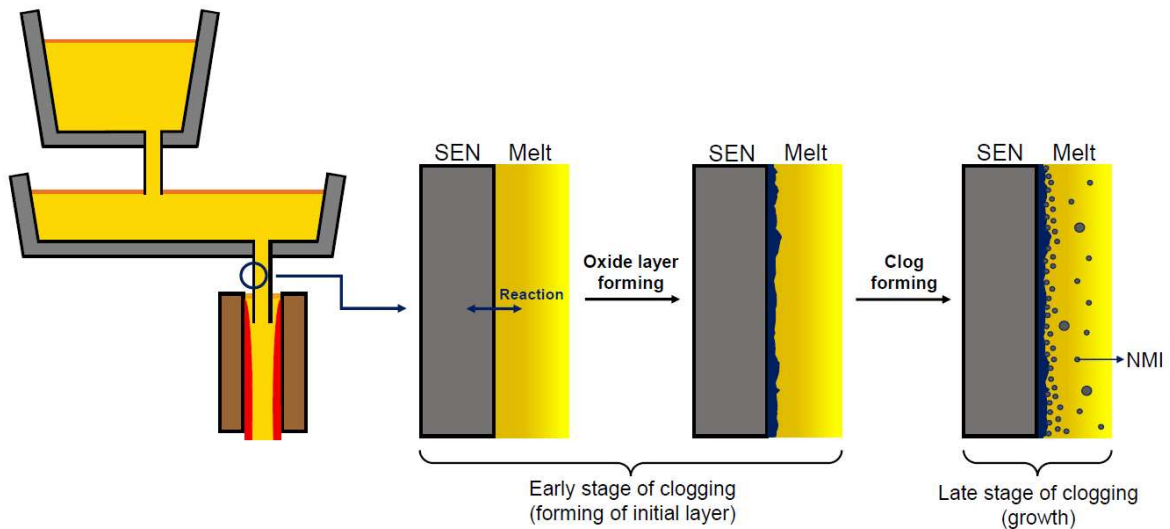

Figure 2-2: Two-stage clogging model; separation between initial layer formation and clogging growth, based on Barati et al. [41]

Another possibility for studying how clogging deposits influence the mold flow is the application of physical models. The usage of water models has also been adapted to study the changed mold flow in a clogged SEN [41, 42]. Even though the utilization of physical and numerical methods delivers good approximations to explain and predict the clogging layer formation as well as the mold flow, it cannot substitute the experimental investigation.

3 Analytical focus

The implementation of tracing methods is intricately interlinked with the characterization of NMIs in steel since the modification of NMIs needs to be tracked throughout the process, particularly in the context of active tracing using REEs. Different characterization methods are currently applied to assess the cleanness of steel [43 – 45]. The measurement tools can be divided into indirect and direct methods [46]. With regard to the former, parameters of steel production are used in connection with thermodynamics to deliver information about the steel cleanness during the process [47]. The primary technique for indirect characterization is the determination of the total oxygen content [48]. In the case of the latter methods, parameters, such as the size, morphology, position, number, and chemical composition of NMIs, are directly determined in steel samples [45]. The most established analyzing techniques concerning tested sample size, analyzing time, tested sample area to volume ratio, two- and three-dimensional investigation method, as well as determination of morphology and/or chemical composition are summarized in the publication of Michelic et al. [49]. An overview of the most common characterization methods is shown in **Figure 3-1**.
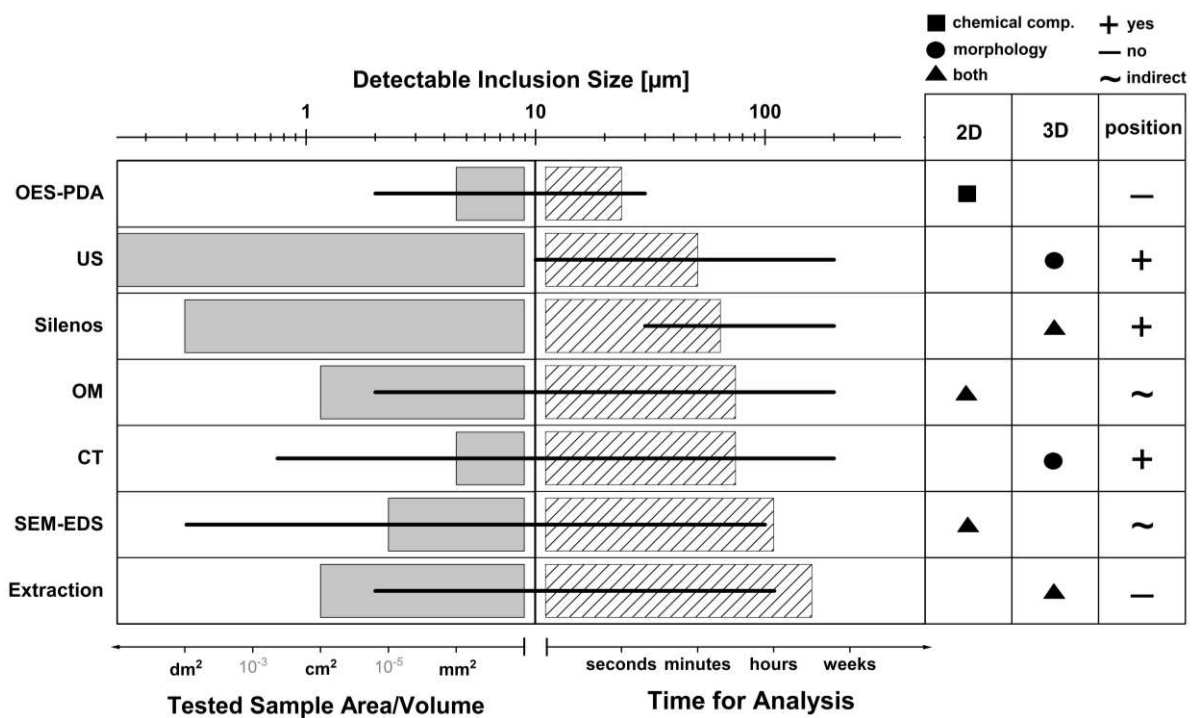
Figure 3-1: Overview of established analyzing techniques for steel cleanness characterization redrawn from Mayerhofer [50]; optical emission spectrometry with pulse discrimination analysis (OES-PDA); ultra-sonic (US); steel cleanness level-evaluation by a numerical optical system (Silenos); optical microscope (OM); computer tomography (CT); scanning electron microscopy with energy dispersive spectroscopy (SEM/EDS).

In particular, the micro-cleanness of steel is focused since macroscopic NMIs are mostly controllable in the present metallurgical processes and microscopic NMIs represent the majority of the particles concerning size distribution. Nowadays, the state-of-the-art method for two-dimensional characterization of micro-cleanness in steels is the automated scanning electron microscopy with energy dispersive spectroscopy (SEM/EDS) analysis. The main reason is the amount of comprised data, such as chemical composition or morphological data. The application of the active tracing technique using REEs requires optimization of existing characterization methods, especially the automated SEM/EDS analysis, and the subsequent validation as complex multiphase NMIs are formed.

4 Tracing approaches for NMIs

The interest in identifying the origin and tracking the modification of NMIs over the process arises due to the increasing demands on steel properties and, thus, steel cleanness. The state-of-the-art method for analyzing the source and the path of NMIs is a so-called active tracing technique, in which rare earth elements (REEs) are directly added to the melt. Since properties, such as the wetting behavior of the microscopic particles, are influenced by REE addition, developing and implementing novel tracing approaches is required [51]. Therefore, this thesis investigated the feasibility of two tracing techniques. On the one hand, the REE-Fingerprint, an intrinsic method and on the other hand, the isotopic spiking, an extrinsic method. **Figure 4-1** illustrates the active and passive tracing approaches and how they are linked to each other. The fourth method, the isotopic fingerprint, is only covered theoretically in this thesis.
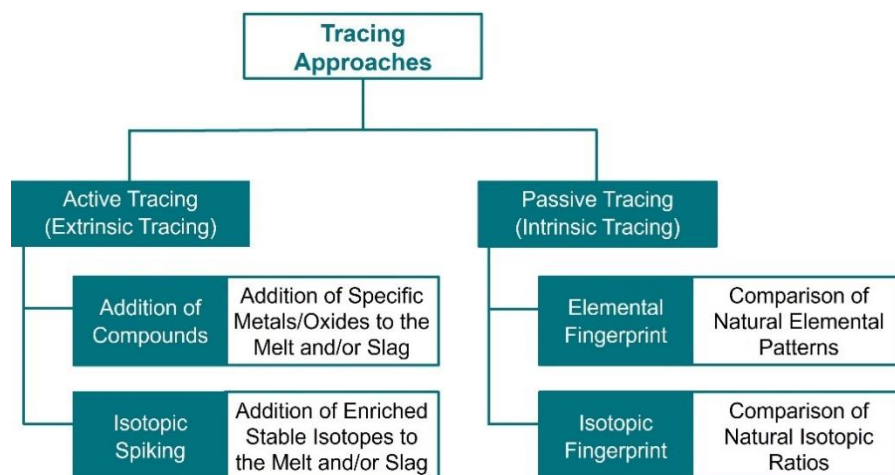

Figure 4-1: Overview of the active and passive tracing approaches implemented in this thesis.

4.1 Active tracing by REEs

The impact of REEs on steel properties has been tested and studied for decades. The first documented investigation of Gillett and Mark [45] found that the S content and the steel cleanness decreased after REE addition. A brief history of REEs in steel and other metals, as well as the main findings concerning their influence on properties are collected in the publication of Collins et al. [52]. Nowadays, REEs, especially Ce, are used as grain refiner in the steel industry. The advantage of Ce is the formation of microscopic NMIs which provoke heterogeneous nucleation [53, 54]. According to the study of Wang et al. [55], the addition of Ce increases the number of NMIs that, however, were smaller in size than without added Ce which resulted in a decrease of the total area covered by NMIs. Furthermore, the addition of REEs leads to uniformly distributed NMIs which are no longer irregularly shaped [56] but instead the morphology of these modified NMIs is mainly globular [57]. Nevertheless, it was found that this reduction in NMI size can be counteracted at critical REE concentrations. The critical value depends on the steel grade as the studies of Li et al. [57] and Mao et al. [58] showed. In the former, the critical Ce concentration was about 340 µg/g while for the latter it was about 425 µg/g of La. Additionally, Ce increases the corrosion resistance as well as mechanical properties, such as impact toughness and tensile strength, of austenitic stainless steel, as was found in the study of Cai et al. [59].

A second possible application of REEs is the utilization as tracers which is feasible since they are ignoble metals. Due to their higher negative free Gibbs energy than traditional deoxidation products, such as Al_2O_3, MnO or SiO_2, REEs have a higher oxygen affinity. As a result, more stable oxides are formed. By considering the stability of chemical bonds at a specific temperature, a prediction of the formed NMI type is possible. The free Gibbs energy of the main chemical bonds for La with O, S, and Al in relation to the temperature can be found in the publication of Ning et al. [60]. The positions of the two primarily used REEs, La and Ce, in the Richardson-Ellingham diagram, are shown in **Figure 4-2** as blue and red lines next to common deoxidation products. As a result of their high oxygen affinity, partial reduction of already existing deoxidation products takes place. Subsequently, complex heterogeneous NMIs are formed due to the incomplete reduction of REEs.
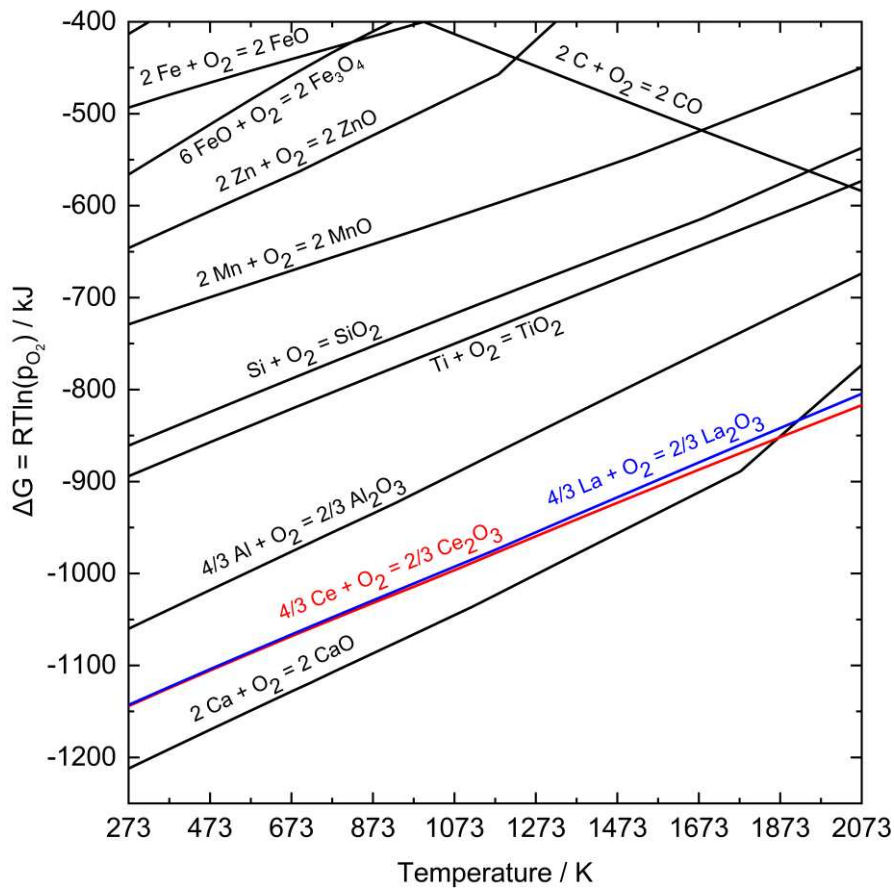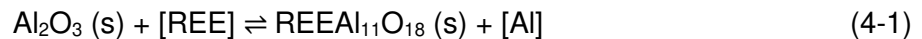
Figure 4-2: Richardson-Ellingham diagram including main deoxidation products as well as La and Ce [61].

The underlying chemical reaction that enables the partial reduction and subsequent tracing is shown in Equation (4-1). The further reduction of the complex multiphase NMI, $REEAl_{11}O_{18}$, leads to the formation of the higher REE concentrated NMI, $AlREEO_3$ (Equation (4-2)). [62, 63]

$$Al_2O_3 \text{ (s)} + [REE] \rightleftharpoons REEAl_{11}O_{18} \text{ (s)} + [Al] \tag{4-1}$$

$$REEAl_{11}O_{18} \text{ (s)} + 5 \text{ [REE]} \rightleftharpoons 6 \text{ } AlREEO_3 \text{ (s)} + 5 \text{ [Al]} \tag{4-2}$$

The second advantage of the use of REEs as tracers is their high atomic numbers. Hence, REE-traced NMIs appear brighter in the backscattered electron (BSE) image at SEM/EDS analysis than the surrounding steel matrix and, especially, than common deoxidation products [64, 65]. Due to the significantly different gray values, an easy and fast distinction between traced and untraced NMIs is possible. The reason for the bright appearance of REE-containing NMIs is the lower penetration depth due to the greater resistance to and the resulting high reflection of the incoming electron beam compared to lighter elements. A comparison between untraced and traced deoxidation products is illustrated in **Figure 4-3**.
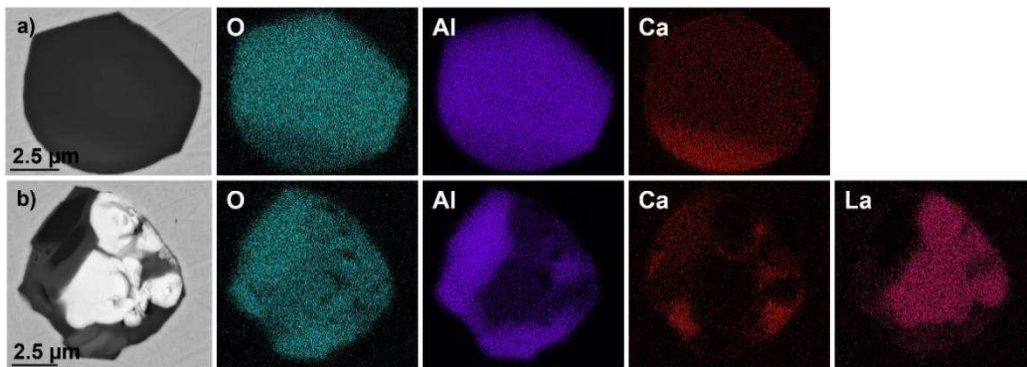
Figure 4-3: BSE-image and elemental mappings of an untraced NMI a); a La-marked NMI b).

4.1.1 Alloying of REEs to steel melt

The original advantage of the high O affinity of REEs is associated with challenges during alloying. Due to their oxidation, the direct addition of REEs is linked to high losses. After the formation of oxides, REEs are lost as tracers. The recovery rates of REEs range between approximately 10 % [56] and up to 60 % [66], depending on the way of addition and the atmospheric conditions. In most of the studies with experiments on industrial scale, the achieved recovery rates were above 50 %. The common way to add Ce in industry is the usage of a ferroalloy with a Ce content of 10 g/100 g [55, 66 – 68]. Due to the indirect addition of Ce the oxidation loss is lowered. Furthermore, the surface-to-volume ratio plays an important role to achieve high yields.

For experiments on a laboratory scale, in most cases, pure REEs are added wrapped in iron foil [58, 62, 63]. The laboratory trial of Wang et al. [56] showed that the direct addition of Ce particles without any prevention leads to high losses of REEs with an achieved recovery rate of about 10 % in their experiments. Although ferroalloys already minimize the reoxidation tendency of REEs, Zhang et al. [69] wrapped ferrocerium (FeCe) with a mass fraction of 30 % Ce additionally in pure iron foil. Thus, the contact time with the atmosphere was further reduced, and reoxidation was subsequently prevented. However, as the studies of Li et al. [62] and Luo et al. [63] point out, even after using similar settings and reoxidation preventions, the yields of REEs can vary widely. Yadav and Roy [70] investigated the evolution of NMIs by alloying mischmetal which is an alloy of La (35 g/100 g) and Ce (65 /100 g). Concerning their findings, similar NMI types as with pure La or Ce are formed. Moreover, the modification of NMIs with increasing REE content is comparable.

Wang et al. [71] list several studies about experiments on industrial and laboratory scale with REE additions in their publication. In their work, the melting and alloying methods are mentioned together with the resulting NMI types and recovery rates. Concerning their comparison of the resulting recovery rates, it was found that the highest REE yields were achieved with the usage of master alloys, followed by the direct addition of REEs. The lowest recovery rate of 2.9 % was obtained by utilizing an REE oxide-containing slag [72]. Similar findings were determined in **Paper I** [61], in which the addition of La and Ce as ferroalloy, wrapped in Al-foil or in a steel tube, was tested in a high-frequency remelting furnace on a laboratory scale. Furthermore, the production of FeCe on a laboratory scale by utilizing hydrogen plasma smelting reduction is explained in **Paper I** [61].

The required REE amount to trace pre-existing deoxidation products depends on the chemical composition of the steel and must be thermodynamically calculated. Concerning the calculations, the REE amount must be above a critical value so that no pure Al_2O_3 NMIs are predicted to be formed. A thermodynamic prediction of the formed NMI types and, subsequently, the essential amount of La and Ce to trace alumina inclusions is shown in **Paper I** [61] on the example of Al deoxidized electrolytic iron.

4.1.2 Modification of NMIs by REEs

The direct addition of REEs leads to modification of homogeneous NMIs to complex, heterogeneous multiphase NMIs, as **Figure 4-3** shows. Furthermore, complex REE-traced NMIs, such as $CeAlO_3 \cdot CeAl_{11}O_{18}$, tend to decompose into different phases during cooling. In many cases, the REE-containing phase is enclosed in the center of the multiphase NMIs. Hence, it is difficult to identify whether a modification of pre-existing NMIs took place or an agglomeration of nucleated NMIs occurred. Therefore, the originally formed deoxidation product is not traceable over the process since it cannot be assessed which NMIs were formed first. The process of decomposition can be comprehended by applying thermodynamic calculations.

The modification of the deoxidation product, Al_2O_3, with increasing Ce content was observed in the laboratory trials carried out for **Paper IV** [73] and is schematically shown in **Figure 4-4**. Those observations were similar to the findings of Pan et al. [74] and Li et al. [62]. A higher Ce content influences NMI modification and consequently leads to a different phase composition in the liquid steel. The study of Pan et al. [74] compares the modification of NMIs over the process with the thermodynamically predicted NMI types for the austenitic stainless steel Fe-17Cr-9Ni. Additional to the influence of Ce also the impact of Ti on the modification was

analyzed. Thermodynamic calculations that show the influence of an increasing Ce content on the phase composition of NMIs were carried out using FactSage™ 8.3 with database integration of FactPS, FToxid and FSstel. Furthermore, the decomposition behavior during cooling of the formed heterogeneous NMI was investigated.
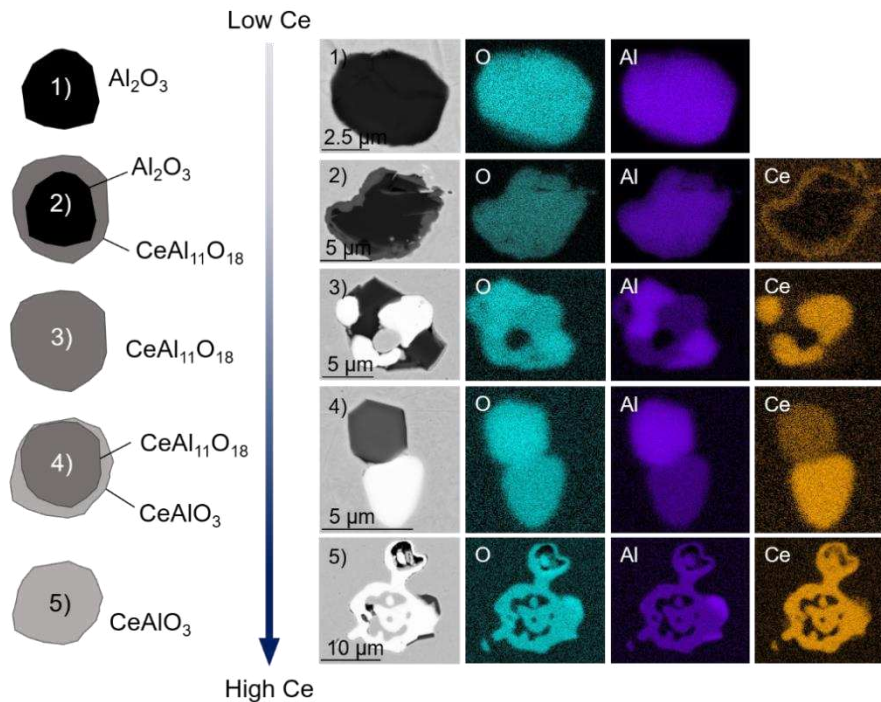

Figure 4-4: Schematic illustration of the modification of the deoxidation product, Al_2O_3, with increasing Ce content together with BSE images and elemental mappings of actual NMIs at different stages, based on the modification steps of Pan et al. [74] and Li et al. [62].

The aluminum oxides, marked with 1) are irregularly shaped, significantly darker than the surrounding steel matrix and formed by the absence of Ce. The first modification by Ce leads to the formation of an aluminum oxide surrounded by the Ce-containing $CeAl_{11}O_{18}$ phase, as shown in 2). The NMI predicted with the thermodynamic calculation fits with the corresponding BSE image at low Ce contents, as the image on the right side shows. Decomposition arises in the next stage, step 3), in which a homogeneous $CeAl_{11}O_{18}$ according to thermodynamic calculations should be formed. As the corresponding BSE image shows, the formed multiphase NMI split during cooling into dark alumina phases and bright, highly Ce-concentrated $AlCeO_3$ phases. By further increasing the Ce content (stage 4)), the complex $CeAl_{11}O_{18}$ NMI with a ring of $CeAlO_3$ around it is thermodynamically predicted to be formed. Also, in this step, a split into two phases

occurs. Based on the thermodynamic cooling calculations, heterogeneous NMIs consisting of the Al_2O_3 and the $AlCeO_3$ phases are formed during cooling. However, a distinction between NMIs of stages 3) and 4) is difficult since decomposition during cooling occurs. As the BSE image next to step 4) shows, a split can also appear in a high ($AlCeO_3$) and a low Ce-containing phase ($CeAl_{11}O_{18}$). A homogeneous NMI consisting of the phase $CeAlO_3$ occurs at high Ce concentrations (step 5)). However, complex NMIs consisting of sulfidic phases can also be formed at high Ce contents when oxygen is already bound.

Since the schematic illustration and the BSE image of an actual NMI significantly differ for the $CeAl_{11}O_{18}$, thermodynamic calculations were done to determine whether decomposition occurs or not. The decomposition behavior of NMI types can be thermodynamically calculated and explained. **Figure 4-5** shows the decomposition of the complex $CeAl_{11}O_{18}$ into Al_2O_3 and $AlCeO_3$ in an equilibrium state. Concerning the FactSage™ calculations, $CeAl_{11}O_{18}$ is decomposed at 1376.87 °C. The resulting mass fraction of Al_2O_3 is about 0.70 and of $AlCeO_3$ about 0.30.

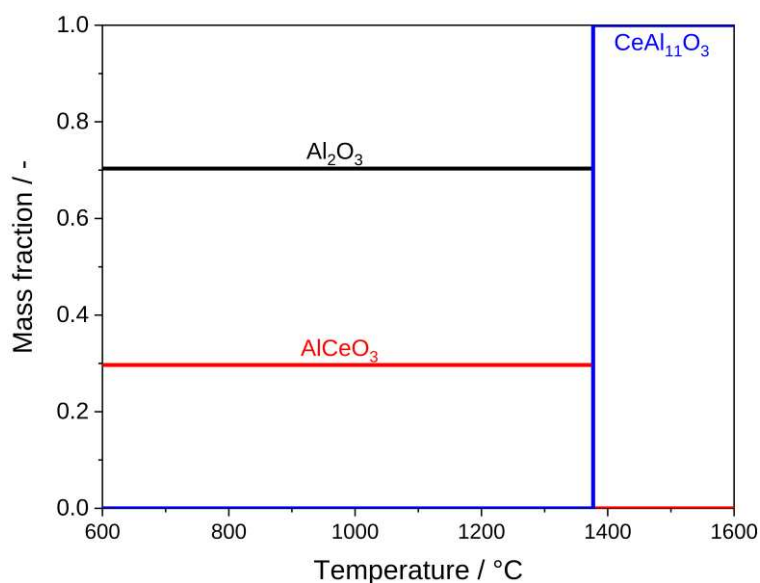**Figure 4-5:** Thermodynamic calculation of the decomposition behavior of $CeAl_{11}O_{18}$ during cooling.

The content of REEs plays an important role in the formation of NMIs. Relating to thermodynamic calculations, the NMI types formed during solidification are decisively influenced by REEs. Ning et al. [60] found that the complex $La_2O_3 \cdot 11Al_2O_3$ is no longer present when La content is increased and instead the existence of the S compound LaS is predicted at high La contents. Their thermodynamic calculations were performed to determine the occurring NMI types for high-carbon hard wire steel. In the case of Ce, the thermodynamic

calculations for a high-strength wire rope steel showed that increasing Ce content leads to a delay in formation of the originally existing NMI types, Al_2O_3 and MnS, due to the formation of different Ce compounds [56].

For high-Al steels, it was determined that the evolution route of Al_2O_3 NMIs changes from $Al_2O_3 \rightarrow LaAl_{11}O_{18} \rightarrow LaAlO_3$ to $Al_2O_3 \rightarrow LaAl_{11}O_{18} \rightarrow LaAlO_3 \rightarrow La_2O_2S \rightarrow La_2S_3$ for La contents above 40 µg/g [62]. Similar findings concerning oxide-sulfide or sulfide formation with increasing REE concentration were obtained for Ce. Increasing content of REEs leads to the modification of Al_2O_3 to oxide-sulfides that mainly consist of Ce [56]. Similar tendencies occurred in gear steel, in which the main NMI types without Ce were Al_2O_3 and MnS [63]. The influence of other alloying elements on the NMI evolution is low compared to O, S, and REEs as several studies showed [56, 62, 75 – 77]. Although the elemental compositions of theses investigated steels differ, the thermodynamically predicted NMI types are similar. With increasing REE content, the modification of Al_2O_3 NMIs is as follows: $Al_2O_3 \rightarrow Al_{11}REEO_{18} \rightarrow AlREEO_3$. A different transformation of Al_2O_3 NMIs was found in the study of Li et al. [57], in which a low-carbon, high-manganese steel was investigated. Concerning their findings, in the first modification step the Al_2O_3 inclusion is wrapped by a Ce-rich band consisting of Ce_2O_2S. Further increase of the Ce-content then leads to the formation of homogeneous Ce_2O_2S. The NMI type prediction at increasing La and Ce contents was thermodynamically calculated using the software FactSage™ 8.2 with FSstel, FToxid and FactPS 2022 databases for Al deoxidized electrolytic iron and can be found in **Paper I** [61]. The predicted modifications of NMI types with increasing REE contents were quite similar to the findings of Luo et al. [63] and Pan et al. [74]. **Figure 4-6** illustrates the thermodynamically calculated modification of NMIs with increasing La and Ce content.
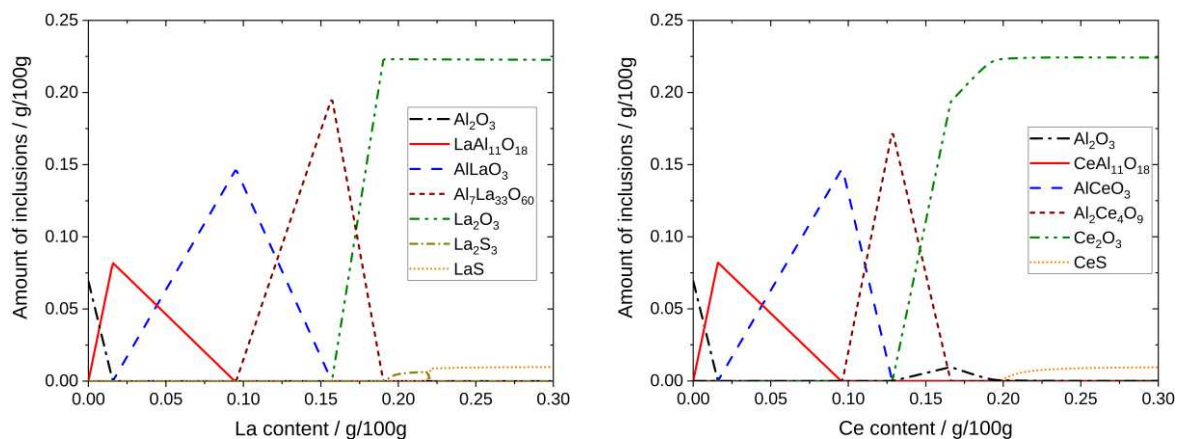

Figure 4-6: Modification of NMIs with increasing La content a); and Ce content b) [61].

As the thermodynamic calculations and the NMI evolution point out, the affinity for O is higher than for S. The impact of O on the NMI type formation with increasing La content is depicted in the study of Ren et al. [75] for non-oriented electrical steel at constant S content. According to thermodynamic calculations, the NMI type $LaAl_{11}O_{18}$ is not even formed at an O content of 5 µg/g. Furthermore, in the case of similar O and S contents, the sulfide formation is prevented, and the oxide-sulfide formation is delayed to higher La contents. The absence of sulfides at high O to S ratios at increasing Ce contents was also detected in the study of Adabavazeh et al. [78]. Since the O to S ratio primarily determines the NMI type, phase stability diagrams are necessary to identify which NMI type is formed. Phase stability diagrams, which show the impact of S and Ce as well as S and O on NMI formation, are illustrated in Ren and Zhang [77] for Al-killed ULC steel.

One significant problem of the predicted REE-modified aluminum oxides is the formation of high-melting phases. As shown in the phase diagram of the La_2O_3-Al_2O_3 system, illustrated by Li et al. [79], all chemical compounds melt at around 1800 °C. The formation of high-melting phases has the disadvantage that these NMIs stay solid throughout the steelmaking process. Concerning the findings of Bernhard et al. [80], a high number of solid oxides in the flow control system increases the clogging tendency in Ti-stabilized ULC steel due to their deposition on the SEN wall. One potential countermeasure is Ca treatment. By utilization of Ca, the melting point of the formed deoxidation products can be lowered. However, an insufficient Ca treatment can be even more harmful for nozzle clogging [81]. The reason is the formation of solid calcium aluminates. Since the REE-modification of aluminum oxides also leads to high-melting phases, the influence of Ca-treatment on these NMIs was studied by Geng et al. [66]. In their study the liquid calcium aluminates were first modified by Ce to $CeAlO_3$ wrapped in a liquid Ca-Ce-Al oxide. Subsequently, a Ca-treatment let to the formation of multiphase NMIs. However, their investigation showed that these Ce-containing NMIs cannot be modified by Ca anymore.

The utilization of La as chemical tracer was already tested in a study of Burty et al. [82]. Their experiment focused on tracking the deoxidation product, Al_2O_3, in steel samples to investigate if reoxidation occurs. Furthermore, the deposits in the SEN were analyzed to research clogging formation. A continuation of the tracer experiments was done by Nadif et al. [25], where different sources for reoxidation in Ti-ULC steels, such as slags, air, and refractory, were controlled. However, in the study of Katsumata et al. [83], in which REEs were used as deoxidizers and also as nuclei to provoke the delta-ferrite formation in stainless steel, REEs were found in the clogging layer at the SEN. According to their results, REEs tend to form clusters and further increase clogging tendency.

Differences and similarities between industrial and laboratory trials concerning tracing pre-existing NMIs to follow their modification over the process are investigated and discussed in **Paper IV** [73]. In this publication the findings from literature confirmed that the mean ECD was reduced after REE addition while the number of NMIs increased. Additionally, tracing with REEs was applied to study the separation tendency of traced deoxidation products into the slag at the industrial trial.

Liang et al. [67] used this active tracing technique for the investigation of clogging layer formation. Concerning their findings, the clogging on the SEN wall can be divided into three parts depending on the detected NMIs. In the first reaction zone near the SEN wall mainly $MgO\text{-}Al_2O_3$ NMIs were found. In this case it was considered that the MgO originates from the refractory material of the SEN. The second zone consisted of a mixture of Ce-, Al- and Ca-oxides while primarily $CeAlO_3$ and CaO were found in the third zone next to the solidified steel. In the study of Zhao et al. [84], the clogging layer was examined in a Ce-containing micro-alloyed steel to identify its origin. Relating to their results, clogging was primarily initiated by the deposition of solid NMIs. In **Paper IV** [73], the clogging layer was also investigated. The analysis of the clogging layer and in particular the La and Ce concentrations over the layer thickness enabled a distinction between the different heats cast through the SEN. In addition, the determination of La and Ce concentrations and, subsequently, the occurrence of REE-containing NMIs in the analyzed clogging layer in **Paper IV** [73] led to the conclusion that pre-existing aluminum oxides were involved in clogging formation. Additionally, slag analysis showed an increase of La and Ce concentration over the process confirming seperation of REE-traced NMIs into the slag.

4.1.3 Characterization of REE-traced NMIs

After investigation of the modification and handling the REE addition, the next step is the characterization of the formed multiphase NMIs. As illustrated in **Figure 4-7 a**, complex heterogeneous NMIs consist of different phases that can be brighter or darker than the surrounding steel matrix depending on the REE content. The automated SEM/EDS analysis has to be optimized to detect all phases of REE-traced NMIs, as can be seen in **Figure 4-7 b**. The difficulty that occurs is the split of the complex NMI into multiple single phases. As a result, the evaluation of the received chemical and morphological data is incorrect concerning the chemical composition of the whole NMI as well as morphological parameters such as their equivalent circular diameter (ECD) [85].
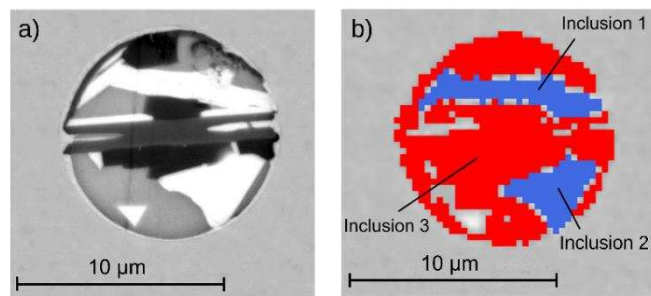
Figure 4-7: BSE image of a REE-traced multiphase NMI a); detected particles by SEM b).

One possible solution for the issue of erroneously split multiphase NMIs is discussed in **Paper II** [86] by implementing a recombination tool for a less error-prone validation. The mathematical modeling is inspired by the findings of Meng et al. [87]. In their study, the double-threshold scan was applied to detect all phases of a multiphase NMI. Afterwards, the conditions for coupling of REE-containing phases and NMIs consisting of light elements, such as Al or Si, were checked in three steps. Firstly, the shapes of the particles are divided into circles or ellipses based on the aspect ratio. In the second step, the distance between the centers of the particles that should be recombined is calculated as well as the summed-up radii in the direction that connects their centers. Finally, depending on the ratio between the distance and the summed-up radii, it is decided whether the inclusions belong together or not. One major difference between the mathematical modeling by Meng et al. [87] and the recombination tool developed in **Paper II** [86] is the implementation of a safety factor. In the recombination tool, the distance between the central points of the particles is decreased by an empirically determined safety factor. Subsequently, the sum of the particles' radii is subtracted. The implementation of a safety factor is essential to compensate for errors that occur between the measured and the calculated shapes of inclusion. A detailed explanation of the merging procedure, as well as the recalculation of the chemical composition and the ECD of recombined multiphase NMIs, can be found in **Paper II** [86].

While the recombination tool is an essential program to improve the characterization and evaluation of REE-modified NMIs, it is still connected to the time-consuming automated SEM/EDS analysis. Hence, novel approaches are needed to diminish the time and cost involved in characterizing the micro-cleanness in steel. A promising concept is the implementation of artificial intelligence (AI) which has already been applied in steel research and production [88 – 90]. Three types of AI algorithms can be distinguished: supervised, unsupervised and reinforcement learning. The main difference between these categories is the learning process of the algorithms. In the case of supervised learning, labeled datasets (e.g. images with meaningful tags) are used and the algorithm tries to identify correlations

between the data and the corresponding labels. In comparison, unsupervised learning algorithms detect similarities in unlabeled datasets. Reinforcement learning uses feedback (reward or punishment) of past behavior for training. [91]

Guo et al. [92] connected in their study process parameters, chemical compositions and steel properties to calculate possible boundaries of characteristics under certain conditions. Another example of using AI in metallurgy is the research of Xie et al. [93]. In their study, the mechanical properties of hot-rolled steel plates were controlled based on chemical composition and production parameters. Due to the implementation of a deep neural network model online in the steel plant, it is possible to adapt the mechanical properties of the steel sample during production by adjusting process parameters. Another possibility is the usage of AI-assisted tools for the automated detection of, e.g., surface defects on steel products. In this case, the samples are automatically scanned by an optical-digital control system, and the deep learning algorithms subsequently highlight the detected defect [94, 95]. Nevertheless, AI-applications have not been effectively implemented in metallurgy today. One major reason is the difficulty of interpreting the achieved result, which is often quite complex [96].

A few studies already dealt with the application of AI-enhanced tools in the field of inclusion metallurgy. Trials by Abdulsalam and Webler [97] connected the support by AI-based image processing with SEM/EDS analysis. The aim of their study was to determine the chemical composition of NMIs based on the gray value of the BSE image since it is linked to the atomic number of the element [64]. Although only elements such as S, Ca, Al and Mn were considered, difficulties appeared, if the element content showed a broad distribution. AI-based image processing solutions need huge data sets for the training of the algorithms. Since the usage of supervised learning assumes the manual, time-consuming and human error-prone labeling of images, Abdulsalam et al. [98] applied unsupervised learning algorithms to identify NMI clusters in steel. In a further study, Abdulsalam et al. [99] used deep learning algorithms to predict different NMI types based on the BSE images from SEM. Although they tested two different machine learning algorithms (random forest and convolution neural network), the binary distinction between inclusion and non-inclusion led to high accuracies of about 90 % in both cases. For a more precise distinction, four and five different NMI classes were defined. In the case of the 4-class model, the algorithms should distinguish between oxides, sulfides, oxysulfides and non-inclusions, decreasing the accuracy to values below 80 %. For the 5-class model, an accuracy of 60 % was reached, since the algorithms had to differentiate between specific NMI types, such as alumina or calcium aluminates. Regarding the two applied algorithms, the random forest achieved slightly better results during all classifications.

Another approach to support the automated SEM/EDS analysis with AI-powered image processing for an accelerated steel cleanness evaluation was done by Ramesh Babu et al. [100]. Compared to the concept of Abdulsalam [99], they did not utilize the BSE images directly. Their machine learning models use the morphological data and the mean gray value from the SEM analysis without an EDS measurement. The algorithm used for the binary categorization (inclusion or non-inclusion) achieved similar results as the image-based concept of Abdulsalam [99]. With an increasing number of classes, the accuracy also decreased significantly for this approach. The maximum accuracy in their 8-class model, where the algorithm should distinguish between different NMI classes (oxides, nitrides, sulfides, their mixed phases and rejected data), was 61 %. However, they also tried to improve the accuracy of the model by optimizing the BSE image settings. Concerning their results, the contrast-to-brightness ratio significantly influences the model's prediction accuracy. Although their approach seems promising for a faster NMI classification, the results achieved must be treated with caution since the particles tested in this study were mainly oxides, sulfides, oxide-sulfides, and rejected data. The distinction of NMI classes based on the mean gray value and morphological data can be difficult, especially for multiphase NMIs.

In **Paper III** [101], a machine learning algorithm is applied for a faster steel cleanness analysis of La-traced NMIs. A random forest classifier was chosen based on the findings of Abdulsalam [99] to predict the NMI class based on the processed BSE images. The first step was similar to the previously mentioned studies, using a model for the binary distinction between NMI and non-NMI. The achieved accuracy was almost 95 %. In the next step, a 4-class model was applied to classify particles into La-traced heterogeneous, La-traced homogeneous, high La-containing homogeneous and untraced NMIs. The classes for the image-based characterization by AI-assisted tools can be seen in **Figure 4-8**. Accuracies over 97 % were obtained for the classes of high La-containing homogeneous NMIs and traced homogeneous NMIs, while the distinction of the other two classes was connected to difficulties in the 4-class model due to too little data. This approach supports the accurate evaluation of traced NMIs. The manual and the AI-based evaluation of La-traced NMIs are described in **Paper III** [101].
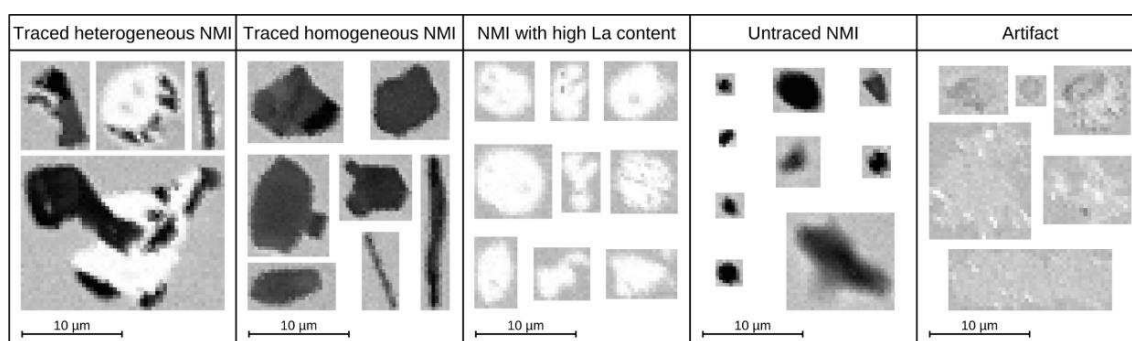
Figure 4-8: BSE images of detected particles at automated SEM/EDS analysis for image classification with AI-assisted tools [101].

Since NMIs are randomly cut at cross-section samples, the actual size and shape of the investigated NMIs cannot be determined [49]. One possible remedy for this problem is three-dimensional analysis by applying extraction techniques. The selection of a suitable extraction method depends on the steel grade as well as on other parameters, such as the expected size of the analyzed NMIs. In the study of Janis et al. [102], characterization results of a cross-section sample, an etched cross-section sample and a filter after electrolytic extraction were compared with each other. Concerning their findings, electrolytic extraction can be applied to determine NMI and cluster size as well as their chemical composition. The morphology of NMIs can be investigated precisely using this method. However, the location of NMIs and their distribution in the steel cannot be studied by utilizing this technique. In addition, Doostmohammadi et al. [103] found that the precipitated compounds of the steel matrix can partly cover the extracted NMIs. Hence, the exact NMI size is difficult to determine. Zhang et al. [104] compared different extraction methods and discussed their advantages and disadvantages. However, it must be noted that the choice of extraction technique and agent depends on the steel grade. An overview of different extraction methods, together with the used reagents for different steel grades, can be found in the review of Ramesh Babu and Michelic [105].

Moreover, some NMI classes, in particular sulfides, are less stable than others [105]. One approach to extracting and studying these less-stable NMIs is the sequential chemical extraction technique using nitric acid as an extraction agent [12]. In **Paper II** [86], this technique was applied to extract and subsequently analyze REE-containing multiphase NMIs. Since the stability of these NMIs was not known, 3 vol.-% nitric acid, which is a weak acid, was chosen as the extraction agent. **Figure 4-9 a** and **b** illustrate REE-containing multiphase NMIs on the cross-section for two-dimensional analysis and the filter after extraction for three-dimensional investigation. As can be seen, the MnS did not dissolve after extraction.
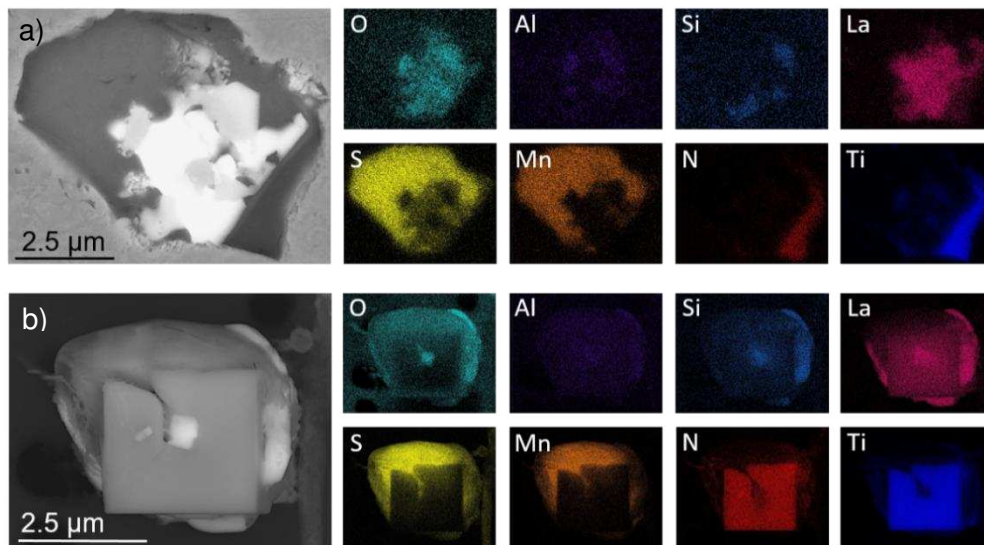
Figure 4-9: BSE image and elemental mapping of a multiphase NMI consisting of (Al, Si, La) oxide, surrounded by MnS and TiN two-dimensional a) and three-dimensional investigation b) [106].

The results of the automated SEM/EDS analysis of the filters containing extracted NMIs after successful extractions can be found in **Paper II** [86]. In this study, the mean ECD of the extracted NMIs on the filter was smaller compared to the value detected in cross-section samples. Similar findings were obtained in the study of Karasev et al. [107]. The reason for this apparent decrease in NMI size is the discovery of NMIs with an ECD of about 1 μm which was previously below the detection limit at the automated SEM/EDS analysis.

Extraction techniques are also suitable to investigate clusters in more detail. The electrolytic extraction method was, e.g., applied to study the impact of Al_2O_3 clusters on clogging layer formation. Due to the extraction, it was possible to determine the morphology of the Al_2O_3 NMIs. It was found that the morphology changes over the process and that the NMIs in the cluster mainly had a spherical shape [108]. In the studies of Bi et al. [109] and Nabeel et al. [110], the morphology and size of REE-containing clusters were investigated by applying electrolytic extraction. Additionally, Nabeel et al. [110] connected the REE-containing cluster size distribution in the steel samples to study the formation and growth mechanisms of these clusters over the process.

Besides the precise study of an inclusion's morphology, the three-dimensional characterization can also be applied to determine the number of NMIs per volume [111]. For this purpose, a defined volume of the steel sample is dissolved, and the subsequently extracted NMIs are counted using the single-particle optical sensing (SPOS) method. Thus, the volume

density of NMIs can be evaluated and, additionally, the size distribution can be determined. **Figure 4-10** shows schematically the structure and operating principle of the SPOS method.
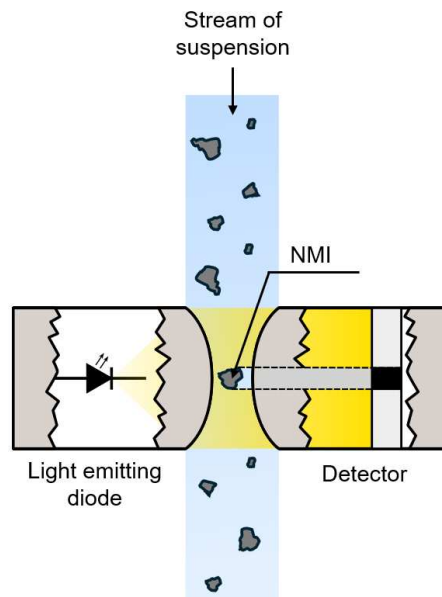

Figure 4-10: Schematic illustration of single-particle optical sensing (SPOS) method to determine size and number of particles in suspensions, based on Karasev and Suito [111].

Another option to determine the number of NMIs per volume is the Woodhead method [112]. This statistical method is based on the SEM/EDS results of the two-dimensional NMI characterization. Since the NMIs are presumed to be spheres in this model, it uses the cutting probability of said spheres. Concerning the detected circular area of cut NMIs at cross-section samples, the actual NMI size can be predicted. Based on the actual spatial expansion of the single NMIs, the NMI density per volume can be evaluated. Schickbichler et al. [113] used the SPOS method to determine the volume fraction of REE-containing NMIs. Subsequently, the observed number of particles per volume was compared to the statistical Woodhead method. Concerning their findings, the calculated NMI density per volume coincided with the one determined by the SPOS method for small particles. In their case, a significant distinction occurred above 7 μm.

The actual status of this active tracing technique can be summarized as follows:

- The active tracing technique adding REEs is suitable for marking pre-existing deoxidation products.
- Traced NMIs can easily be distinguished from untraced NMIs in the BSE image at SEM/EDS analysis.
- Challenges occur concerning alloying, correct characterization, and evaluation of traced NMIs.

- REEs influence the properties of NMIs.

- New approaches to identify the origin of NMIs are necessary.

4.2 Passive tracing with elemental fingerprint technique

The REE-Fingerprint is a passive tracing method and a novel approach in metallurgy that enables the determination of the source of NMIs. In comparison to active tracing with REEs, the NMIs are not modified or influenced by any additional tracing agent. In this technique, the natural concentration of REEs is measured in materials. Besides the lanthanides, Sc and Y are counted among REEs since these elements have similar properties and further occur in the same mineral deposits. One of the most important characteristics of REEs is the contraction of lanthanides, which means that the ionic radius successively shrinks with the increase in atomic number. [114, 115] **Figure 4-11** highlights the 17 elements in the periodic table that count to the REEs.
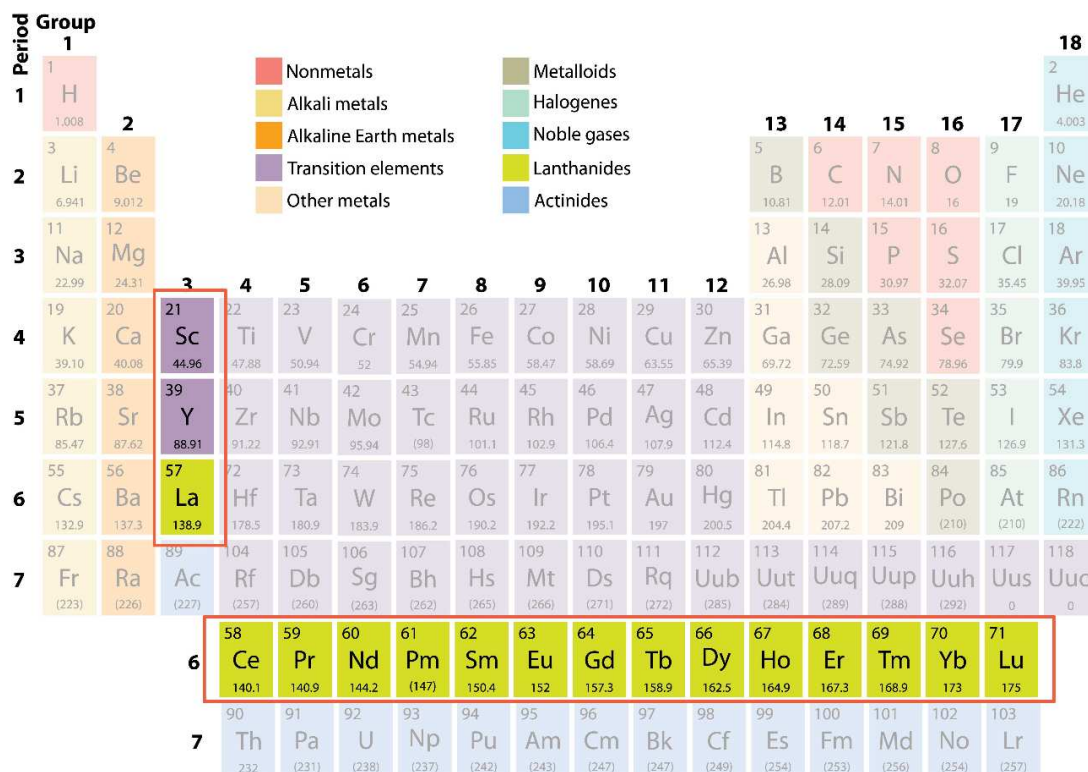

Figure 4-11: Periodic table of elements, highlighting lanthanides (La to Lu), Sc and Y [116].

REEs are not as rare as their name assumes. Due to their lithophile characteristic, these elements are found in nature bound to O in rocks on the Earth's surface [114]. Their average

concentration in the Earth's crust is between 130 and 240 µg/g [117]. In other materials such as soils or water the natural concentrations of REEs are between a few µg/g and ng/L or µg/L respectively [118, 119]. The REE-Fingerprint is based on measuring those low natural concentrations.

Due to these low concentrations, an adequate analytical instrument is required to make precise and accurate determinations. In the study of Balaram [117], the most popular analyzing techniques are listed together with their detection limits of REEs. Different types of inductively coupled plasma–mass spectrometers (ICP-MS) are the most suitable analytical instruments for this purpose, with detection limits of µg/g and even lower in the case of high-resolution ICP-MS of ng/L. Solid samples can be analyzed with ICP-MS after digestion or, in the case of heterogeneous samples by applying laser ablation (LA) ICP-MS. [120, 121] One big benefit of (LA)-ICP-MS is that these analyses do not take place under a vacuum compared to other techniques, such as e.g., secondary ion mass spectrometry. Hence, the sample preparation is less sensitive and time-consuming. Besides the detection of low concentrations of elements, it is further possible to measure the isotopes of elements. At the LA-ICP-MS, choosing between a line scan or single-point analysis is possible. Concerning the former one, the laser scans the sample continuously. In this case, many overlapping spots are created. With regard to the latter, the laser stays on the same spot for a defined time. [122, 123]

The steps for an LA-ICP-MS analysis of solid samples can be summarized as follows [122]:

1. Sample preparation
   (can include grinding and cleaning)
2. Calibration of the system with a suitable matrix-matched standard
   (Here, the standard must have a matrix close to the sample. Further, it is beneficial that the used standard and the sample are inside the ablation chamber at the same time and measured successively.)
3. Ablation of the material in the LA chamber by a focused laser beam
4. Transport of the ablated material by a carrier gas steam into ICP
   (This can be He, Ar or air if it is exchanged to Ar after ablation. At this point, the analysis is similar to the common ICP-MS analysis.)
5. Ionization of the aerosol
6. Transport to and through the MS
7. Separation of ions in MS based on their mass-to-charge ratios
8. Detection of ions based on the time-resolved data

Ke et al. [124] approved the applicability of LA-ICP-MS as an analytical method for the quantitative determination of REE concentrations in REE-rich minerals with concentrations

about a few µg/g. In their study as well as in other works where the REE concentrations were measured, the external standard reference material 610 based on the national institute of standards and technology (NIST) was used for calibration. Besides the condition that the matrix of the standard should be close to the one of the sample, it is also necessary to adapt the standard to the concentrations of REEs [125]. Based on the study of Sousa et al. [126], there are hardly suitable reference materials that meet the requirements and can subsequently be used as external standards for the determination of REEs.

The application of the REE-Fingerprint technique necessitates to normalize the measured natural concentrations of REEs to chondrites. Chondrites are meteoritic rocks with a similar composition in terms of non-volatile elements as the planet Earth. The mass fraction of lanthanides in the chondrites used for normalization can be seen in **Table 4-I**. By examining this list, it is noticeable that Pm is missing. The reasons for the exclusion of this element are its radioactivity, as well as its short half-live of less than 17.7 years. Relating to the absence of Pm in nature, this element is not detectable. [127, 128]

Table 4-I: Mass fractions of lanthanides in chondrites (used for normalization) (ng/g) [127].

La	Ce	Pr	Nd	Sm	Eu	Gd	Tb	Dy	Ho	Er	Tm	Yb	Lu
236	616	92.9	457	149	56.0	197	35.5	245	54.7	160	24.7	159	24.5

As a result of this chondrite normalization, a unique and comparable pattern occurs for the investigated material. Without the normalization, the resulting patterns would appear as a sawtooth curve. The reason for this trend is the Oddo-Harkins rule. Regarding this rule, elements with even atomic numbers are more frequent in nature than those with odd numbers. Besides the altering trend, the concentration of REEs drops from light to heavy REEs before the normalization. [115] Since the resulting curves of the measured REE-concentrations are quite similar before normalization, bigger differences between the patterns of the single substances occur after the chondrite normalization [129].

Furthermore, the measured REE-concentrations can be normalized to one potential source to verify whether a material exactly corresponds to it. In the case of a complete match of two materials, a straight line would appear. [130]

REEs primarily appear as trivalent cations in nature. Exceptions are Ce, Pr, and Tb, which can also be tetravalent, as well as Sm, Eu, and Yb, which can be divalent. The different oxidation states enable the selective oxidation or reduction for a separation of these elements. However, in the case of Eu the oxidation state allows conclusions about the process conditions.

Depending on whether a positive or a negative Eu anomaly occurs at the REE-Fingerprint, oxidizing and reducing conditions can be distinguished. A negative Eu anomaly means that Eu is reduced and subsequently present in the divalent state. Furthermore, the occurrence of negative anomalies indicate that chemical modifications happened over the process. [115, 128, 131 – 133]

The elemental fingerprint has already been a common technique in other fields such as archaeology, geo- or food-chemistry for years [134 – 141]. The study of Kamber [142] is focused on the geochemical fingerprint and its improvement over decades to an everyday analyzing method. The geochemical fingerprint assumes that the chemical composition of minerals or rocks provides information concerning their formation and the geological process due to chemical and isotopic patterns. Compared to the REE-Fingerprint, not only are the concentrations of REEs measured, but also other trace elements that occur in minerals. [142, 143] Kamber [142] gave some examples to show how versatile the fingerprint technique can be applied. Besides determining the origin of Chinese ceramics, this method can be applied to indicate kimberlite (deposits of diamonds) or to monitor dust transport and, subsequently, atmospheric pollution [142].

The REE-Fingerprint in particular can also be applied for similar investigations. One example for the utilization of this technique is shown in the study of Šmit [144] by determining the origin of façon-de Venise glass. Optically, it is not possible to differentiate between the original and imitation versions. However, applying the REE-Fingerprint technique and the resulting REE patterns allow a distinction between imitations where glass from Slovenia was used and the original Venetian white glass.

Furthermore, the REE-Fingerprint is an important tool in food chemistry where it is implemented to track or confirm the origin of fruits, vegetables or meat [139, 145]. Based on the natural life cycle and their interaction with soil, the received REE patterns of fruits or vegetables are distinguishable concerning their geographical origin. In the case of meat, it is possible to identify whether it originated from an animal in the wild or a domesticated one since the resulting patterns differentiate due to their nutrition [138].

How varying REE patterns can look with the same product but different origins is shown in **Figure 4-12** by the example of pumpkin seed oil. In both diagrams, two intermediate products of the pumpkin seed oil, the pressed and the extracted one, are compared. On the left side (a), the oil originated from Lower Austria. On the right side (b), the investigated oil was from Styria. Both regions are within Austria, but there is a significant difference between these patterns. However, the patterns of pressed and extracted oil do not show a big distinction within one region since the anomalies, as well as the distribution of the heavy REEs are similar [146, 147].

In the study of Bandoniene et al. [147], the topsoil and other parts of the pumpkin were also analyzed by applying the REE-Fingerprint technique. Analogically, according to the patterns in **Figure 4-12**, the different stages of the product had similarities, while pumpkins from other regions and, subsequently, other soils deviate significantly.
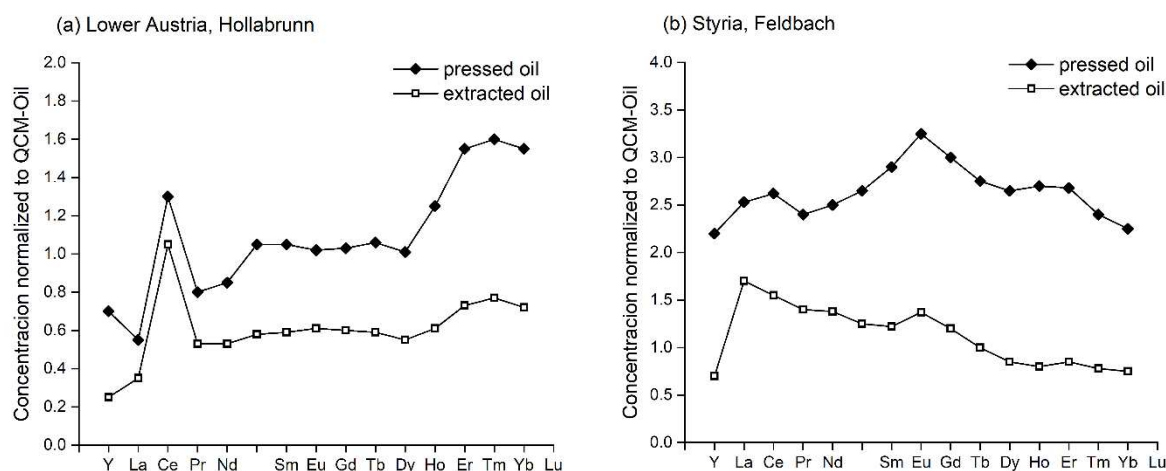

Figure 4-12: Comparison of REE patterns from different intermediates of pumpkin seed oil and from various producers in different regions; redrawn from Bandoniene et al. [147].

A further study by Bandoniene et al. [148] combined the addition of REEs with fingerprinting. For this purpose, tomatoes were labeled by watering the soil with Nd and Er-spiked water as an indicator or the direct addition of Nd and Er oxides to the soil. Therefore, the origin of local tomatoes can be guaranteed, and the resulting unique Nd- and Er-enriched fingerprints are distinguishable from products of foreign origin.

The REE-Fingerprint can also be applied in metallurgy. In the study of Sousa et al. [126], this technique was utilized to identify different mineral stages of iron ore by their different REE patterns. Another approach for implementing the elemental fingerprint in metallurgy is shown in the study of Wibner et al. [130]. Their research focused on investigating the behavior of REEs during the remelting process of aluminum dross with salt in a top-blown rotary converter. During the Al recycling, REEs enter the process route via electronic scrap because of inadequate scrap processing. Since their behavior during recycling is unexplored, the REE-Fingerprint should clarify whether REEs separate into the slag during the recycling process. REE are enriched aluminum dross, an oxygen-rich by-product of the Al production in the smelter, as they have a higher oxygen affinity than Al. The results of the REE-Fingerprint showed that the pattern of salt slag and dross were almost identical. Hence, it can be concluded that the REEs in the dross pass nearly directly into the salt slag at the recycling process.

As part of this thesis, two studies applying the REE-Fingerprint were conducted. The first (shown in **Paper V** [149]) aimed to identify if pre-existing deoxidation products agglomerated and attached to the SEN wall, leading to clogging layer formation. Regarding the results of the passive tracing, the patterns of Al granules and the sliding gate sand had similarities with the REE pattern of the clogging layer. Hence, both auxiliaries contributed to clogging. Since the active tracing by using La and Ce was also performed for the investigated melt and REE-traced alumina NMIs were determined in the clogging layer, the results of the REE-Fingerprint were confirmed.

In **Paper VI** [150], both active and passive tracing were also applied on an industrial scale. At the active approach, six melts of Ti-IF steel were cast. The first and last heats were untraced. For the second and fourth heat, La was applied as a tracer. Ce functioned as a tracer for the third and fifth heats. Due to the active tracing, dividing the clogging layer concerning the heat cast was possible since La and Ce were found in specific sections of the SEN. Consequently, the layer growth per melt can be studied. For the REE-Fingerprint, the clogging layer of the first SEN, mesoscopic NMIs, and several auxiliaries, such as Al granules, casting powder and slag former, as well as mold and tundish slags, were analyzed. The resulting pattern of the SEN also showed an increase in heavy REEs, such as the sliding gate sand. Similar results were previously achieved in **Paper V** [149] concerning the contribution of the sliding gate sand to clogging. In contrast to the former study, no relation between Al granules and the clogging layer was found. Besides the clogging layer, the REE-Fingerprint was further applied to determine the origin of mesoscopic NMIs detected in the steel samples. Regarding the passive tracing approach, the source of the investigated NMIs was mold slag and, thus, casting powder.

The elemental fingerprint is already a common method in food chemistry and archaeology, but novel for metallurgy. In the following a short overview over elemental fingerprinting is given:

- It can be used to identify the source of NMIs or clogging.
- This method depends on the natural REE concentration in the material.
- Limitation of quantification for some materials due to a too low REE concentration, therefore, restricting the applicability of this method [147].
- This method is sensitive to changes since contamination caused by one process step can significantly influence the pattern. [151]
- The sensitivity can be advantageous in the case of identifying the impact of single process steps.

4.3 Isotopic spiking with enriched stable isotopes

With this tracing technique, the isotopic ratio of an element of interest is artificially changed using enriched stable isotopes. The targeted change of the isotopic composition results in an unambiguously extrinsic tag of the altered element. Therefore, the isotopically modified element can be tracked over time or process. Enriched stable isotopes are non-radioactive tracers. Further, the method is non-destructive and does not influence the properties of the investigated element. [152, 153] The principle of extrinsic marking by enriched stable isotopes is illustrated in **Figure 4-13** using the example of Sr isotopes. The isotopic composition of the used spike (**Figure 4-13 b**) consists primarily of ^{84}Sr and ^{86}Sr and is significantly different to natural Sr (**Figure 4-13 a**) where ^{88}Sr amount to over 80 %. The resulting isotopic composition of this mixture is shown in **Figure 4-13 c** and clearly differentiates from both, the natural and the enriched isotopes.
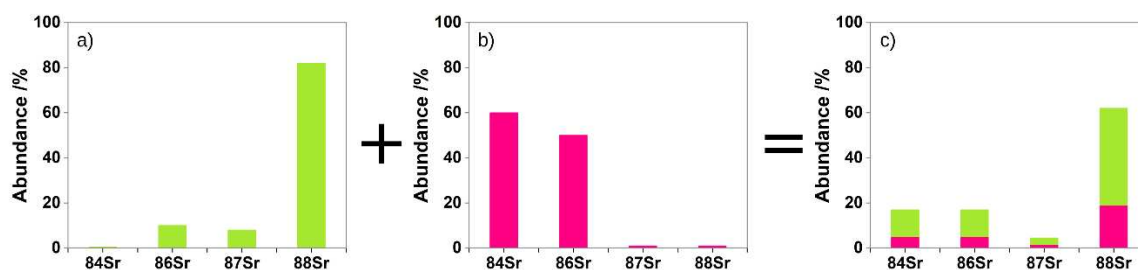

Figure 4-13: Principle of the isotopic spiking by extrinsic marking on the example of Sr isotopes; natural isotope a); enriched stable isotope b); resulting isotopic composition of the mixture c) [153].

De Hevesy [154] first applied the isotopic tracing by using radioactive isotopes. In their investigation, Ra D was used as an indicator to determine the solubility of low-soluble Pb compounds since Ra D and Pb are inseparable. [154] Today, there are still studies with radioactive isotopes. One example is the administration of ^{11}C or ^{18}F choline tracers to detect different kinds of cancers [155].

The utilization of enriched stable isotopes instead of radioactive ones is advantageous since these isotopes do not disintegrate after an element-specific half-life period and therefore no radiation is emitted [153]. Isotopes count as stable isotopes when no half-life period has been known or detected by today [156]. The distinction of stable isotopes is based on their mass differences, while unstable, radioactive isotopes are distinguished by their emitted radiation [157]. Enriched stable isotopes, which are used as spikes, cannot be isolated from the element. They can only be enriched by implementing several successive separation steps.

Although there are different techniques for isotope separation, primarily centrifugal cascades are used to economically separate medium- and heavy-mass elements. [158, 159]

Further, the application of enriched stable isotopes as tracers is beneficial when the natural isotopic-abundance variation is small or nonexistent [153]. An additional advantage of these isotopes is that they are nontoxic and therefore can be used as spikes for investigations on living organisms [160]. Subsequently, this method is an essential tool in medical [161, 162], biological [163] and ecological [152, 164] studies. In the review of Stürup et al. [160], several applications of enriched stable isotopes as tracers in terrestrial systems, animals or even humans are listed concerning their aim, labeling technique and applied analytical method. Dang et al. [164] used isotopically enriched [109]Ag as a tracer to track Ag-containing nanoparticles and study their uptake pathway into plants as well as their subsequent entry into the human food chain. Medications with enriched stable isotopes are applied in medical or clinical studies to investigate the elemental pathway in organisms or metabolic processes [165]. For instance, Bonaventura et al. [166] added a stable [70]Zn isotope as a spike to study the immune response of human bodies. In their case, the focus was on how inflammation is linked to Zn deficiency. In the study of Draxler et al. [167], Mg pins were modified by enriched stable isotopes and implemented in the femoral bones of rats. Due to the modified isotopic composition, the elemental migration of Mg in the rats' bodies can be studied. The degradation of the bone implants was investigated by measuring the isotopic ratio of [26]Mg/[24]Mg in different organs of the rats. Further, it is possible to distinguish whether Mg is enriched in one organ or excreted over time. Concerning their findings, applying Mg pins as implants leads to a full recovery of the bones. Moreover, it was found that the organism can handle the excessive amount of Mg that occurs.

Differences in isotope ratios are expressed by the isotope ratio of a sample relative to a known standard and multiplied by 1000 since the differences are in most cases very low. This term is called the δ-notation and exemplarily shown on O isotopes in Equation (4-3) [168].

$$\delta^x O = \left(\frac{\left(\frac{^xO}{^{16}O} \right)_{sample}}{\left(\frac{^xO}{^{16}O} \right)_{standard}} - 1 \right) \times 1000 \qquad (4\text{-}3)$$

One disadvantage of the isotopic spiking technique with enriched stable isotopes compared to radioactive isotopes is that a higher amount of isotopes must be added. Since stable isotopes are present in the natural isotopic abundance of the element, sufficient addition of the spike is required to achieve a significant shift in the isotopic composition. As this method is

based only on the mass differences of the various isotopes of an element, accurate and precise measurements by applying mass spectrometers are necessary. [160] In the review of Stürup [169], different analyzing methods as well as various specific ICP-MS types, are explained and compared using the example of studies in humans.

The isotopic pattern deconvolution (IPD) is a mathematic tool for quantifying the components in an isotopic mixture that consists of enriched stable isotopes and the natural-abundance of isotopes [170]. The method is based on the corresponding isotope pattern of the investigated sample. The application of IPD facilitates the determination of the contribution of a single component to the chemical composition of a sample as well as the individual contribution of different sources to the mixture. In the study of Irrgeher et al. [171], an enriched Sr double spike was used as a distinctive tracer. Due to the significant contribution of natural Sr to the overall Sr isotopic composition in this case, IPD was applied to calculate the isotopic composition of the used spike. By utilizing IPD, it is not necessary to know how much of the spike is incorporated into the matrix of the natural sample to deconvolute the isotope pattern. The studies of Meija et al. [172, 173] provide detailed explanations of the mathematical considerations behind IPD regarding the multiple linear regression model for the evaluation of isotope data. Furthermore, the IPD method can be used to determine spikes with ultra-low concentration levels, as the study of Irrgeher et al. [174] demonstrated. In their research, it was possible to calculate the actual enrichment by the spike ^{204}Pb, although its concentration was below 1 pg/g blood in human bodies.

Since slags are potential sources contributing to the formation or modification of NMIs in the steelmaking process, the isotopic spiking was applied in **Paper VII** to study their influence. In this research, enriched stable ^{26}Mg isotopes were used as a spike to shift the isotopic composition of the slag concerning Mg and subsequently isotopically modify the slag. For the steel/slag experiments performed on a laboratory scale, two potential sources of Mg existed: a natural one and the isotopically modified slag. The amount of added spike to significantly influence the isotopic composition of the slag accounts for approximately 0.6 % of the total slag weight. In comparison, common slag tracer, such as BaO or SrO, require amounts of 5 to 15 % of the slag's mass fraction [179]. By measuring the isotopic composition of the NMIs found in the steel samples, it can be determined whether the slag contributed to their formation or modified them over the process. The results of the investigated NMIs revealed that a modification of NMIs occurred in these steel/slag experiments. Furthermore, the investigation of the slag before and after the trials regarding its isotopic composition confirmed that the slag and its isotopic ratio were stable throughout the process. Due to the low levels of enriched

stable ^{26}Mg isotopes, IPD was applied to evaluate the isotope data. Detailed information on this topic can be found in **Paper VII**.

The studies conducted in this work suggest that this tracing approach has the potential to be applied in metallurgy as shown by the following aspects:

- The findings in **Paper VII** confirmed that the source of NMIs can be identified by applying the isotopic spiking method.
- In contrast to active tracing using REEs, this method does not influence the properties of NMIs.
- Accurate and precise analyzing techniques are required to receive reasonable results with this technique.

4.4 Isotopic fingerprinting

Another approach to isotopic fingerprinting is the detection of O isotopes, where no further addition of enriched stable isotopes is needed. In the study of Rodrigues et al. [175], the natural isotope abundance ratios of O and Sr were measured to distinguish the geographical origin of 20 different green coffees.

The first applications of isotopic fingerprinting in metallurgy were also based on the determination of the difference in isotopic ratios of O. This passive tracing technique was applied to identify the origin of the clogging layer in the SEN. The three-component-model of Toulouse et al. [176] took sliding gate sand, deoxidation products and air oxygen as possible oxygen sources into account. According to the measured δ^{18}O values of the isotope analysis, the contribution of the three components was determined. The analysis of the O isotopes suggest that the clogging layer consists primarily of the sliding gate sand and deoxidation products since the δ^{18}O value varies between +2 and +13 ‰. The impact of air oxygen can almost be excluded since δ^{18}O is + 23.5 ‰ [177]. The evaluation of the different O sources is difficult since the isotopic ratios of O differ only in small ranges and contaminations by air oxygen can occur. Furthermore, the large analytical uncertainties are critically for a precise determination. [176, 178]

5 Objectives

This PhD research aims to develop novel methodologies to trace the origin of NMIs and track their modification over the process. The focus is primarily on determining the cause of clogging during continuous casting of Ti-stabilized IF steels. In the first step, active tracing by direct addition of REEs is applied and improved on a laboratory scale. In the next step, characterization methods are optimized for a correct evaluation of REE-modified NMIs and also AI-driven tools are applied to improve and support the automated SEM/EDS analysis for classification and distinction between NMIs and non-NMIs (such as scratches or grinding residues). Active tracing experiments are planned and performed on industrial as well as laboratory scales to investigate NMI formation and modification. Furthermore, NMI separation into the slag and formation of the clogging layer are studied by means of active tracing with REEs. Finally, two innovative tracing approaches are developed and applied to trace the origin of NMIs in metallurgy. One applied technique is the elemental fingerprint based on the natural concentration of REEs in different auxiliaries. By using this passive method, it is possible to identify the source of NMIs or the clogging layer by comparison of the resulting patterns in the distribution of REEs with the ones from the tested auxiliaries. The second novel tracing technique is the isotopic spiking method. In this case, one possible source for NMIs has a modified isotopic composition. The shift in the isotopic composition is performed by actively adding enriched stable isotopes.

The main objectives of this PhD research are summarized as follows:

1. Implementation and improvement of active tracing by REEs on a laboratory scale by developing an alloying concept.

2. Optimization of two- and three-dimensional characterization techniques to correctly evaluate REE-traced NMIs.

3. Application of AI-assisted tools to distinguish between NMIs and non-NMIs, to classify traced and untraced as well as homogeneous and heterogeneous multiphase NMIs by SEM analysis without additional EDS evaluation.

4. Conception and validation of tracing trials on industrial and laboratory scales to assess similarities and differences in inclusion formation and modification over the process. At the industrial experiments, the NMI separation into the slag was studied as well as the clogging layer formation by active tracers.

5. Development and implementation of alternative tracing techniques to identify the origin of NMIs – elemental fingerprinting and isotopic spiking.

This thesis is composed of seven publications (**Papers I – VII**). **Figure 5-1** shows graphically how the publications are linked to each other and to the main topics of the thesis.
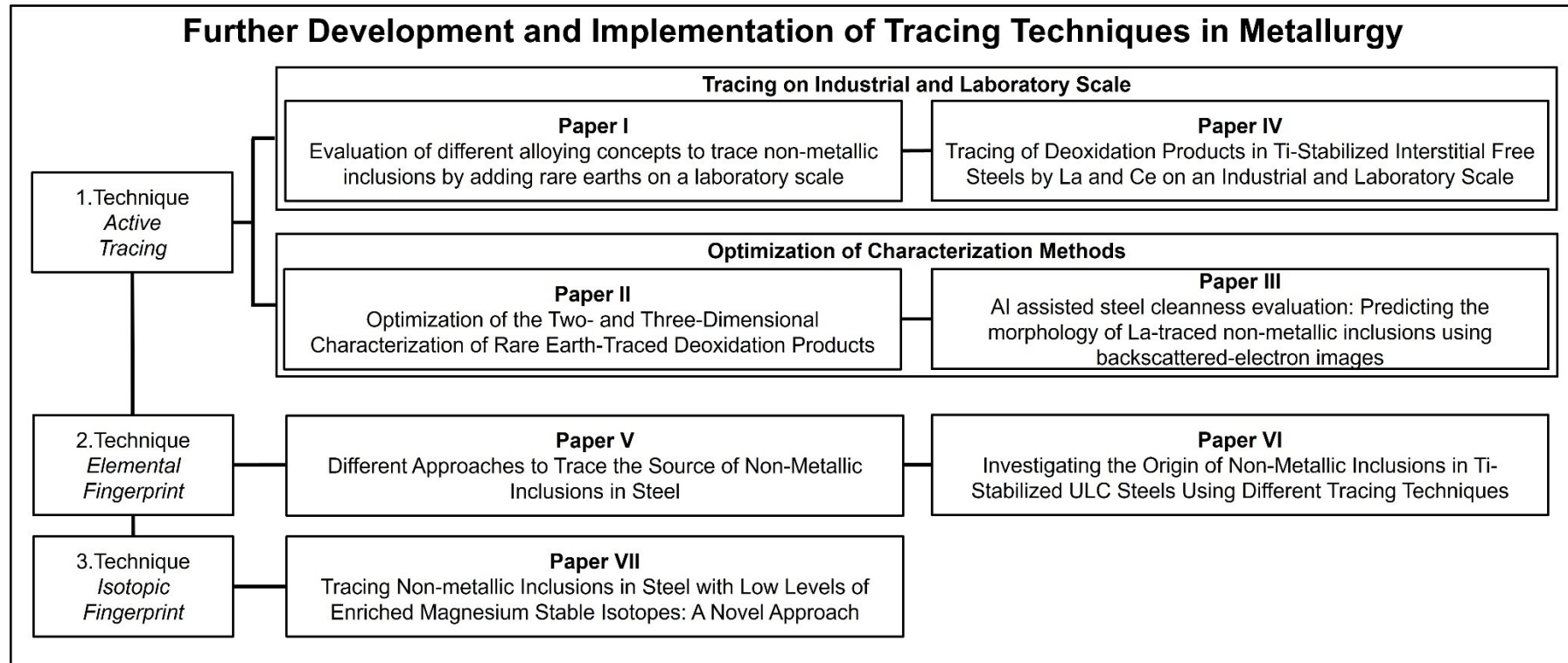

Figure 5-1: Overview of the structure of this thesis including all publications.

6 Methods

The experiments on laboratory scale, the applied extraction techniques and the automated SEM/EDS analyses were performed at the Chair of Ferrous Metallurgy, Montanuniversität Leoben, Austria. The industrial trials were performed at voestalpine Stahl GmbH, Linz, Austria. The analytical investigations were mainly done at the Chair of General and Analytical Chemistry, Montanuniversität Leoben, Austria.

Table 6-I lists the applied metallurgical aggregates, analytical instruments and software for each publication in this thesis. A detailed description of the analyzing methods with their corresponding instrumental settings and operating parameters can be found in the respective publications (**Papers I – VII**) in **Chapter 7**.

Table 6-I: Aggregates, techniques, instruments and software used in this thesis.

Publication	Metallurgical aggregates	Extraction techniques	Analytical instruments	Software
Paper I	Plasma reactor; HFR furnace		SEM/EDS; ICP-QMS	AZtec Feature
Paper II	HFR furnace; Tammann-type furnace	Sequential chemical extraction	SEM/EDS	AZtec Feature; MATLAB R2020b
Paper III	Tammann-type furnace		Spark-OES; SEM/EDS	AZtec Feature; Python (version 3.11.5)

Paper IV	Industrial trials (voestalpine); Tammann-type furnace	Spark-OES; ICP-OES; SEM/EDS	AZtec Feature; MATLAB R2020b
Paper V	Industrial trials (voestalpine)	Spark-OES; XRF; SEM/EDS; ICP-MS; LA-ICP-MS	AZtec Feature
Paper VI	Industrial trials (voestalpine)	SEM/EDS; ICP-MS; LA-ICP-MS	AZtec Feature
Paper VII	Induction furnace; Tammann-type furnace	XRF; SEM/EDS; LA-ICP-MS	AZtec Feature

Concerning the metallurgical aggregates used in this thesis, a laboratory scale hydrogen plasma smelting reduction (HPSR) reactor and a Lifumat-Met-3,3-vac high-frequency remelting (HFR) furnace (Linn High Therm GmbH, Eschenfeld, Germany) – both of which are located at the Chair of Ferrous Metallurgy, Montanuniversität Leoben, Austria, were applied for the experiments in **Paper I**. The latter was also used for sample production in **Paper II**. In **Papers II, III, IV** and **VII**, a resistance-heated Tammann-type furnace (Ruhrstrat HRTK 32-Sond., Ruhstrat Power Technology GmbH, Bovenden, Germany), located at the Chair of Ferrous Metallurgy, Montanuniversität Leoben, Austria, was applied for the experimental work. The isotopically modified slag in **Paper VII** was produced in an induction furnace (MU-900, Indutherm Erwärmungsanlagen GmbH, Walzbachtal/Wössingen, Germany) at Montanuniversität Leoben. The industrial experiments from **Papers IV, V** and **VI** were performed at voestalpine Stahl GmbH, Linz, Austria.

For the three-dimensional characterization of REE-traced NMIs a sequential chemical extraction with 3 vol-% nitric acid solution was done to expose the NMIs by dissolving the surrounding steel matrix.

The instruments for the determination of the REE concentration in the steel samples of **Paper I** was an inductively coupled plasma – quadrupole mass spectrometer (ICP-QMS) (Agilent 7500ce; Agilent Technologies, Tokyo, Japan) at the Chair of General and Analytical Chemistry, Montanuniversität Leoben, Austria. The chemical composition of the steel samples in **Paper III** was determined by a SPECTROMAXx (SPECTRO Analytical Instruments GmbH, Kleve, Germany) at the Chair of Ferrous Metallurgy, Montanuniversität Leoben, Austria, while in **Paper IV,** an ARL iSpark 8880 instrument (ThermoFisher Scientific, Waltham, MA, USA) and in **Paper V** a QSG 750 (OBLF Spektrometrie, Witten, Germany) were used, both located at voestalpine Stahl GmbH, Linz, Austria.

The slags in **Paper IV** were analyzed by inductively coupled plasma – optical emission spectroscopy (ICP-OES) (SPECTRO ARCOS ICP-OES, SPECTRO Analytical Instruments GmbH, Kleve, Germany) at voestalpine Stahl GmbH, Linz, Austria. The slag analyses in **Paper V** were performed by an XRF ARL 9900 (ThermoFisher Scientific, Waltham, USA) for semiquantitative analysis and via wet chemical analysis with open digestion utilizing HCl, HNO_3 and H_2O_2 for quantitative analysis, also performed at voestalpine Stahl GmbH, Linz, Austria. The elemental compositions of the ^{26}Mg-enriched slags in **Paper VII** were analyzed by using the XRF (Axios, PANalytical, Malvern, United Kingdom).

The REE-Fingerprint evaluation in **Papers V** and **VI** of dissolved, homogenous samples was performed by applying an ICP-MS Agilent 7500 (Agilent Technologies, Santa Clara, CA, USA). For solid samples an Agilent 8800 Triple Quadrupole ICP-MS (Agilent Technologies, Santa Clara, CA, USA) coupled to an NWR 213 LA-system (ESI-NWR, Omaha, NE, USA), both located at the Chair of General and Analytical Chemistry, Montanuniversität Leoben, Austria, were used.

The determination of the $^{26}Mg/^{24}Mg$ isotope ratios in slag, refractory, and NMIs for **Paper VII** was done at the Chair of General and Analytical Chemistry, Montanuniversität Leoben, Austria, by using two different LA systems. Firstly, a 213 nm solid-state Nd:YAG LA system (NWR213, Elemental Scientific Lasers, Bozeman, MT, USA) equipped with a TwoVol2 ablation chamber connected to a customized Liebig-type quartz gas mixer for aerosol transport was utilized. Secondly, a 193 nm exciplex ArF LA system (imageGeo193, Elemental Scientific Lasers, Bozeman, MT, USA) equipped with a TwoVol3 ablation chamber with an analytical cup connected to a dual concentric injector for aerosol transport was used. Both LA systems were coupled to a quadrupole ICP-MS (NexION 2000, Perkin Elmer, Waltham, MA, USA).

A field emitting SEM (JEOL 7200F; JEOL Germany GmbH, Freising, Germany) equipped with a 100 mm² SDD-EDS detector (Oxford Instruments Ultim Max 100; Oxford Instruments GmbH NanoAnalysis, Wiesbaden, Germany), located at the Chair of Ferrous Metallurgy,

Montanuniversität Leoben, Austria, was used for the characterization of microscopic NMIs in all seven publications. For the clogging layer investigation, a TESCAN CLARA (TESCAN GmbH, Dortmund, Germany) with an additional 80 mm² SDD EDS detector (Oxford Instruments X-MaxN 80, Oxford Instruments GmbH NanoAnalysis, Wiesbaden, Germany) at voestalpine Stahl GmbH, Linz, Austria was used.

The software AZtec Feature (AZtec 5.0, Oxford Instruments GmbH Nano Analysis, Wiesbaden, Germany) was applied for the automated SEM/EDS analysis in **Papers I and II**. In the publications **Paper III – VII** the novel version of AZtec Feature (AZtec 6.0, Oxford Instruments GmbH NanoAnalysis, Wiesbaden, Germany) was used. A self-developed MATLAB tool (MATLAB R2020b) was developed and utilized for the correct characterization of heterogeneous, REE-traced NMIs in **Papers II – IV**. The AI-based data evaluation in **Paper III** was based on a code in Python programming language (version 3.11.5).

7 Publications

The publications (**Papers I – VII**) included in this thesis are enclosed in this chapter and were co-authored with other researchers. The authorship contribution for each publication based on the Contributor Role Taxonomy (CRediT) described in Brand et al. [180] is depicted in **Table A-II** in Appendix A.4.

The publications are assigned to four sub-sections that are similar to the primary research objectives of this thesis:

1. Active tracing by using REEs on laboratory scale and industrial scale (**Paper I, IV**)
2. Optimization of characterization methods for REE-traced NMIs (**Paper II, III**)
3. REE-Fingerprint – a passive tracing technique (**Paper V, VI**)
4. Tracing with enriched stable isotopes (**Paper VII**)

While **Papers I – VI** are already published open access with the license (CC BY or CC BY-NC-ND), **Paper VII** is still under review.

7.1 Active tracing by using REEs on laboratory and industrial scale

Paper I: K. Thiele, P. Presoly, D. Ernst, S.R. Babu and S.K. Michelic, Evaluation of different alloying concepts to trace non-metallic inclusions by adding rare earths on a laboratory scale. Ironmaking and Steelmaking 50 (2023), 5, pp. 507–516. doi:10.1080/03019233.2022.2124816.

Paper IV: C. Truschner, K. Thiele, S. Ilie, R. Rössler, A. Jungreithmeier and S.K. Michelic, Tracing of Deoxidation Products in Ti-Stabilized Interstitial Free Steels by La and Ce on an Industrial and Laboratory Scale. Steel Res. Int. 95 (2023), 3, pp. 2300665. doi:10.1002/srin.202300665.

Papers I and **IV** are about active tracing by directly alloying REEs to the steel melt. **Paper I** deals with the evaluation of different alloying concepts to mark NMIs on a laboratory scale. The trials were performed utilizing a high-frequency remelting furnace, and the following NMI characterization was done with automated SEM/EDS analysis. The topic of **Paper IV** was the comparison of active tracing on an industrial scale and in the laboratory regarding the formed NMIs and their modification over the process. The separation behavior of NMIs into the slag and the influence of pre-existing NMIs on clogging layer formation was also investigated in industrial experiments. **Papers I** and **IV** were published in **Ironmaking & Steelmaking** and **Steel Research International**, respectively.

I·M3
Institute of Materials,
Minerals & Mining

Taylor & Francis
Taylor & Francis Group

Evaluation of different alloying concepts to trace non-metallic inclusions by adding rare earths on a laboratory scale

Kathrin Thiele [a], Peter Presoly [b], Daniel Ernst [b], Shashank Ramesh Babu [a] and Susanne K. Michelic [a]

aChristian Doppler Laboratory for Inclusion Metallurgy in Advanced Steelmaking, Montanuniversitaet Leoben, Leoben, Austria; bChair of Ferrous Metallurgy, Montanuniversitaet Leoben, Leoben, Austria

ABSTRACT
Different alloying concepts to trace deoxidation products, mainly aluminium oxides, using rare earth elements (REEs), were tested on the laboratory scale by melting trials with a high-frequency remelting furnace. Lanthanum and Cerium, which belong to the group of light REEs, were used for these experiments. The formed multiphase inclusions were characterized by scanning electron microscopy with energy dispersive spectroscopy. Concerning the higher atomic numbers of REEs, traced non-metallic inclusions (NMIs) seem brighter than the steel matrix compared to deoxidation products. REE-traced aluminium oxides showed a primarily heterogeneous and almost globular morphology. The mean equivalent circle diameter of REE-containing NMIs is for all trials similar and is about 2 μm. The experimental results pointed out that the recovery rates of the various alloying concepts differ only slightly. In contrast, the values mainly depend on the surface-to-volume ratio and the amount of oxygen in the melt.
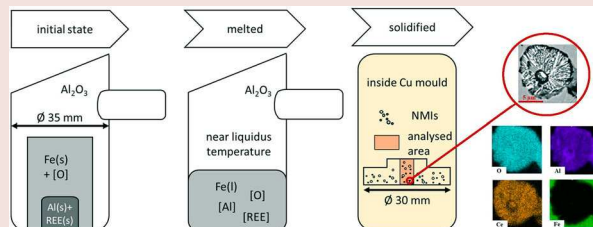
Introduction

The formation and modification of non-metallic inclusions (NMIs) have become an important research focus today due to the increased requirements for steel cleanness in the recent years. The type, size, shape and distribution of these particles can significantly impact the mechanical properties, such as toughness, fatigue properties or fracture toughness, and further the corrosion resistance of steels [1–8]. NMIs can also cause problems during production [9,10], in addition to the effect on the final product quality. For instance, clogging during continuous casting is a possible consequence of the deposition of alumina inclusions, which have a higher liquidus temperature than steel [10–13]. The melting point of the deoxidation products (Al_2O_3) can be lowered through a calcium treatment. Furthermore, the tendency for deposition in the flow control system is significantly decreased due to changes in interfacial conditions. However, mistakes during Ca-treatment or even the reactions between metal and slag can lead to solid Ca-aluminates, further inducing severe clogging problems [14,15].

Tracing NMIs is one option to increase the knowledge regarding inclusion evolution over different process steps since the clogging mechanism is not entirely clarified. Therefore, rare earth elements (REEs) can be applied for tracking

deoxidation products, such as Al_2O_3. Especially, Lanthanum and Cerium are proven as tracers during steel production [16–18]. In addition, REEs start interacting with aluminium oxides on the interface, whereby REE-containing complex inclusions occur [19,20]. As mentioned by Šuler et al. [21], REEs are not best suited for following the modification steps of inclusions because they also interact and influence the morphology, size, number and distribution of NMIs. The addition of rare earths lowers the melting point of inclusions, resulting in modified liquid-type inclusions at production temperatures, similar to the classical Ca-treatment [21–24].

Furthermore, rare earth elements, mainly Ce, are used in the industry for grain refinement. The study of Baumgartner et al. [25] shows the significant influence of Ce on the grain size using the example of super austenitic stainless steel. The refinement is caused by the formation of small NMIs, primarily $AlCeO_3$, which initiate heterogeneous nucleation. More profound knowledge of the inclusion formation and the interaction with Al is essential since REE-containing inclusions are promising for the grain refining of steels.

Many studies on IF(Interstitial Free)- or ULC(Ultra-Low Carbon)- [20,26–28] and high alloyed steel grades [29,30] show that the interactions between deoxidation products and REEs result in modified NMIs, concerning their size,

CONTACT Kathrin Thiele kathrin.thiele@unileoben.ac.at Christian Doppler Laboratory for Inclusion Metallurgy in Advanced Steelmaking, Montanuniversitaet Leoben, Franz – Josef – Straße 18, 8700, Leoben, Austria

Table 1. Chemical composition of used electrolytic iron.

C [ppm]	Si [wt-%]	Mn [wt-%]	P [ppm]	S [ppm]	Al [wt-%]	Ti [wt-%]	N [ppm]	O [ppm]	Fe [wt-%]
65	0.001	0.102	5	19	0.0005	0.0008	10	330	Bal.

shape and distribution. Referring to Wang et al. [26], the addition of rare earths increases the number density of inclusions, and, aside from that, the NMIs get smaller and spherical. Similar tendencies are observed by Li et al. [31] and Wang et al. [32]. In both studies, the irregularly shaped inclusions become more globular, and at low Cerium addition, their sizes decrease. Furthermore, they found that inclusions start to grow again at a critical amount of Ce, dependent on the chemical composition of the steel.

The present study investigates the tracing of inclusions by adding the rare earths Lanthanum and Cerium at a laboratory scale. The expected inclusion scenario for different additions is determined based on thermodynamic calculations. Small-scale laboratory experiments are performed to test and compare various alloying concepts for rare earth additions. Subsequent inclusion analyses are done using manual and automated scanning electron microscopy with energy dispersive spectroscopy analysis (SEM/EDS). Furthermore, the formed NMIs are characterized by their type, size and distribution. The amount of traced particles is also determined. Finally, predicted and observed inclusion populations are compared.

Methods and materials

Electrolytic iron

Electrolytic iron was used as raw material for the laboratory trials to ensure reproducible conditions for the whole experimental series providing a possibly low and homogeneous inclusion content. The chemical composition of the electrolytic iron is given in Table 1. The O content of the material was 330 ppm, which is in the range of crude steel before deoxidation in industry, provoking the formation of Al_2O_3 after deoxidation with Al.

The preexisting inclusion population primarily consisted of (Si,Mn)-oxides with a mean equivalent circle diameter (ECD) of 2.1 μm. No pure Al_2O_3 inclusions were observed in the raw material.

Alloying concepts

Three different alloying methods were tested and compared in this work. La and Ce were protected from fast oxidation in the atmosphere by two various concepts. First, the rare earths were put inside steel tubes with closed ends. Second, La and Ce were wrapped with Al-foil.

Besides the addition of REEs as pure substances, a ferroalloy with Cerium was also produced and tested. The mass of rare earth elements is also related to the melting weight. 300 ppm of pure La or Ce was added for every alloying concept. Therefore, only around 19.5 mg of pure REEs are needed, depending on the small melt weight of about 65 g.

Addition via pure substances

The first consideration was to add rare earths inside steel tubes of E235, with an inner diameter of 4 mm. Since the use of steel tubes can lead to the contamination of the melt, low alloyed steel was utilized to keep the impact of the pipe relatively small. The chemical composition after DIN EN 10305-1, 10305-2 and 10305-3 of the E235 tubes is shown in Table 2. Additional deoxidizers, such as Mn and Si, come into the melt by E235 steel tubes. Precise Al addition for the deoxidation is necessary to suppress the reaction of Mn and Si with oxygen and subsequently the formation of other deoxidation products than Al_2O_3.

Another option to add La or Ce was to wrap the pure elements inside a foil. For this study, an Al-foil was used to minimize the oxidation of La and Ce. The amount of pure aluminium for deoxidation must be adapted due to the additional insert of Al as a foil.
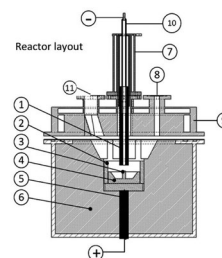
Addition via ferroalloys

For the FeCe production under inert conditions, a plasma reactor, layout seen in Figure 1, located at the Chair of Ferrous Metallurgy at the Montanuniversitaet Leoben, was used as a pre-melting unit. For this purpose, Cerium metal and electrolytic iron were melted with an Argon plasma to prevent Cerium oxidation.

The water-cooled plasma reactor consists of a DC power supply with a maximum output of 16 kW, a visual observation via a camera, an off-gas analysis with a mass spectrometer and a current/voltage measurement by a four-channel analogue logger. A DC transferred arc was ignited between a hollow graphite electrode (cathode) and a steel crucible (anode) with a welded ignition pin to produce the FeCe alloy. A mixture of 85 g Cerium and 20 g electrolytic iron was batch-wise charged into the crucible. After the reactor was evacuated entirely with Argon, an arc was ignited by contact of the graphite electrode with the ignition pin and an electrode gap of 20 mm was set. About 5 l min⁻¹ of Argon 5.0 was supplied through the hollow electrode to stabilize the arc during the process.

Experimental procedure

Laboratory experiments were performed in a Lifumat-Met-3,3-vac high-frequency remelting (HFR) furnace (Linn High Term GmbH, Eschenfeld, Germany) with a spin caster unit.

1. Hollow Graphite Electrode
2. Refractory ring
3. Ignition pin
4. Steel crucible
5. Bottom electrode (anode)
6. Refractory lining
7. Electrode holder
8. Orifices
9. Reactor lid
10. Gas supply
11. Camera viewport

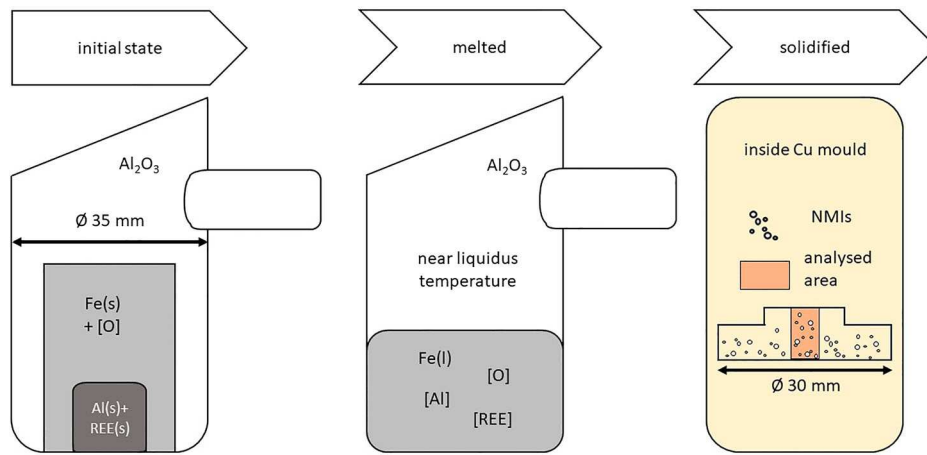**Figure 1.** Layout of the plasma reactor, used as pre-melting unit [34].

Table 2. Maximal amounts of the chemical composition of E235 steel tubes in wt-% [33].

C	Si	Mn	P	S	Fe
0.170	0.350	1.200	0.025	0.025	Bal.

Figure 2. States during sample production in HFR, adapted from Mayerhofer et al. [35].

This furnace was chosen since a homogenized melt can be produced without oxygen absorption during the process. Furthermore, the whole procedure is under an inert Ar atmosphere. Continuous bath movement is ensured due to the inductive heating and stirring.

The steel sample ($18 \times 18 \times 22$ mm, appr. 65 g) was heated and melted close above the liquidus temperature ($T_{Liquidus} + 30–50$ K). Afterward, the steel was cast through copper by centrifugal casting. The high mean cooling speed is an additional benefit, leading to quick solidification. Therefore, inclusion interaction is limited. A new, highly purified corundum crucible was used for every trial. The contact time between melt and crucible is about 1 min due to the fast melting and cooling. Hence, the influence on the inclusions is negligible.

The deoxidation agent (Al) and alloying elements (La/Ce) were placed in a blind hole (Ø 6mm) drilled inside the steel samples to prevent too early melting or evaporation losses. Subsequently, the samples were turned upside down. The addition of deoxidation and tracing agents was simultaneous compared to the industry, where the deoxidation takes place several minutes before REEs are alloyed. Hence, the deoxidation products were almost concurrent formed and traced due to the fast melting at the HFR process. Figure 2 shows a schematic overview of the three main states during the sample production in HFR. In addition, in the right picture in Figure 2, the area subsequently analysed with automated SEM/EDS is illustrated.

It was essential to keep the time between cutting off a small piece of the REE metal, weighing in, and heating as short as possible for alloying rare earth elements. Otherwise, REEs oxidize and are lost as tracers for deoxidation products.

Methods of analysis

Determination of rare earths content

The amounts of Lanthanum and Cerium were determined with an inductively coupled plasma-quadrupole mass spectrometer (Agilent 7500ce ICP-QMS; Agilent Technologies, Tokyo, Japan). Small pieces of each sample with a total mass of approximately 500 mg were digested and measured. Bandoniene et al. [36] described the ICP-QMS measuring procedure in detail. The sample digestion differs for solid steel samples. Complete dissolution was achieved by additionally adding drops of nitric acid and longer dwell times on the heating plate.

Analysis of REE-traced NMIs

The steel samples were cut in half, conductive embedded, ground with SiC paper and polished with diamond suspension for 9, 3 and 1 µm. A field-emitting SEM (JEOL 7200F; JEOL Germany GmbH, Freising, Germany) equipped with a 100 mm^2 SDD-EDS detector (Oxford Instruments Ultim Max 100; Oxford Instruments GmbH NanoAnalysis, Wiesbaden, Germany) was used for the measurements. The chemical composition was automatically analysed with AZtec Feature (AZtec 5.0, Oxford Instruments GmbH Nano Analysis, Wiesbaden, Germany) and manually with AZtec Mapping. First, the automated detection and measurement of the particles were performed. The size distribution of non-metallic inclusions and the amount of traced and non-traced NMIs were determined by this method. Afterward, the representative NMIs were targeted and manually measured. Microscopic NMIs were the focus of this paper. Therefore, inclusions larger than 15 µm were deleted at the characterization step.

A threshold for the greyscale needs to be specified before an automated measurement. Therefore, all the particles defined within this threshold were analysed with the AZtec Feature tool. Since rare earth elements have higher atomic numbers than typical inclusion forming elements, such as Al or Si, their associated greyscales are significantly brighter. Hence, two greyscale sectors were necessary to detect the traced and non-traced particles within the same measurement. The measurement duration is extended within this method, and multiphase NMIs with high contrast are divided into two separate particles.

The double-threshold scan splits heterogeneous multiphase inclusions into several particles. This split results in an inaccurate description of the distribution and the number of NMIs in the investigated area. This error can be solved using a custom-built Matlab tool wherein the related parts of a divided inclusion were recombined. Finally, the correct size, shape and chemical composition of NMIs obtained.

Thermodynamic considerations

One major characteristic of REEs is their high oxygen affinity. Rare earths, such as Lanthanum and Cerium, have a higher

negative free Gibbs energy than manganese, silicon or aluminium oxides. Consequently, the formed oxides were more stable than the common deoxidation products, e.g. Al_2O_3 or SiO_2 [16]. The Richardson-Ellingham diagram (Figure 3) illustrates the stability of the most frequent oxides in secondary metallurgy. The calculation of the free Gibbs energies for deoxidation products and other typical alloying elements in steel was done by the thermodynamic software HSC Chemistry 6.1.

The thermodynamic calculations to analyse the needed REEs amount for tracing alumina inclusions are performed using the software FactSage 8.2 with FSstel, FToxid and FactPS 2022 databases. The influence of the rare earths, La and Ce, on the inclusion formation is also pointed out within these evaluations.

Results

The recovery rates of rare earth elements for different alloying concepts

The chemical analyses of the molten steel samples were summarized in Table 3.

The ICP-QMS was used to measure the amount of REEs in the samples. From these measurements, the recovery rates of all tested concepts were calculated. The results can be seen in Table 4. The alloying technique of adding Ce as a ferroalloy led to the highest recovery rate with 38.40%. The recovery rates for the second concept, REEs wrapped in Al-foil, were 30.78% for La and 36.40% for Ce. Whereas the method

Table 3. Measured chemical composition of steel samples in wt-%.

Sample Nr. – concept	C	Si	Mn	Al	Fe
1 – La in steel tube	0.0073	0.0010	0.1040	0.0664	Bal.
2 – La in Al-foil	0.0060	0.0010	0.0938	0.0696	Bal.
3 – Ce in steel tube	0.0067	0.0010	0.1030	0.0695	Bal.
4 – Ce in Al-foil	0.0058	0.0010	0.0937	0.0650	Bal.
5 – FeCe (56 wt-% Ce)	0.0050	0.0010	0.0946	0.00665	Bal.

Table 4. Recovery rates [%] of rare earth elements in different alloying concepts.

REE	In steel tube	In Al-foil	Ferroalloy
La	[Sample 1] 24.83	[Sample 2] 30.78	—
Ce	[Sample 3] 24.33	[Sample 4] 36.40	[Sample 5] 38.40

where La and Ce were added inside a steel tube resulted in the lowest recovery rate of REEs with 24.83% and 24.33%, respectively.

Characteristics of REE-traced inclusions

It was observed that most of the inclusions were heterogeneous multiphase types with isolated parts representing the REEs oxides being brighter than the steel matrix. Almost all inclusions in the samples were Al_2O_3(>99%). Hence, only this inclusion type was considered for the evaluation.

Table 5 lists the amount of traced Al_2O_3 for all the alloying concepts studied in this paper. It can be seen that over 95% of the Al_2O_3-NMIs were traced in all the samples. The best tracing results were achieved in samples 4 and 5 with over 99%. The two La-marked samples (1 and 2) obtained about
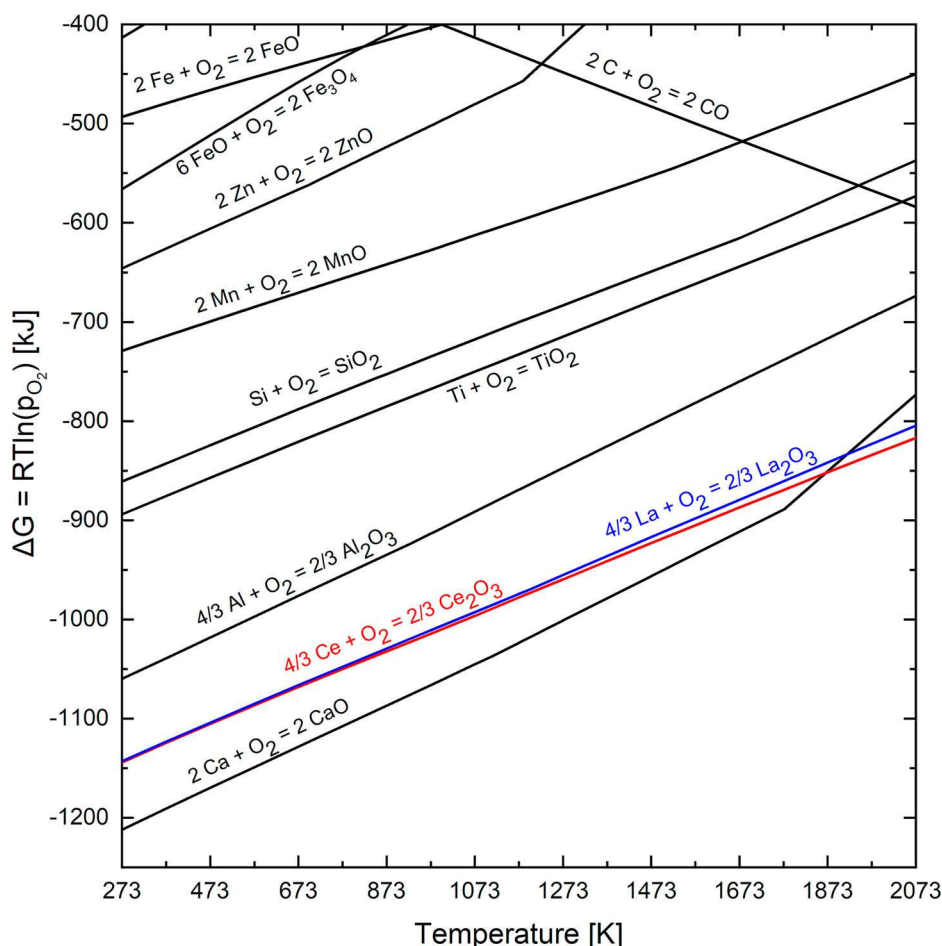

Figure 3. Richardson-Ellingham diagram including Lanthanum and Cerium.

Table 5. Amount of traced Al_2O_3–NMIs [%] and corresponding sample number.

REE	In steel tube	In Al-foil	Ferroalloy
La	[Sample 1] 98.04	[Sample 2] 97.66	—
Ce	[Sample 3] 95.95	[Sample 4] 99.13	[Sample 5] 99.04

Table 6. Mean ECD and deviation for traced Al_2O_3–NMIs [μm].

REE	In steel tube	In Al-foil	Ferroalloy
La	[Sample 1] 2.09 ± 1.21	[Sample 2] 2.32 ± 1.23	—
Ce	[Sample 3] 2.56 ± 1.48	[Sample 4] 2.00 ± 1.10	[Sample 5] 1.92 ± 0.92

98% traced Al_2O_3-NMIs. Sample 3 had the lowest amount of traced alumina inclusions at approximately 96%.

The mean ECD for each sample refers only to traced Al_2O_3-NMIs since the tracing rate was high, above 95%. Table 6 lists the mean ECD and their standard deviations. Although inclusions larger than 4 μm were found, most of the traced NMIs were in the range of 1 and 4 μm ECD in all samples. Sample 3, Ce addition in a steel tube, had the highest deviation with 1.48 μm. The deviations of the ECD for samples 1 and 2, where La was added, were about 1.2 μm. Samples 4 and 5 had a lower deviation with 1.10 and 0.92 μm, respectively.

Cross-sections of the samples were analysed by manual and automated SEM/EDS measurements. Figure 4 shows BSE images of representative NMIs traced by Lanthanum in samples 1 and 2. Furthermore, the distribution of the chemical composition is seen in Figure 4. In both cases, the traced NMIs have a similar size. Sample 1 has a distinct border between the lanthanum oxide in the core and the surrounding alumina inclusion. In comparison, no segregation could be observed in sample 2.

BSE images of typical NMIs traced with Ce and their chemical compositions for the three tested alloying concepts can be seen in Figure 5. The Ce-enriched parts were finely distributed in the Al_2O_3 inclusions in all cases. More agglomerated minor inclusions can be observed in sample 5 (Figure 5(c)).

Discussion

The output of FeCe production

An option to trace inclusions was to produce a ferroalloy of Ce wherein it was added directly to the melt as in industry.

The amount of Cerium in FeCe used in the industry is usually much lower than the alloying material in laboratory trials. Ren et al. [39] added FeCe to trials on the laboratory scale. This study used a significantly higher Ce-concentrated ferroalloy with 30 wt-% for experiments with an ULC-steel in a Si–Mo high-temperature tube furnace.

The lab-produced FeCe was analysed, and the real composition was compared with the FactSage predicted value. A deviation in the chemical composition can be observed, as seen in Figure 6. The FeCe system was calculated with the software FactSage 8.0 and the databases FactPS and FSstel 2020. At 93 wt-% Ce, a low melting eutectic is formed between Ce and Fe. The planned Ce amount was 81 wt-% concerning the added amount of Fe and Ce as described in the materials section. The produced alloy had finally only 56 wt-% Ce according to the analysis. On the one hand, this difference can be attributed to a slight pre-oxidation of the pure Cerium during the comminution of large pieces into chargeable grain sizes. On the other hand, a deviation can occur due to its reaction to the residual oxygen present in the electrolytic iron during the melting process.

Evaluation of the alloying concepts

Examining different alloying concepts for trials in the laboratory is essential because smaller amounts of tracers were added compared to the industry. Former studies have already dealt with the problem of a smaller output for rare earths, which were significantly lower in the case of laboratory experiments [19,29] compared to industrial trials [26,37]. The main reason behind this is its high oxygen affinity. The associated oxidation rate is faster due to a large surface-to-volume ratio in the small dimensions of the added tracers. Therefore, only a little part of the original content can act as a tracer and interact with deoxidation products. The vapour pressure of light REEs, such as La and Ce, is relatively low at process temperatures compared to heavy REEs, as mentioned by Okabe et al. [38] Hence, the losses for heavy REEs would be significantly higher due to evaporation.

The amount of La or Ce depends on the oxygen content in the steel and the number of deoxidation products intended to be traced.
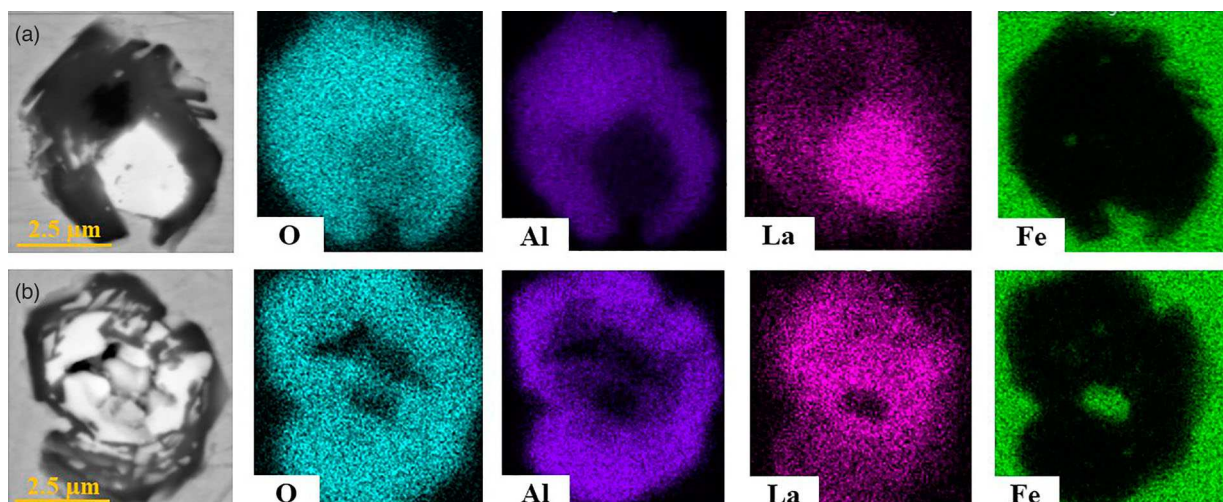
Figure 4. BSE images and mappings of La-traced NMIs: (a) sample 1, La inside steel tube, (b) sample 2, La wrapped in Al-foil.
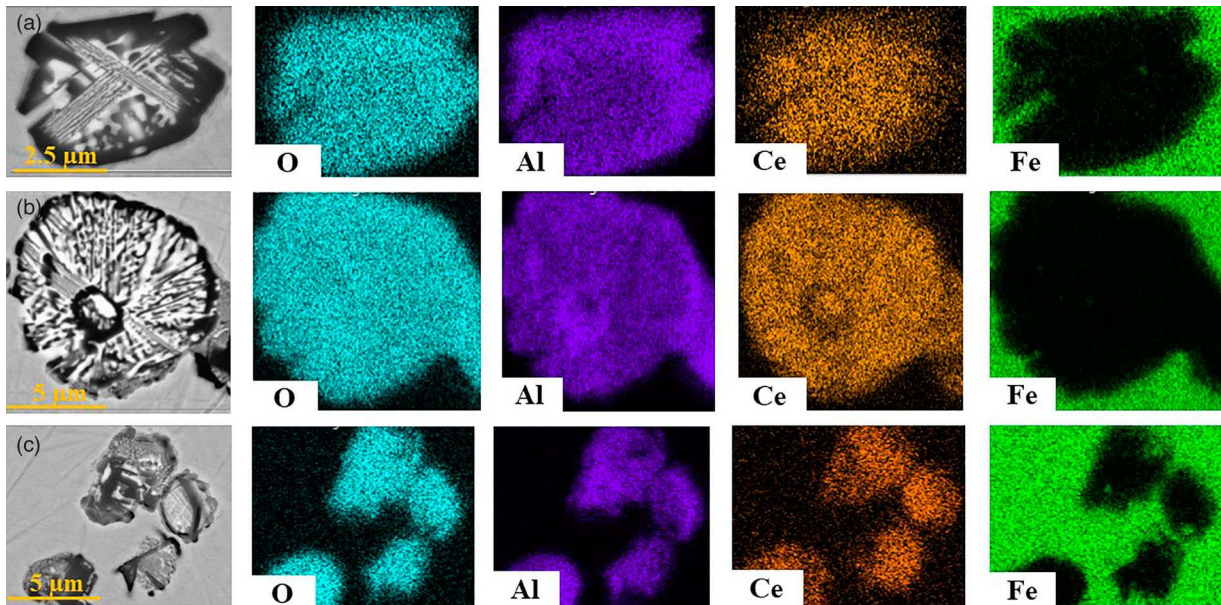
Figure 5. BSE images and mappings of Ce-traced NMIs: (a) sample 3, Ce inside steel tube, (b) sample 4, Ce wrapped in Al-foil, (c) sample 5, Ce as FeCe (56 wt-% Ce).
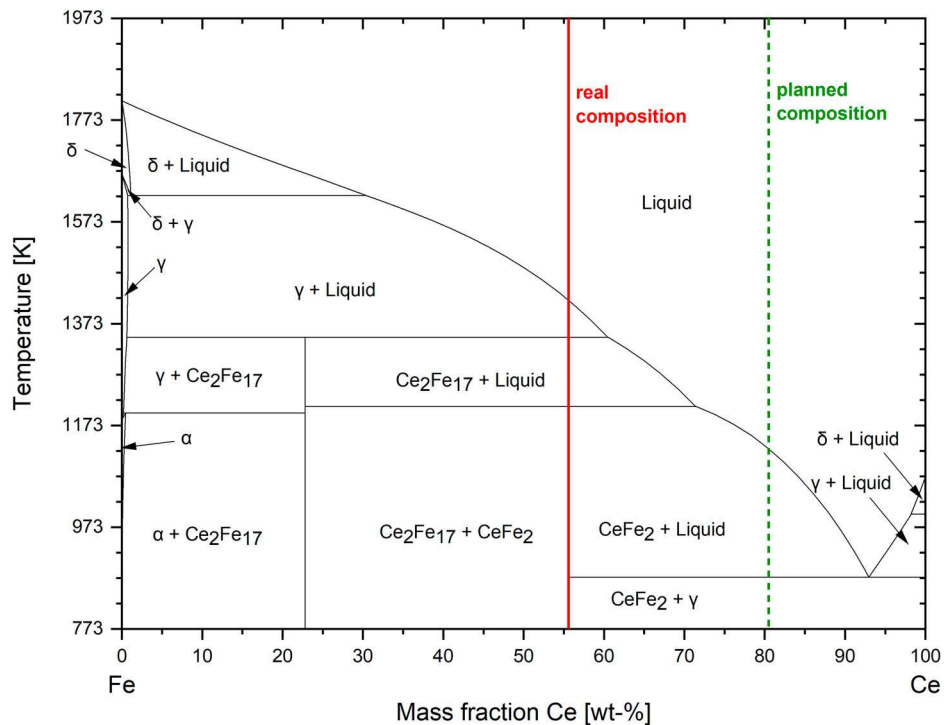

Figure 6. Equilibrium diagram of the FeCe system (including planned and real composition).

Various methods have already been used in the literature for laboratory and industrial trials. Lanthanum [19] and Cerium [29] were wrapped in pure iron foils for alloying in the laboratory trials of Li et al. [19] and Luo et al. [29] with Si–Mo high-temperature tube furnaces. Based on the REE content in these two studies, the recovery rate for Lanthanum was about 40% and for Cerium 20%. These results must be carefully evaluated since many parameters influence the outcome of REEs, such as the oxygen content in the melt, the flow rate of the protective gas and the duration of stirring, which were different for these two studies. The results in the present study were about 30% for La and about 36% for Ce concerning the tested alloying concept,

REEs inside an Al-foil. The findings are comparable to the prior research mentioned where a pure iron foil was used.

In comparison, when Al-foil wrapped La and Ce were added as described in this paper, the losses for Lanthanum were slightly higher, within a difference of approximately 6%. This recovery rate difference between La and Ce could be possible as the added REEs wrapped inside the Al-foil were not completely air-tight. Further deoxidation will occur within this alloying method, and the amount of Al in the melt will subsequently increase. The reason, therefore, is the additional Al-source, which leads to the formation of extra Al_2O_3 inclusions. The rare earths reduce these NMIs, so the Al content in the melt continues to rise.

In contrast, losses of REEs due to oxidation can appear, especially by adding La or Ce using steel tubes. The reason was the relatively high amount of oxygen and the resulting unavoidable oxidation inside the tubes. As a result, the recovery rates were comparatively lower than for the other methods described in this work. Furthermore, using a steel tube for insertion can contaminate the melt due to the introduction of new alloying elements and preexisting NMIs which might be present in the steel tube.

Considerably lower losses were expected when Ce was added as a ferroalloy because the interaction between REEs and oxygen is inhibited. As anticipated, the highest recovery rate at about 38% was achieved in this case.

The obtained recovery rates for each alloying concept in this study can only serve as guide values for the industry since parameters, such as treatment time or bath movement, differ. The tendency between the tested concepts would be similar on the industrial scale, but to evaluate the total achieved recovery rates of REE addition in the industry further experiments are needed. Further studies are necessary to determine the output of the different alloying methods at various furnaces to obtain accurate recovery rates for rare earths on the laboratory scale.

Assessment of the inclusion characterization

Mainly alumina inclusions (>99%) were found in the investigated samples. The Al_2O_3 inclusions would have originated from the Al-deoxidation of the samples since the raw material consists of only (Si,Mn)-oxides and no Al_2O_3.

No pure REE-containing inclusions were found in the manual and automated measurements in the samples. There are two possibilities for the occurrence of REE-containing inclusions. On the one hand, rare earth oxides can nucleate on preexisting alumina inclusions, and on the other hand, new oxides can form, which contain REE and Al.

Owing to the fast cooling, the difficulties of a precise temperature setting and the centrifugal cast, NMIs were not homogeneously distributed in all samples. Thus, directly comparing the five samples regarding their number of inclusions and distribution was impossible. However, the samples can be compared concerning their amount of traced Al_2O_3-NMIs and their inclusion size. No significant differences occurred with respect to the mean ECD of the inclusions. The values for all samples were in the range of 1.92–2.56 μm. The ECD deviation was relatively similar for all samples and between 0.92 and 1.48 μm.

As mentioned, the alloying concepts were not only compared by their resulting recovery rates but additionally by their achieved tracing rate. The alloyed amount of REEs was 300 ppm, about 1.75 times higher than the required addition for complete tracing. Therefore, all five samples reached a high tracing rate. Sample 3 achieved the lowest tracing rate compared to the others, with around 96%.

The morphologies of traced inclusions were analysed and compared for all five samples. First, a comparison of the La-traced samples was made. It was found that the La-containing areas of sample 2 were more irregularly distributed than in sample 1 (Figure 4). Furthermore, there was no fixed border between pure Al_2O_3 and the La-enriched parts in sample 2, where La was added wrapped in an Al-foil. The fineness of the distribution for marked areas inside inclusions mainly depends on the reaction time concerning segregation tendency. Larger and coarser distributed areas were formed at longer reaction times.

Moreover, complex multiphase inclusions would show stronger distinct boundaries between traced and non-traced regions if there was enough time for segregation. It can be concluded that sample 1 had a longer reaction time than sample 2 based on the clearly formed border between the different areas inside the inclusion. La-traced NMIs were irregularly shaped and were more globular than elongated.

Compared to the La-marked NMIs in Figure 4, no significant differences were found in manual SEM/EDS measurements for the Ce-containing inclusions in Figure 5. The segregation process is identical to the inclusion in sample 2 (Figure 4(b)). Even size, shape and elemental distribution are similar. Furthermore, this analysing method can identify no variations between the alloying concepts. The fine distributed areas of REE oxides are primarily owed to the used melting aggregate and the fast cooling within the HFR process. The REE-traced inclusions formed within this aggregate differ from REE-containing aluminium oxides of industrial experiments. The reasons are the tendency of REEs to segregate and the longer reaction and dwell times in the industry. Hence, the REE-containing areas of NMIs formed at industrial trials are more clearly separated and larger compared to the inclusions in this study. An attempt will be made in the next series of experiments to map the industrial process sequence more precisely, i.e. REEs will be added a certain time after deoxidation.

Thermodynamic calculation of inclusion formation after the addition of REEs

The modification of Al_2O_3 inclusions due to the REE addition on electrolytic iron is shown for Lanthanum (a) and Cerium (b) in Figure 7.

The inclusion evolution was comparable between La and Ce at REE concentrations below 0.13 wt-%. The $LaAl_{11}O_{18}$- or $CeAl_{11}O_{18}$-NMIs originate after aluminium oxides, Al_2O_3, were formed. Higher La-concentrated, complex $Al_7La_{33}O_{60}$ inclusions were generated through the Lanthanum addition above 0.1 wt-%. Compared to La addition, a different complex inclusion type, $Al_2Ce_4O_9$, occurred for Ce. Parallel to the appearance of Ce_2O_3 inclusions, Al_2O_3 has formed again. REE-containing sulphides were formed in both cases at around 0.2 wt-%. The prediction for La contains two different sulphide types, La_2S_3 and LaS; for Ce, only CeS is predicted. From these thermodynamic calculations, the predicted inclusion path for Ce is $Al_2O_3 \rightarrow CeAl_{11}O_{18} \rightarrow AlCeO_3 \rightarrow Al_2Ce_4O_9 \rightarrow Ce_2O_3 + Al_2O_3 \rightarrow Ce_2O_3 + CeS$, and for La, it is $Al_2O_3 \rightarrow LaAl_{11}O_{18} \rightarrow AlLaO_3 \rightarrow Al_7Ce_{33}O_{60} \rightarrow La_2O_3 + La_2S_3 \rightarrow La_2O_3 + LaS$. Luo et al. [29] and Pan et al. [30] determined similar modification processes for Ce additions at high alloyed steels. The changes for ULC steels were illustrated by Wang et al. [27], where the inclusion type $CeAl_{11}O_{18}$ is defined as a complex of $Ce_2O_3 \cdot 11Al_2O_3$.

The oxygen content for the electrolytic iron was much higher compared to the steel grades used in these studies. Although the required amount of REE is not comparable to the mentioned studies, the modification steps of inclusions are equal. The inclusion evolution of Lanthanum up to the formation of $Al_7La_{33}O_{60}$ has not yet been described in the literature.
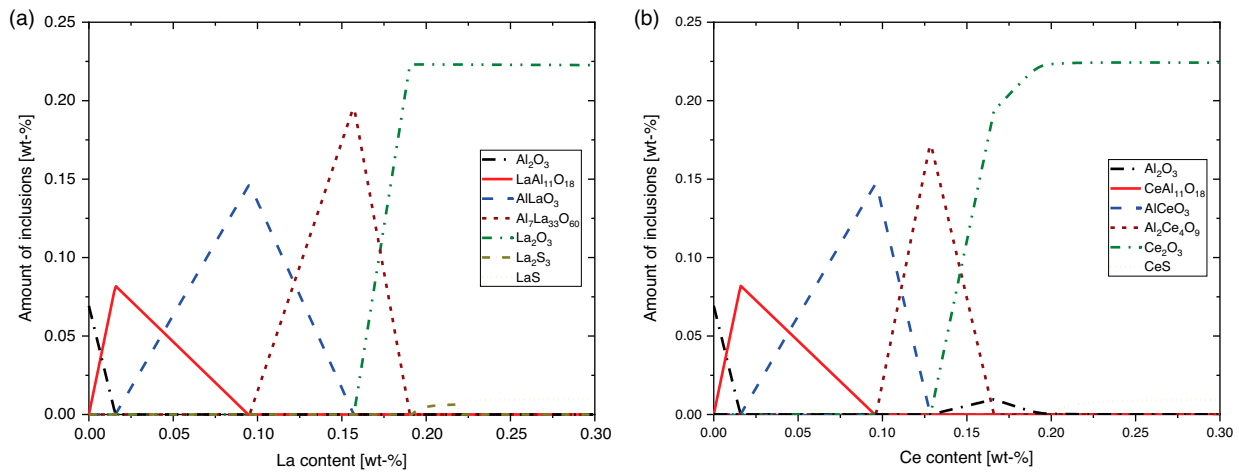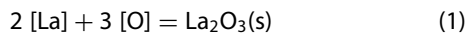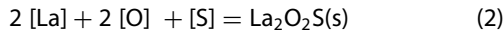
Figure 7. Inclusion evolution process of electrolytic iron at 1873 K (a) for La and (b) Ce addition.

Since REEs bind with oxygen in the melt, the already existing aluminium oxides get reduced and thus modified. Furthermore, an excessive amount of rare earths can also lead to the formation of homogeneous pure REE oxides. Wang et al. [40] have cited the free Gibbs energies for forming oxide, oxide-sulphide and pure sulphide REE bonds. The reactions and the associated free Gibbs energies are shown below [40]:

$$2\,[La] + 3\,[O] = La_2O_3(s) \tag{1}$$

$$\Delta G^\circ = -1\,511\,520 + 379.2\,T\left[\frac{J}{mol}\right]$$

$$2\,[La] + 2\,[O] + [S] = La_2O_2S(s) \tag{2}$$

$$\Delta G^\circ = -1\,425\,820 + 351.0\,T\left[\frac{J}{mol}\right]$$

$$[La] + [S] = LaS(s) \tag{3}$$

$$\Delta G^\circ = -490\,000 + 171.0\,T\left[\frac{J}{mol}\right]$$

It can be concluded from these reactions that REEs have a greater affinity for oxygen than sulphur. Therefore, mainly modified aluminium oxides and pure REE oxides are formed. It is also possible that chemical oxide-sulphide bonds occur in the presence of sufficient sulphur. Furthermore, it must be noted that dissolved REEs are essential for interactions with aluminium oxides. Concerning thermodynamics, small amounts of dissolved REEs partly reduce the deoxidation product Al_2O_3 and lead to the modification of these NMIs, as the following equation shows for dissolved [Ce] [19,29]:

$$6\,Al_2O_3(s) + [Ce] = CeAl_{11}O_{18}(s) + [Al] \tag{4}$$
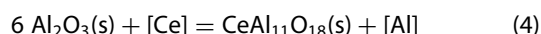
The formed complex REE–Al–O inclusions, $REEAl_{11}O_{18}$, react to higher REE-concentrated NMIs due to an increased REEs addition. The proceeding reaction for Ce is illustrated below [19,29]:

$$CeAl_{11}O_{18}(s) + 5\,[Ce] = 6\,AlCeO_3(s) + 5[Al] \tag{5}$$
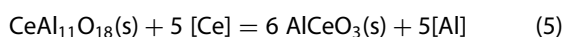
REEs reduce aluminium oxides in both reactions and form new complex inclusions enriched with REEs. Moreover, the amount of dissolved aluminium in the melt increases. The presence of dissolved rare earths also leads to interactions

with refractory wear. The melt would be even more enriched with dissolved Al if corundum crucibles were used. [19] No further reactions are predicted in the present study since the reaction time between the crucible and the melt is low during the HFR-melting process.

Comparison between predicted and effectively traced NMIs

Concerning the thermodynamic calculations in Section '4.4. Thermodynamic calculation of inclusion formation after the addition of REEs', the predicted inclusion types depend on the two parameters, REE content and process temperature. Owing to melting in the HFR furnace and accompanying fast cooling, the state of the melt was as-frozen, and so were the therein-contained NMIs. Furthermore, no modification and segregation of other inclusion types took place.

Hence, the addition of 300 ppm of REEs predicts mainly complex Al–REE–oxides. $REEAl_{11}O_{18}$ and AlREEO₃ were formed as per thermodynamic calculations (shown in Figure 7). The amount of La or Ce effectively achieved in the melt was only between 72 and 114 ppm for all samples. A high number of Al_2O_3 inclusions was also predicted to be present in addition to $REEAl_{11}O_{18}$ for these REE contents. The theoretically predicted inclusion population was compared to the measured NMIs of the samples using the automated SEM/EDS analysis. The measurement results showed mainly REE–Al–oxides and nearly no pure Al_2O_3 inclusions. Further, no pure REE oxides were found in any of the investigated samples.

The ternary systems of La–Al–O and Ce–Al–O, illustrated in Figure 8, show the distribution of REE-containing Al_2O_3 inclusions for all samples. Furthermore, the areas of the predicted $REEAl_{11}O_{18}$ and $REEAlO_3$ inclusions are marked in the diagrams. All trials led to a similar distribution of REE–Al–O inclusions in the ternary systems. The most significant number of inclusions lies in the region of 25 wt-% of REE, next to the predicted $REEAl_{11}O_{18}$–NMIs.

Thermodynamics only depicts the formation of complex REE-containing inclusions and modification of existing alumina inclusions in an equilibrium state. The higher number of traced NMIs can also result from the heterogeneous nucleation of REE oxides to the preexisting Al_2O_3 inclusions. Comparisons between the predicted and actual inclusion numbers were challenging because kinetics plays
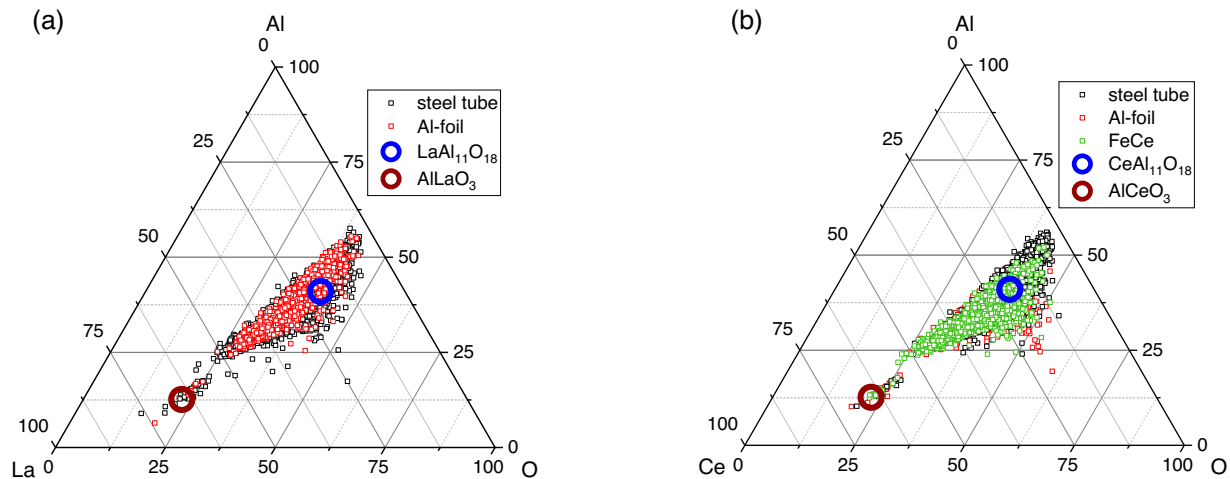
Figure 8. Ternary system of (a) La–Al–O with the area of $LaAl_{11}O_{18}$ and $AlLaO_3$ marked, (b) Ce–Al–O with the area of $CeAl_{11}O_{18}$ and $AlCeO_3$ marked.

a substantial role in forming NMIs within the HFR furnace. However, the influence of kinetics is not considered in thermodynamic calculations. Therefore, thermodynamically expected inclusion types are also valid for industrial trials. Models to contemplate kinetics are necessary for precise prediction of trials on a laboratory scale as well as industrial ones.

Conclusion

In this study, different alloying concepts for the addition of rare earth elements to the steel were investigated on a laboratory scale. The percentage of traced inclusions for three alloying concepts and the associated recovery rates were determined. The formed NMIs were characterized in detail. The main findings relating to the recovery rate of rare earth elements on the laboratory scale can be summarized as follows:

(1) On the laboratory scale, significant losses of alloying elements with a high oxygen affinity, such as La and Ce, occur due to the high surface-to-volume ratio and the small added amounts. At the tested alloying concepts for Lanthanum, the addition inside an aluminium foil led to a recovery rate of 30.78%. The recovery rate was higher than the result of the second concept, where La was alloyed inside a steel tube. The difference between them was about 6%.

(2) Similar tendencies for the recovery rates of the different alloying concepts occurred for Cerium. The lowest output, 24.33%, was measured by sealing Ce inside a steel tube. The alloying of Ce inside an aluminium foil led to a higher recovery rate of 36.40%. Compared to this concept, the addition of Ce as a ferroalloy with 56 wt-% achieved a slightly higher recovery rate of 38.40%.

Further, the tracing potential and the modification of inclusions due to the rare earth elements La and Ce were investigated, and the following findings can be concluded:

(3) The evolved NMIs traced with REEs were similar in size with mean ECDs ranging between 1.9 and 2.6 μm. The inclusion types are mainly REE-marked deoxidation products (Al_2O_3 + La/Ce) after treatment in the high-

frequency remelting furnace. Despite the excessive addition of rare earth elements, no pure REE oxides occurred.

(4) As determined by SEM/EDS measurements, complex REE–Al–oxides are the dominating inclusion type in all samples. These NMIs are primarily $REEAl_{11}O_{18}$, as seen from thermodynamics and the experimental results. Accelerated cooling in the HFR furnace prevents inclusion modification during solidification, and only partial segregations occur.

(5) Concerning the effective REE contents in the samples, thermodynamics predicted less traced NMIs than effectively observed in the samples. Based on the thermodynamic calculations, only complex REE-containing inclusions are expected. Considering that heterogeneous nucleation plays an important role, complex multiphase NMIs can also be formed. Since kinetics is not taken into account in thermodynamic calculations, it is primarily a good indicator of which NMIs are produced rather than an accurate prediction. The thermodynamic inclusion predictions can be related to both – industrial scale trials and experiments on the laboratory scale. A detailed analysis of the morphologies via three-dimensional characterization is planned to differ between these inclusion types.

ORCID

Kathrin Thiele http://orcid.org/0000-0003-4324-5297
Peter Presoly http://orcid.org/0000-0002-7391-6891
Daniel Ernst http://orcid.org/0000-0002-9323-2200
Shashank Ramesh Babu http://orcid.org/0000-0003-1288-5953
Susanne K. Michelic http://orcid.org/0000-0002-4325-8648

References

[1] Costa e Silva ALVd. The effects of non-metallic inclusions on properties relevant to the performance of steel in structural and mechanical applications. J Mater Res Technol. 2019;8:2408–2422. DOI:10.1016/j.jmrt.2019.01.009

[2] Garrison WM, Wojcieszynski AL. A discussion of the effect of inclusion volume fraction on the toughness of steel. Mat Sci Eng A. 2007;464:321–329. DOI:10.1016/j.msea.2007.02.015

[3] Wang Y, Cheng G, Wu W, et al. Role of inclusions in the pitting initiation of pipeline steel and the effect of electron irradiation in SEM. Corros Sci. 2018;130:252–260. DOI:10.1016/j.corsci.2017.10.029

[4] Maciejewski J. The effects of sulfide inclusions on mechanical properties and failures of steel components. J Fail Anal Preven. 2015;15:169–178. DOI:10.1007/s11668-015-9940-9

[5] Ray A, Paul SK, Jha S. Effect of inclusions and microstructural characteristics on the mechanical properties and fracture behavior of a high-strength low-alloy steel. JMEP. 1995;4:679–688. DOI:10.1007/BF02646444

[6] Dub VS, Safronov AA, Movchan MA, et al. Effect of a secondary metallurgy technology on the types of forming nonmetallic inclusions and the corrosion resistance of steel. Russ Metall. 2016;2016:1135–1144. DOI:10.1134/S0036029516120077

[7] Tervo H, Kaijalainen A, Pikkarainen T, et al. Effect of impurity level and inclusions on the ductility and toughness of an ultra-high-strength steel. Mat Sci Eng A. 2017;697:184–193. DOI:10.1016/j.msea.2017.05.013

[8] Park JH, Todoroki H. Control of MgO·Al₂O₃ spinel inclusions in stainless steels. ISIJ Int. 2010;50:1333–1346. DOI:10.2355/isijinternational.50.1333

[9] Da Costa e Silva ALV. Non-metallic inclusions in steels – origin and control. J Mater Res Technol. 2018;7:283–299. DOI:10.1016/j.jmrt.2018.04.003

[10] Gorkusha D, Karasev AV, Komolova O, et al. Characterization of non-metallic inclusions and clusters during production of low-carbon IF steel. ISIJ Int. 2020;60:2819–2828. DOI:10.2355/isijinternational.ISIJINT-2020-202

[11] Bernhard C, Xia G, Egger M, et al. Experimental investigation into the influence of Ti on the clogging of ULC steels in continuous casting. AIST—Association for Iron & Steel Technology; 2012, Atlanta, USA.

[12] Dorrer P, Michelic SK, Bernhard C, et al. Study on the influence of FeTi-addition on the inclusion population in Ti-stabilized ULC steels and its consequences for SEN-clogging. Steel Res Int. 2019;90:1800635. DOI:10.1002/srin.201800635

[13] Kaushik P, Kruse D, Ozgu M. Assessment of castability issues in interstitial-free (IF) steels. Rev Met Paris. 2008;105:92–101. DOI:10.1051/metal:2008020

[14] Nadif M, Lehmann J, Burty M, et al. Control of steel reoxidation and CC nozzle clogging: an overview. Rev Met Paris. 2007;104:493–500. DOI:10.1051/metal:2007209

[15] Tehovnik F, Burja J, Arh B, et al. Submerged entry nozzle clogging during continuous casting of Al-killed steel. METALURGIJA. 2015;54:371–374.

[16] Burty M, Dunand P, Ritt J, et al. Control of DWI steel cleanness by lanthanum tracing of deoxidation inclusions, ladle slag treatment and a methodical approach; 1997.

[17] Nadif M, Burty M, Soulard H, et al. Control of steel re-oxidation and CC nozzle clogging. IISI study on clean steel; 2004.

[18] Zhang L-f. Indirect methods of detecting and evaluating inclusions in steel—a review. J Iron Steel Res Int. 2006;13:1–8. DOI:10.1016/S1006-706X(06)60067-8

[19] Li B, Zhu H, Zhao J, et al. Effect of rare-earth La on inclusion evolution in high-Al steel. Steel Res Int. 2022;93:2100347. DOI:10.1002/srin.202100347

[20] Gao S, Wang M, Guo J-l, et al. Characterization transformation of inclusions using rare earth Ce treatment on Al-killed titanium alloyed interstitial free steel. Steel Res Int. 2019;90:1900194. DOI:10.1002/srin.201900194

[21] Šuler B, Burja J, Medved J. Modification of non-metallic inclusions with rare-earth metals in 50CrMoV13-1 steel. Mater Tehnol. 2019;53:441–447. DOI:10.17222/mit.2018.271

[22] Pan F, Zhang J, Chen H-L, et al. Effects of rare earth metals on steel microstructures. Materials (Basel, Switzerland). 2016;9:417. DOI:10.3390/ma9060417

[23] Li Y, Liu C, Zhang T, et al. Liquid inclusions in heat-resistant steel containing rare earth elements. Metall Mater Trans B. 2017;48:956–965. DOI:10.1007/s11663-016-0873-9

[24] Waudby PE. Rare earth additions to steel. Int Met Rev. 1978;23:74–98. DOI:10.1179/imtr.1978.23.1.74

[25] Baumgartner K, Bernhard C, Presoly P, et al. The potential for grain refinement of a super austenitic stainless steel with a cerium grain refiner. Associazione Italiana di Metallurgia; 2017, Bergamo, Italy.

[26] Wang H, Bao Y-p, Zhi J-g, et al. Effect of rare earth Ce on the morphology and distribution of Al₂O₃ inclusions in high strength IF steel containing phosphorus during continuous casting and rolling process. ISIJ Int. 2021;61:657–666. DOI:10.2355/isijinternational.ISIJINT-2020-053

[27] Wang M, Gao S, Li X, et al. Reaction behaviour between cerium ferroalloy and molten steel during rare earth treatment in the ultra-low carbon Al-killed steel. ISIJ Int 2021;61:1524–1531. DOI:10.2355/isijinternational.ISIJINT-2020-678

[28] Ren Q, Zhang L, Liu Y, et al. Transformation of cerium-containing inclusions in ultra-low-carbon aluminum-killed steels during solidification and cooling. J Mater Res Technol. 2020;9:8197–8206. DOI:10.1016/j.jmrt.2020.05.077

[29] Luo S, Shen Z, Yu Z, et al. Effect of Ce addition on inclusions and grain structure in gear steel 20CrNiMo. Steel Res Int. 2021;92:2000394. DOI:10.1002/srin.202000394

[30] Pan C, Hu X, Lin P, et al. Evolution of inclusions after cerium and titanium addition in aluminum deoxidized Fe-17Cr-9Ni austenitic stainless steel. ISIJ Int 2020;60:1878–1885. DOI:10.2355/isijinternational.ISIJINT-2020-028

[31] Li H, Yu Y-c, Ren X, et al. Evolution of Al₂O₃ inclusions by cerium treatment in low carbon high manganese steel. J Iron Steel Res Int. 2017;24:925–934. DOI:10.1016/S1006-706X(17)30135-8

[32] Wang Y, Li C, Wang L, et al. Modification of alumina inclusions in SWRS82B steel by adding rare earth cerium. Metals (Basel). 2020;10:1696. DOI:10.3390/met10121696

[33] Seeberger GmbH & Co. KG. Material data sheet E235. https://www.seeberger.net>pdf>werkstoffe>stahl.

[34] Zarl MA, Farkas MA, Schenk J. A study on the stability fields of arc plasma in the HPSR process. Metals (Basel). 2020;10:1394. DOI:10.3390/met10101394

[35] Mayerhofer A, You D, Presoly P, et al. Study on the possible error due to matrix interaction in automated SEM/EDS analysis of nonmetallic inclusions in steel by thermodynamics, kinetics and electrolytic extraction. Metals (Basel). 2020;10:860. DOI:10.3390/met10070860

[36] Bandoniene D, Meisel T, Rachetti A, et al. A tool to assure the geographical origin of local food products (glasshouse tomatoes) using labeling with rare earth elements. J Sci Food Agr. 2018;98:4769–4777. DOI:10.1002/jsfa.9124

[37] Geng R, Li J, Shi C. Evolution of inclusions with Ce addition and Ca treatment in Al-killed steel during RH refining process. ISIJ Int. 2021;61:1506–1513. DOI:10.2355/isijinternational.ISIJINT-2020-672

[38] Okabe TH, Kong L, Ouchi T. Thermodynamic consideration of direct oxygen removal from titanium by utilizing vapor of rare earth metals. Metall Mater Trans B. 2022;53:1269–1282. DOI:10.1007/s11663-021-02342-z

[39] Ren Q, Zhang L. Effect of cerium content on inclusions in an ultra-low-carbon aluminum-killed steel. Metall Mater Trans B. 2020;51:589–600. DOI:10.1007/s11663-020-01779-y

[40] Wang H, Yu P, Jiang S, et al. Evolution of inclusions in steelmaking process of rare earth steels containing arsenic with alumina crucibles. Metals (Basel). 2020;10:275. DOI:10.3390/met10020275

RESEARCH ARTICLE

steel
research
international

www.steel-research.de

Check for updates

Tracing of Deoxidation Products in Ti-Stabilized Interstitial Free Steels by La and Ce on an Industrial and Laboratory Scale

Christoph Truschner, Kathrin Thiele, Sergiu Ilie, Roman Rössler, Alfred Jungreithmeier, and Susanne K. Michelic*

The continuous casting of Al-killed Ti-stabilized interstitial free steels is often affected by clogging. By today, the mechanism behind this phenomenon is not entirely clarified. The active tracing method, which involves the direct addition of rare-earth elements (REEs), enables tracking of nonmetallic inclusions (NMIs) over process time. Due to the high oxygen affinity of these elements, preexisting NMIs are partially reduced and marked by this tracer. Using scanning electron microscopy with energy-dispersive spectroscopy, it is possible to differentiate such labeled NMIs from particles formed at later stages in the process by the absence of these tracing elements. Active tracing is used in industrial and laboratory settings to trace preexisting alumina NMIs with La or Ce. In the investigation, it is revealed that the number of small NMIs increases after the addition of REEs, and subsequently, the size increases again after FeTi is alloyed. In both settings, traced and untraced Al–Ti oxides are found. The separation tendency of traced NMIs is studied over time by analyzing the composition of the slags. Furthermore, the impact of deoxidation products on the formation of the clogging layer within the submerged entry nozzle is investigated, indicating that these NMIs contribute to its formation.

1. Introduction

Clogging of the submerged entry nozzle (SEN), defined as the accumulation of solid particles on the inner nozzle wall during the continuous casting of steel, is a major problem that

C. Truschner, S. Ilie, R. Rössler, A. Jungreithmeier
Business Unit Bramme BTT/ R&D
voestalpine Stahl GmbH
voestalpine-Straße 3, Linz 4020, Austria

K. Thiele, S. K. Michelic
Christian Doppler Laboratory for Inclusion Metallurgy in Advanced Steelmaking
Montanuniversitaet Leoben
Franz Josef–Straße 18, Leoben 8700, Austria
E-mail: kathrin.thiele@unileoben.ac.at

The ORCID identification number(s) for the author(s) of this article can be found under https://doi.org/10.1002/srin.202300665.

diminishes the quality of steel products and compromises process efficiency.[1,2] The clogging phenomenon may induce changes in the flow dynamics of the molten steel at the SEN outports by affecting the internal cross-sectional geometry of the SEN, and consequently, the flow conditions within the mold. As described by Zhang et al.[3] such alterations can cause asymmetric flow and irregular temperature distribution in the mold. These deviations can result in slag entrapment, hinder the separation of inclusions, or may even lead to breakouts during the continuous casting process.

Acknowledging the complexity of practical scenarios, Michelic et al.[4] highlighted that clogging deposits often result from a combination of multiple mechanisms. Nevertheless, in theory, four basic formation mechanisms are defined, each distinguished by its origin: agglomeration of deoxidation products, reaction product buildup, aspiration of atmospheric oxygen leading to reoxidation, and solid steel buildup.[4,5] It is essential to underscore the distinct vulnerabilities inherent to specific steel grades. Several studies illustrated that this becomes particularly evident in casting Al-killed steels, for instance, ultralow-carbon (ULC) steel and interstitial free (IF) steel, which commonly encounter nozzle clogging.[6] The problem intensifies when ferrotitanium (FeTi) is alloyed to Ti–ULC or Ti-stabilized interstitial free steels (Ti–IF) to bind dissolved carbon or nitrogen. Despite numerous studies addressing the fundamental mechanisms leading to the increased tendency, this topic remains a subject of ongoing research projects.[7–9] Barati et al.[9] have summarized critical key factors that contribute to the deterioration of the casting behavior of Ti-stabilized steels, which include 1) reduction in surface tension between the steel melt and the SEN refractory due to Ti, and 2) modification of preexisting NMIs' interfacial properties, impacting agglomeration, wetting to liquid steel, and other aspects. As stated by Kang et al.[10] the detrimental castability is also attributed to the susceptibility of these Ti–IF steels to reoxidation. Local oxygen input, which may be induced for instance by reactions between the SEN refractory and the liquid steel, contributes to the formation of the initial clog deposit. This oxidic layer has a high wettability

to other phases and may act as a subsequent buildup site for NMIs in the steel phase.

One way to minimize clogging is to modify inclusions using a calcium treatment.[11] In this process, the existing alumina population is modified to form liquid or partially liquid calcium aluminates, which show a decreased driving force for agglomeration and adhesion to the casting system. However, this option is only available to a limited extent for ULC and IF steels, as their ladle slag often contains high amounts of wustite (FeO). The interaction between this FeO-rich slag and the steel can notably reduce the calcium yield, leading to an incomplete inclusion modification.[4] Consequently, the types of inclusions formed under these circumstances may further intensify the clogging tendency.

As previously mentioned, the factors influencing clogging can be multifaceted and complex. A significant factor in reducing clogging is determining the actual sources of inclusions that are involved in the formation of the clogging layer. Consequently, countermeasures can be taken to suppress these inclusions formation in advance. As described in the review by Costa e Silva,[12] NMIs continuously interact chemically with their environment (steel melt, slag, and refractory) throughout the entire steelmaking process. This interaction can modify the morphology and composition of these particles to such an extent that tracking these NMI back to their original source is no longer possible. The state-of-the-art tracer method for tracking NMIs over the steelmaking process is the direct addition of rare-earth elements (REEs) to the steel melt.

In addition to using these REEs as tracers, these metals can also be deliberately used for inclusion modification. As described by Li et al.[13] the NMIs can be modified by REEs; their melting points fall below the liquidus temperature of the steel. This can achieve a similar effect as the conventional Ca treatment. The work of Wang et al.[14] can be used as a reference for practical application of the inclusion modification by REEs on an industrial scale. In this experiment, a Ce–Fe alloy was added to a high-strength IF steel during the Ruhrstahl Heraeus (RH) treatment in the secondary metallurgy. The existing alumina inclusions were modified to Ce-containing oxide or oxide–sulfide types during this process. The modification by Ce significantly reduced the effective inclusion size and achieved a spherical inclusion shape. Furthermore, the tendency to cluster was suppressed.

There are also risks associated with using REEs for inclusion modification. According to research by Li et al.[15] inappropriate contents of these elements can form additional solid inclusions, increasing the proneness to clogging. Furthermore, REEs have the potential to react with refractory materials and alter their interfacial properties.[16]

For the present study, trials are performed both in an industrial setting and on a laboratory scale. Several Ti–IF heats are alloyed with either La or Ce in the industrial trial. The laboratory trials simulate the production process and track the modification of NMIs. In both cases, steel samples are taken and analyzed regarding cleanness. Since the steel melts are sampled over the processing time, the changes in morphology due to REEs and FeTi addition can be analyzed. In the industrial experiment, tundish and mold slag samples are taken and investigated for their REE content to study the separation tendency of traced deoxidation products. Furthermore, the formed clogging layer on the wall of the SEN is also part of the investigation, which is analyzed with automated scanning electron microscopy with energy-dispersive spectroscopy (SEM/EDS). Thus, it is possible to investigate the involvement of preexisting NMIs in forming the clogging layer.

2. Experimental Section

2.1. Ti–IF Steel

The industrial experiments were conducted at the integrated steel mill of voestalpine Stahl GmbH in Linz, Austria. The Ti–IF steel grade was selected for these experiments due to its higher sensitivity to SEN clogging. **Table 1** presents an exemplary analysis of a Ti–IF steel sample obtained from a tundish of the steel plant of voestalpine Stahl GmbH.

2.2. Input Material for Laboratory Trial

Pure iron was used as a raw material for the laboratory experiments since it has a high purity and a carbon content similar to a Ti–IF steel. The chemical composition of pure iron is shown in **Table 2**. An O-rich master alloy with around 0.2 wt% O was added for these trials to achieve a comparable oxygen content as slightly before the Al killing, where $\approx$300 ppm O were in the steel. The prominent inclusions in the raw material were SiO_2 and MnO. The further input materials were Al, La, Ce, and FeTi70, with an O_{total} of 0.18 wt%.

2.3. Industrial Trial

The production process for Ti–IF and Ti–ULC steels mainly involved using a basic oxygen furnace, ladle treatment at the ladle

Table 1. Chemical composition of a Ti–IF steel sample provided by the steel plant of voestalpine Stahl GmbH.

C [ppm]	Si [wt%]	Mn [wt%]	P [ppm]	S [ppm]	Al [wt%]	Ti [wt%]	N [ppm]	O_{total} [ppm]	Fe [wt%]
14	0.0061	0.1483	0.0085	0.0056	0.0518	0.0572	55	33	Bal.

Table 2. Chemical composition of pure iron for the laboratory trials.

C [ppm]	Si [wt%]	Mn [wt%]	P [ppm]	S [ppm]	Al [wt%]	Ti [wt%]	N [ppm]	O_{total} [ppm]	Fe [wt%]
15	0.0030	0.0270	0.0020	0.0013	0.0010	–	60	120	Bal.

furnace, refining at the RH degasser, and subsequent casting on a continuous slab caster. A schematic illustration of the Ti–IF steel production route, including the REE addition, is shown in **Figure 1**.

Typically, 180 tons of steel were tapped into the steel ladle, containing ≈600 ppm of oxygen and 300 ppm of carbon. Subsequently, the temperature of the melt was adjusted for later casting, and slag formers were liquified using the ladle furnace. The melt was then transferred to the RH vacuum facility for decarburization and afterward killed with Al. Following a brief RH circulation phase of 6 min, 6.5 kg of metallic La or Ce was added through the vacuum chamber of the RH degasser. The purpose of the REE addition was to mark primary deoxidation products. The employed amount was adopted from other industrial trials documented in the literature.[15,17,18] A compromise was sought to achieve the highest possible REE content within the steel without negatively impacting the castability. Subsequently, another circulation period of 8 min ensured proper homogenization of La or Ce within the melt and promoted inclusion removal, thereby ensuring a high level of cleanness. Toward the end of the treatment, FeTi was alloyed

to reduce nitrogen and carbon to a minimum, thus improving these steels' aging resistance. Following this secondary steel treatment, the melt was transferred to the continuous caster. In this particular case, the Ti–IF heats were cast using a single-strand continuous casting machine with a tundish capacity of 32 tons. As illustrated in **Figure 2**a, the exceptional inclusion treatment with Ce or La was carried out on an entire Ti–IF casting sequence. The sequence consisted of 6 heats, with the first and last not receiving any REE treatment. La was used as a tracer for the second and fourth heat, while Ce was an alternative tracer for the third and fifth heat. This alternating addition of REEs was intended to assess the individual contribution of each melt, particularly in the formation of clogging layers in the SEN.

The utilized SEN was changed multiple times throughout the casting sequence, as indicated by the local minima of the stopper rod position in Figure 2b. The first SEN (SEN 1) was picked to investigate the buildup of clogging further. As depicted in Figure 2c, both tundish and mold slag samples were taken throughout the experiment. Tundish slag samples were taken approximately every 10 min after each ladle exchange operation. Mold slag sampling primarily focused on the 20th and 40th
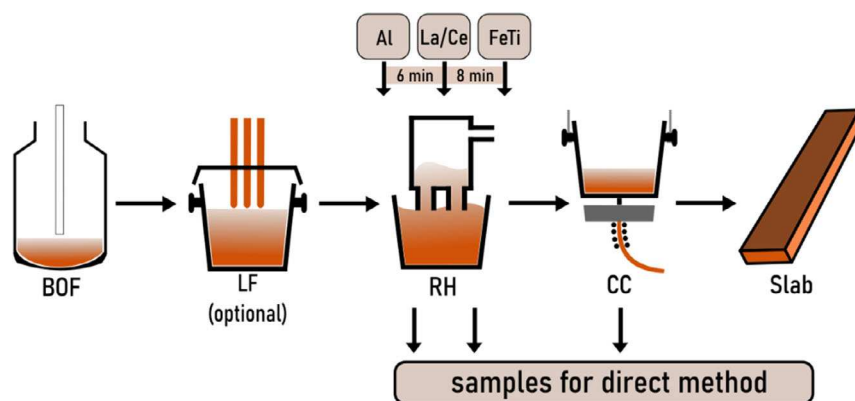

Figure 1. Production route of Ti-stabilized interstitial free (Ti–IF) steel with additional rare-earth elements (REE) treatment.
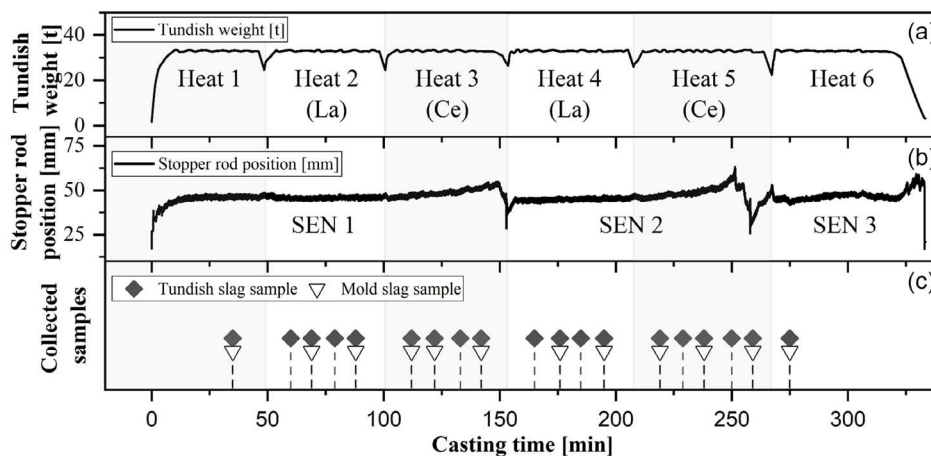

Figure 2. Ti–IF casting sequence and sampling procedure: a) tundish weight over casting time and division of heats, b) stopper rod position over casting time and changes of SEN, and c) sampling of tundish and mold slag over time.

ADVANCED
SCIENCE NEWS
www.advancedsciencenews.com

steel research
international

www.steel-research.de

minutes of casting from each respective heat. Black diamonds denote tundish slag samples, while mold slag samples are represented by white triangles in Figure 2c.

Additional standard lollipop samples were taken within the steel production to analyze the modification of preexisting deoxidation products over the process. The initial state of the deoxidation products before the REE treatment was assessed by taking a steel sample immediately after the Al deoxidation. Further sampling was done after the REE treatment and the addition of FeTi alloy to monitor the modifications caused by these elements. Additionally, the melt in the tundish was sampled to investigate changes of the NMIs after an extended reaction time.

2.4. Laboratory Trial

The two laboratory trials were performed under an inert atmosphere in a resistance-heated Tammann-type furnace (Ruhrstrat HRTK 32 Sond.). The schematic of the used furnace is illustrated in **Figure 3**. A detailed description of this furnace can be found in Dorrer et al.[8] The benefit of this aggregate was that sampling and alloying were possible during the experiment. Hence, the changes in the inclusion landscape after REE and FeTi addition can be studied.

The laboratory trials were based on the industrial experiment. Thus, the time frames between deoxidation by Al, the REE

addition, and the FeTi alloying were similar. A detailed schedule of the laboratory trials, including sampling and alloying, is shown in **Figure 4**. In both experiments, 300 g of pure iron and 10 g of the O-rich master alloy were heated up to 1600 °C. Adding an O-rich master alloy was essential to achieve a comparable O content of $\approx$250 ppm as in industry at the RH degasser directly after the vacuum decarburization. The target value for Al was 400 ppm in the remaining melt. A thermodynamic calculation was necessary to determine the amount of La and Ce for an effective tracing success. For this melt, 160 ppm of REEs were required. The recovery rate for the REEs of 30% was assumed based on the findings of Thiele et al.[19] where different alloying concepts for REEs were tested on a laboratory scale in a high-frequency remelting furnace. The REEs were wrapped in an Al foil to prevent oxidation. The aspired Ti/Al ratio was 1.0. Since this aggregate had only a weak bath movement, stirring with a quartz rod was applied after Al, La/Ce, and FeTi addition.

2.5. Methods of Analysis

The standard lollipop samples taken during the industrial experiment were analyzed for bulk chemistry and the content of REEs using spark optical emission spectroscopy (Spark-OES). For this purpose, the ARL iSpark 8880 instrument (Thermo Fisher Scientific, Waltham, USA) was used. The composition
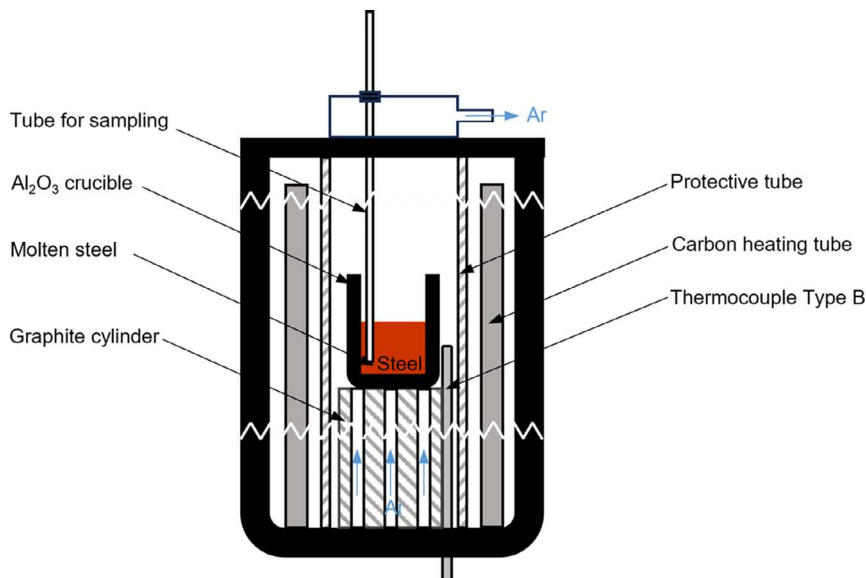

Figure 3. Schematic illustration of resistance-heated Tammann-type furnace (modified). Reproduced under the terms of the CC-BY license.[8] Copyright 2019, The Authors. Published by Wiley-VCH GmbH.
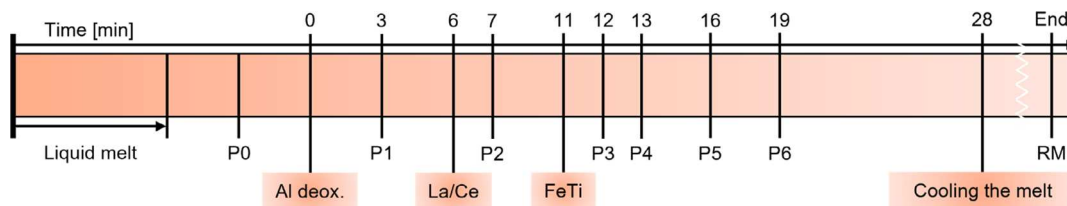

Figure 4. Schedule of the two laboratory trials.

ADVANCED
SCIENCE NEWS

www.advancedsciencenews.com

steel
research
international

www.steel-research.de

of the different slag samples obtained from the ladle, tundish, and mold was determined using inductively coupled plasma OES (ICP-OES, SPECTRO ARCOS ICP-OES, SPECTRO Analytical Instruments GmbH, Kleve, Germany). Before the slag analysis, the samples were ground, dried, and homogenized. An open digestion process utilizing HCl, HNO_3, and H_2O_2 was employed to dissolve the slag components in an aqueous solution.

The standard lollipop samples and the steel samples obtained from the laboratory trials were analyzed for their micro-cleanness to study the modification of the deoxidation products during various process steps. For the characterization of NMIs, a JEOL 7200F field-emission SEM (JEOL Germany GmbH, Freising, Germany) equipped with a $100 \, mm^2$ silicon drift detector (SDD) EDS detector (Oxford Instruments Ultim Max 100; Oxford Instruments GmbH NanoAnalysis, Wiesbaden, Germany) was used. Only particles with an equivalent circle diameter (ECD) greater than $1 \, \mu m$ were detected at the automated measurement. The duration of EDS analysis for each particle was set to 1 s. This method enabled an evaluation of the existing inclusion population regarding chemical and morphological characteristics.

For the inclusion evaluation of this REE-traced steel, using an additional MATLAB tool for the specific assessment of REE-containing inclusions was necessary. Due to the backscattered electron (BSE) coefficient being a function of the mean atomic number of the interacted volume,[20] REE-containing phases appeared brighter in the BSE imaging mode compared to the surrounding Fe-based matrix. In contrast, regular oxide particles exhibited lower BSE yield than the surrounding steel, resulting in a lower BSE intensity (darker appearance in the BSE image) than the matrix. The observed inclusions often have a heterogeneous structure, with regions containing higher REE content and phases with no REEs. As a result, heterogeneous REE-traced NMIs often have multiple contrasting gray values, which can be mistakenly identified as individual particles by standard software. A software was developed to reassemble these particles into a single multiphase inclusion to address this issue. The principle of the recombination software has been previously published by Thiele et al.[21]

As mentioned earlier, the formed clogging layer structure within the used SEN was also examined in detail. For this purpose, a section from the central part of the straight area of each SEN was cut out using an angle grinder, which was then halved (**Figure 5**a). Each sample of the SEN refractory material and the corresponding clogging layer counterpart were further cut to an appropriate size (Figure 5b), washed with ethanol, and then dried. Subsequently, the sample was embedded using a Sn–Bi alloy, to prevent the separation of the inner wall of the SEN and the clogging material during the following polishing. The polishing procedure of the sample was performed analog to the sample preparations of the particle analysis but was additionally sputtered with Au to prevent electrical charging during SEM/ EDS inspections. As shown in the overview BSE image in Figure 5b, specific sample area was defined to study the layer formation in detail. The selected area (Figure 5c) was investigated with a TESCAN CLARA (TESCAN GmbH, Dortmund, Germany) with an additional $80 \, mm^2$ SDD EDS detector (Oxford Instruments X-Max^N 80, Oxford Instruments GmbH NanoAnalysis, Wiesbaden, Germany).

The SEN consisted of an anti-clogging layer and zirconia-based materials in the slag zone to prevent clogging and refractory wear. **Table 3** presents the chemical composition of the anti-clogging layer of the SEN, revealing that it mainly consisted of alumina silicate.

3. Results

3.1. Chemical Composition of Steel and Slag Samples

Table 4 presents the chemical compositions of each IF steel heat after the RH treatment (H1–H6) and the two remaining melts from the laboratory trials (LM1 and LM2). As explained in the previous chapter, 6.5 kg of La or Ce were added in the second
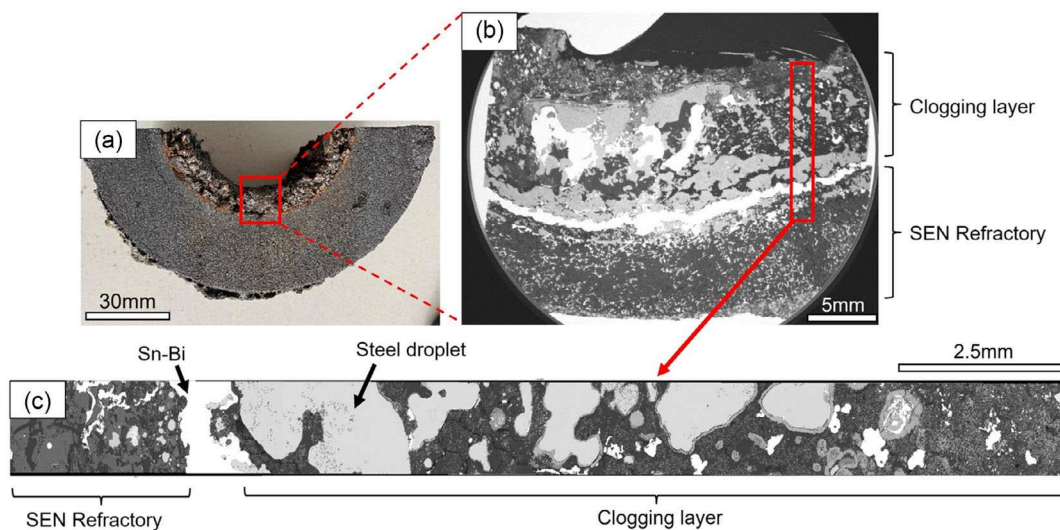

Figure 5. a) Cross-sectional view of halved submerged entry nozzle (SEN); b) backscattered electron (BSE) image: embedded SEN and clogging structure; and c) BSE image: magnified view of SEN refractory and clogging deposits.

Table 3. Chemical composition of the anti-clogging refractory in wt%.

SiO$_2$	TiO$_2$	Al$_2$O$_3$	CaO	B$_2$O$_3$	Fe$_2$O$_3$
44.2	0.1	52.7	0.1	2.7	0.2

to fifth heats. The chemical composition of the steel samples was determined using Spark-OES. The content of La or Ce was analyzed by using ICP mass spectrometry (ICP-MS).

Figure 6 illustrates the changes of La and Ce concentrations in the analyzed lollipop steel samples from the industrial trials. Due to the incomplete filling of the lollipop mold during the sampling process, the second tundish sample from the fourth heat was unavailable for analysis.

The chemical analysis of the steel samples showed that the highest REE content was observed immediately after the addition. Afterward, a steady reduction in the REE concentration was observed. In the case of the fifth heat, Ce traced, a lower concentration was measured immediately after REE addition. Compared to the taken sample after REE addition, the subsequent lollipop sample (after RH) had a higher Ce content.

Figure 7 provides an overview of the changes in the chemical compositions of the tundish and mold slag samples throughout the entire Ti–IF casting sequence. The REE content in the

tundish slag shows a stepwise increase, correlating different heats with distinct tracers in the tundish at specific times (Figure 7). During the casting of the La-traced heats, a significantly higher increase in the La concentration was observed within the slag (Figure 7b—black diamonds) compared to the Ce concentration at the Ce-traced melts inside the tundish (Figure 7c—black squares). The variations of La and Ce concentrations within the mold slag are depicted as white triangles in Figure 7b,c. The REE concentration fluctuated periodically depending on the heat and which particular tracer was added.

3.2. Micro-Cleanness Evaluation

The results of the automated SEM/EDS analysis to determine the micro-cleanness of the lollipop samples of the industrial trial and the laboratory samples are shown in this section. The inclusions were categorized into different classes based on their nonmetallic bonding partner (O, S, N, oxide–sulfide, oxide–nitride, nitride–sulfide, and oxide–nitride–sulfide). The specific typification of these inclusions depends on the metallic bonding partner (e.g., Al, Mg, or Ca).

To understand the ongoing inclusion modification resulting from the addition of REEs, SEM/EDS analysis was performed on samples from two melts in an industrial-scale experiment

Table 4. Chemical composition of industrial steel samples (H1–H6) at the end of RH refining and the remaining melt of the laboratory trials (LM1 and LM2) in wt%.

No.	C	Si	Mn	S	Al	Ti	La	Ce	REE (theor.)
H1	0.0014	0.0015	0.1415	0.0048	0.0543	0.0592	–	–	–
H2	0.0015	0.0028	0.1329	0.0048	0.0577	0.0639	0.0015	–	0.0037
H3	0.0011	0.0036	0.1121	0.0052	0.0563	0.0678	–	0.0002	0.0036
H4	0.0015	0.0018	0.0995	0.0037	0.0539	0.0582	0.0017	–	0.0037
H5	0.0011	0.0021	0.0902	0.0050	0.0509	0.0631	–	0.0009	0.0037
H6	0.0011	0.0020	0.0900	0.0050	0.0510	0.0630	–	–	–
LM1	0.0120	0.0505	0.1360	0.0042	0.0335	0.0266	0.0029	–	0.0160
LM2	0.0097	0.0306	0.0994	0.0033	0.0372	0.0340	–	0.0061	0.0160

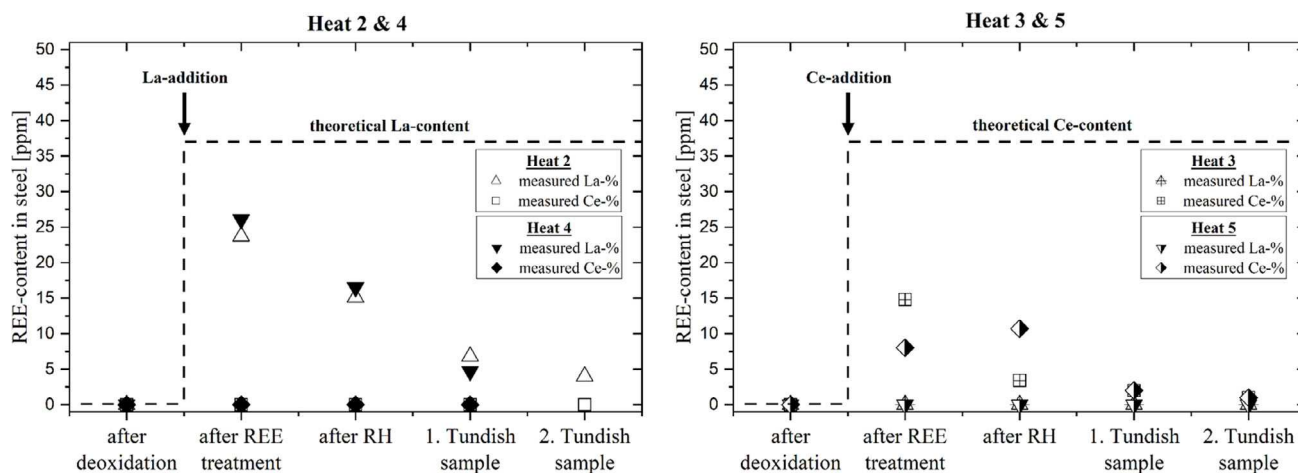**Figure 6.** Changes of La and Ce content in steel samples during Ruhrstahl Heraeus (RH) treatment and casting process.

**ADVANCED
SCIENCE NEWS**

www.advancedsciencenews.com

**steel
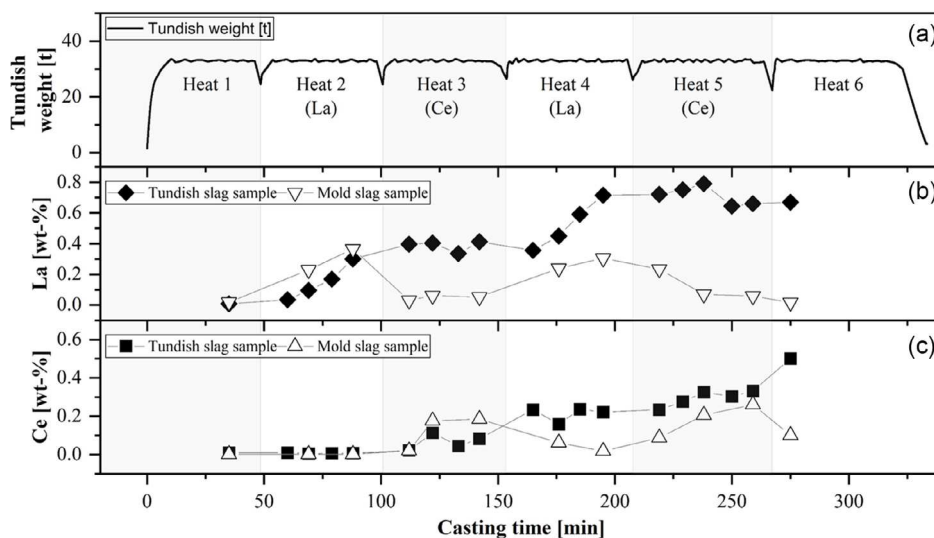research**
international

www.steel-research.de

Figure 7. a) Tundish weight during casting sequence; b) La and c) Ce concentrations within tundish and mold slag samples.

and two melts in a laboratory-scale experiment. The aim was to compare and highlight the differences between the industrial and laboratory scales, for instance, the influence on the achievable inclusion tracing rates. A representative La-traced melt (Heat 2 and LM1) and a melt in which Ce was added as a tracer (Heat 3 and LM2) were examined for each setting. This section focuses on the La-modification results, as similar findings were observed for the Ce-traced samples. In the four investigated samples taken directly after Al deoxidation, mainly Al-containing oxides were detected, regardless of whether they originated from the laboratory or industrial setting. In **Figure 8**, the results of the micro-cleanness evaluation of the two La-traced melts, Heat 2 and LM1, are presented. This overview includes only the three main types of inclusions that were predominantly found, with the addition of TiN for completeness, despite it not being part of the study. The reported mean ECD contains the entire population of traced and untraced inclusion types. The samples within each column correspond to their respective counterparts from the industrial- and laboratory-scale experiments taken during the same process period. As shown in Figure 8a,e, similar-sized alumina particles were found in both melts. For Heat 2, the Al_2O_3 particles had a mean ECD of 1.69 μm with a standard deviation of ±0.93 μm, while for sample P1, a mean ECD of 2.29 μm ± 1.04 μm was observed. In the case of the laboratory melt (LM), a higher proportion of $MgO–Al_2O_3$ and $CaO–MgO–Al_2O_3$ oxides was detected.

Significant differences in the tracing rates between the industrial and laboratory trials were revealed during the investigation of the samples taken immediately after the addition of La. In the case of the LM (P3), a substantial proportion of the existing alumina particles (70%) were traced and modified. In contrast, only 17.6% of the occurring alumina particles were marked within the second heat's industrial lollipop sample (after REE). All samples, taken directly after the REE addition, showed an increase in inclusion number per unit area. A change in the mean ECD was also observed. In the lollipop sample from Heat 2, the ECD of the untraced alumina was approximately

1.48 ± 0.28 μm, while for the traced, it was 1.52 μm ± 0.34 μm. Similar findings were observed in the laboratory sample, where the mean ECD of pure alumina was slightly smaller (1.49 ± 0.33 μm) compared to La-modified Al_2O_3 (1.87 ± 0.96 μm). In both cases, the La-modified alumina NMIs showed in the manual investigation a heterogeneous structure and, in most cases, a spherical shape. In the industrial samples, aside from the dominant inclusion type of traced and untraced Al_2O_3, single $SiO_2–Al_2O_3$ and $MnO–Al_2O_3$ were also identified. Following the alloying of FeTi, the content of alumina decreased, accompanied by a raised presence of $Al_2O_3–TiO_x$ and TiN. This increase is more distinct in the industrial-scale experiment. The highest proportion of $Al_2O_3–TiO_x$ and TiN was observed in the tundish lollipop samples.

3.3. Investigation of SEN Clogging Layer

The utilized SEN and their clogging layers were also subjected to investigate the correlation between the deoxidation products and the formation of these clogging structures. For this purpose, the used nozzles and their corresponding clogging layers were analyzed using SEM/EDS. **Figure 9** displays the results of the elemental mapping of the first SEN (changed after the third heat), providing insight into the spatial distribution of elements. On the left side, the SEN refractory is depicted. As shown in the EDS mapping, the refractory material was infiltrated by the liquid steel, extending to a depth of approximately 1 mm into the material.

Within the clogging layer of SEN 1, three distinct zones can be identified. The first section extends from approximately 0.25 to 2.5 mm, measured from the inner wall of the SEN (Figure 9—Zone 1). Aside from pure alumina, $Al_2O_3–TiO_x$ and solidified steel were found within this zone. A significant portion of the observed oxide network is marked with La in the second region (Figure 9—Zone 2), which extends between 2.5 and 4.5 mm. The last section (Figure 9—Zone 3), which is located approximately 4.5–8.7 mm from the inner wall of the
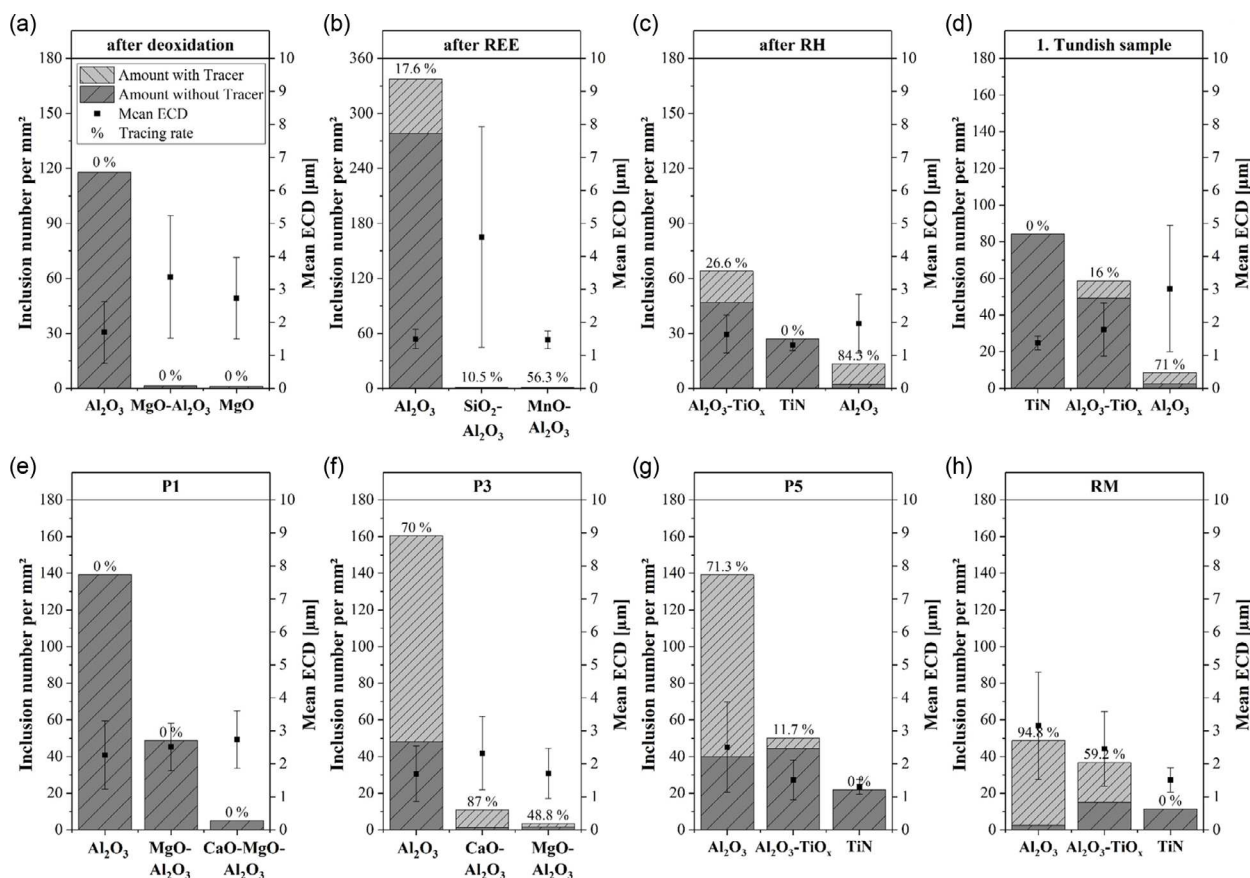
Figure 8. Comparison of inclusion number and size over process time in La-traced melts between the industrial trial and LM: a–d) Heat 2 and e–h) LM1.
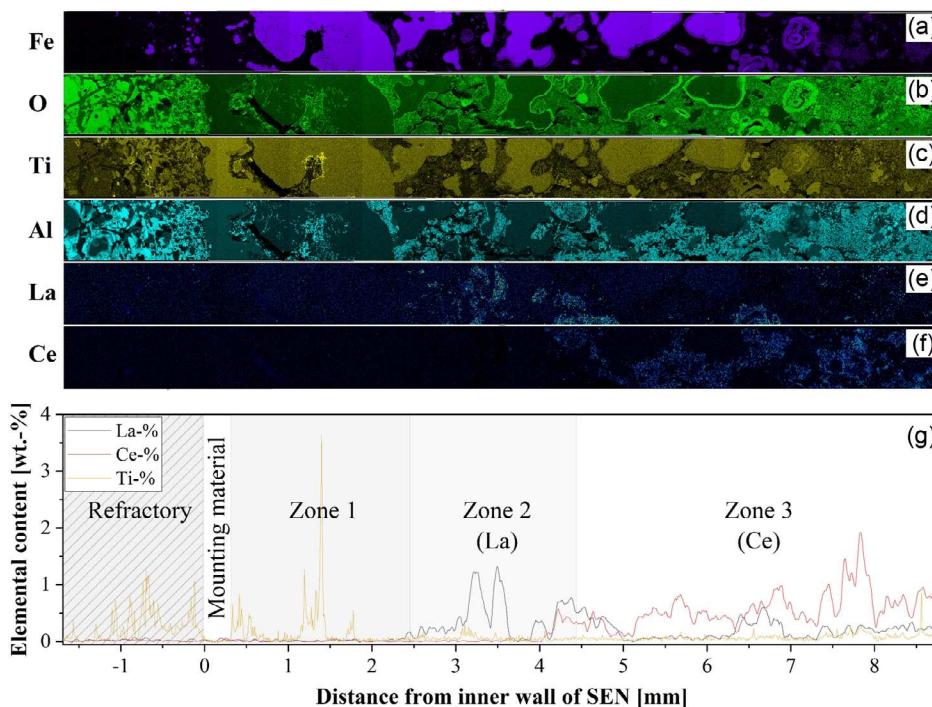

Figure 9. a–f) Elemental mapping of SEN refractory and clogging layer and g) corresponding EDS line scan concentration profiles for the measured section.

**ADVANCED
SCIENCE NEWS**

www.advancedsciencenews.com

**steel
research**
international

www.steel-research.de

SEN, is characterized by a notable presence of Ce-traced alumina inclusions within the clogging structure. In the second and third zone, areas with solidified steel can also be observed, although their size and quantity decrease with increasing distance from the SEN refractory. In contrast to the part of the clogging layer of zone 1, only small amounts of Ti-containing particles could be detected within the sintered clogging networks of the second and third clogging zone.

4. Discussion

4.1. Recovery Rates

The addition of La and Ce led to high losses in both cases, the industrial and the laboratory trials. In the industrial experiment, the amount of REEs was approximately 40 ppm, similar to the studies of Gao et al.[17] and Geng et al.[18] where Ce was used as a tracer. The amount was significantly lower compared to the laboratory trials since the previous investigation of Tian et al.[22] found that REEs may increase the clogging tendency. The effective amount of La was about 23 ppm for the second heat and 26 ppm for the fourth. In comparison, only 15 and 8 ppm Ce were measured in the third and fifth heat. Hence, the losses for Ce were significantly higher than for La. Several studies used ferrocerium with a Ce content of approximately 10 wt% and a recovery rate of 50%, leading to lower losses of this element.[14,17,18,23] Furthermore, the amount of La and Ce decreased over the process, as shown in Figure 6, due to the deposition of traced NMIs into the slag.

Compared to the industrial experiments, higher losses of the tracers were expected for the laboratory trials since only a low mass of these highly oxygen affine elements had to be alloyed. Hence, a recovery rate of 30% based on the findings of Thiele et al.[19] was set. The results of the ICP-MS investigation of all samples led to the assumption that the losses at the resistance-heated Tammann-type furnace were higher than expected. Only 5.4% of the added amount of La was found in the remaining melt of the trial LM1 and 11.3% of Ce at LM2. The reason for the lower recovery rates is the longer contact time between the REEs and the atmosphere at the resistance-heated Tammann-type furnace compared to the high-frequency remelting furnace used for the study of Thiele et al.[19]

Besides the higher amount of REEs in the melt, a higher tracing rate for Al-containing NMIs results for the laboratory trials. The tracing rate in the laboratory was 70.59% for La and 92.82% for Ce. In the industry, the values of the tracing rates were about 10.23% and 34.26% for La and Ce in the example of the second and third heat. The reasons for the higher REE content were the assumption of a recovery rate for the laboratory experiment compared to the industrial ones and the presence of slag in the industry. The tracing rate was higher for Ce at the laboratory due to the higher losses of La. For the industrial trial, the tracing rate was also higher for Ce although Ce's measured content was lower than La's. In this case, the interaction between slag and steel as well as the lower uptake of traced inclusions into the slag must be considered.

4.2. Separation Behavior of NMI (Steel and Slag Samples)

As previously mentioned, a steady decline of the REE content in the industrial samples could be observed after adding these tracers at the RH degasser. This decline could indicate the separation behavior of the traced deoxidation products during this period. The micro-cleanness evaluations of these lollipop samples show a similar trend (**Figure 10**). A lower Ce concentration was observed in the sample taken after the Ce addition compared to the sample after the FeTi addition at the fifth heat. This difference could be attributed to inadequate homogenization within the molten steel during the sampling procedure at the RH facility. According to Yang et al.[24] the decrease in the number of inclusions during the RH treatment is primarily attributed to their coagulation through collisions caused by the intense turbulence within the steel melt during its circulation. These particles coalesce into clusters, increasing their susceptibility to removal through buoyancy forces. Moreover, their high surface-to-volume ratio facilitates the attachment of the particle clusters to the argon bubbles' surface, supporting their transport to the slag–steel interface.[12] The REE content decreased between the last sample
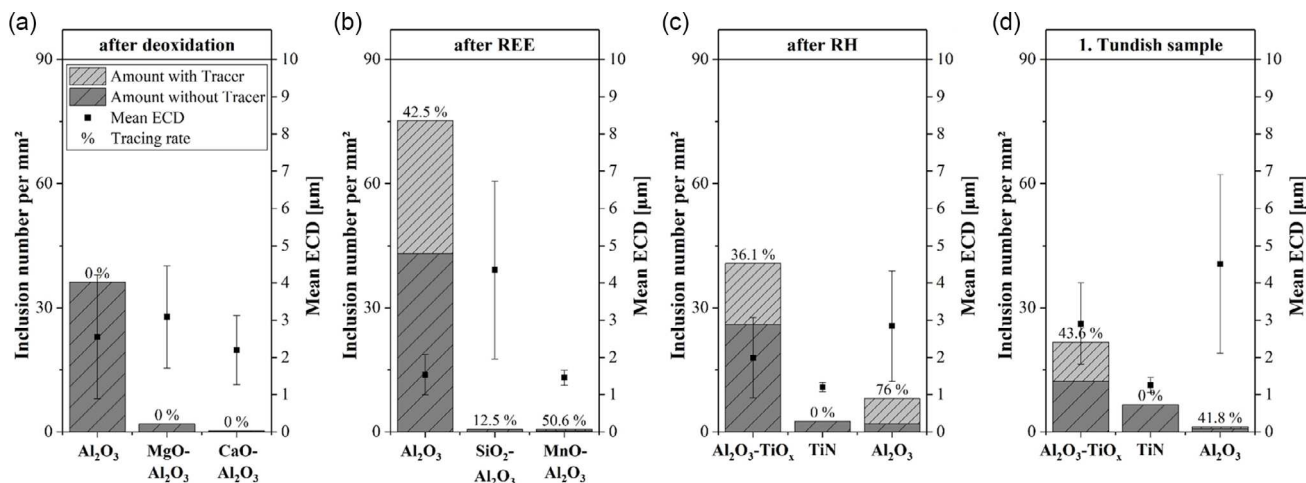

Figure 10. a–d) Comparison of inclusion number, size, and tracing rate over process time: Ce-traced Heat 3.

**ADVANCED
SCIENCE NEWS**

www.advancedsciencenews.com

**steel
research**
international

www.steel-research.de

taken at the RH degasser (after RH) and the subsequent tundish steel samples. This can be attributed to the inclusion removal process that occurs within the steel ladle during the transport of the melt to the continuous caster and the subsequent holding time at the ladle turret. In the absence of injected stirring gas in this process period, temperature stratification occurs within the steel melt, resulting in a certain degree of bath circulation. The occurring circulation subsequently facilitates the transport of existing particles to the slag–steel interface.[25] According to Zhang et al.[26] the main mechanism for inclusion removal in the continuous casting tundish is the particle growth through turbulence collision, followed by floating of particles to the free surface. Another possibility of inclusion removal is by adhesion to solid surfaces, such as the refractory lining of the tundish.[26]

In addition to the decrease in REE content within the lollipop samples, these elements were gradually enriched in the respective process slags. The analysis of the ladle slag samples taken immediately after the RH treatment indicated that approximately 12–15% of the total La or Ce added to the steel was detected in the slag within approximately 10 min. Considering the La and Ce content of the tundish slag samples, a successive enrichment of these elements can also be observed throughout the entire casting period, indicating the separation behavior of these traced particles into the slag over the casting time. The analysis of the mold slag samples led to similar results. The contents of REE follow a distinctive oscillating pattern, which can be attributed to the interaction between the continuous separation of inclusions and the addition of new casting powder to the mold slag. At the same time, a part of the emulsion formed by the molten casting powder and preexisting mold slag is entrapped in the gap between the oscillating copper mold and the solidifying steel shell. A characteristic periodic variation of the REE concentration, depending on which heat is being cast at a given time, results.

These findings highlight the method's effectiveness in tracking the steel's deoxidation products throughout the entire production process and their deposition within the respective process slags. In this study, REEs were added following a standard production procedure of Ti–IF steels. The tracers in the steel plant can be used for a wide range of purposes, including assessing the effectiveness of various measures (such as gas stirring operations, tundish inserts, casting parameters, etc.) aimed at improving the cleanness of the existing steelmaking process. However, one critical aspect needs to be considered when utilizing this method. As stated in the review of Zheng et al.,[27] the interfacial properties of the inclusions play a significant role in the removal process. These properties affect the agglomeration behavior, the capacity to adhere to bubbles, and the potential of NMIs to pass the slag-steel interface for subsequent dissolution into the slag phase.

Based on this background, ongoing research is focusing on developing an alternative method that does not require the active addition of tracer elements. In the study conducted by Thiele et al.[28] patterns of natural trace element distribution, including REEs, were analyzed in input materials such as alloying elements, auxiliaries, and refractory materials using ICP-MS and laser-ablation ICP-MS. The mass fractions of REEs were then normalized to a reference material and compared to the REE pattern obtained from the analysis of an SEN clog. During this investigation, a clear correlation was found between Al granules, used as deoxidizer, and the clogging material within the used SEN.

4.3. Micro-Cleanness of Steel Samples

To gain insight into the changes in the inclusion population caused by the addition of REEs, SEM/EDS analysis was performed on lollipop samples from the industrial trials and steel samples from the laboratory experiments. The analysis aimed to provide more information about the reaction between the existing inclusion population and the REEs. To achieve this objective, a comparison was made between La-traced melts (Heat 2 and LM1) and melts with Ce added as a tracer (Heat 3 and LM2). The purpose was to observe differences between the occurring NMIs at the laboratory and industrial trials regarding their morphology and composition after REE and FeTi addition. Similar types of inclusions could be found in all four samples, which were taken immediately after the Al deoxidation. The majority of the detected inclusions consisted of pure Al_2O_3. An increased presence of $MgO–Al_2O_3$ (MA) spinel inclusions was also seen in the laboratory sample analysis. The presence of MA spinels is due to residuals in the used pure iron where these particles were formed due to a possible reaction between alumina and the refractory lining of the crucible.[29] After the addition of REEs, existing inclusions were modified, but the achieved tracing rates varied significantly. In the industrial-scale experiment, specifically in Heat 2 with La addition, the tracing agent was detected in 17.6% of the alumina inclusions in the taken sample after REE addition. Figure 10 depicts approximately 42.5% of the Al_2O_3 inclusions being marked with Ce.

Compared to the results from the industrial trials, the laboratory-scale experiments achieved a higher tracing rate, which can be attributed to the higher concentration of REEs used in the laboratory setting. Nonetheless, a similar pattern is observed when comparing the La- and Ce-traced melts in both the industrial and laboratory settings. In both cases, a significantly higher tracing rate could be achieved by using Ce as a tracer. A similar pattern is observed when comparing the La- and Ce-traced melts in the laboratory experiments, with a higher tracing rate measured in the case of Ce addition. In the case of the industrial trial, many submicroscopic inclusions were found in the manual SEM/EDS analysis of the taken samples after Ce addition. The minimum size detected at the automated SEM/EDS measurement was 1 μm. Hence, these presumably newly formed inclusions were not analyzed. Similar findings appeared in the industrial sample after La addition. The inclusions were slightly larger compared to the sample after Ce addition, and thus, more newly formed NMIs could be measured. An explanation for this increase in NMIs after REE addition provides the study of Geng et al.[30] They found that REEs lead to an input of O and S in the melt and, as a result, to reoxidation. Since more newly formed NMIs were measured after the La addition, the number of particles per square millimeter increased, and further, the tracing rate of Al-containing NMIs decreased.

According to calculations performed by Thiele et al.[19] it is predicted that the following inclusion phases become thermodynamically stable with increasing La content after the
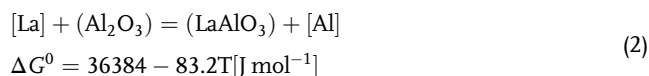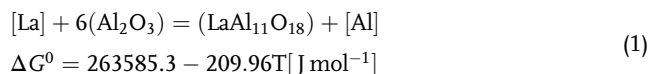
**ADVANCED
SCIENCE NEWS**

www.advancedsciencenews.com

**steel
research**
international

www.steel-research.de

Al deoxidation: $Al_2O_3 \rightarrow LaAl_{11}O_{18} \rightarrow AlLaO_3 \rightarrow Al_7La_{33}O_{60} \rightarrow La_2O_3 + La_2S_3 \rightarrow La_2O_3 + LaS$. For Ce, the thermodynamically predicted sequence is as follows: $Al_2O_3 \rightarrow CeAl_{11}O_{18} \rightarrow AlCeO_3 \rightarrow Al_2Ce_4O_9 \rightarrow Ce_2O_3 + Al_2O_3 \rightarrow Ce_2O_3 + CeS$. Based on the added amount of REEs (La/Ce), the alumina inclusions will mainly form complex Al–REE oxides ($REEAl_{11}O_{18}$ and $AlREEO_3$). Furthermore, in both cases, the REE content is insufficient to form pure REE oxides or REE sulfides. The prediction of similar inclusion modification steps in the case of Ce was reported by Wang et al.[23] and in the case of La by Mao et al.[31]

Figure 11 shows the ternary system of Ce–Al–O including the detected NMIs of the industrial sample after RH and the remaining melt of the laboratory trial LM2. In addition to these results, the positions of $CeAl_{11}O_{18}$ and $AlCeO_3$ are marked as reference points.

These theoretical considerations are consistent with the experimental observations. The analysis of the industrial and laboratory samples revealed that most of the REE-traced alumina consisted of complex REE–Al oxides, primarily in the form of $REEAl_{11}O_{18}$. One La-modified example of such an inclusion type is shown in **Figure 12**c. As shown in Figure 11, $REEAlO_3$ inclusions were mainly found in the laboratory setting, which is consistent with the higher concentration of added REEs. Most REE-modified NMIs were heterogeneous multiphase inclusions and showed a strong segregation tendency. This has also been documented in other publications, such as Ren et al.[32] Single inclusions of Al–REE oxide–sulfide (Figure 12b) were observed in the industrial lollipop samples taken immediately after adding the tracer at the RH degasser. In the later stage of the process, no inclusions of this type were found. This inclusion phase was likely formed immediately after the addition of REEs, as it may have led to the formation of a region with elevated REE concentration within the melt at that time. As the steel is homogenized during the ongoing RH circulation and the local REE

activity decreases, the formation of these types of inclusions is suppressed as they become thermodynamically unstable. In contrast, these oxidic–sulfidic phases were not found in the samples of the LMs, which is likely due to lower sulfur contents within the pure iron.

The chosen tracing technique is possible, as these REE metals have a higher oxygen affinity at the given steelmaking temperatures than classic deoxidants (such as Al). REEs can partially reduce oxides formed during deoxidation. These REEs are incorporated into the inclusion complex in this process, effectively marking the existing NMIs.[14] The chemical reactions describing the formation of REE–Al oxides through the interaction between preexisting alumina and La and the corresponding free Gibbs energies are expressed by Equation (1) and (2)[33]

$$[La] + 6(Al_2O_3) = (LaAl_{11}O_{18}) + [Al]$$
$$\Delta G^0 = 263585.3 - 209.96T [J\,mol^{-1}] \tag{1}$$

$$[La] + (Al_2O_3) = (LaAlO_3) + [Al]$$
$$\Delta G^0 = 36384 - 83.2T [J\,mol^{-1}] \tag{2}$$

As shown in Figure 10, there was a significant decrease in the measured ECD of alumina particles immediately after the addition of Ce ($1.54 \pm 0.60\,\mu m$), compared to the sample taken directly after deoxidation ($2.55 \pm 1.66\,\mu m$). This change in inclusion size was also reported by Li et al.[34] Their study demonstrated that the Ce treatment influenced the size distribution and quantity of NMI per unit area. According to the documented results, there was a decrease in the percentage of inclusions larger than 5 μm as the Ce content increased. Nevertheless, a critical threshold of 0.034 wt% Ce was reported, above which the inclusion size increased once again. Similar observations were made in the present study. In the case of the industrial trial with a lower REE addition, a significant reduction in ECD was achieved. However, only a slight change in the inclusion size was observed in the laboratory experiments with higher La/Ce content. Li et al.[34] concluded that there exists an optimal Ce addition content that can facilitate the formation of finer and more dispersed NMIs. Since the results of the Ce and La treatments showed a similar pattern, the same likely applies to La.

As presented in Figure 10, a significant increase in Al_2O_3–TiO_x was observed after adding FeTi. Dorrer et al.[8] demonstrated that immediately after the addition of FeTi, this inclusion type was formed. Similar to the findings in this work, it was observed that the newly formed Al_2O_3–TiO_x inclusions were relatively small, and the amount of pure alumina significantly decreased. The presented mean ECD values in Figure 8 and 10 are strongly influenced by the fraction of traced Ti-containing oxides, which exhibited a larger ECD in this case. Figure 12d represents an example of an untraced Al_2O_3–TiO_x inclusion. However, it should be noted that the X-ray intensity map displays a misleading La concentration due to the overlapping X-ray peaks of the La–L_α and the Ti–K_α lines. Manual SEM/EDS measurements of the traced Al_2O_3–TiO_x revealed that it consisted partly of agglomerated REE–Al oxides and Al–Ti oxides (Figure 12e). Furthermore, it was observed that submicroscopic Ti-containing phases formed on the surface of existing REE–Al oxides.
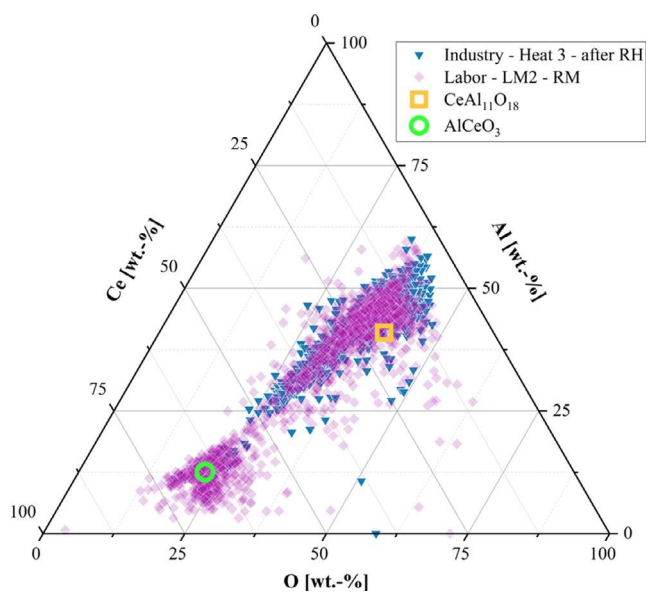

Figure 11. Ternary system of Ce–Al–O, including the detected NMIs of the third heat from the industrial trial, the remaining melt of the LM2, and the theoretical composition of $CeAl_{11}O_{18}$ and $AlCeO_3$.
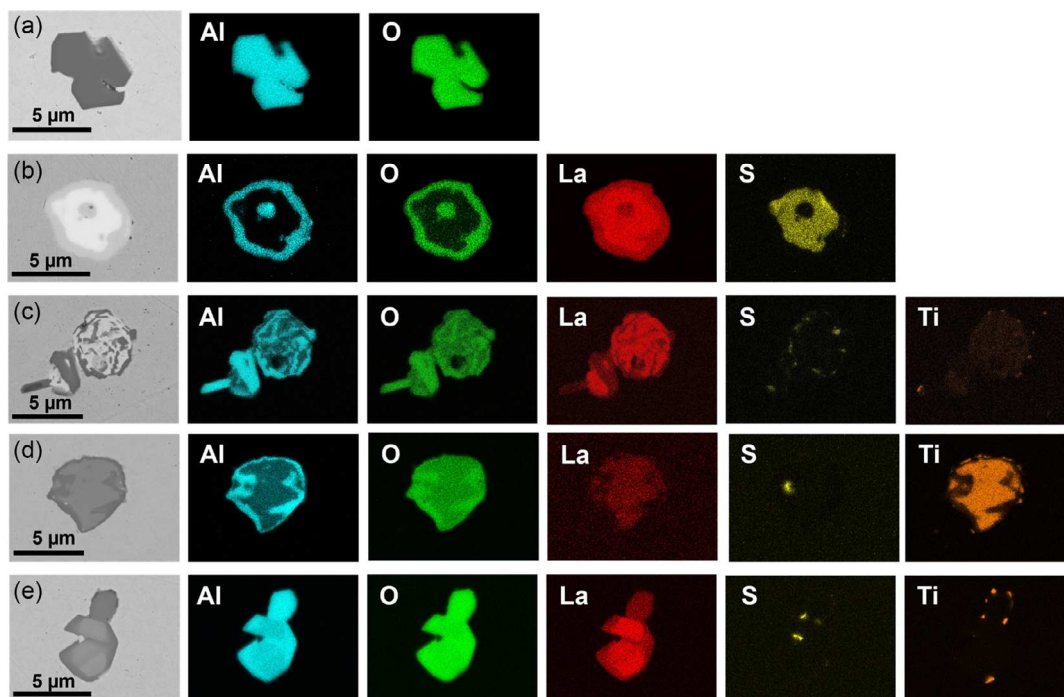
Figure 12. Change of NMIs due to La and FeTi on the example of the industrial trial: a) Al_2O_3 after Al; b) La-traced Al_2O_3 after La; c) La-traced Al_2O_3 after RH; d) Al_2O_3–TiO_x after RH; and e) La-traced Al_2O_3 of 1. Tundish sample.

A trend observed in both the industrial and laboratory settings is the increase in the tracing rate over process time. The rise of traced NMIs may be attributed to the previously described changes in interfacial properties. As Zheng et al.[27] reported, REE oxides have a decreased wetting angle compared to regular alumina, which lowers their driving force to form clusters or chance to attach to argon bubbles. Additionally, the ongoing modification by REEs leads to an increase in their density. Based on the findings of Waudby et al.[35] REE oxides have a similar density to liquid steel. The reduction of the resulting buoyancy force, combined with the altered wetting properties, decreases the deposition probability compared to untraced alumina inclusions.

In summary, similar results were obtained regarding inclusion modification and size distribution when using La or Ce as tracers. The only noticeable difference observed in both settings was that the tracing rate using Ce was significantly higher compared to La. Further investigation is required to determine the underlying cause for the observed discrepancy between Ce and La.

4.4. Analysis of SEN Clogging Layer

The SEM/EDS investigations of the clogging layer within SEN 1 unveiled the presence of three distinct zones. The first zone, situated closest to the inner wall of the SEN, was characterized by a composition primarily consisting of pure alumina, Al_2O_3–TiO_x, and solidified steel. No REE-marked oxides were detected in this region since the first heat was a standard heat without adding tracers. Steel droplets in the clogging layer have been observed

in previous studies.[36,37] The presence of steel in the layer is attributed to changes in the wetting characteristics between the liquid steel and the refractory material of the SEN. A local concentration peak of Ti appeared within the first clogging zone in the area surrounded by solidified steel droplets (**Figure 13**). Further the elemental mappings indicate the formation of a CaO–Al_2O_3–TiO_x (CAT) boundary layer at the interface between the steel and the alumina clogging network.

The formation of such a layer structure has also been addressed and discussed in the study of Lee et al.[36] based on their previous findings documented in ref. [7]. Their work[36] proposed a mechanism involving a reaction between carbon and SiO_2 within the SEN refractory. This reaction leads to the formation of CO, which acts as a local source of reoxidation and oxidizes Al, Ti, and Fe. The resulting complex FeO–Al_2O_3–TiO_x (FAT) compound is liquid at the prevailing temperatures and exhibits high wettability, serving as a binder between refractory, steel, and inclusions. Additionally, it is described that a reduction of this FAT oxide compound can occur through the dissolved Al in the steel or through reactions with CaO from the SEN refractory. As a result, the formation of the CAT boundary layer and the reduction of Fe droplets may occur. This mechanism could have also contributed to the formation of the initial clogging layer in the present study, especially during its early stage.

In the second zone, situated within the central part of the developed clogging layer, a notable amount of the observed oxide network is marked by La. An exemplary EDS mapping from an area with elevated La concentration is shown in **Figure 14**. Considering the absence of any additional La source in this experimental series, it can be presumed that the observed alumina oxides of zone 2 were formed during the Al killing process
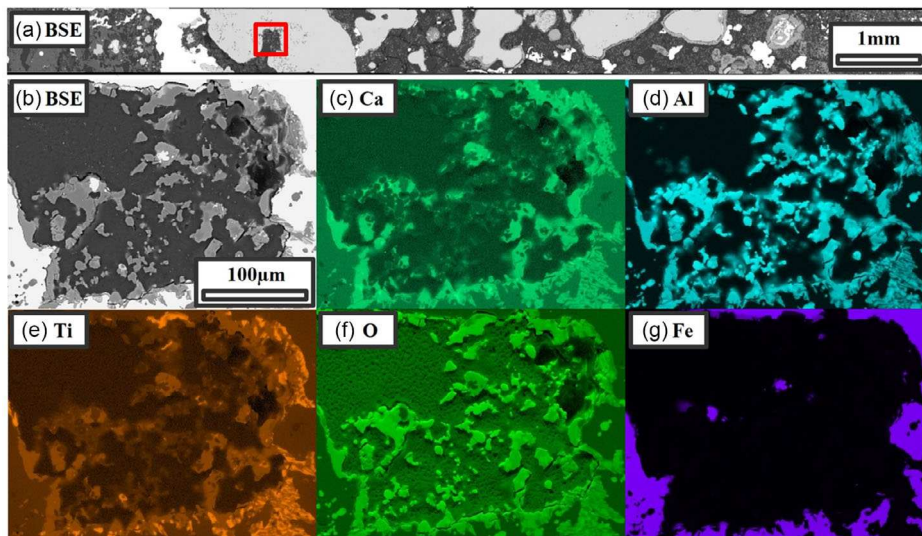
**ADVANCED
SCIENCE NEWS**

www.advancedsciencenews.com

**steel
research**
international

www.steel-research.de

Figure 13. CaO–Al$_2$O$_3$–TiO$_x$ layer on the interface of Fe droplet and oxide network: a) BSE image of SEN refractory and clogging structure; b) BSE image of the region of interest; and c–g) corresponding elemental mappings.
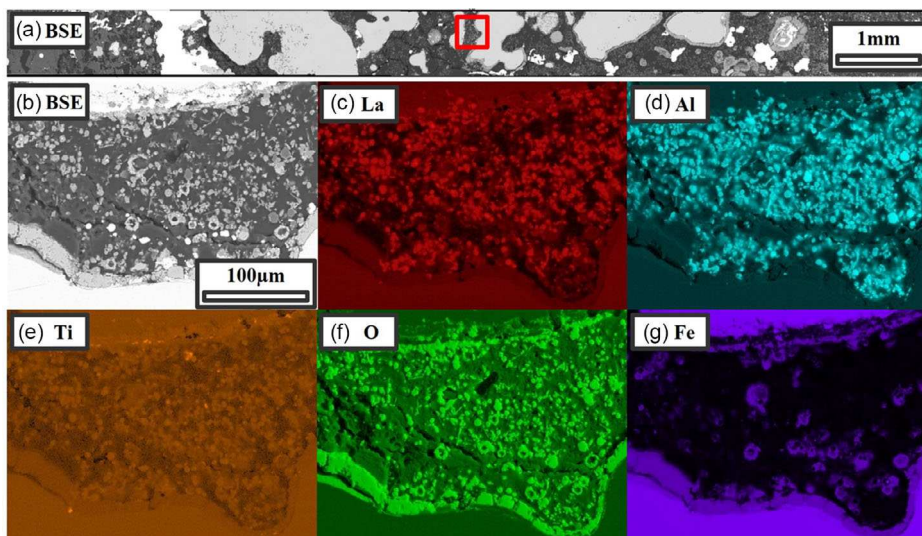

Figure 14. La-traced deoxidation products within the middle layer of clogging deposits: a) BSE image of SEN refractory and clogging structure; b) BSE image of the region of interest; and c–g) corresponding elemental mappings.

and subsequently modified by the presence of REE. Specifically, it can be attributed to the deoxidation products originating from the second heat of the Ti–IF casting sequence, as only this melt was alloyed with La and subsequently cast using the first SEN.

The SEM/EDS analysis was performed on the inner layer (closest to SEN center) of the clogging structure, as depicted in **Figure 15**. Within this specific region, alumina networks marked with Ce were observed. Similar to the second zone, the found coral-shaped sintered alumina particles are deoxidation products originating from the third and final heat, which was cast using this SEN. According to Michelic et al.[4] the primary mechanism causing the attaching and sintering of

deoxidation products to the preexisting clogging layer is the combination of surface tension and fluid flow effects. A comprehensive analysis of the underlying mechanisms that contribute to the continued growth of NMIs on the existing layer structure is presented by Barati et al.[1] and Solórzano et al.[38]

As shown in the overview of the investigated clogging layer, illustrated in Figure 9, overlapping regions were observed within the La- or Ce-marked clogging structure. This overlap can be attributed due to the mixing between the respective heats during the ladle exchange process within the tundish. The absence of distinct boundaries between these La- or Ce-traced oxide regions, especially in the inner part of the clogging network, indicates a
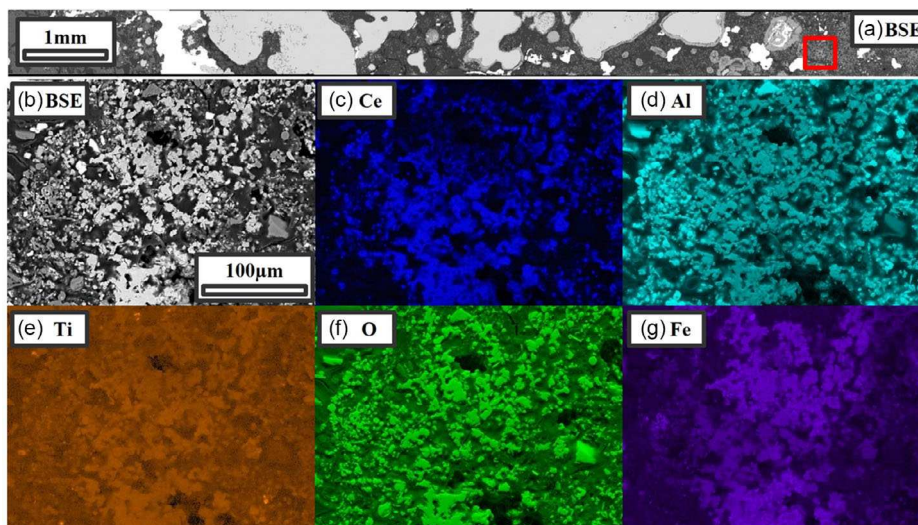
Figure 15. Ce-traced deoxidation products within the inner layer (closest to SEN center) of clogging deposits: a) BSE image of SEN refractory and clogging structure; b) BSE image of the region of interest; and c–g) corresponding elemental mappings.

nonuniform layer formation with overlapping and intertwined clogging areas. Such a type of branched clogging structure is also predicted by model calculations performed by Barati et al.[39]

5. Conclusion

The following findings can be drawn from this research: 1) In both the industrial and laboratory trials, preexisting deoxidation products were traced. The tracing rates in the remaining melts were significantly higher for the laboratory trials, with 70.59% for La and 92.82% for Ce, compared to 10.23% for La and 34.26% for Ce in the tundish sample of Heat 2 and 3. The separation of traced NMIs into the used slags played an essential role in this case in addition to the higher added amount of REEs in the laboratory. 2) During its application at the steel plant of voestalpine Stahl GmbH, the method proved effective in tracking the deoxidation products in Ti–IF steel throughout the production process. A steady decline of the REE content in the industrial samples could be observed during the period between the RH treatment and casting. Simultaneously, a successive enrichment of these elements was measured in the respective slags, indicating the separation tendency of NMIs into the slag phase. 3) Micro-cleanness evaluations of steel samples revealed that due to the addition of REEs, existing alumina inclusions were modified to the complex heterogeneous REE–Al oxides, $REEAl_{11}O_{18}$ and $AlREEO_3$, similar to previous studies. An increase in the inclusion number per unit area was observed, but the ECD decreased significantly. For example, in Heat 2 of the industrial trial, the addition of La resulted in a reduction of the ECD from 1.69 ± 0.93 to $1.49 \pm 0.29\,\mu m$. In the laboratory-scale experiment (LM2), a decrease from 2.29 ± 1.04 to $1.70 \pm 0.83\,\mu m$ was observed. In both settings, the inclusions' size increased again after adding FeTi, and Al–Ti oxides were formed. When comparing changes in inclusion modification and size distribution due to the REEs, no significant differences were found between using La and Ce as tracers. 4) Through

SEM/EDS examinations of the SEN, it was shown that the REE-marked preexisting deoxidation products were involved in the formation of the clogging layer. The clogging layer network could be split into three distinct zones. The formation of each zone within the clog could be attributed to the specific heats based on their corresponding tracer (or the absence of one).

Conflict of Interest

The authors declare no conflict of interest.

Data Availability Statement

Research data are not shared.

[1] H. Barati, M. Wu, A. Kharicha, A. Ludwig, *Powder Technol.* **2018**, *329*, 181.

[2] V. Yves, B. Coletti, B. Blanpain, P. Wollants, J. Vleugels, *ISIJ Int.* **2002**, *42*, 1234.

[3] L. Zhang, Y. Wang, X. Zuo, *Metall. Trans. B* **2008**, *39*, 534.

[4] S. K. Michelic, C. Bernhard, *Steel Res. Int.* **2022**, *93*, 2200086.

[5] K. Rackers, B. G. Thomas, in *78th Steelmaking Conf. Proc.*, Nashville, TN **1995**, pp. 723–734.

[6] a) M. Long, X. Zuo, L. Zhang, D. Chen, *ISIJ Int.* **2010**, *50*, 712; b) F. Tehovnik, J. Burja, M. Knap, *Metalurgija (Zagreb, Croatia)* **2015**, *54*, 371; c) P. Kaushik, D. Kruse, M. Ozgu, *Rev. Metall. (Paris)* **2008**, *105*, 92.

[7] J. H. Lee, M. H. Kang, S. K. Kim, Y. B. Kang, *ISIJ Int.* **2018**, *58*, 1257.

[8] P. Dorrer, S. K. Michelic, C. Bernhard, A. Penz, R. Rössler, *Steel Res. Int.* **2019**, *90*, 1800635.

[9] H. Barati, M. Wu, S. Michelic, S. Ilie, A. Kharicha, A. Ludwig, Y.-B. Kang, *Metall. Trans. B* **2021**, *52*, 4167.

[10] Y. Kang, D. Kim, J. Lee, Y. Park, in *8th Proc. Int. Congress on Science & Technology of Steelmaking*, Montreal, Canada **2022**, pp. 329–336.

[11] a) Y. Higuchi, M. Numata, S. Fukagawa, K. Shinme, *ISIJ Int.* **1996**, *36*, 151; b) N. Verma, P. Pistorius, R. Fruehan, M. Potter, M. Lind, S. Story, *Metall. Trans. B* **2011**, *42*, 720; c) N. Verma, P. C. Pistorius, R. J. Fruehan, M. Potter, M. Lind, S. Story, *Metall. Trans. B* **2011**, *42*, 711; d) F. Gyakwaa, M. Aula, T. Alatarvas, T. Vuolio, M. Huttula, T. Fabritius, *ISIJ Int.* **2019**, *59*, 1846; e) W. Yang, L. Zhang, X. Wang, Y. Ren, X. Liu, Q. Shan, *ISIJ Int.* **2013**, *53*, 1401; f) F. Yuan, X. Wang, X. Yang, *J. Univ. Sci. Technol. Beijing* **2006**, *13*, 486.

[12] A. L. V. Da Costa e Silva, *J. Mater. Res. Technol.* **2018**, *7*, 283.

[13] Y. Li, C. Liu, T. Zhang, M. Jiang, C. Peng, *Metall. Trans. B* **2017**, *48*, 956.

[14] H. Wang, Y. Bao, J. Zhi, C. Duan, S. Gao, M. Wang, *ISIJ Int.* **2021**, *61*, 657.

[15] G. Li, H. Y. Tang, X. Y. Jiang, J. W. Liu, P. Lan, J. Q. Zhang, *Ceram. Int.* **2022**, *48*, 19732.

[16] a) J. K. S. Svensson, F. Larsson, A. Memarpour, S. Ekerot, V. Brabie, P. G. Jönsson, *Ironmaking Steelmaking* **2018**, *45*, 105; b) C. Tian, J. Yu, E. Jin, T. Wen, D. Jia, Z. Liu, P. Fu, L. Yuan, *J. Alloys Compd.* **2019**, *792*, 1; c) C. Tian, L. Yuan, J. Yu, D. Jia, T. Wen, G. Liu, H. Li, *J. Mater. Res. Technol.* **2021**, *11*, 404.

[17] S. Gao, M. Wang, J. Guo, H. Wang, J. Zhi, Y. Bao, *Steel Res. Int.* **2019**, *90*, 1900194.

[18] R. Geng, J. Li, C. Shi, *Steel Res. Int.* **2020**, *91*, 2000117.

[19] K. Thiele, P. Presoly, D. Ernst, S. R. Babu, S. K. Michelic, *Ironmaking Steelmaking* **2023**, *50*, 507.

[20] A. Assa'd, M. M. El Gomati, *Scanning Microsc.* **1998**, *1*, 185.

[21] K. Thiele, R. Musi, S. Ramesh Babu, S. K. Michelic, *Adv. Eng. Mater.* **2023**, *25*, 2201748.

[22] C. Tian, J. Yu, E. Jin, T. Wen, D. Jia, Z. Liu, P. Fu, L. Yuan, *J. Alloys Compd.* **2019**, *792*, 1.

[23] M. Wang, S. Gao, X. Li, G. Wu, L. Xing, H. Wang, J. Zhi, Y. Bao, *ISIJ Int.* **2021**, *61*, 1524.

[24] G. Yang, X. Wang, F. Huang, W. Wang, Y. Yin, *Steel Res. Int.* **2014**, *85*, 26.

[25] D. Haojian, Y. Ren, L. Zhang, *Metall. Trans. B* **2019**, *50*, 1476.

[26] L. Zhang, S. Taniguchi, K. Cai, *Metall. Trans. B* **2000**, *31*, 253.

[27] L. Zheng, A. Malfliet, B. Yan, Z. Jiang, B. Blanpain, M. Guo, *ISIJ Int.* **2022**, *62*, 1573.

[28] K. Thiele, S. Ilie, T. Meisel, S. Michelic, T. Prohaska, R. Roessler, C. Walkner, in *8th Proc. Int. Congress on Science & Technology of Steelmaking*, Montreal, Canada **2022**, pp. 88–94.

[29] Y. Li, W. Yang, L. Zhang, *Metals (Basel, Switz.)* **2020**, *10*, 444.

[30] R. Geng, J. Li, C. Shi, J. Zhi, B. Lu, *Metall. Res. Technol.* **2020**, *117*, 616.

[31] N. Mao, W. Yang, D. Chen, W. Lu, X. Zhang, S. Chen, M. Xu, B. Pan, L. Han, X. Zhang, Z. Wang, *Materials* **2022**, *15*, 7952.

[32] Q. Ren, L. Zhang, Y. Liu, L. Cui, W. Yang, *J. Mater. Res. Technol.* **2020**, *9*, 8197.

[33] B. Li, H. Zhu, J. Zhao, M. Song, J. Li, Z. Xue, *Steel Res. Int.* **2022**, *93*, 2100347.

[34] H. Li, Y. Yu, X. Ren, S. Zhang, S. Wang, *J. Iron Steel Res. Int.* **2017**, *24*, 925.

[35] P. E. Waudby, *Int. Met. Rev.* **1978**, *23*, 74.

[36] J.-H. Lee, M.-H. Kang, S.-K. Kim, J. Kim, M.-S. Kim, Y.-B. Kang, *ISIJ Int.* **2019**, *59*, 749.

[37] X. Deng, C. Ji, Y. Cui, Z. Tian, X. Yin, X. Shao, Y. Yang, A. McLean, *Ironmaking Steelmaking* **2017**, *44*, 739.

[38] M. Solórzano, R. Ávila, C. Muñiz-Valdés, A. Bastida, *Casting Processes and Modelling*, IntechOpen, UK **2021**.

[39] H. Barati, M. Wu, A. Kharicha, A. Ludwig, *Steel Res. Int.* **2020**, *91*, 2000230.

7.2 Optimization of characterization methods for REE-traced NMIs

Paper II: <u>K. Thiele</u>, R. Musi, S. Ramesh Babu and S.K. Michelic, Optimization of the Two- and Three-Dimensional Characterization of Rare Earth-Traced Deoxidation Products. Adv Eng Mater 25 (2023), 11, pp. 2201748. doi:10.1002/adem.202201748.

Paper III: <u>K. Thiele</u>, R. Musi, T. Prohaska, J. Irrgeher and S.K. Michelic, AI assisted steel cleanness evaluation: Predicting the morphology of La-traced non-metallic inclusions using backscattered-electron images. J. Mater. Res. Technol. 28 (2024), pp. 2247–2257. doi:10.1016/j.jmrt.2023.12.172.

The research of **Paper II** is focused on the characterization of REE-traced NMIs as the common automated SEM/EDS analysis needs to be optimized to detect and recombine traced multiphase NMIs correctly. **Paper II** was published in **Advanced Engineering Materials**.

Paper III implements AI-assisted tools for the distinction between NMIs and non-NMIs as well as the classification between traced and untraced homogeneous or heterogeneous NMIs. **Paper III** was disclosed in the **Journal of Materials Research and Technology**.

RESEARCH ARTICLE

Optimization of the Two- and Three-Dimensional Characterization of Rare Earth-Traced Deoxidation Products

Kathrin Thiele, Robert Musi, Shashank Ramesh Babu, and Susanne K. Michelic*

Tracing by means of the light rare earths (REs), particularly La and Ce, is a state-of-the-art method used to track deoxidation products during the steelmaking process. Traced heterogeneous multiphase inclusions are analyzed using scanning electron microscopy with energy-dispersive spectroscopy (SEM/EDS) to perform a 2D characterization. The sequential chemical extraction technique is implemented for a 3D investigation to determine traced particles' actual sizes and shapes. The automated SEM/EDS measurement must be optimized since RE oxides appear brighter in the backscattered electron images due to their high atomic numbers. Therefore, two grayscales are implemented for the detection of RE-containing multiphase inclusions. Within this technique, individual RE-traced heterogeneous nonmetallic inclusions (NMIs) are counted as separate particles. Thus, the measured NMIs must be recombined, which is achieved using a self-developed MATLAB tool. The extracted particles are also analyzed by automated and manual SEM/EDS measurements to determine the 3D morphologies and sizes of traced NMIs.

1. Introduction

The topic of steel cleanness has received a lot of research attention over the last few years. Nevertheless, the influence of different nonmetallic inclusion (NMI) types on mechanical properties[1–3] remains somewhat unclarified. A similar uncertainty applies to the cause of the clogging phenomenon[4–6] observed during continuous casting. The aim to improve downtimes during production is achieved by getting deeper knowledge about the formation and evolution mechanisms of NMIs.[7,8] Especially the evolution of inclusions in Ti-stabilized ultra-low carbon steels is the focus of recent research projects since this steel grade is especially prone to clogging.[9,10] Another interesting inclusion type regarding steel cleanness is the MA-spinel. In the study of Deng et al.,[11] the formation and evolution of this inclusion type are explained in detail over the steelmaking process.

K. Thiele, R. Musi, S. Ramesh Babu, S. K. Michelic
Christian Doppler Laboratory for Inclusion Metallurgy in Advanced Steelmaking
Montanuniversitaet Leoben
Franz Josef-Straße 18, 8700 Leoben, Austria
E-mail: susanne.michelic@unileoben.ac.at

One option for studying the formation of inclusions and how they behave throughout processing is to use tracing with rare earths (REs), especially La[12,13] and Ce.[14,15] This technique enables the tracking of deoxidation products, such as Al_2O_3, across the process. Tracing the changes of alumina inclusions in their morphology and behavior throughout the process is necessary since these NMIs tend to clog in, for example, Ti-stabilized ultra-low carbon steels. The clogging phenomenon is still not entirely clarified. Hence, it is essential to gain more information concerning possible reoxidation processes during production.

The higher deoxidation potential of REs leads to interactions with preexisting alumina inclusions and results in a partial reduction of these deoxidation products. As a result, the REs are bonded to the preexisting inclusions.[12] Several studies have already investigated and described the modification of, for example, alumina inclusions by La[16,17] and Ce.[18,19]

Using automated scanning electron microscopy with energy-dispersive spectroscopy (SEM/EDS), RE-containing inclusions can easily be relocated since these particles appear brighter, due to their higher atomic numbers than the surrounding steel matrix.[16] However, REs modify preexisting deoxidation products and, thus, influence the morphologies, properties, and behaviors of these particles.[17–20]

Different approaches are necessary for characterizing nonmetallic inclusions, as a single technique cannot be used to identify all parameters. The reviews of Kaushik et al.[21] and Zhang et al.[22] describe direct and indirect characterization methods. Additionally, Mayerhofer[23] listed and compared various instruments for evaluating steel cleanness, regarding tested sample size, duration of analysis, detectable inclusion size, and determination of chemical composition, morphology, and spatial distribution. For the 2D characterization of microscopic NMIs, the most applied and comprehensive method is SEM/EDS analysis. Using this technique, information regarding spatial distribution and chemical composition can be determined for small samples. 3D methods can be additionally applied to investigate the actual sizes and shapes of particles since NMIs are randomly cut in cross-section samples.[24] Principally, extraction techniques are divided into chemical and electrolytic procedures. The choice of extraction method and extractant depends on several parameters, such as the stability of the inclusions or the chemical composition of the steel, which must be dissolved.[25,26] 2D and 3D

characterization methods for nonmetallic inclusions were compared by Doostmohammadi et al.[27] and Zhang et al.[28]

Janis et al.[29] studied the impact of clusters on clogging formation. For this investigation, they extracted clusters by applying the electrolytic extraction technique. The studies by Bi et al.[30] and Nabeel et al.[31] also dealt with the extraction of clusters. Compared to Janis et al.,[29] RE-containing clusters were investigated. This kind of cluster differs in its wetting behavior and clogging tendency. These two characterization techniques must be optimized for correct analyses since REs tend to form heterogeneous multiphase inclusions, mainly oxides, oxide–sulfides, or sulfides.

The present work involves characterizing RE-traced alumina inclusions by using different methods. The optimization of characterization methods for RE-containing multiphase inclusions is crucial since the usage of REs, especially Ce, continues to increase primarily for their grain refining effect but also due to further tracing experiments. In addition to a state-of-the-art technique—the automated SEM/EDS analysis—the sequential chemical extraction method and its optimization for these specific inclusion types are also discussed. Concerning the 2D characterization, a double-threshold scan must be implemented for the detection of heterogeneous RE-containing multiphase inclusions. Furthermore, a developed MATLAB tool is essential for the location and recombination of erroneously split particles. The sequential chemical extraction method, a 3D analysis technique, is utilized to determine the actual sizes and shapes of inclusions. Later, the extracted particles are investigated using automated SEM/EDS analysis to obtain the mean equivalent circle diameters (ECDs) of the traced particles. Ultimately, the benefits and disadvantages of 2D and 3D characterization methods are compared.

2. Methods and Materials

2.1. Experimental Section

The 2D and 3D characterizations of RE-traced nonmetallic inclusions were performed on six samples. Samples 1 to 5 were produced in a high-frequency remelting (HFR) furnace (Linn High Therm GmbH, Eschenfelden, Germany) on a laboratory scale. Electrolytic iron with a high oxygen content of ≈330 ppm was used for the trials. The samples were melted at temperatures slightly above the liquidus temperature of pure iron (1550–1570 °C) under an inert atmosphere. After a short dwell time, the melts were centrifugally cast at a high mean cooling speed. Aluminum was added through a drilled hole for deoxidation. As a consequence, mainly aluminum oxides were formed. Besides Al, either La or Ce was additionally alloyed; hence, the deoxidation products, Al_2O_3 NMIs, were traced using these elements. A detailed description and a schematic illustration of the single states of the samples' production in an HFR furnace could be found in Thiele et al.[32]

The production route differs for Sample 6. This sample was produced in a resistance-heated Tammann-type furnace (Ruhrstrat HRTK 32-Sond.) and heated to 1600 °C under an inert atmosphere. Al was added to the melt for deoxidation, and 6 min later, La, wrapped in an Al foil for alloying to prevent oxidation. After 10 s of stirring, the melt was held for 10 min, slowly cooled to 1350 °C, and then quenched in water. Inclusion types

similar to those in Samples 1–5 were formed in this process; however, larger inclusion sizes were observed as a result of slower cooling. A previous study by Dorrer et al.[33] illustrates the experimental setup of a resistance-heated Tammann-type furnace. Furthermore, the addition of alloying elements over the process is explained.

The chemical compositions of the raw material and the investigated samples for the 2D and 3D characterizations are listed in **Table 1**. The composition of Sample 6 differs in the case of C and Al contents compared to the samples produced using HFR. Three different alloying concepts were used for the REs. In Samples 1 and 3, REs were put in a steel tube. In Samples 2, 4, and 6, REs were wrapped in Al foil, and in Sample 5, ferrocerium was used as an alloying element. The influence of the alloying concepts on the output of REs has previously been discussed by Thiele et al.[32]

The composition in terms of REs varies across the six samples, depending on the various alloying concepts and furnaces used.

2.2. Characterization Methods for RE-Traced Nonmetallic Inclusions

Two methods were used in this study to characterize nonmetallic inclusions—one 2D and one 3D approach. For the 2D analysis, cross-section samples were investigated using manual and automated SEM/EDS. With this technique, information regarding the NMIs' spatial distributions, chemical compositions, and number per square millimeter could be obtained for a predefined sample area. For the 3D characterization method, the particles in the steel samples must be isolated from the steel matrix to reveal the entire morphology of the particles and provide additional information about their individual sizes. The 3D characterization method used in this research work was the sequential chemical extraction technique. All particles containing >0.1 wt% La or Ce were defined as traced NMIs.

2.2.1. Sequential Chemical Extraction

The sequential chemical extraction technique was used to separate nonmetallic inclusions from the steel matrix. The principle of extraction is to dissolve the surrounding steel matrix with acid without dissolving or modifying the NMIs. An essential advantage of sequential chemical extraction is the conservation of rather unstable inclusions, such as sulfides, on the filters.[25]

Table 1. Chemical compositions of characterized samples.

Sample	C [wt%]	Si [wt%]	Mn [wt%]	Al [wt%]	La [ppm]	Ce [ppm]	Fe [wt%]
Raw material	0.007	0.010	0.102	0.001			Bal.
1	0.007	0.010	0.104	0.066	72		Bal.
2	0.006	0.010	0.094	0.070	100		Bal.
3	0.007	0.010	0.103	0.070		72	Bal.
4	0.006	0.010	0.094	0.065		130	Bal.
5	0.005	0.010	0.095	0.067		147	Bal.
6	0.014	0.030	0.103	0.045	53		Bal.

**ADVANCED
SCIENCE NEWS**

www.advancedsciencenews.com

**ADVANCED
ENGINEERING
MATERIALS**

www.aem-journal.com

By using samples with a high surface-to-volume ratio, a greater amount of matrix could be dissolved in the same amount of time. In addition, the samples must be thoroughly cleaned so that no corroded passages or scale residues were left on the sample and the dissolution of the steel matrix was not affected. As a next step, the steel sample was put inside a beaker. A 3% nitric acid solution was added as an extracting agent until the sample's surface was completely covered. Reactions causing the dissolution of already-extracted NMIs, such as sulfides, were inhibited by utilizing the sequential technique. The precipitation was steadily pipetted every 15 min and subsequently transferred into another beaker. A schematic illustration is shown in **Figure 1**.

The total duration of the sequential chemical extraction for this study was 1 h. A vacuum filtration system with polycarbonate filters was utilized to separate the extracted inclusions via consecutive filtering with different pore sizes (12 and 1 μm). The 12 μm filter mainly removed matrix and grinding residuals. Extracted NMIs were primarily found on the 1 μm filter since many inclusions were in the microscopic range. After drying the filter on air for 12–14 h, the filters were cut and stuck on pin sample holders with high-purity, double-sided, conductive carbon adhesive pads. The pins were sputtered with carbon to achieve optimized high-resolution SEM measurements. Automated SEM/EDS analyses of the extracted particles were possible due to the carbon layer on the surface of the filters.

2.2.2. Optimization of the Automated SEM/EDS Measurement

The automated SEM/EDS analysis has to be optimized when analyzing RE-traced inclusions. In general, inclusions are detected due to a gray scale difference in the backscattered electron (BSE) image since the contrast of the image is highly dependent on the material's atomic number. Thus, classical oxide

Figure 1. Schematic representation of sequential chemical extraction equipment (adapted from Mayerhofer[23]).

inclusions appear darker than the surrounding steel matrix. Conversely, REs appear brighter than the surrounding steel matrix in BSE images. In most cases, the detection of the entire RE-containing NMIs is inhibited since traced deoxidation products are mainly multiphase inclusions with brighter and darker parts depending on the dominating element. Particles brighter than the steel matrix can be detected in addition to the darker ones using a double-threshold scan with the automated SEM/EDS measurement. In this study, a field-emitting SEM (JEOL 7200 F; JEOL Germany GmbH, Freising, Germany) equipped with a 100 mm^2 SDD-EDS detector (Oxford Instruments Ultim Max 100; Oxford Instruments GmbH NanoAnalysis, Wiesbaden, Germany) was used for the characterization of the NMIs. The EDS spectra were collected by an area scan. The SEM software AZtec Feature (AZtec 5.0, Oxford Instruments GmbH NanoAnalysis, Wiesbaden, Germany) was utilized for automated particle analysis. The main measurement parameters for the automated SEM/EDS analyses were a beam energy of 15 keV, a probe current of 14 PC, a working distance of 10 mm, and a resolution of 2048 × 1024 px at an EDS evaluation time per particle of 1 s. Different settings were required for cross-section samples and filters in terms of resolution and magnification. The resolution for cross-sections was 2048 px at a magnification of 200×, and for filters, 1024 px at 400×.

The use of a double-threshold scan means that a section is scanned twice. In this case, the thresholds were set in a manner to ensure that all particles darker than the matrix were detected first. The second step involved obtaining information regarding the brighter particles.

The same SEM was used for the 3D characterization, in which manual and automated SEM/EDS analyses of the extracted NMIs were performed.

2.2.3. Recombination Tool for Heterogeneous Nonmetallic Inclusions

During the automated SEM/EDS analysis, RE-containing multiphase inclusions were separated into two sections—a Ce/La-enriched one and one containing light elements, such as Al-oxides—as shown in **Figure 2**a,b. The colors represent the two different user-defined thresholds. Inclusions 1 and 2 (marked in blue) belong to the higher threshold value and Inclusion 3 (labeled in red) to the lower. This splitting process leads to a systematic error in the subsequent evaluation because one multiphase inclusion is treated as several individual parts. To address this problem, a MATLAB tool was developed and used to identify and merge parts of the inclusions that initially belonged together. The input data for this tool are the measurement results of the automated SEM/EDS analysis exported from AZtec Feature as an Excel file, which contains the morphological parameters and the chemical composition for every measured inclusion.

The first step of the recombination process is to identify particles that were split due to the double-threshold scan. Therefore, the algorithm iterates over all measured particles of the higher threshold value and examines a defined merging-condition with every low threshold inclusion. Within this examination, parameters for the shape and distance of the corresponding inclusions
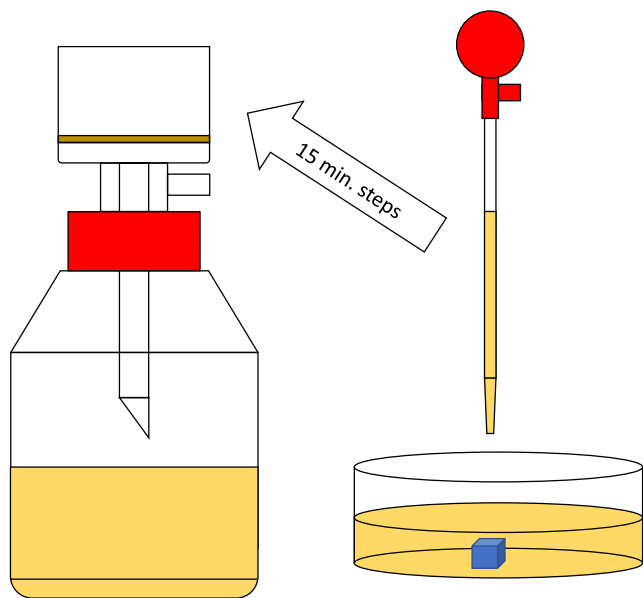
**ADVANCED
SCIENCE NEWS**

www.advancedsciencenews.com

**ADVANCED
ENGINEERING
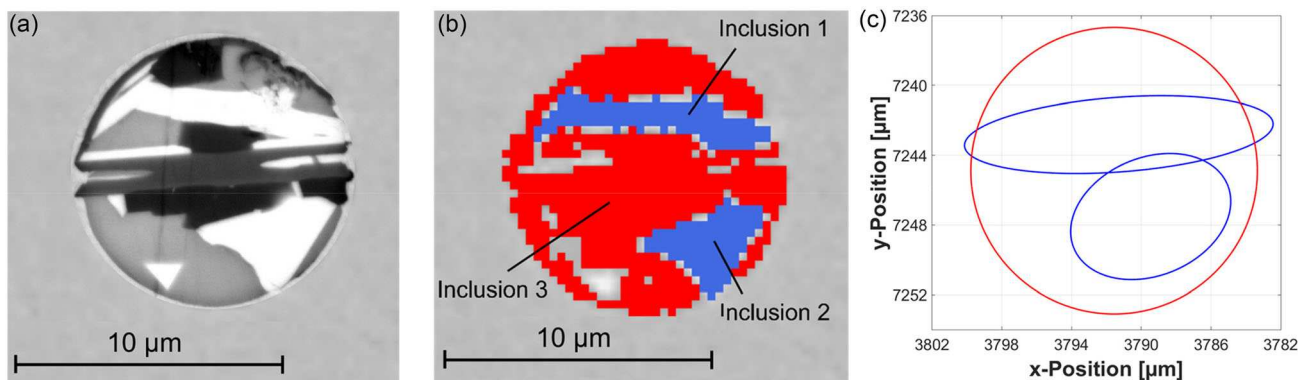MATERIALS**

www.aem-journal.com

Figure 2. Split of heterogeneous multiphase inclusions due to double-threshold scan, a) BSE image of multiphase inclusion, b) split of the NMI by different thresholds, and c) calculated shapes of the three separated inclusions based on morphological parameters.

are calculated. When the heavy-element particle is below a defined distance (Equation (1)) to the compared light-element particle, the merging condition is fulfilled, and the algorithm combines them to form a postprocessed inclusion.

The merging condition for putting the split inclusions together is set as follows

$$(Distance_{Center} - Distance_{Shape}) - Safety\ Factor \leq 0 \quad (1)$$

$Distance_{Center}$ defines the space between both centroids. The calculation of $Distance_{Shape}$ depends on the shapes of both inclusions. SafetyFactor is included to compensate for the difference between a measured and a calculated inclusion shape caused by the limitation to using only two geometric forms with the available data and the low resolution of the automated SEM/EDS analysis. This factor reduces the distance between the two centroids and increases the possibility that inclusions are merged. The value for SafetyFactor was set as 3 μm, which was empirically determined by testing the algorithm on different datasets and validating the results by reviewing whether the inclusion findings were correct. The resulting output of the cluster finding process is a list of inclusions with their supposed partners, which will be merged in the next step to redisplay a split RE-traced heterogeneous NMI. The IDs of the listed inclusions can be searched in the original data from the automated SEM/EDS measurement with the AZtec Software. The validation is done on a random basis by manually comparing the supposed heterogeneous inclusions with the original SEM images.

The three different possibilities for the merging conditions are listed below: 1) Both inclusions are equiaxed: $Distance_{Shape}$ is the sum of both ECDs. 2) One inclusion is equiaxed, the other one elliptical: $Distance_{Shape}$ is the sum of the ECD for the equiaxed inclusion and the ellipse radius in the direction of the connection line for the elongated inclusion. The centroids of both inclusions define the connection line. 3) Both inclusions are elliptical: $Distance_{Shape}$ is the sum of both ellipses' radii in the direction of the connection line.

During the automated SEM/EDS analysis, the AZtec Feature software determines morphological parameters such as the aspect ratio (Equation (2)), ECD, length, breadth, and direction of the particles.

$$Aspect\ Ratio = \frac{Length\ (longest\ diameter)}{Breadth\ (shortest\ diameter)} \quad (2)$$

The algorithm uses those parameters to calculate a theoretical inclusion shape, simplified as a circle or an ellipse. The aspect ratio defines the distinctive feature between the two geometric forms. Inclusions with aspect ratios below a certain threshold value are treated as circular; otherwise, the shape will be set as an ellipse. This is important for the $Distance_{Shape}$ parameter in the merging-condition (Equation (1)). Equiaxed inclusions can show an aspect ratio higher than 1 because the lengths and breadths do not necessarily need to be perpendicular. This is the case for squared shapes, which have an aspect ratio of 1.41 and, therefore, represent the algorithm's threshold value. For circular-treated inclusions, the ECD determines the radius for the calculated shape. For elliptical inclusions, the magnitude of the major axis is defined by the particle's length and the magnitude of the minor axis by the particle's breadth. A particle's direction represents the inclination angle between the horizontal and major axes. Figure 2c shows the calculated shapes of three different inclusions on the same particle that was used as an example in Figure 2a. Inclusions 1 and 2 have an aspect ratio higher than 1.41 and, therefore, they are treated as ellipses. The aspect ratio of Inclusion 3 is lower than 1.41; hence, it is represented as a circle.

The magnitude of the ellipse radius in a specific direction for the possibility of one equiaxed and one elliptical inclusion can be calculated using Equation (3). All variables in this equation are defined during the double-threshold scan. The length of the particle determines the value 2a (major axis of the ellipse) and the breadth of the particle determines the value 2b (minor axis of the ellipse). α is the inclusion's direction and describes the angle of inclination between the horizontal axis, x, and the inclusion's length value. θ is the angle between the major axis of the ellipse and the direction of the second particle. Depending on the value of α, either Equation (4) or (5) is used for the calculation of θ. Δy and Δx describe the distances along the vertical and horizontal axes, respectively, between the centers of the area.

$$r = \frac{a \cdot b}{\sqrt{(b\cos\theta)^2 + (a\sin\theta)^2}} \quad (3)$$
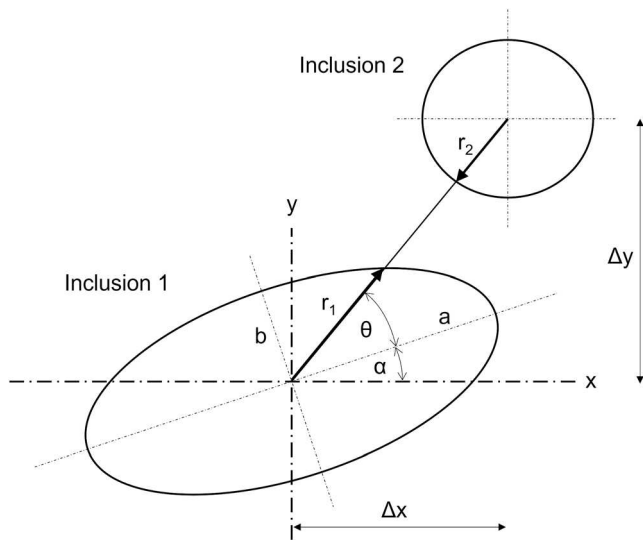
Figure 3. Example of an elliptical and circular inclusion with the corresponding geometric parameters (adapted from Meng et al).[35]

$$\theta = \arctan\left(\frac{\Delta y}{\Delta x}\right) - \alpha \text{ if } 0° < \alpha < 90° \tag{4}$$

$$\theta = 180° - \alpha - \arctan\left(\frac{\Delta y}{\Delta x}\right) \text{ if } 90° < \alpha < 180° \tag{5}$$

Figure 3 shows two inclusions with their corresponding geometric parameters. The radius r_1 of the elliptical inclusion is defined by Equation (3). Due to the circular shape of Inclusion 2, the ECD determines the value of r_2. In this example, the sum of r_1 and r_2 is smaller than the distance between the centers of the area. Therefore, these inclusions will not be merged.

After validating all of the merging conditions, the algorithm's output is a list of inclusions. The user can review the results by comparing the listed entries with their representations in the actual SEM image. The respective inclusions can be manually removed from the list if discrepancies arise. Afterward, the inclusions in the finalized list are merged by calculating a new chemical composition based on the area-weighted percentage of their corresponding parts. The final output of this tool is an Excel file

including the corrected number of inclusions with all of their properties.

3. Results

3.1. Two-Dimensional Characteristics of Traced Inclusions

The 2D characterization was performed using automated SEM/EDS analyses of cross-section samples and the subsequent application of the recombination tool. The data files from the automated SEM/EDS measurements were then used to determine the number of particles and the typification of NMIs. All particles without nonmetallic bonding partners were removed before the inclusions were rated in the respective single-phase classes (O, S, and N) or multiphase classes (OS, ON, NS, and ONS). The typification of the classified inclusions depends on which metallic bonding partner was present. In the HFR-produced samples that were investigated, over 99.5% of all measured NMIs were alumina inclusions. For Sample 6, approximately 85.0% of all detected particles were alumina inclusions. The other NMIs were preexisting silicon and manganese oxides from the raw material. As a result, only traced and untraced Al_2O_3 NMIs were observed in this study. The tracing rate was $\approx 98.23 \pm 1.16\%$ across all samples. Particles with a mean ECD of at least 1 μm were detected within these measurements. Across all cross-section samples, the mean ECD was $\approx 2.33 \pm 0.42$ μm. Sample 6 had a significantly higher mean value of 3.16 μm and the largest standard deviation of 1.56 μm. The inclusions were mostly globular, with a mean aspect ratio of $\approx 1.35 \pm 0.08$. The number of NMIs per square millimeter varied for the samples produced in HFR between 158.48 Nr/mm^2 for Sample 3 and 369.70 Nr/mm^2 for Sample 5, as shown in **Table 2**. Sample 6, produced in a heat-resistance furnace, had the lowest inclusion density with 51.45 $Nr\,mm^{-2}$.

Figure 4 shows three separate Ce-traced Al_2O_3 inclusions in Sample 4. Due to the use of a double-threshold scan, the particles were erroneously split up into seven smaller particles depending on their different grayscales. In Figure 4, the three brighter parts are marked in blue, and the four darker ones in red. By using the developed MATLAB tool, the particles, which fit together, were found and merged into three heterogeneous NMIs.

The relative numbers and percentage of the recombined NMIs and their corresponding parts (pseudoinclusions) can be seen in Table 2. In addition, the consequential errors between inclusions in the original and recombined results were calculated and listed. The error is defined as the difference between the percentage of

Table 2. Total number of Al_2O_3 inclusions, pseudoinclusions, and recombined inclusions per mm^2, percentage of pseudo- and recombined NMIs, and consequential error between original and recombined results.

Sample	Total NMIs [$Nr\,mm^{-2}$]	Pseudo-NMIs [$Nr\,mm^{-2}$]	Recombined NMIs [$Nr\,mm^{-2}$]	Percentage pseudo-NMIs [%]	Percentage recombined NMIs [%]	Error [%]
1	316.12	6.40	2.48	2.06	0.80	1.26
2	236.41	1.92	0.87	0.83	0.38	0.45
3	158.48	1.33	0.54	0.87	0.36	0.51
4	248.21	7.17	2.79	2.86	1.11	1.75
5	369.70	5.97	2.70	1.62	0.73	0.88
6	51.45	11.24	4.24	21.84	8.24	13.60

**ADVANCED
SCIENCE NEWS**

www.advancedsciencenews.com

**ADVANCED
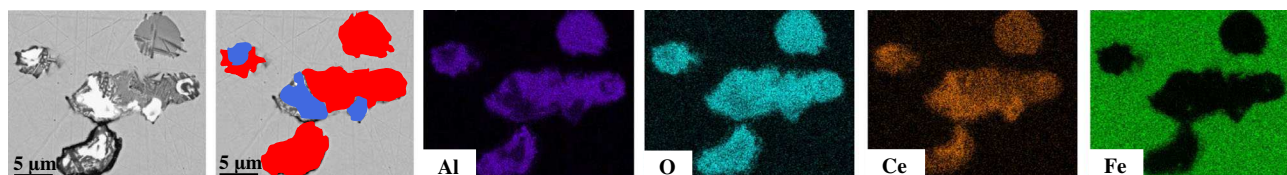ENGINEERING
MATERIALS**

www.aem-journal.com

Figure 4. BSE image and mappings of three traced Al_2O_3 inclusions in Sample 4.

Table 3. Mean ECDs (in μm) and mean RE content (wt%) of all Al_2O_3 inclusions of the six samples before and after recombination.

Sample	Mean ECD before recombination	Mean ECD after recombination	Mean RE cont. before recombination	Mean RE cont. after recombination
1	2.10 ± 1.20	2.09 ± 1.23	10.57 ± 6.52	10.28 ± 5.59
2	2.32 ± 1.22	2.32 ± 1.23	11.36 ± 5.88	11.21 ± 5.34
3	2.54 ± 1.44	2.54 ± 1.45	11.81 ± 7.48	11.69 ± 7.09
4	1.99 ± 1.08	1.99 ± 1.11	14.75 ± 7.81	14.28 ± 6.48
5	1.91 ± 0.91	1.92 ± 0.92	13.31 ± 6.78	13.06 ± 5.94
6	3.16 ± 1.64	3.43 ± 1.91	19.04 ± 13.65	18.41 ± 12.87

pseudo-NMIs and assembled NMIs after using the recombination tool.

Between 0.45% and 1.75% of the detected Al_2O_3 inclusions in Samples 1–5 originally fit together. Sample 6 had a significantly higher amount of erroneously split multiphase inclusions, with a total of 13.60%.

Changes in the main parameters, such as the mean ECDs, chemical compositions, and tracing rates, were investigated and compared before and after applying the recombination tool. **Table 3** lists the mean ECDs values for the Al_2O_3–NMIs before and after recombining. The mean ECDs were almost unchanged, with a slight increase in standard deviation for Samples 1–5. For Sample 6, the mean ECD increased by over 0.27 μm to a mean value of 3.43 μm. After recombining the particles, the mean RE contents decreased, and the standard deviations were minimized for all six samples. Concerning the tracing rates, no changes were observed for any sample.

3.2. Three-Dimensional Characteristics of Traced Inclusions

In **Figure 5**, 2D and 3D inclusion mappings of Sample 3 are compared. The chemical distribution of NMIs was similar to the investigation of the cross-section. Hence, the NMIs were finely dispersed and heterogeneous for the five samples produced in the HFR furnace. Moreover, the RE oxides were brighter and mainly in the center of the inclusions.

The inclusions in Sample 6 (as seen in **Figure 6**) show a stronger segregation tendency and a tighter separation between the different phases of the complex inclusions. The NMIs are larger and have greater RE-containing areas in multiphase inclusions than Samples 1–5.

The topography of the extracted particles can be investigated in more detail with the secondary electron (SE) image. By comparing the BSE image with the SE image for Ce (**Figure 7**), it was determined that the supposed-centered RE-containing
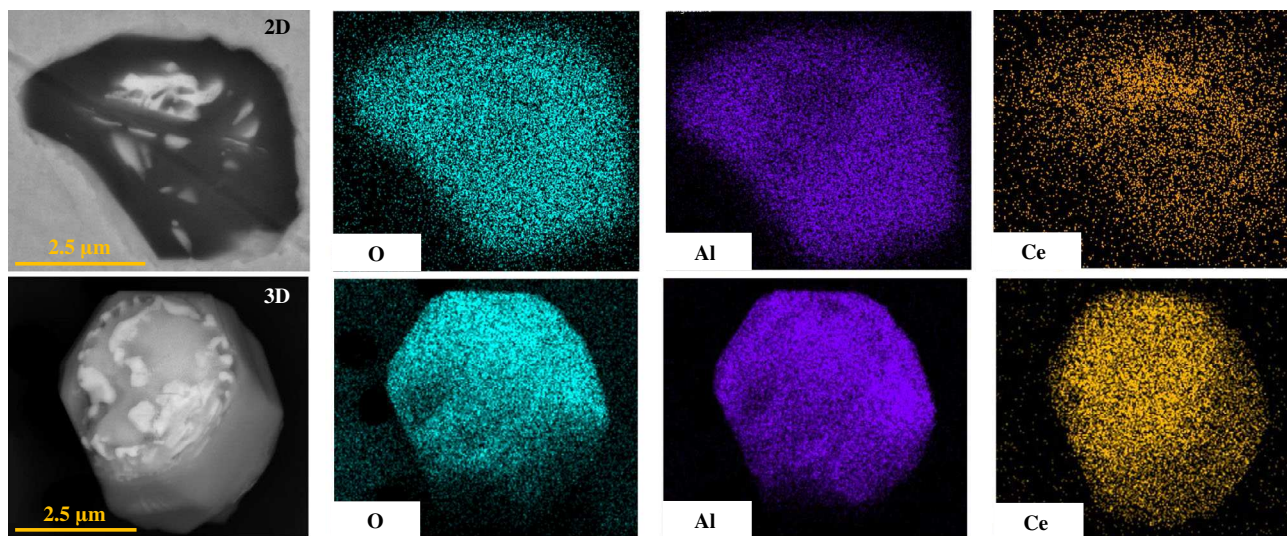
Figure 5. Comparison of 2D and 3D images of Ce-traced NMIs in Sample 3 (HFR).
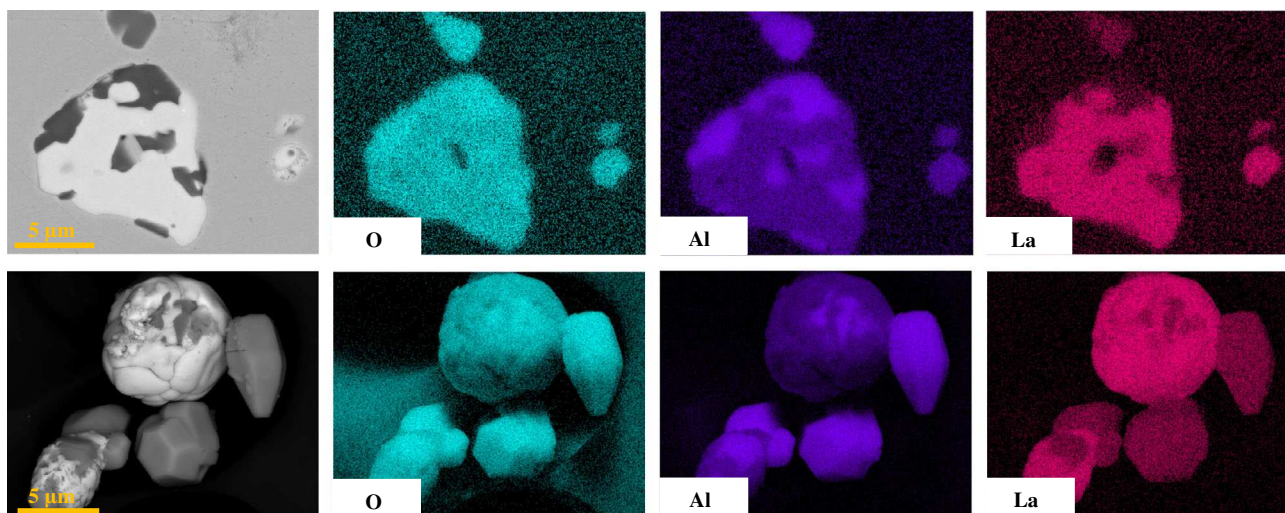
Figure 6. Comparison of 2D and 3D images of La-traced NMIs in Sample 6 (resistance furnace).
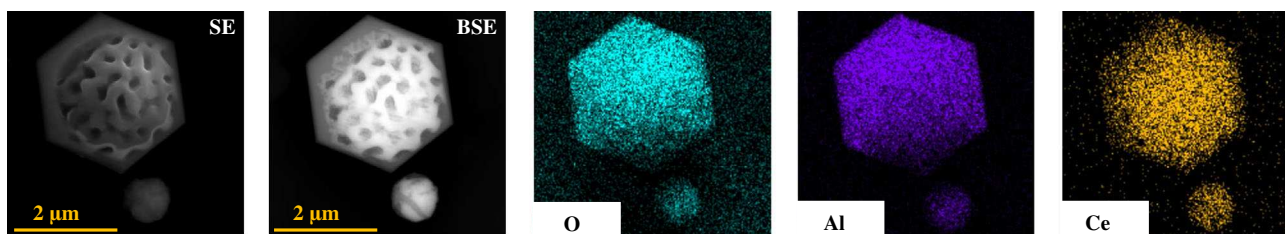

Figure 7. SE image, BSE image, and mappings of an extracted Ce-traced Al oxide in Sample 3.

parts of the NMI were effectively agglomerated Ce oxide on the surface of the alumina inclusion. As shown in Figures 5 and 7, the morphology of traced alumina inclusions primarily consists of relatively globular and hexagonal NMIs. No elongated or cubic RE-containing alumina inclusions were detected with manual SEM/EDS measurements for these samples.

Automated SEM/EDS measurements were performed, similar to the 2D characterization. Therefore, the 1 μm filter containing the extracted inclusions was coated with carbon before the investigation. All particles seemed brighter on the BSE images in the SEM/EDS since the inclusions were no longer surrounded by steel matrix and mounted upon conductive carbon adhesive pads. Due to this, only one grayscale was required as a detection-limiting automated measurement. The analyzed areas were minor concerning the high number of extracted inclusions on the filters. The measured area for each filter varied between 2 and 20 mm^2 since the extracted NMIs were irregularly distributed on the filters. The areas of the cross-section samples were relatively constant, however, at ≈10 mm^2 each.

Figure 8 illustrates the number of Al$_2$O$_3$ inclusions per square millimeter on the 1 μm filter and the number of traced inclusions. The number of inclusions varied considerably for all samples. Samples 2 and 3 had similar particle densities of 1932 and 1891 Nr mm^{-2}, respectively. In contrast, the difference between Samples 4 and 6 was substantial. Sample 6 had the lowest
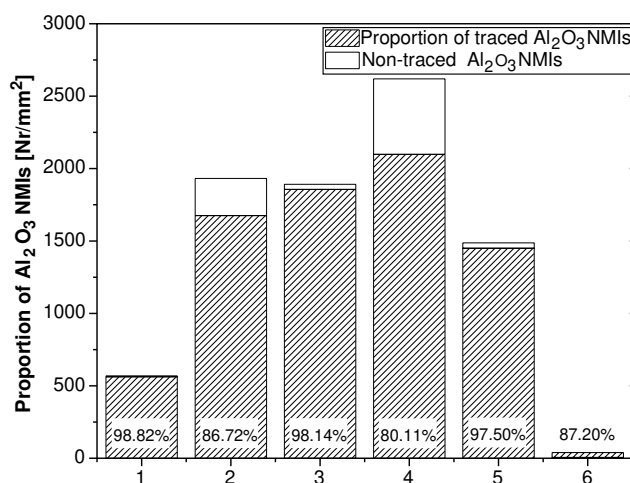
Figure 8. Proportion of Al$_2$O$_3$ NMIs on the filter after extraction and percentage of RE-traced Al$_2$O$_3$ NMIs.

density, with 44.85 Nr mm^{-2}, while Sample 4 was ≈80 times denser, with over 2620 Nr mm^{-2}. The particle density of Sample 5 was somewhere in the middle, at 1487 Nr mm^{-2}, and that of Sample 1 was relatively low, at 569 Nr mm^{-2}.

The percentage of RE-traced particles was high for Samples 1, 3, and 5, with over 97.5% of a similar value to those of the

**ADVANCED
SCIENCE NEWS**

www.advancedsciencenews.com

**ADVANCED
ENGINEERING
MATERIALS**

www.aem-journal.com

Table 4. Mean ECDs (in μm) of all Al_2O_3 inclusions of the six samples following 2D and 3D characterization.

Sample	Mean ECD cross-section	Mean ECD cross-section recombined	Mean ECD extracted
1	2.08 ± 1.20	2.09 ± 1.23	1.68 ± 0.74
2	2.32 ± 1.22	2.32 ± 1.23	1.68 ± 0.58
3	2.54 ± 1.44	2.54 ± 1.45	1.65 ± 0.70
4	1.99 ± 1.08	1.99 ± 1.11	1.84 ± 0.85
5	1.91 ± 0.91	1.92 ± 0.92	1.67 ± 0.72
6	3.16 ± 1.64	3.43 ± 1.91	2.16 ± 1.14

cross-section measurement results. Samples 2, 4, and 6 dropped off with tracing rates of 86.72%, 80.11%, and 87.20%, respectively, for Al_2O_3 NMIs. The tracing rates were, in total, lower than those of the cross-section measurements.

3.3. Mean ECDs of the NMIs in Cross-Sections and Filters

Table 4 lists the mean ECDs of all measured NMIs in cross-section samples and on filters following automated SEM/EDS analyses. The mean ECDs varied between 1.99 and 2.78 μm for the six samples following the 2D characterization. In contrast, the mean ECDs were almost identical for Samples 1–5 for extracted NMIs, at ≈1.68 μm. Only Sample 4 had a slightly higher mean ECD with 1.84 μm. The largest mean ECDs for cross-sections (3.16 μm before and 3.43 μm after merging) and filters (2.16 μm) were measured for Sample 6, which was produced in a heat-resistance furnace. Lower values and variations were found between the standard deviations of the filter samples compared to those of the cross-section samples.

Only Al_2O_3 inclusions were found in the cross-section samples following SEM/EDS analyses. In addition to traced and untraced alumina inclusions, residuals from beaker glasses—mainly silicon oxides—were also detected on the filters. These residuals were likely produced by the attack of the acid that was used for the chemical extraction. These erroneously detected inclusions were excluded from the evaluation to better compare the 2D and 3D analyses.

The values of the mean ECDs in Table 4 refer to all measured Al_2O_3 inclusions. Samples 1–5 exhibited discrepancies in mean ECD of at least 0.01 μm between traced and untraced NMIs. Sample 6 had a slightly higher deviation of ≈0.25 μm between traced and untraced NMIs on the filter. Since the tracing rates were high across all samples, the mean ECDs can be related to RE-containing NMIs.

3.4. Distribution of Traced NMIs in the Ternary System RE–Al–O

Figure 9 shows ternary systems of RE–Al–O for each sample. A comparison between the chemical compositions of traced alumina inclusions is possible after 2D and 3D analyses.

The chemical composition for each cross-section sample ranged from 25 to 45 wt% for O, 5 to 50 wt% for REs, and

8–60 wt% for Al. Rare exceptions were also found; these deviated NMIs were mainly located in areas with higher La content. Groups of isolated NMIs with values up to 80 wt% for La or Ce were detected.

Compared to the cross-section samples, the chemical compositions of extracted NMIs differed in several ways. Higher oxygen contents were measured for all NMIs on filters. The NMIs on filters for Samples 1–5 ranged from 50 to almost 100 wt% for O, 1 to 35 wt% for REs, and 2–25 wt% for Al. Single NMIs with higher RE concentrations were also detected. The extracted inclusions for Sample 6 were lower in oxygen content (20−65 wt%), more varied in La content (15−65 wt%), and slightly higher in Al content (5−40 wt%).

4. Discussion

4.1. Evaluation of Sequential Chemical Extraction Technique

Extractions offer the possibility to investigate the morphologies of NMIs in more detail compared to the 2D analyses of cross-section samples, in which inclusions are randomly cut.[24] In addition to allowing the determination of the actual sizes and shapes of inclusions, extractions enable the distinction between large multiphase inclusions and clusters of NMIs, which may be detected as one particle when using automated SEM/EDS measurements of cross-sections.

One particular advantage of the sequential chemical extraction technique is that the dissolution of RE-containing Al_2O_3-inclusions can be inhibited with this method, even if the behavior of La- and Ce-containing NMIs was not known before. Further benefits of this method compared to the electrolytic extraction are the simple setup, the possibility of using stronger acids if necessary, and suppressed formation of $FeCl_2$.[34] Especially, the last point is crucial for investigations of filters in the SEM. Although previous studies[23,25,34] have shown that unstable inclusions such as Ca-containing NMIs or sulfides remain on the filter following extraction with the sequential procedure, this has not yet been confirmed for RE-containing inclusions.

Despite the benefit of extracting even less stable inclusions, this method also has some disadvantages. An oxide layer is gradually formed during the sequential chemical extraction, delaying interactions between the steel sample and the extracting agent; thus, the reaction speed is reduced. Other extraction methods, especially electrochemical techniques, may be faster but are also more likely to dissolve less-stable inclusions, such as sulfides. Another disadvantage is that the acid interacts with the beaker glass. As a result, residuals from the beaker, mainly SiO_2 NMIs, contaminate the filter; hence, a correction of the SEM/EDS measurement results concerning SiO_2 NMIs is required. Furthermore, it is recommended to use new pipettes for every extraction to prevent contamination with the inclusions from previous extractions.

After comparison of the benefits and detriments, the sequential chemical extraction technique with 3% nitric acid suits for extractions of unstable NMIs and NMIs, whose dissolution behavior is not entirely clarified.
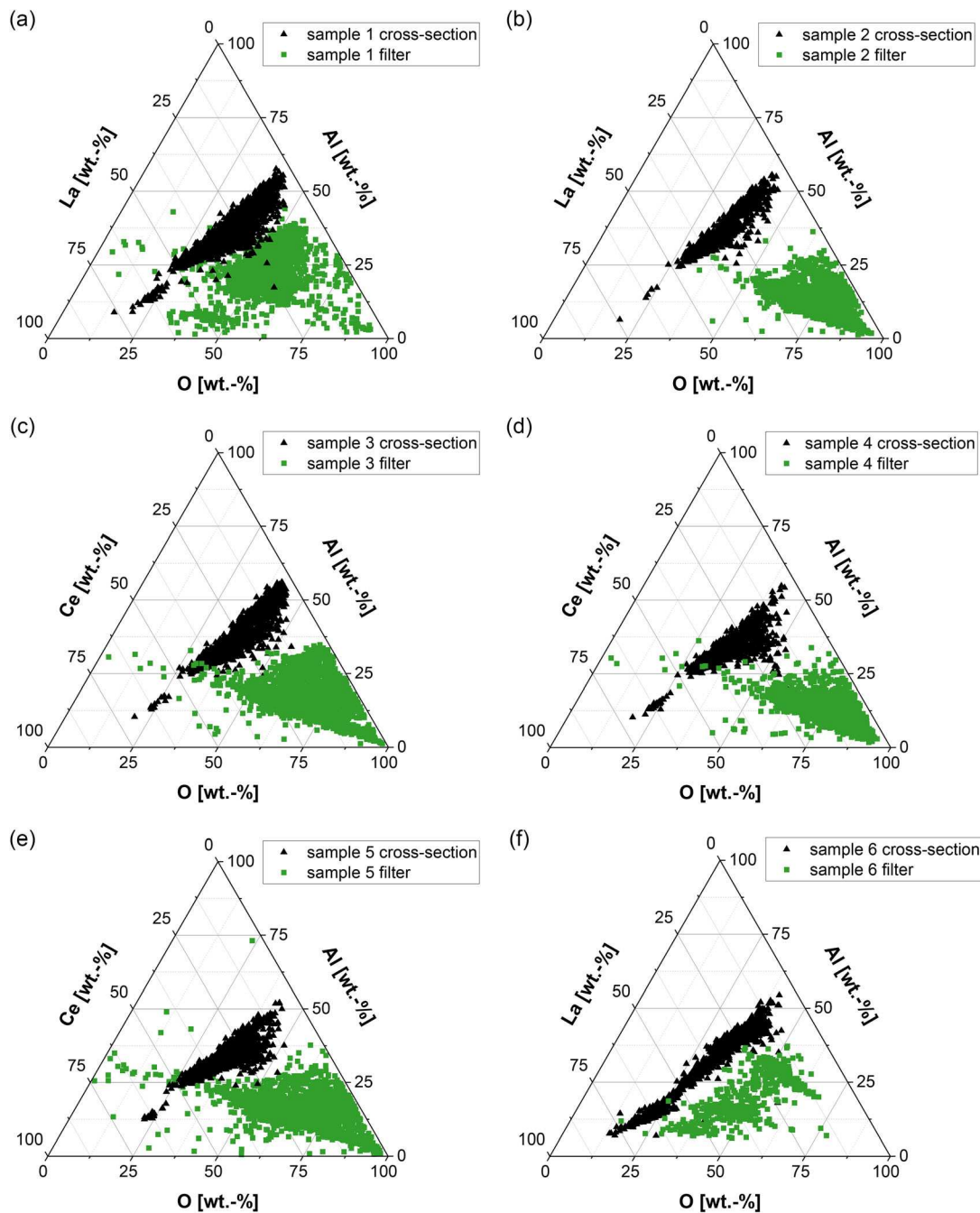
Figure 9. Ternary systems comparing the chemical compositions of NMIs following cross-section and filter analyses: a, b, f) La–Al–O; c–e) Ce–Al–O.

4.2. Comparison of Two- and Three-Dimensional Characteristics

SEM/EDS analysis is the current state-of-the-art method for the characterization of NMIs. This analysis technique provides information regarding the number of NMIs per square millimeter, spatial distributions, and types of NMIs; however, the actual sizes and shapes of NMIs cannot be determined using this method. The error between the actual mean ECDs of the inclusions and the ones measured using automated SEM/EDS analysis of cross-sections is substantial since inclusions are randomly cut during sample preparation.[24] Therefore, 3D characterization methods become further necessitated. The sample areas of the investigated filters analyzed by SEM/EDS differed significantly from those of the cross-sections. The lack of uniform measurement areas results from the random, inhomogeneous distribution of the inclusions on the filters. Furthermore, the inhomogeneous distribution on the filters prevents the determination of spatial distribution. Moreover, corrections concerning residuals from beaker glass, mainly SiO_2 NMIs, must be performed following the analyses of the extracted particles.

**ADVANCED
SCIENCE NEWS**

www.advancedsciencenews.com

**ADVANCED
ENGINEERING
MATERIALS**

www.aem-journal.com

Additionally, matrix residuals may adhere to single inclusions after an incomplete extraction, which requires further correction.

The percentage of traced inclusions was over 80% for all samples. The tracing rate was even higher for Samples 1, 3, and 5, with over 97.5%. One explanation for the lower number of RE-marked inclusions in Samples 2 and 4 could be the different alloying concept compared to Samples 1, 3, and 5, resulting in the additional formation of small, untraced deoxidation products. The use of a heat-resistance furnace for Sample 6 led to higher losses for Al and La. Furthermore, a lower number of NMIs per square millimeter were formed in the heat-resistance furnace. The reason for this is the longer dwell time resulting in agglomeration and enhanced removal of existing inclusions. Additional Al entered the melt with the alloying of La, and small inclusions were formed, similar to those in Samples 2 and 4.

By comparing the mappings of Samples 3 and 6 (in Figure 5 and 6), the RE-containing areas in Sample 3 were finely distributed within the alumina inclusions and not as clearly separated as those in Sample 6. This difference in the phase distribution of heterogeneous RE-containing inclusions could be due to the longer reaction time in the resistance-heated furnace and the segregation tendency of REs. Another distinction between these two production routes can be seen in the sizes of the NMIs. Slightly larger NMIs appeared in Sample 6, which could be due to slower cooling conditions or due to agglomeration tendencies of small NMIs caused by the longer dwell times in this furnace.

In addition, another finding was that the determined mean ECDs for the filters were smaller than for the cross-section samples. Concerning these results, many inclusions may have been below the detection limit since they were partly covert in cross-section samples. After extraction, the actual sizes of inclusions of at least 1 μm become visible, and the total mean ECD of the samples lowers. Karasev et al. previously commented on this phenomenon.[25]

No reliable statements can be made about the number of NMIs per square millimeter in the sample or their spatial distributions on filters compared to cross-section samples. These characteristics primarily depend on the selected section of the filter.

As shown in **Figure 10**, extracted inclusions can also be very close to each other so that an automated measurement can detect them as one mesoscopic irregular-shaped particle instead of many partly globular finely dispersed multiphase (Al, La) oxides.

The ternary systems in Figure 9 show the different distributions of RE-containing Al-oxides of the cross-sections and filters from automated SEM/EDS measurements of each sample. The compositions of the majority of the NMIs in cross-section samples were in the range of complex $REAl_{11}O_{18}$ inclusions (19.2 wt% RE, 41.0 wt% Al, and 39.8 wt% O), similar to the

distribution described in Thiele et al.[32] In addition, accumulations of several inclusions were detected in all samples; these had similar compositions to that of the complex $REAlO_3$ (65.0 wt% RE, 12.6 wt% Al, and 22.4 wt%). Particularly for Sample 6, many inclusions were found with compositions similar to that of the complex $REAlO_3$. A lower number of extracted particles were located in the oxygen corner of Sample 6 compared to the other samples since more matrix residuals were on the filters, weakening the carbon signal.

Concerning the extracted particles, the chemical compositions shifted to higher oxygen values. The cause behind this change to the oxygen corner was a falsification during SEM/EDS measurements. An oxygen bias occurs due to the double carbon signals that reach the detector simultaneously since the filters are mounted upon an adhesive carbon pad. The detector cannot correctly allocate the signal because oxygen has approximately twice the energy level of carbon.[16,34] Furthermore, the composition of the single extracted inclusions scatters in a broader range than the NMIs on the cross-section.

The characterization of RE-traced NMIs is improved due to the implementation of a double-threshold scan in the automated SEM/EDS measurement of cross-section samples. The usage of the sequential chemical extraction technique with 3% nitric acid as an extractant was essential since the stability of RE-containing inclusions in different extracting agents and methods was not entirely clarified before this study.

Due to the aforementioned reasons, the investigation of filters mainly delivers additional information regarding the morphologies of NMIs and, for multiphase inclusions, also regarding their phase distributions. However, an automated SEM/EDS analysis of cross-section samples cannot be replaced by filter investigations since information regarding the distributions and chemical compositions is not provided.

4.3. Optimization of Evaluation Regarding RE-Traced NMIs

The recombination of split-up multiphase inclusions is essential for correctly analyzing the data of automated SEM/EDS measurements after double-threshold scans. Without this correction, the number of NMIs per square millimeter and the mean ECDs of the inclusions would be incorrect. Due to the erroneous split-up, many small inclusions were detected before merging the NMIs. Hence, more NMIs per square millimeter are detected, and as a result, the mean ECDs are slightly lower before applying the recombination tool.

In addition to the mean ECDs, the chemical compositions of the split multiphase NMIs also changed after merging. Most notably, the mean RE-contents in the samples were reduced.
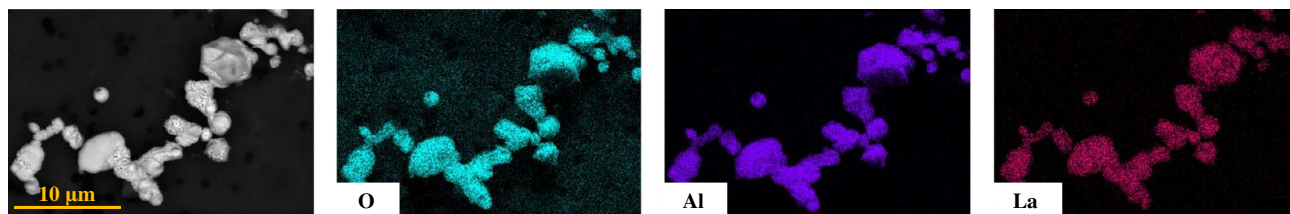

Figure 10. BSE image and mappings of piled La-traced NMIs in Sample 1 on 1 μm filter.

Before recombination, mainly small parts of the detected inclusions contained high amounts of La and Ce, which negatively impacted the mean value. The recombination tool corrects the chemical composition depending on the area fractions of the recombined parts of the NMI. Therefore, small, incorrectly split, highly RE-concentrated particles no longer influence the mean RE content.

The tracing rate did not change after recombining the inclusions because low contents of REs were detected in the Al_2O_3-dominated parts of incorrectly split particles, and inclusions are defined as "traced" if containing at least 0.1 wt% of La or Ce. The number of incorrectly separated RE-containing multiphase inclusions compared to the number of correct inclusions was very low for Samples 1–5, with a maximum error of 1.75% for Sample 4, compared to 13.60% for Sample 6. The error is significantly bigger for the sample produced in the resistance furnace since longer interaction times between REs and alumina inclusions occurred. Therefore, most inclusions are not completely segregated or segregated enough to be split up by the double-threshold method. Hence, the recombination tool is necessary to prevent an incorrect evaluation of the automated SEM/EDS measurement results for RE-containing particles.

Meng et al.[35] discussed the merging of erroneously split RE-containing multiphase inclusions. Their study inspired the development of the recombination tool used in this work. The percentage of merged multiphase inclusions was larger in the study conducted by Meng et al.[35] since a higher BSE image resolution was set and submicroscopic NMIs were detected. By applying these settings in combination with the double-threshold scan, multiphase inclusions were more frequently split into smaller parts below 1 μm. As a result, more submicroscopic and microscopic particles were identified when detecting heterogeneous NMIs. The drawback of these settings is a higher measurement time due to the requirement of higher-resolution BSE images. The measurement of submicroscopic inclusions is seldom applied in industry, as detecting them requires increasing the measurement time, and NMIs from industrial samples show larger areas due to a more precise separation of multiphase inclusions, similar to Sample 6.

All extracted particles appeared brighter in the SEM compared to the inclusions on cross-section samples since filters were mounted upon carbon adhesive pads. Hence, traced multiphase inclusions were not divided into smaller NMIs, so no recombination was required for the NMIs on filters.

This MATLAB tool fits, especially for samples with clearly separated areas of the traced multiphase NMIs, such as Sample 6 or industrial samples, since rare earth elements tend to segregate and modify existing deoxidation products after a sufficient reaction time.[20,36]

5. Conclusion

Based on the performed experiments and evaluations, the following conclusions can be drawn: 1) A sequential chemical extraction was implemented for the 3D investigation of NMIs. This optimized method can be used for inclusions whose behaviors are not entirely researched, such as RE-traced Al_2O_3, since even less-stable NMIs, such as sulfides, can remain stable. The extraction output depends on both the duration of the whole extraction and the surface-to-volume ratio of the sample. 2) The 3D analysis of extracted particles offers an additional method to determine other characteristics of NMIs, such as the actual sizes and morphologies of the particles. The analysis of the extracted particles was performed using SEM/EDS measurements. The automated measurement of filters does not replace the analysis of cross-sections, as the particles are inhomogeneous and randomly distributed. 3) The detection of RE-traced NMIs in cross-section samples implicates the need for a double-threshold scan with the automated SEM/EDS analysis. Due to the tendency of REs to modify deoxidation products, it is necessary to recombine the split-up multiphase inclusions with the developed MATLAB tool. Within this tool, the evaluation is corrected concerning the actual number of inclusions per square millimeter, the mean ECD, the mean chemical composition, and the number of clusters. The importance of recombination is illustrated in Sample 6, with a consequential error between the original and recombined results of approximately 13.60%. The production of this sample differed from Samples 1–5 due to a longer reaction time, and as a consequence, more clearly segregated inclusions were found. Concerning the production conditions for the different samples, Sample 6 most resembles industrial samples. 4) Differences between the 2D and 3D characterization of traced NMIs occurred for all samples concerning mean ECDs, tracing rates, and chemical compositions. The mean ECDs and tracing rates decreased for all samples from cross-sections to filters. The chemical composition of filters shifted to the oxygen corner due to the double-detected carbon signal. Both methods prove to be advantageous for use in further inclusion characterizations since information regarding actual sizes and shapes can be gained by applying sequential chemical extraction as a 3D method.

Conflict of Interest

The authors declare no conflict of interest.

Data Availability Statement

The data that support the findings of this study are available from the corresponding author upon reasonable request.

**ADVANCED
SCIENCE NEWS**

www.advancedsciencenews.com

**ADVANCED
ENGINEERING
MATERIALS**

www.aem-journal.com

[1] N. Choi, K.R. Lim, Y.S. Na, U. Glatzel, J.H. Park, *J. Alloys Compd.* **2018**, *763*, 546.

[2] N. Ånmark, A. Karasev, P.G. Jönsson, *Materials* **2015**, *8*, 751.

[3] J. Kasińska, *Arch. Foundry Eng.* **2018**, *18*, 37.

[4] S.K. Michelic, C. Bernhard, *Steel Res. Int.* **2022**, *93*, 2200086.

[5] K.G. Rackers, B.G. Thomas, in *78th Steelmaking Conf. Proc.*, Iron and Steel Society, **1995**, pp. 723–734.

[6] K.G. Rackers, *Master* **1995**.

[7] V. Tusset, C. Marique, H. Mathy, B. Gommers, N. van Poeck, *Ironmaking Steelmaking.* **2003**, *30*, 142.

[8] F. Ruby-Meyer, G. Willay, *La Revue de MÃtallurgie-CIT* **1997**, 367.

[9] M. Wang, Y. Bao, H. Cui, H. Wu, W. Wu, *ISIJ Int.* **2010**, *50*, 1606.

[10] B. Li, H. Zhu, J. Sun, M. Song, J. Zhao, *Steel Res. Int.* **2022**, *93*, 2200064.

[11] Z. Deng, Z. Liu, M. Zhu, L. Huo, *ISIJ Int.* **2021**, *61*, 1.

[12] M. Burty, P. Dunand, J. Ritt, H. Soulard, A. Blanchard, G. Jeanne, F. Penet, R. Pluquet, I. Poissonnet, in *Ironmaking Conf. Proc.* **1997**, pp. 711–717.

[13] M. Nadif, J. Lehmann, M. Burty, J.-F. Domgin, *Rev. Met. Paris* **2007**, *104*, 493.

[14] W. Liang, J. Li, B. Lu, J. Zhi, S. Zhang, Y. Liu, *J. Iron Steel Res. Int.* **2022**, *29*, 34.

[15] B. Peng, F. Li, S. Zheng, H. Li, in *TMS 2017 146th Annual Meeting & Exhibition Suppl. Proc.*, Springer, Cham **2017**, pp. 403–411.

[16] J.I. Goldstein, D.E. Newbury, J.R. Michael, N.W. Ritchie, J.H.J. Scott, D.C. Joy, *Scanning Electron Microscopy And X-Ray Microanalysis*, Springer, New York, NY **2018**.

[17] G. Cai, C. Li, *J. Mater. Eng. Perform.* **2015**, *24*, 3989.

[18] R. Geng, J. Li, C. Shi, *J. Iron Steel Res. Int.* **2022**, *29*, 1659.

[19] H. Li, Y. Yu, X. Ren, S. Zhang, S. Wang, *J. Iron Steel Res. Int.* **2017**, *24*, 925.

[20] B. Li, H. Zhu, J. Zhao, M. Song, J. Li, Z. Xue, *Steel Res. Int.* **2021**, 2100347.

[21] P. Kaushik, H. Pielet, H. Yin, *Ironmaking Steelmaking* **2009**, *36*, 561.

[22] L. Zhang, B. Thomas, *ISIJ Int.* **2003**, *43*, 271.

[23] A. Mayerhofer, *Ph.D. Thesis*, Leoben, Austria, **2021**.

[24] S.K. Michelic, G. Wieser, C. Bernhard, *ISIJ Int.* **2011**, *51*, 769.

[25] S. Ramesh Babu, S.K. Michelic, *Materials* **2022**, *15*, 3367.

[26] D. Janis, R. Inoue, A. Karasev, P.G. Jönsson, *Adv. Mater. Sci. Eng.* **2014**, *2014*, 210486.

[27] H. Doostmohammadi, A. Karasev, P.G. Jönsson, *Steel Res. Int.* **2010**, *81*, 398.

[28] X. Zhang, L. Zhang, W. Yang, Y. Zhang, Y. Ren, Y. Dong, *Metall. Res. Technol.* **2017**, *114*, 113.

[29] D. Janis, A. Karasev, R. Inoue, P.G. Jönsson, *Steel Res. Int.* **2015**, *86*, 1271.

[30] Y. Bi, A.V. Karasev, P.G. Jönsson, *ISIJ Int.* **2014**, *54*, 1266.

[31] M. Nabeel, A. Karasev, P.G. Jönsson, *ISIJ Int.* **2015**, *55*, 2358.

[32] K. Thiele, P. Presoly, D. Ernst, S.R. Babu, S.K. Michelic, *Ironmaking Steelmaking* **2022**, 1, https://doi.org/10.1080/03019233.2022.2124816.

[33] P. Dorrer, S.K. Michelic, C. Bernhard, A. Penz, R. Rössler, *Steel Res. Int.* **2019**, *90*, 1800635.

[34] K. Thiele, S. Ilie, R. Roessler, S. Michelic, in *Conf. Proc. at ICS, 8th Int. Congress on the Science and Technology of Steelmaking*, AIST, Montreal **2022**, pp. 80–87, https://doi.org/10.33313/531/009.

[35] Y. Meng, C. Yan, X. Yang, X. Ju, *ISIJ Int.* **2020**, *60*, 534.

[36] C. Pan, X. Hu, P. Lin, K. Chou, *ISIJ Int.* **2020**, *60*, 1878.

AI assisted steel cleanness evaluation: Predicting the morphology of La-traced non-metallic inclusions using backscattered-electron images

Kathrin Thiele [a,*], Robert Musi [a], Thomas Prohaska [b], Johanna Irrgeher [b], Susanne K. Michelic [a]

[a] *Christian Doppler Laboratory for Inclusion Metallurgy in Advanced Steelmaking, Montanuniversitaet Leoben, Franz Josef–Straße 18, 8700, Leoben, Austria*
[b] *Chair of General and Analytical Chemistry, Montanuniversitaet Leoben, Franz Josef–Straße 18, 8700, Leoben, Austria*

ARTICLE INFO

ABSTRACT

This study shows how computer vision, a field of artificial intelligence (AI), can be used to gain access to morphological information for a better process understanding and furthermore, how it can be implemented in the evaluation of active tracing experiments. Non-metallic inclusions (NMIs) play a crucial role in determining the chemical and physical properties of the final steel product. The active tracing technique allows for tracking the formation and modification mechanisms of detrimental NMIs throughout the steelmaking process by adding rare earth elements (REEs) to the melt. The interaction of REEs with NMIs results in the formation of traced multiphase particles and, therefore, lead to challenges for accurate evaluation by automated scanning electron microscopy with energy-dispersive spectroscopy (SEM/EDS). However, obtaining information about the REE distribution in traced NMIs without extensive, time-consuming human effort is not feasible using the existing method. A two-step classification process with AI was established, which included training and testing of two random forest classifiers (RFC). The first RFC achieved for the binary NMI/non-NMI classification an accuracy of 94.8 %. Four different morphology-based classes were considered in the second classification, whereas traced homogeneous NMIs and NMIs with a high La content got classified with a precision exceeding 90 %. However, caution is required in interpreting results for traced heterogeneous NMIs, as they have a higher prediction error of 37.2 %.

1. Introduction

Constantly increasing quality requirements necessitate steel producers to monitor and control steel cleanness. This term considers factors such as quantity, chemical composition, morphology, size, and distribution of non-metallic inclusions (NMIs). Modern steelmaking is inevitably connected with steel cleanness and, consequently, NMIs, as these micrometer-sized particles are always present and negatively impact steel performance [1–4]. Low number of inclusions are beneficial for most applications; however, the required steel cleanness depends on the specific use case. Active tracing with rare earth elements (REEs) is an important tool for acquiring information about the origin, formation, and modification of NMIs during the steelmaking process [5,6]. Furthermore, this technique allows for a more specific study of undesirable phenomena related to NMIs, such as clogging [7–9]. At active tracing, REEs are directly added to the melt at certain process stages. REEs act as reducing agents to other NMIs due to their higher oxygen

affinity compared to typical deoxidation products, such as aluminum oxide (Al_2O_3), silicon dioxide (SiO_2), or manganese (II) oxide (MnO) [5, 10]. Several studies have already focused on modifying alumina inclusions after the addition of lanthanum (La) and cerium (Ce) in the industry [11,12] and on laboratory scale [13–16]. Ever since the launch of steel production, analytical methods have played a key role to assess the composition - and with this the quality - of all components used and the steel product itself [17–19]. The state-of-the-art analytical method to characterize NMIs is scanning electron microscopy with energy-dispersive spectroscopy (SEM/EDS). SEM/EDS analysis is one of the essential measurement tools for material research and metallurgical process development, as it provides information about particles' size, chemical composition, spatial distribution, and morphological factors such as aspect ratio and mean equivalent circle diameter (ECD) on a sample surface [20–24]. Micro steel cleanness evaluations (NMI 1–15 μm) done by Mayerhofer [20] revealed particle contents of 500–1000 Nr/mm^2 in construction steels, about 250 Nr/mm^2 in spring and railway

steels, and 1–10 Nr/mm² for remelted grades. The operating mode is based on a brightness difference in backscattered electron (BSE) images between particles or, in general, region of interest (ROI) and the surrounding steel matrix. Common NMI types, such as the previously mentioned deoxidation products, occur in BSE images darker than the steel matrix, as they consist of elements with lower molar mass than iron. This fact enables the automatization of SEM/EDS analysis. An operator-defined gray value threshold separates the ROI from the surrounding steel matrix by binarizing the BSE image. Subsequently, detected particles are automatically focused with the electron gun and their chemical composition is determined with EDS measurement. The evaluation of steel samples with REE-marked NMIs requires a more advanced approach, as described by Meng et al. [25] and Thiele et al. [26]. Due to the higher molar mass of REEs compared to iron, the gray value of REE-rich phases in traced heterogeneous NMIs exceeds the operator-defined threshold and counts as steel matrix after image binarization for the automated measurement. This issue is addressed by applying a double-threshold scan in which a second threshold separates the brighter, REE-rich areas from the steel matrix and adds these to the subsequently measured ROI. However, the interpretation of measurement results is still limited. The number of detected particles gets falsified if traced heterogeneous NMIs are counted as several singular sub-inclusions. Furthermore, difficulties during data evaluation concerning inclusion size distribution, chemical composition, or number per square millimeter arise. Fig. 1 shows a traced heterogeneous NMI, for which the double-threshold scan led to a falsely split measurement result with two singular parts.

In contrast to this, Fig. 2 illustrates a homogeneous REE-containing NMI with the associated elemental mappings where no split-up occurs.

A possible solution to this problem, also used in previously evaluated tracer experiments [26], includes a post-measurement recombination tool to combine irregularly split NMIs. The condition, which decides if inclusions get merged, contains approximated particle shapes, the chemical composition, and a user-defined safety factor to consider small deviations regarding inclusions' position and calculated ECD values due to the low magnification of BSE images. Even though the overall calculation error decreases, time-consuming manual supervision is still inevitable to verify the results of the double-threshold scan and the recombination tool.

Therefore, the present study focuses on a novel approach build on a morphology-based classification of traced NMIs in steel samples using computer vision, a field of artificial intelligence (AI). A similar procedure with AI was applied for common NMIs on BSE images [27,28]. Using AI as a support system for metallurgists, who evaluate tracer experiments, has the potential to enhance the information content of existing measurement results, leading to a better understanding of the active tracing technique. The goal is to provide information about the inclusion landscape of a steel sample by predicting pre-defined morphological classes for extracted particles from BSE images. In this study, the investigated steel sample was produced on a laboratory scale using additions of La to create an inclusion landscape containing traced NMIs similar to industrial trials. The conventional steel cleanness evaluation was done with automated double-threshold SEM/EDS analysis followed by the recombination tool parallel to applying the AI-supported solution. The results of both methods are described using various metrics. Furthermore, the strengths and the weaknesses, as well as improvement potentials of the AI-based method, are presented and discussed.

2. Methods and materials

Fig. 3 shows a flowchart containing information about the necessary process steps in the respective domains of automated SEM/EDS analysis, manual data evaluation, and AI data evaluation. Furthermore, it illustrates how the measurement data was generated and manipulated over the course of the different evaluation methods. The following chapters present each process step in detail.

2.1. Test material

A steel sample produced on a laboratory scale was used in this study to evaluate and compare the manual and AI analyzing methods of steel cleanness. The raw material consisted of pure iron with an oxygen content of 300 μg/g. After melting 300 g of pure iron at 1600 °C and deoxidizing with Al in a resistance-heated Tammann-type furnace (Ruhrstrat HRTK 32 Sond.) under an inert atmosphere, the formed deoxidation products, mainly alumina inclusions, were partially reduced through the addition of 162 mg La from Treibacher Industrie AG with a minimum La content of 98 wt.-% and counted in the
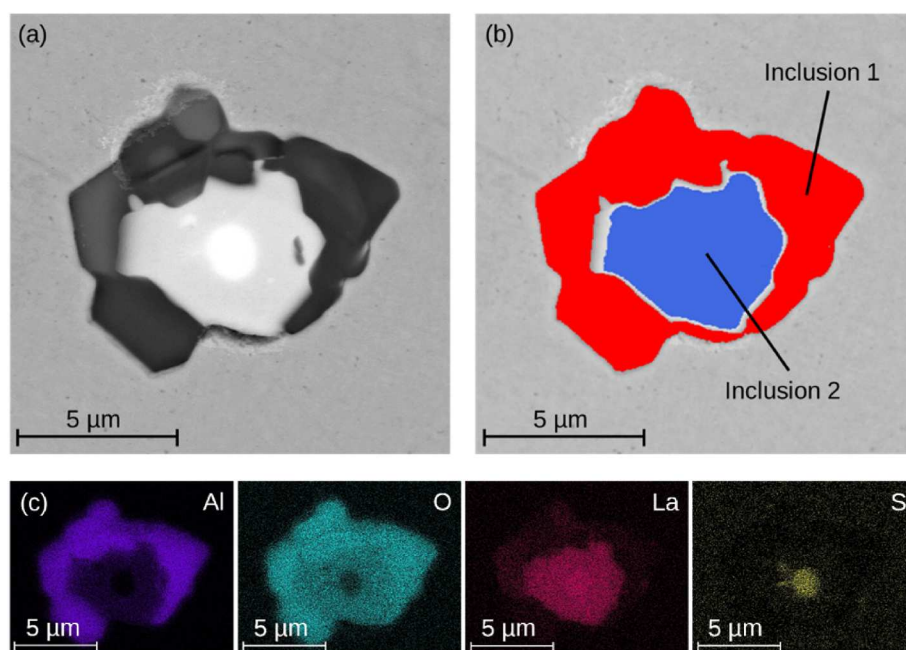

Fig. 1. Heterogeneous REE-marked NMI (a), NMI after evaluation with double-threshold scan (b), element mappings (c).
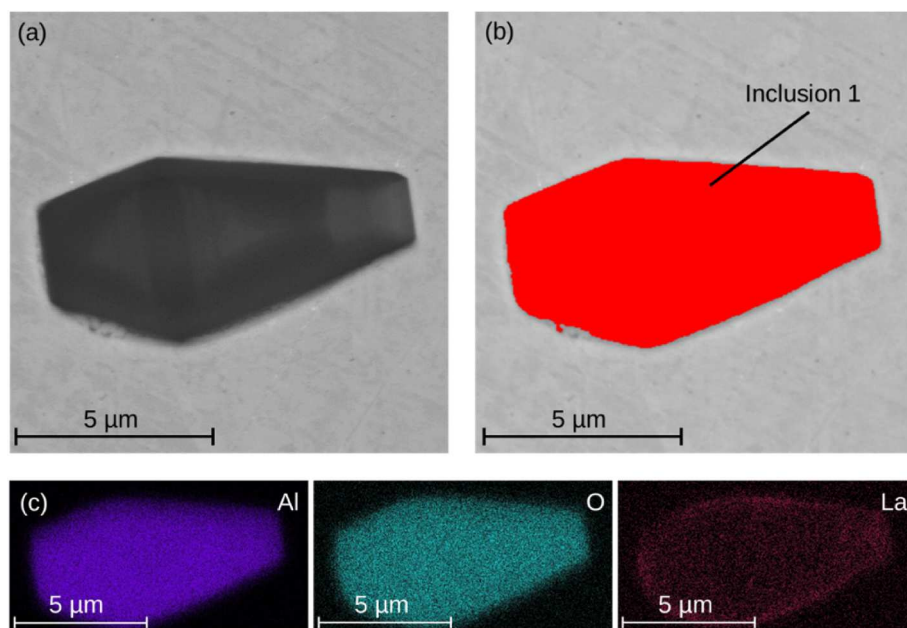
Fig. 2. Homogeneous REE-marked NMI (a), NMI after evaluation with double-threshold scan (b), element mappings (c).
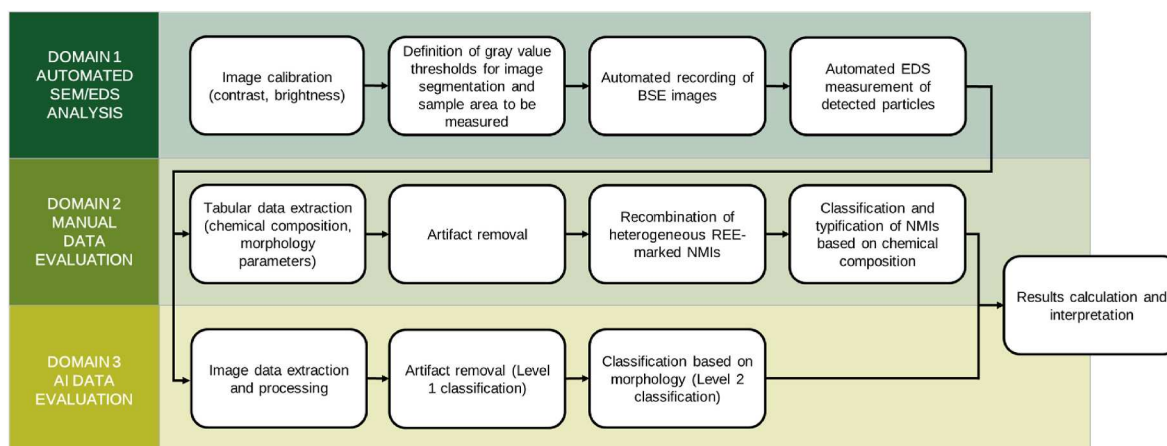

Fig. 3. Flowchart of the active tracing experiment evaluation.

subsequent evaluation as traced. The addition of REEs to steel is challenging because of their intensive interaction with the surrounding atmosphere. In this study, La was alloyed using small pieces of metallic La wrapped inside Al-foil. Based on the findings of Thiele et al. [10], 30 % as recovery rate was taken into account for the present trial. The operating mode of experiments carried out on the Tammann-type furnace is explained in more detail by Dorrer et al. [29]. The chemical composition of the steel sample, consisting of carbon (C), silicon (Si), manganese (Mn), phosphorus (P), sulfur (S), aluminum (Al), nitrogen (N), La and iron (Fe) measured by SPECTROMAXx optical emissions spectrometry (spark OES, SPECTRO Analytical Instruments GmbH, Kleve, Germany), is listed in Table 1.

2.2. Automated SEM/EDS analysis (domain 1)

For the steel cleanness analysis, microscopic particles in the steel sample were detected and investigated regarding their size, spatial distribution, and chemical composition. The instrument in this study was a JEOL 7200F field emission SEM (JEOL Germany GmbH, Freising, Germany) equipped with a 100 mm^2 SDD EDS detector (Oxford Instruments Ultim Max 100; Oxford Instruments GmbH NanoAnalysis, Wiesbaden, Germany). The software used for automated particle detection analysis at the SEM was AZtec Feature (AZtec 6.0, Oxford Instruments GmbH NanoAnalysis, Wiesbaden, Germany). The sample preparation included cutting, conductive embedding, grinding, and polishing (diamond suspension with 9, 3 and 1 μm). During image calibration at the SEM, the gray value of the BSE image was measured along a line scan observing a NMI with the surrounding steel matrix and adjusted using different

Table 1
Chemical composition of the steel sample in wt.-% measured by spark OES.

C	Si	Mn	P	S	Al	N	La	Fe
0.024	0.031	0.103	0.008	0.003	0.045	0.004	0.005	Bal.

contrast and brightness settings. The gray value of the steel matrix was set to approximately 24,000, whereas the range of particle detection was defined from 0 to 22,461 and from 25,834 to 32,767, respectively. The subsequent applied EDS measurement detected and analyzed particles with a gray value below the lower or higher than the upper threshold on a scanned area of approximately 100 mm². The automated analysis determined geometrical data such as ECD, length, breadth, and area in addition to the particles' chemical composition. Particles smaller than 1 μm in diameter were excluded from further analysis due to the resolution limit of the SEM used. The following settings were utilized for the automated analysis: 15 keV beam energy, 13 PC probe current, 10 mm working distance, 2048 × 1024 resolution with 200× magnification, and 1 s EDS measurement time for an area scan of a single particle.

2.3. Manual data evaluation (domain 2)

For manual data evaluation, the measured data from the automated double-threshold SEM/EDS analysis was exported into an Excel file, which represented the initial dataset. The first types of artifacts were removed by comparing whether the measured chemical composition of a particle mainly matches the chemical composition of the surrounding steel matrix or grinding and polishing residues such as alkali metals or Si. The applied matrix correction removed all particles, for which the sum of Fe, Mn, C, chromium (Cr), nickel (Ni), molybdenum (Mo), niobium (Nb), titanium (Ti), and vanadium (V) (main constituents of the steel matrix) accounted for over 99.99 wt.-%. Similar removal rules existed for grinding and polishing residues, which also included the concentrations of Si and alkali metals. The next correction step considered the removal of particles without a non-metallic bonding partner since NMIs must contain oxygen (O), N, or S. As the automated SEM/EDS analysis is a tool for micro-cleanness evaluation, particles with an ECD over 15 μm were excluded from the dataset. The evaluation of REE-marked NMIs required an additional correction step compared to common steel cleanness evaluations. Depending on the interaction time of REEs with other NMIs in liquid steel and the cooling conditions, their distribution can either be homogeneous across the NMI surface or heterogeneous and, therefore, separated entirely due to segregation (Figs. 1 and 2). Heterogeneous NMIs lead to wrongly determined particles during the double-threshold scan due to the detection of several sub-inclusions (Fig. 1b). A previous study by Thiele et al. [26] focused on this problem and resulted in the development of a MATLAB tool, which was also applied in this study. This recombination tool iterates through each particle of the dataset and examines every other NMI on a condition that includes the position, distance, shape (based on the aspect ratio approximated as an ellipse or circle), and chemical composition. If the surfaces of NMIs touch and at least one of them has a La content of 0.1 wt.-% or more, the condition is fulfilled, and the corresponding particles are recombined by calculating a new area-weighted chemical composition. To determine the remaining error between the actual inclusion population and the inclusion population generated with the recombination tool, a human supervisor reviewed and validated the BSE images of heterogeneous NMIs. Fig. 4a shows an example of a validated image. After recombination, the remaining particles were classified, according to their non-metallic bonding partner, into oxides, sulfides, nitrides, and multiphase inclusions such as oxide-sulfides or oxide-nitrides. The final step of the steel cleanness evaluation was the typification based on the chemical composition, in which NMIs were categorized into specific inclusion types, such as Al_2O_3 or manganese sulfide (MnS). The artifact removal and the final NMI dataset were evaluated by calculating commonly used metrics to describe the inclusion landscape, such as spatial distribution, number of NMIs per square millimeter, as well as NMI class and type distribution. Furthermore, the quotient between the number of NMIs traced with La and the total number of detected inclusions was calculated, describing the effectiveness of the active tracing technique. This metric is referred to as the tracing rate. NMIs with a La content over 0.1 wt.-% were considered for this calculation.

2.4. AI data evaluation (domain 3)

As shown in Fig. 3, the AI data evaluation consisted of image data extraction with subsequent processing as well as two classification steps. Classification level 1 dealt with removing artifacts from the dataset, whereas in classification level 2, the actual NMI class was determined. A two-step process enhanced the ability to finetune the AI model regarding specific requirements for the respective classification level. The Python programming language (version 3.11.5) was used for this approach with different libraries referred to in the specific chapters.

2.4.1. Data preprocessing

The recorded BSE images with a resolution of 2048 × 1024 pixels (px) were exported from the AZtec software as "png" files. A similar approach to the automated SEM/EDS analysis with the OpenCV library [30] (version 4.8.1) was applied for subsequent image processing. In the first step, ROIs were identified by binarizing the BSE image with two gray value thresholds, which matched the value of the SEM/EDS measurement (Fig. 4b). Image areas with gray values between both thresholds were not considered, as they were assigned to be steel matrix. Every detected particle on the BSE images was assigned to a rectangular bounding box and a unique number (Fig. 4c).

During the extraction process, every ROI inside a bounding box with an area larger than 5 px was exported and saved as "png" file. The value was defined as lower than the actual minimum particle size in AZtec of 9 px due to slight variations in the image processing techniques. This ensured that every particle detected during the automated measurement was also considered by the OpenCV method. However, the lower minimum particle size led to additional ROIs, which were initially not measured by the SEM due to the chosen settings. This mismatch between the detected particles by using OpenCV and the automated SEM/EDS analysis with AZtec can be seen as exemplary for bounding box 3 in
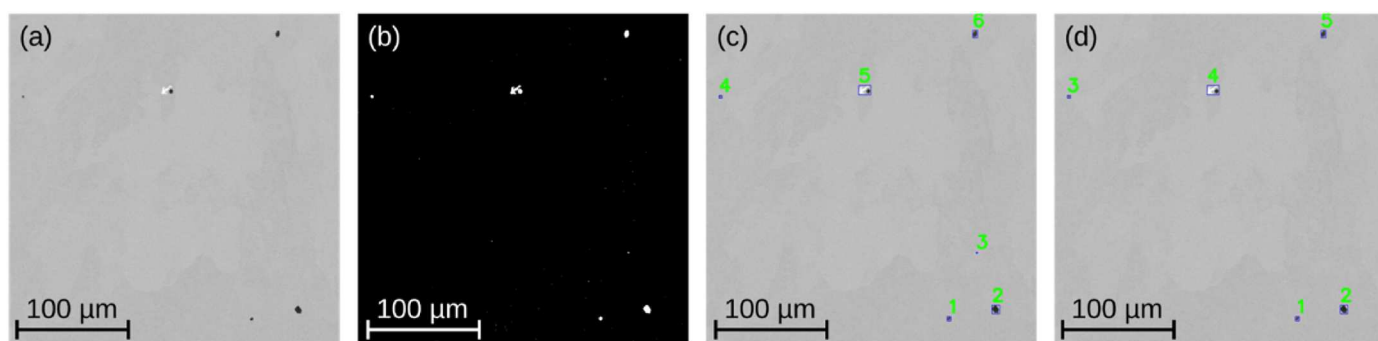

Fig. 4. Original BSE image (a), BSE image after binarizing (b), BSE image with detected particles using OpenCV (c), BSE image with detected particles during automated SEM/EDS analysis with AZtec.

Fig. 4c and d. Overall, 58 % more ROIs were detected with the OpenCV method. The additional areas were treated as artifacts during the following classification. The given variations in spatial dimensions of the detected particles and the resulting differences in image sizes required padding to 100×100 px to ensure a consistent image input size for the classification model.

2.4.2. Data labeling

Training a classification model necessitates a labeled dataset. Therefore, five classes of NMIs were defined based on the different particle morphologies: traced heterogeneous NMI, traced homogeneous NMI, NMI with high La content, untraced NMI, and artifact. Exemplary images of each class are given in Fig. 5. By manual supervision, every extracted particle was assigned to a certain class depending on the depiction in the BSE image and the chemical composition.

2.4.3. Model training and testing

The random forest classifier (RFC), an ensemble of several decision trees, was used as the model of choice due to achieving the best performance on similar inclusion classification tasks compared to other common classifiers [31]. Training and testing included similar procedures for both classification levels, only differing in the used datasets. For classification level 1, the four non-artifact classes were combined, resulting in a binary classification into NMI or non-NMI. As for level 2, artifacts were disregarded, and the second model predicted one of the other four NMI classes. During application, the second model gets fed with the results of the previous model, and therefore, the error is dragged along in the classification process. However, during training and testing, both classification levels were treated separately, and the occurred error in the first level did not get considered for the performance metrics in the second level. Fig. 6 shows the initial number of labeled images in the datasets.

An overview of the training and testing procedure performed with the Python library scikit-learn [32] (version 1.3.1) is given in Fig. 7. After the initial dataset was split into a 70/30 ratio to obtain a training and test dataset, a RFC was trained using the 3-fold cross-validation strategy and standard hyperparameters. For each iteration in this validation strategy, the training set was separated randomly into three equally sized parts, 3-folds, where two of them were used for training the RFC and the third one for validation. The following shallow performance evaluation represented an initial check on how well the classifier predicts out-of-the-box. During the subsequent optimization, the following hyperparameters of the RFC were randomly changed in certain ranges, represented by the values in the brackets, for 1000 iterations based on the guidelines presented in Refs. [33,34]: number of tress (25–1000), number of features to consider when looking for the best split (4–100), minimum number required for an internal node split (2-50), minimum number required at a leaf node (1-50). For each iteration, a new RFC
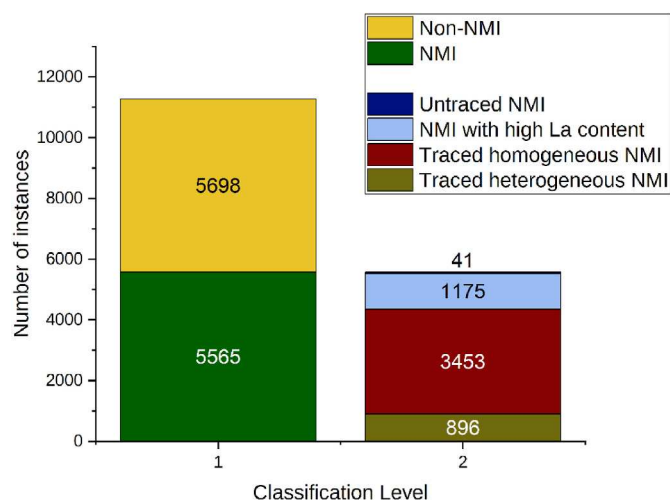
Fig. 6. Class distribution for the respective classification levels.

went through training and evaluation using the 3-fold cross-validation strategy. Ultimately, the combination of hyperparameters that achieved the highest value of a specific performance metric (equations summarized in the appendix) was chosen as the optimal configuration. The accuracy (Equation (1)) was considered as the quality criteria for the first classification, whereas the micro-averaged F1-score, another metric to determine a model's performance (Equations (2)–(5)), was preferred for the second classification due to the imbalanced distribution of the NMI classes [35].

The classification model's output represents the determined probability of the input being associated with a class. A value of 0.5, or 50 %, is the standard binary classification threshold. If the predicted probability exceeds this threshold, the input gets classified as the positive class, otherwise as the negative class. In this case, the terms positive and negative class refer to NMI and non-NMI. Exclusively for the binary NMI/non-NMI classification, the threshold separating the predicted class based on the probability scores generated by the RFC was adjusted using the Youden-Index (Equation (6)) to optimize the result further [36]. The maximum Youden-Index is defined as the optimum value of the threshold. After the configuration process, the RFC went through a final training on the whole training dataset. During testing, the optimally configured model predicted the label for every image from the test dataset. The performance metrics accuracy, precision (Equation (7)), recall (Equation (8)), confusion matrix as well as the receiver operating characteristic (ROC) curve were calculated by comparing the predictions of the RFC with the actual NMI class. In a ROC curve, the true positive rate (Equation (9)) is plotted against the false positive rate
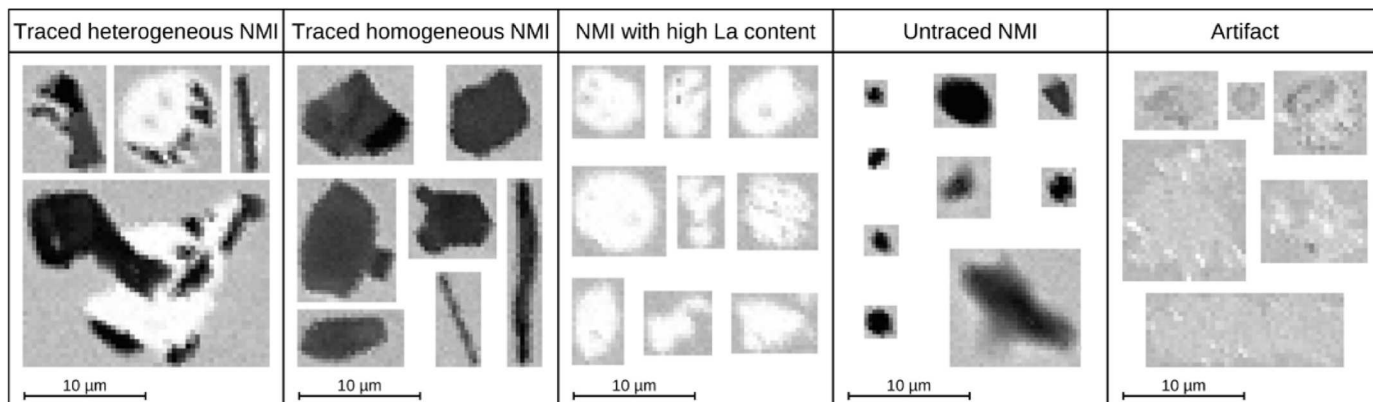

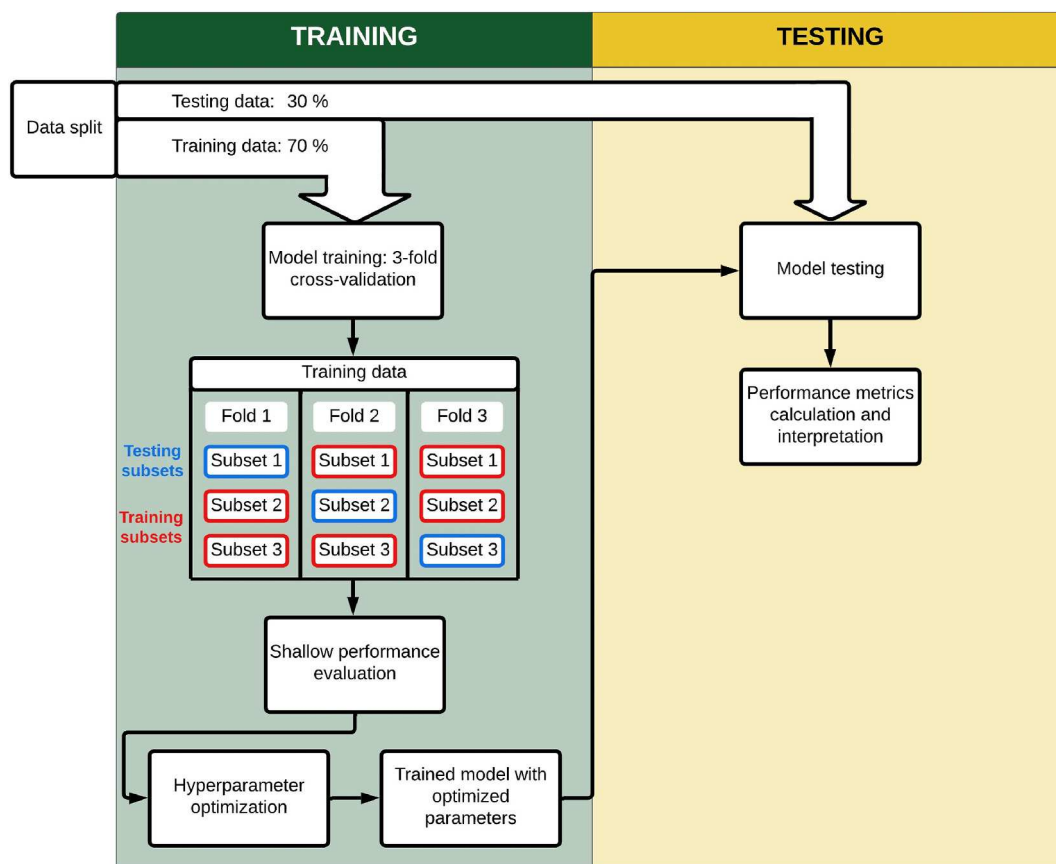**Fig. 5.** Exemplary NMIs of the defined classes (1 px $\triangleq$ 0.33 μm).

Fig. 7. Model training and testing procedure.

(Equation (10)) at each classification threshold setting. The area under curve (AUC) summarizes the performance of a model regarding its ROC curve with a value ranging from 0.5 (random classifier) and 1.0 (perfect classifier).

The final training with a subsequent performance evaluation on the test dataset was repeated 100 times to ensure that the achieved results stayed within a certain range and to calculate the corresponding confidence intervals.

3. Results

3.1. Manual evaluation of automated SEM/EDS analysis

The particle density in the steel sample before any manual correction was 66.77 Nr/mm^2. Scratches, polishing residues, and other artifacts were removed in the first step of the manual SEM/EDS data evaluation. The amount of rejected data due to matrix-, polishing residue-, and bonding partner correction is listed in Table 2, along with the number of detected particles per square millimeter before and after the manual corrections. About 7.72 % of the particles had a chemical composition similar to the surrounding steel matrix. The detected polishing residues

accounted for approximately 2.79 %. The particles without a bonding partner contributed another 0.22 %.

In processing the data with the recombination tool, the metrics presented in Table 3, were calculated by comparing the inclusion population before and after this step. The relative number of NMIs that were split by automated SEM/EDS measurement but actually belonged together was roughly 17 %, and the relative number of newly defined heterogeneous NMIs was 6.63 %. The number of NMIs before and after recombination, as indicated by the double-threshold scan error, showed a difference of approximately 10 %.

The next manual data evaluation step was the classification of the remaining particles depending on their non-metallic bonding partners. Oxides constituted approximately 91.05 % of all NMIs, with the rest being oxide-sulfides. During the typification of NMIs, it was found that the oxide-sulfides were mainly Al_2O_3 with traces of CaS and that the majority of oxides were La-traced alumina inclusions.

The overall tracing rate, including all NMI types, was 95.65 %, and for Al-containing inclusions, 99.30 %. Fig. 8 illustrates the traced inclusion types of the oxide class in the steel sample after recombination. Approximately 76 % of the oxides were alumina NMIs, followed by 9.67 % magnesium aluminate spinel ($Al_2O_3 \cdot MgO$; MA-spinel), 6.98 % calcium aluminate ($CaO \cdot Al_2O_3$) and 3.51 % of the complex multiphase inclusion consisting of calcium oxide with alumina and magnesium oxide ($CaO \cdot Al_2O_3 \cdot MgO$). The remaining 3.72 % of the oxides consisted

Table 2
Number of NMIs per square millimeter before and after the corrections, amount of rejected data concerning matrix-, polishing residue- and bonding partner correction in % for the investigated steel sample.

Nr/mm^2 particles before corrections	Nr/mm^2 particles after correction	%-Matrix correction	%-Polishing residue correction	%-Bonding partner correction
66.77	59.43	7.72	2.79	0.22

Table 3
Relative number of wrongly split and recombined NMIs and appearing error between evaluation without and with recombined results.

Rel. number of wrongly split NMIs [%]	Rel. number of recombined NMIs [%]	Double-threshold scan error [%]
16.79	6.63	10.17
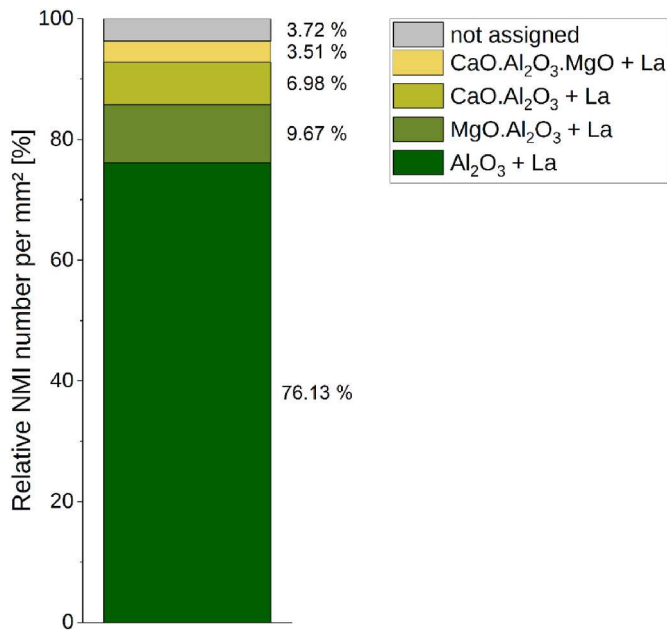
Fig. 8. Overview of traced NMI types from the oxide class in the steel sample.

of inclusion types such as $Al_2O_3 \cdot SiO_2$, CaO, or complexes like $Al_2O_3 \cdot SiO_2 \cdot CaO$.

Fig. 9 depicts the comparison between the absolute number of NMI types from the oxide class after recombination with the actual amount, defined by manually evaluating the BSE images for every measured particle with a human expert. The recombination tool generated the greatest discrepancy for Al_2O_3 inclusions with 1.40 additional recombined NMIs per mm^2. The deviations for the MA-spinel and the $CaO \cdot Al_2O_3 \cdot MgO$ type were in a similar range of approximately 0.25 NMIs per mm^2, whereas the calculated error for $CaO \cdot Al_2O_3$ inclusions was negligibly small.
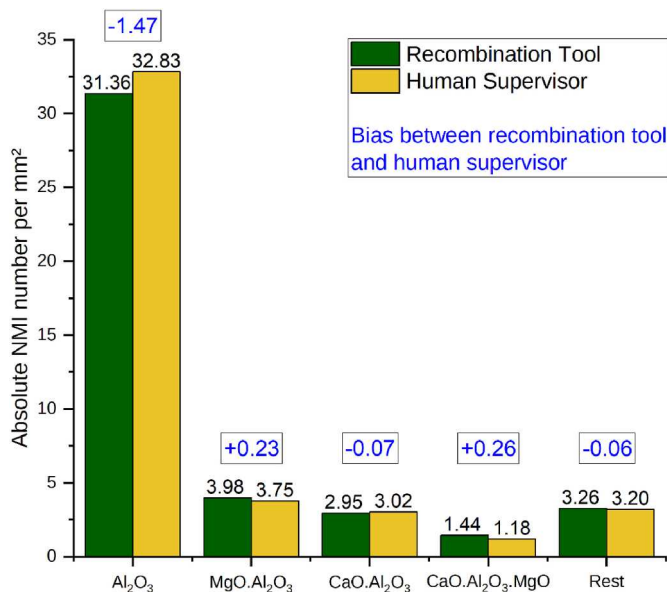
Fig. 9. Comparison between the absolute number of NMIs after using the recombination tool (green) and after evaluation by human supervisor (yellow). (For interpretation of the references to colour in this figure legend, the reader is referred to the Web version of this article.)

3.2. Evaluation with artificial intelligence

3.2.1. Level 1 classification

The out-of-the-box RFC trained with the 3-fold cross-validation strategy achieved an accuracy of 85.0 % during the shallow performance evaluation. The highest value for the accuracy within the hyperparameter optimization was reported with 94.8 % using the following settings: 948 trees, 100 considered features for the best split, 22 required observations for an internal node split, and one sample required at a leaf node. Based on the calculated ROC curve in Fig. 10 after training the optimized RFC, the classification threshold was adjusted to a value of 0.48 using the Youden-Index, represented by the blue dot in the plot. This threshold was considered for further evaluation.

The nomenclature for the following performance metrics includes, as the first number, the mean of the 100 performed trials and, in the brackets afterward, the calculated lower and upper limit of the 95 % confidence interval. Using the most suitable settings for the RFC resulted in an accuracy of 95.9 % (95.2, 96.6) during the evaluation with the test set. For the NMI class, the measured area under the ROC curve was 0.991 (0.984, 0.998), and the calculated F1-score 0.960 (0.953, 0.967). Fig. 11 shows the confusion matrix comparing the actual class (y-axis) with the prediction of the trained RFC (x-axis) for every image in the test dataset. Fields along the diagonal starting from the top left to the bottom right, describe the correct number of predictions. If an actual NMI gets predicted correctly as NMI, as it was the case for 1576 images, the value in the upper left field increases. The lower right field, which represents the second case of matching classes, contains 1660 correctly classified images. The relative values in these fields describe the precision. All other areas, in which the ground truth and the predicted class are not equal, provide information about the misclassifications or the confusion of the RFC. Regarding the first row in the confusion matrix, 4.6 % of the NMIs were wrongly classified as non-NMIs (artifacts). The other misclassification included 3.6 % of the images from the non-NMI class, which were predicted as NMIs by the RFC.

3.2.2. Level 2 classification

The non-optimized RFC with standard parameters achieved a micro-averaged F1-score of 0.85. During the random search, the following values were found as the optimal configuration: 879 number of trees, 97 considered features when searching for the best split, 35 required observations for an internal node split, and 1 sample required at a leaf node. This setup led to a micro-averaged F1-score of 0.910 (0.900, 0.920). Fig. 12 represents the confusion matrix with the calculated
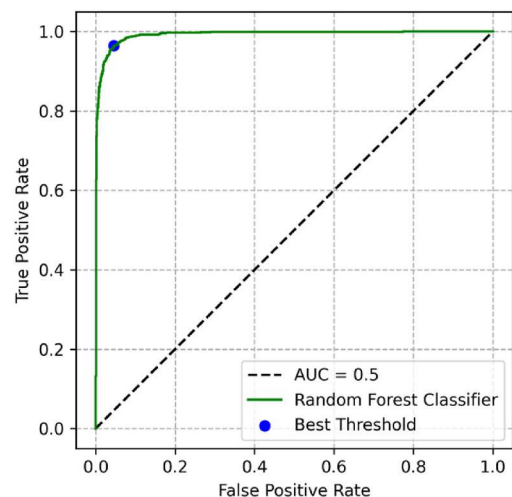

Fig. 10. Calculated ROC curve for threshold adjustment using a 3-fold cross-validation strategy.
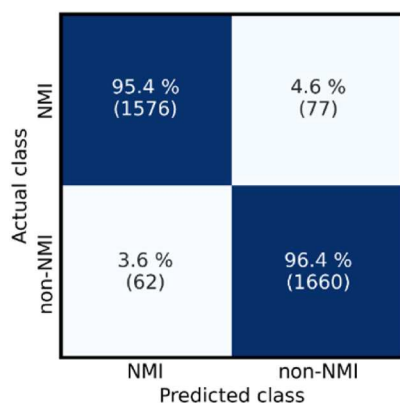
Fig. 11. Confusion matrix with absolute and relative values for classification level 1 after evaluation of the test set.
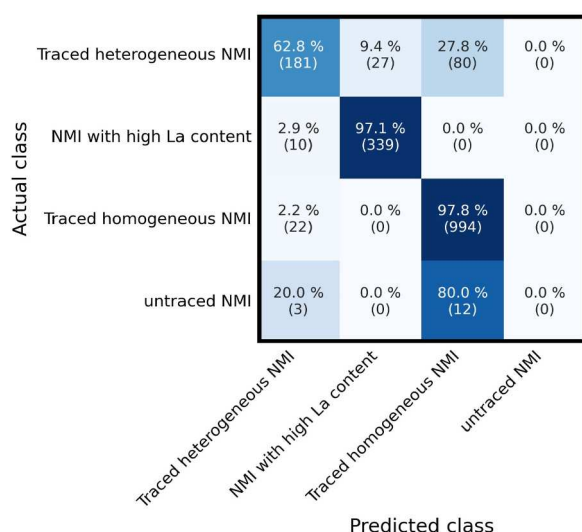

Fig. 12. Confusion matrix with absolute and relative values for classification level 2 after evaluation with the test dataset.

relative and absolute mean values. Traced homogeneous NMIs and NMIs with high La content were predicted with a precision of approximately 97 %, representing the classes with the best results. Traced heterogeneous NMIs were correctly classified in 62.7 % of the cases. An amount of 27.8 % was predicted as traced homogeneous NMI and 9.4 % as NMI with high La content. The RFC completely neglected the untraced NMIs, resulting in 0 % correct predictions.

Table 4 lists the calculated precision, recall as well as the F1-score (Equation (2)) of each class for a more in-depth analysis. Precision and recall values for the traced homogeneous NMIs and the NMIs with high La content were above 90 %. The classification of traced heterogeneous NMIs resulted in a precision of 62.7 % and a recall of 84.0 %,

Table 4
Precision, recall, and F1-score with 95 % confidence interval for each class of classification level 2.

Class	Precision [%]	Recall [%]	F1-score
Traced homogeneous NMI	97.9 (96.9, 98.9)	91.5 (90.5, 92.5)	0.941 (0.931, 0.951)
Traced heterogeneous NMI	62.7 (61.7, 63.7)	84.0 (83.0, 85.0)	0.718 (0.708, 0.728)
NMI with high La content	97.1 (96.1, 98.1)	92.5 (91.5, 93.5)	0.947 (0.937, 0.957)
Untraced NMI	0	0	–

whereas not any of the untraced inclusions got classified correctly.

4. Discussion

4.1. Manual evaluation

The density of detected particles without any correction was 66.7 Nr/mm^2. Due to the removal of artifacts in the first evaluation step, 14.5 % of the detected particles were sorted out as matrix, grinding/polishing residue or because of a missing non-metallic bonding partner. The highest number of rejected data was categorized as detected matrix with about 7.7 % of all particles. The reason for the high proportion of matrix is scratches in the steel sample that occur darker than the matrix in BSE images due to topographical differences on the sample surface. The grinding or polishing residues' second largest group of rejected data was mainly SiO_2 NMIs and amounted to 2.8 % of the detected particles.

Even though the overall evaluation error decreased by approximately 10 %, split NMIs still got overlooked by the recombination tool if the merging condition was not fulfilled. Furthermore, recombination led to additional deviations from the real inclusion state if the merging condition was wrongly considered to be true for nearby particles. The calculated error considers the number of NMIs before and after recombination and, therefore, is not able to describe the remaining deviation from the actual inclusion population. Only time-consuming manual validation by looking at every single BSE image with the measured particles enables the correct evaluation of REE-traced heterogeneous multiphase NMIs. Nevertheless, the error between the corrected data from the recombination tool and the actual number of NMIs in the investigated sample is negligible, with about 1.5 Nr/mm^2 in the case of the main inclusion type, Al_2O_3.

At the subsequent NMI classification, it turned out that mainly La-traced Al_2O_3 particles had formed in the steel caused by Al-deoxidation and the following tracer addition. The overall tracing rate for all inclusion types was over 95 % since the main type of inclusion was alumina, with a tracing rate of over 99 %. The reason for the high tracing rate was the considerable amount of REEs (162 mg per 300 g melt) compared to the previous studies on an industrial scale with 10 kg La per 240 t steel [5] or 8 kg Ce per 210 t steel [37], and lower losses due to prevention of oxidation of La.

After recombination and classification, it was found that the most significant error occurred for Al_2O_3 inclusions with 147 wrongly combined NMIs in the measured sample area of approximately 100 mm^2. The reason for this discrepancy is especially the higher number of marked alumina inclusions compared to other NMI types. A value of approximately 0.25 overlooked NMIs per mm^2 for the types of MA-spinel and $CaO·Al_2O_3·MgO$ gives a total number of 25 on the scanned sample area. The occurring deviation can be considered as negligibly small.

Since manual data evaluation is time-consuming and additional human errors cannot be entirely avoided, computer vision was applied in an attempt to decrease the resulting evaluation error.

4.2. Evaluation with AI

The tracer experiment evaluation with AI necessitates data preprocessing, including the extraction of particles using OpenCV. The additionally detected ROIs compared to the automated SEM/EDS measurement, roughly 58 %, were counted as artifacts in classification level 1. Increasing the minimum area of the extracted bounding box leads to a lower number of additional detections but also enhances the risk that particles are overlooked. The considered approach follows the condition that every ROI detected during the automated SEM/EDS analysis with AZtec also needs to be identified during the data preprocessing with OpenCV.

A two-stage classification enables independent finetuning of the AI model's thresholds and hyperparameters in every classification step

based on specific requirements. However, the prediction error made by the model in the first classification also results in misclassifications during the second step. Incorrectly determined NMIs by the first model, originally artifacts, are classified by the second model as one of the four morphological classes. The calculation of the performance metrics from the level 2 classification did not include the generated error from the first level. Regarding the NMI and non-NMI classification, the trained RFC correctly predicted 96.4 % of all artifacts. Only a small proportion of images that are misclassified as NMIs would be fed into the second classification, causing additional prediction errors. The adjusted threshold using the maximum Youden-Index represents a good tradeoff between the true positive rate (relative number of actual NMIs that are detected as NMI by the model; should be maximized) and the false positive rate (relative number of artifacts that are wrongly classified as NMI; should be minimized). A more conservative approach considers it to increase the classification threshold for the NMI class, which results in the model being more sensitive to NMI predictions. The raised threshold leads to an overall lower number of images classified as NMIs (lower recall), but the precision increases and therefore, the dragged error into the second classification minimizes. The approach chosen depends on how critical the appearing error made by the model is for the metallurgist and what type of mistake is the least problematic. It should be aimed for a high recall when using AI in combination with the manual evaluation, whereas a more conservative approach with a high precision should be chosen for a standalone AI application. Ultimately, the optimization choice must be discussed for each evaluation individually.

In the level 2 classification, traced homogeneous NMIs and NMIs with high La content were predicted very accurately with a precision of over 97 % and a recall between 91 % and 92 %. However, a substantial amount of error, 37.2 %, occurred for traced heterogeneous NMIs. Untraced particles were not even considered due to the very low number, exactly 41, of available images. The same argument cannot be made for the heterogeneous class with a high number of 896 instances. Although the overall number of correctly classified traced heterogeneous NMIs was relatively high, with a recall of 84.0 %, the number of correct cases only reached 62.7 % when the RFC predicted this class for an image. The main type of error for the traced heterogeneous NMIs was a misclassification with the homogeneous class. Heterogeneous particles differ in their appearance by showing different distinct white (high La content) and dark (high Al and O content) areas. In some cases, heterogeneous NMIs show mainly dark and few white areas as well as vice-versa. One possible explanation for the high classification error is that heterogeneous NMIs with a distinct dark area and only small white parts look similar to homogeneous NMIs, which are characterized by a low gray value, leading to incorrect predictions. The same can be stated for heterogeneous NMIs with a strongly distinct white area and the occurred misclassifications as NMI with high La content. Further in-depth image analysis must be done to understand the RFC's classification behavior better. Optimizations regarding the pre-defined morphological classes represent a possible improvement potential for better classification results. More data, especially for untraced NMIs, are essential for balancing the class distribution. Additionally, the heterogeneous traced NMI class needs to be defined more precisely, including splitting up into more subclasses, for example, Al_2O_3 dominated, even distinct areas, and La dominated.

Furthermore, using a one-vs-rest strategy, in which the four-class classification problem is split into four binary classifications by training four different RFCs, would also be a possible option. The four models are more tunable regarding their classification thresholds, whereas each value can be adjusted independently for the corresponding class.

Further model limitations are set by experimental conditions and settings during the automated SEM/EDS analysis. The generalizability of the data is not given due to the following facts: If the steel sample production varies, for example, due to different cooling conditions, the NMI

morphology changes compared to trials carried out in the Tammann furnace, as it was done for this work. In addition, different image calibration settings at the SEM, adjusted through contrast and brightness, hugely affect the representation of NMIs in the BSE images [28] and, therefore, need to be set up as precisely as possible to the described settings. However, a subjective influence remains during the image calibration by the SEM user. A larger dataset with images from more steel samples also needs to be considered to reduce potential data bias toward the used sample.

5. Conclusion and outlook

The focus of this study was the implementation of AI as steel cleanness evaluation tool, extending results of manual evaluation for actively traced non-metallic inclusions with morphology predictions. The main findings concerning the comparison of manual and AI-based data evaluation can be summarized as follows.

1. Recombination is a needed additional correction step for REE-traced NMIs during manual data evaluation. This evaluation step is mandatory since heterogeneous multiphase NMIs must be detected by double-threshold scan due to their different gray values in the BSE image. Without recombination, an error of about 10 % occurred.
2. Although recombination is necessary, the tool used generates a small error because individual NMIs, which are too close in distance to each other, wrongly fulfill the underlying recombination condition. 147 alumina inclusions, the main NMI type in the investigated steel, per scanned sample area (~100 mm^2) were recombined incorrectly.
3. The RFC used for the NMI/non-NMI classification showed a high accuracy of over 95 % and hence, can be adapted as a correction step for the subsequent morphology-based classification. The classification threshold must be chosen according to the metallurgist's individual definition of the impact of the appearing error.
4. For classification level 2, the trained RFC accurately predicted homogeneous NMIs and NMIs with high La content within the described limitations, achieving a precision of over 90 %. However, the results of traced heterogeneous NMIs must be taken with cautious because of a higher prediction error of 37.2 %. Untraced NMIs were neglected by the random forest classifier due to the low number of available images.
5. While the time-saving aspect is advantageous for the AI-based evaluation, it currently cannot fully replace the manual approach. Until further enhancements, the application is limited as an additional tool for steel cleanness evaluation to describe the morphology of actively traced NMIs. However, with further in-depth data analysis, as well as an improved dataset and training strategies, AI appears to be a very promising tool to support manual evaluation in future.

The next evaluation step of the AI-based inclusion investigation lies in the determination of the elapsed reaction time between REEs and deoxidation products as well as the recovery rate of REEs by analyzing their morphology and gray value.

Declaration of competing interest

The authors declare that they have no known competing financial interests or personal relationships that could have appeared to influence the work reported in this paper.

Acknowledgements

Appendices.

For a more in-depth explanation of the mentioned performance metrics refer to Ref. [38], regarding the micro-averaged F1-score to Ref. [35].
Accuracy: Ratio of correct predictions over the total number of instances.

$$Accuracy = \frac{TP + TN}{TP + FP + TN + FN} \qquad \text{(Equation 1)}$$

TP True Positives: Number of samples correctly predicted as positive.
FP False Positives: Number of samples wrongly predicted as positive.
TN True Negatives: Number of samples correctly predicted as negative.
FN False Negatives: Number of samples wrongly predicted as negative.
F1-score: Calculated as the harmonic mean of the precision and recall scores. It ranges from 0 to 100 %, with higher values resulting in a better classifier.

$$F1score = \frac{2 \bullet Precision \bullet Recall}{Precision + Recall} \qquad \text{(Equation 2)}$$

Precision (Equation (7)).
Recall (Equation (8)).
Micro-averaged F1-score: A single summary measure used for multiclass classifications.

$$Microaveraged\ F1score = \frac{2 \bullet microa.\ Precsision \bullet microa.\ Recall}{microa.\ Precsision + microa.\ Recall} \qquad \text{(Equation 3)}$$

Micro-a. Precision Micro-averaged Precision (Equation (4)).
Micro-a. Recall Micro-averaged Recall (Equation (5)).
Micro-averaged Precision:

$$Microaveraged\ Precision = \frac{\sum_{i=1}^{r} TP_i}{\sum_{i=1}^{r}(TP_i + FP_i)} \qquad \text{(Equation 4)}$$

r number of classes.
TP_i True positives of the i-th class.
FP_i False positives of the i-th class.
Micro-averaged Recall

$$Microaveraged\ Recall = \frac{\sum_{i=1}^{r} TP_i}{\sum_{i=1}^{r}(TP_i + FN_i)} \qquad \text{(Equation 5)}$$

r number of classes.
TP_i True positives of the i-th class.
FN_i False negatives of the i-th class.
Youden-index: Used to define the optimal classification threshold.

$$YoudenIndex = TPR - FPR \qquad \text{(Equation 6)}$$

TPR True positive rate (Equation (10)).
FPR False positive rate (Equation (9)).
Precision: The ratio of correctly predicted cases from the total predicted cases in the positive class.

$$Precision = \frac{TP}{TP + FP} \qquad \text{(Equation 7)}$$

TP True Positives: Number of samples correctly predicted as positive.
FP False Positives: Number of samples wrongly predicted as positive.
Recall: The ratio of correctly predicted cases for the positive class.

$$Recall = \frac{TP}{TP + TN} \qquad \text{(Equation 8)}$$

TP True Positives: Number of samples correctly predicted as positive.
TN True Negatives: Number of samples correctly predicted as negative.
False Positive Rate: Number of negative instances that are wrongly detected as positive by the model (false alarm rate).

$$False\ Positive\ Rate = \frac{FP}{FP + TN} \qquad \text{(Equation 9)}$$

FP False Positives: Number of samples wrongly predicted as positive.
TN True Negatives: Number of samples correctly predicted as negative.
True Positive Rate: Number of positive instances that are accurately detected as positive by the model.

$$True\ Positive\ Rate = \frac{TP}{TP + FN} \qquad \text{(Equation 10)}$$

TP True Positives: Number of samples correctly predicted as positive.

FN False Negatives: Number of samples wrongly predicted as negative.

References

[1] Li SX. Effects of inclusions on very high cycle fatigue properties of high strength steels. Int Mater Rev 2012;57(2):92–114. https://doi.org/10.1179/1743280411Y.0000000008.

[2] Ray A, Paul S, Jha S. Effect of inclusions and microstructural characteristics on the mechanical properties and fracture behavior of a high- strength low- alloy steel. JMEP 1995;4(6):679–88. https://doi.org/10.1007/BF02646444.

[3] Tervo H, Kaijalainen A, Pikkarainen T, Mehtonen S, Porter D. Effect of impurity level and inclusions on the ductility and toughness of an ultra-high-strength steel. Mater Sci Eng, A 2017;697:184–93. https://doi.org/10.1016/j.msea.2017.05.013.

[4] Wang L, Xin J, Cheng L, Zhao K, Sun B, Li J, et al. Influence of inclusions on initiation of pitting corrosion and stress corrosion cracking of X70 steel in near-neutral pH environment. Corrosion Sci 2019;147:108–27. https://doi.org/10.1016/j.corsci.2018.11.007.

[5] Burty M, Dunand P, Ritt JP, Soulard H, Blanchard A, Jeanne G, et al., editors. Control of DWI steel cleanness by lanthanum tracing of deoxidation inclusions, ladle slag treatment and a methodical approach; 1997.

[6] Gao S, Wang M, Guo J, Wang H, Zhi J, Bao Y. Characterization transformation of inclusions using rare earth Ce treatment on Al-killed titanium alloyed interstitial free steel. steel research int 2019;90(10):1900194. https://doi.org/10.1002/srin.201900194.

[7] Zhang LF. Indirect methods of detecting and evaluating inclusions in steel-A review. J Iron Steel Res Int 2006;13(4):1–8. https://doi.org/10.1016/S1006-706X(06)60067-8. 13.

[8] Zhao B, Wu W, Zhi J, Su C, Zhang J. Study on the formation mechanism of clogging layer of rare earth microalloyed Q355 steel's submerged entry nozzle and process optimization. Ironmak Steelmak 2023;50(7):782–93. https://doi.org/10.1080/03019233.2023.2185738.

[9] Liang W, Li J, Lu B, Zhi J, Zhang S, Liu Y. Analysis on clogging of submerged entry nozzle in continuous casting of high strength steel with rare earth. J Iron Steel Res Int 2022;29(1):34–43. https://doi.org/10.1007/s42243-021-00637-8.

[10] Thiele K, Presoly P, Ernst D, Babu SR, Michelic SK. Evaluation of different alloying concepts to trace non-metallic inclusions by adding rare earths on a laboratory scale. Ironmak Steelmak 2023;50(5):507–16. https://doi.org/10.1080/03019233.2022.2124816. Vol.32.

[11] Li B, Zhu H, Zheng Z, Chen J, Zhao J. Modification of nonmetallic inclusions by Ti and La complex treatment in high-Al transformation-induced plasticity steel. steel research int 2023;94(6). https://doi.org/10.1002/srin.202200566.

[12] Wang Y, Li C, Wang L, Xiong X, Chen L, Zhuang C. Modification of alumina inclusions in SWRS82B steel by adding rare earth cerium. Metals 2020;10(12):1696. https://doi.org/10.3390/met10121696.

[13] Ren Q, Hu Z, Cheng L, Kang X, Cheng Y, Zhang L. Modification mechanism of lanthanum on alumina inclusions in a nonoriented electrical steel. steel research int 2022;93(10):2200212. https://doi.org/10.1002/srin.202200212.

[14] Luo S, Shen Z, Yu Z, Wang W, Zhu M. Effect of Ce addition on inclusions and grain structure in gear steel 20CrNiMo. steel research int 2021;92(3):2000394. https://doi.org/10.1002/srin.202000394.

[15] Ren Q, Zhang L. Effect of cerium content on inclusions in an ultra-low-carbon aluminum-killed steel. Metall Mater Trans B 2020;51(2):589–600. https://doi.org/10.1007/s11663-020-01779-y.

[16] Pan C, Hu X, Lin P, Chou K. Evolution of inclusions after cerium and titanium addition in aluminum deoxidized Fe-17Cr-9Ni austenitic stainless steel. ISIJ Int 2020;60(9):1878–85. https://doi.org/10.2355/isijinternational.ISIJINT-2020-028.

[17] Suzuki S. Present status of microstructural characterization of steel by analytical methods. ISIJ Int 2002;42(Suppl):S93–100. https://doi.org/10.2355/isijinternational.42.Suppl_S93.

[18] Kaushik P, Pielet H, Yin H. Inclusion characterisation - tool for measurement of steel cleanliness and process control: Part 1. Ironmak Steelmak 2009;36(8):561–71.

[19] Zhang L, Thomas B. State of the art in evaluation and control of steel cleanliness. ISIJ Int 2003;43(3):271–91.

[20] Mayerhofer A. Enhanced characterization of non-metallic inclusions for (sub) micro steel cleanness evaluations [Ph.D]. Leoben, Austria: Montanuniversitaet Leoben; 2021.

[21] Schickbichler M, Ramesh Babu S, Hafok M, Turk C, Schneeberger G, Fölzer A, et al. Comparison of methods for characterising the steel cleanness in powder metallurgical high-speed steels. Powder Metall 2023:1–17. https://doi.org/10.1080/00325899.2023.2170848.

[22] Biyik S. Characterization of nanocrystalline Cu25Mo electrical contact material synthesized via ball milling. Acta Phys Pol, A 2017;132(3-II):886–8. https://doi.org/10.12693/APhysPolA.132.886.

[23] Biyik S, Aydin M. The effect of milling speed on particle size and morphology of Cu25W composite powder. Acta Phys Pol, A 2015;127(4):1255–60. https://doi.org/10.12693/APhysPolA.127.1255.

[24] Kaushik P, Lehmann J, Nadif M. State of the art in control of inclusions, their characterization, and future requirements. Metall Mater Trans B Process Metall Mater Process Sci 2012;43(4):710–25. https://doi.org/10.1007/s11663-012-9646-2.

[25] Meng Y, Yan C, Yang X, Ju X. A statistical analysis on the complex inclusions in rare earth element treated steel. ISIJ Int 2020;60(3):534–8. https://doi.org/10.2355/isijinternational.ISIJINT-2019-428.

[26] Thiele K, Musi R, Ramesh Babu S, Michelic SK. Optimization of the two- and three-dimensional characterization of rare earth-traced deoxidation products. Adv Eng Mater 2023:2201748. https://doi.org/10.1002/adem.202201748.

[27] Abdulsalam M, Gao N, Webler BA, Holm EA. Prediction of inclusion types from BSE images: RF vs. CNN. Front. Mater. 2021;8. https://doi.org/10.3389/fmats.2021.754089.

[28] Ramesh Babu S, Musi R, Thiele K, Michelic SK. Classification of nonmetallic inclusions in steel by data-driven machine learning methods. Steel Res Int 2023;94(1):2200617. https://doi.org/10.1002/srin.202200617.

[29] Dorrer P, Michelic SK, Bernhard C, Penz A, Rössler R. Study on the influence of FeTi-addition on the inclusion population in Ti-stabilized ULC steels and its consequences for SEN-clogging. Steel Res Int 2019;90(7):1800635. https://doi.org/10.1002/srin.201800635.

[30] Bradski G. The OpenCV library. Dr. Dobb's Journal of Software Tools120; 2000. p. 122–5.

[31] Musi R. Influence of different hyperparameter settings and data preprocessing methods on the classification of nonmetallic inclusions with machine learning algorithms [master thesis]. Leoben: Montanuniversität Leoben; 2023.

[32] Scikit-learn: machine learning in Python. 2011.

[33] Luo W, Phung D, Tran T, Gupta S, Rana S, Karmakar C, et al. Guidelines for developing and reporting machine learning predictive models in biomedical research: a multidisciplinary view. J Med Internet Res 2016;18(12):e323. https://doi.org/10.2196/jmir.5870.

[34] Bentéjac C, Csörgő A, Martínez-Muñoz G. A comparative analysis of gradient boosting algorithms. Artif Intell Rev 2021;54(3):1937–67. https://doi.org/10.1007/s10462-020-09896-5.

[35] Takahashi K, Yamamoto K, Kuchiba A, Koyama T. Confidence interval for micro-averaged F1 and macro-averaged F1 scores. Appl Intell 2022;52(5):4961–72. https://doi.org/10.1007/s10489-021-02635-5.

[36] Ruopp MD, Perkins NJ, Whitcomb BW, Schisterman EF. Youden Index and optimal cut-point estimated from observations affected by a lower limit of detection. Biom J 2008;50(3):419–30. https://doi.org/10.1002/bimj.200710415.

[37] Geng R, Li J, Shi C. Evolution of inclusions with Ce addition and Ca treatment in Al-killed steel during RH refining process. ISIJ Int 2021;61(5):1506–13. https://doi.org/10.2355/isijinternational.ISIJINT-2020-672.

[38] Hossin M, Sulaiman MN. A review on evaluation metrics for data classification evaluations. IJDKP 2015;5(2):1–11. https://doi.org/10.5121/ijdkp.2015.5201.

7.3 REE-Fingerprint – a passive tracing technique

Paper V: <u>K. Thiele</u>, S. Ilie, R. Rössler, C. Walkner, T. Meisel, T. Prohaska and S.K. Michelic, Different Approaches to Trace the Source of Non-Metallic Inclusions in Steel. Iron & Steel Technology 20 (2023), 7. doi:10.33313/TR/0723.

Paper VI: <u>K. Thiele</u>, C. Truschner, C. Walkner, T.C. Meisel, S. Ilie, R. Rössler and S.K. Michelic, Investigating the Origin of Non-Metallic Inclusions in Ti-Stabilized ULC Steels Using Different Tracing Techniques. Metals 14 (2024), 1, pp. 103. doi:10.3390/met14010103.

The two publications, **Papers V** and **VI** are focused on identifying the source of the clogging layer and mesoscopic NMIs by using the REE-Fingerprint, a novel tracing technique in metallurgy. **Papers V** and **VI** were published in **Iron & Steel Technology** and **Metals**, respectively.

Different Approaches to Trace the Source of Non-Metallic Inclusions in Steel
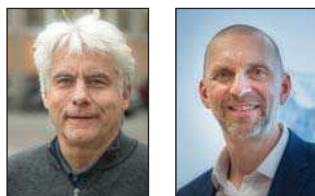
Improvement of steel cleanness requires detailed knowledge about the formation of non-metallic inclusions. Tracing inclusions and potential sources is an effective tool for studying inclusion evolution. In this article, two tracing approaches are evaluated. First, classical tracer experiments are performed, where rare earth elements (REE) like lanthanum or cerium are deliberately added to the melt on an industrial scale to mark the inclusions directly. Second, the natural REE multi-element fingerprint of the inclusions is compared to the REE multi-element pattern of potential sources such as alloying and auxiliary materials. These REE distribution profiles are interpreted by normalizing the REE fractions to reference values. REE contents are analyzed by inductively coupled plasma mass spectrometry in all cases. Both approaches are applied to track the source of clogged material in the submerged-entry nozzle (SEN) from Ti-alloyed ultralow-carbon (Ti-ULC) steel production. Results show a clear connection between inclusions resulting from deoxidation and the clogged layer in the SEN.

Steel cleanness is an essential quality criterion for a wide range of different steel grades. Steels can be sensitive regarding cleanness in terms of final product properties and process stability, e.g., the occurrence of clogging during continuous casting. Titanium-alloyed ultralow-carbon (Ti-ULC) steels used for automotive body part applications in particular show an increased clogging tendency and have been a subject of research for several years.[1–4] Four main mechanisms are described in the literature to explain the appearance of clogging. In many cases, the agglomeration of deoxidation products and their subsequent attachment to the nozzle wall by fluid flow and interfacial tension effects are predominant.[5] Detailed knowledge about inclusion formation and modification over the production process is essential to understand and control clogging.

One promising approach to study the reactions and interaction between steel, slag, inclusions and refractory over different process steps is tracing, which means the specific "marking" of particles and/or other phases (slags, refractories, auxiliaries...) in steelmaking. Different tracing concepts have already been investigated in the field of metallurgy in the past:

- The deliberate addition of tracer elements to the steel-slag-inclusion system: Rare earth metals are especially suited to trace inclusions formed during deoxidation due to their high oxygen affinity. Rare earth elements (REEs) lanthanum and cerium have already been

Authors

Kathrin Thiele (top row, left), Ph.D. Candidate, Christian Doppler Laboratory for Inclusion Metallurgy in Advanced Steelmaking, Chair of Ferrous Metallurgy, Montanuniversität Leoben, Leoben, Austria (kathrin.thiele@unileoben.ac.at); Sergiu Ilie (top row, right), Research and Development Steel Plant Technical Department Business Unit Slab, voestalpine Stahl GmbH, Linz, Austria (sergiu.ilie@voestalpine.com); Roman Rössler (second row, left), Research and Development Steel Plant Technical Department Business Unit Slab, voestalpine Stahl GmbH, Linz, Austria (roman.roessler@ voestalpine.com); Christoph Walkner (second row, right), Senior Lecturer, Montanuniversität Leoben, Leoben, Austria (christoph.walkner@unileoben.ac.at); Thomas C. Meisel (third row, left), Associate Professor/Analytical Geochemist, Montanuniversität Leoben, Leoben, Austria (thomas.meisel@unileoben.ac.at); Thomas Prohaska (third row, right), Full Professor for Analytical Chemistry, Montanuniversität Leoben, Leoben, Austria (thomas.prohaska@unileoben.ac.at); Susanne K. Michelic (bottom), Associate Professor and Head, Christian Doppler Laboratory for Inclusion Metallurgy in Advanced Steelmaking, Montanuniversität Leoben, Leoben, Austria (susanne.michelic@unileoben.ac.at)

Figure 1
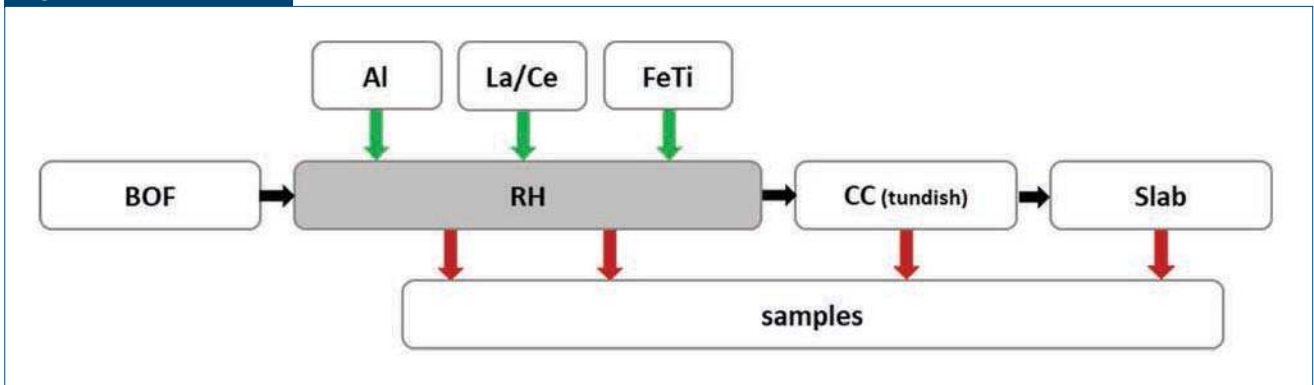
Test procedure for tracing with rare earth elements (REEs) in industry.

applied as potential tracers in this case, as has barium.[6,7]

- The comparison of stable oxygen isotope ratios: Infrared laser fluorination combined with gas mass spectrometry is performed to determine the oxygen isotope composition of inclusions causing clogging and comparing them with possible oxygen sources such as refractory materials, slags and atmospheric oxygen.[8, 9]

Besides these approaches already well-known for metallurgical applications, another promising method exists, which is successfully applied in geochemistry, archeology or food chemistry: Using natural rare earth fingerprints.[10–12] This approach aims to track the source of non-metallic inclusions in steel by determining a fingerprint based on the distribution pattern of REEs in inclusion specimens and potential precursor materials. No deliberate addition of REEs is done in this case.

This article highlights two different approaches tracking the source of non-metallic inclusions observed in the clogged network of a submerged-entry nozzle (SEN) from Ti-ULC production. On the one hand, deoxidation products are traced during the industrial process and tracked until casting. In this case, the main focus was on the possible reaction of REEs with deoxidation products, the separation behavior of non-metallic inclusions in the tundish and mold, and finally, their deposition in the flow control system of the caster. On the other hand, the natural elemental fingerprint of the clog is compared with different potential source materials during steelmaking. Here, potential sources that contribute to forming a clogging layer

should be identified. The main aim of both approaches was to clarify the role of deoxidation products in the clogging deposit built up for Ti-ULC steels.

Addition of Rare Earth Elements

The tracing principle by specific addition of REE in secondary metallurgy is based on their high oxygen affinity. Compared to manganese, silicon or aluminum oxides, rare earths, such as lanthanum and cerium, have a higher negative free Gibbs energy, resulting in more stable oxides than classical deoxidation products Al_2O_3 or SiO_2. An example of a proceeding reaction is given in Eq. 1.

Figure 2
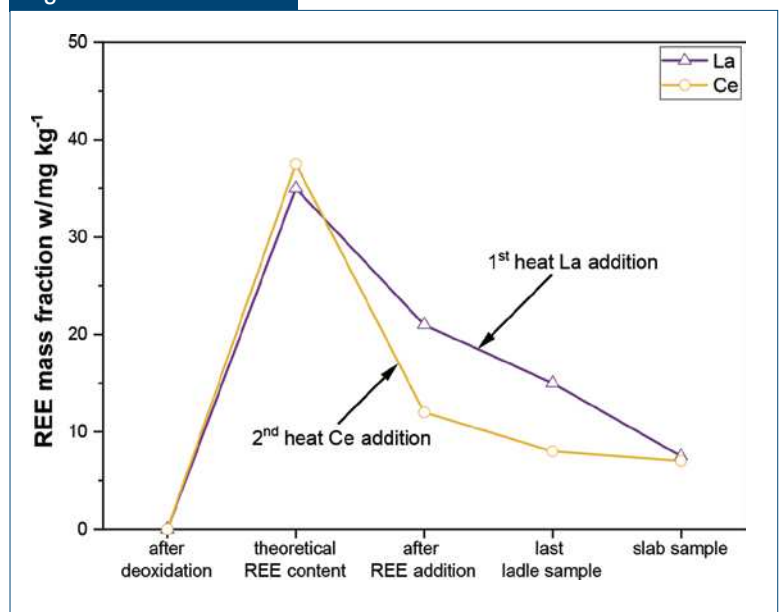
Change of La and Ce content in the steel samples over the different process steps.

Figure 3
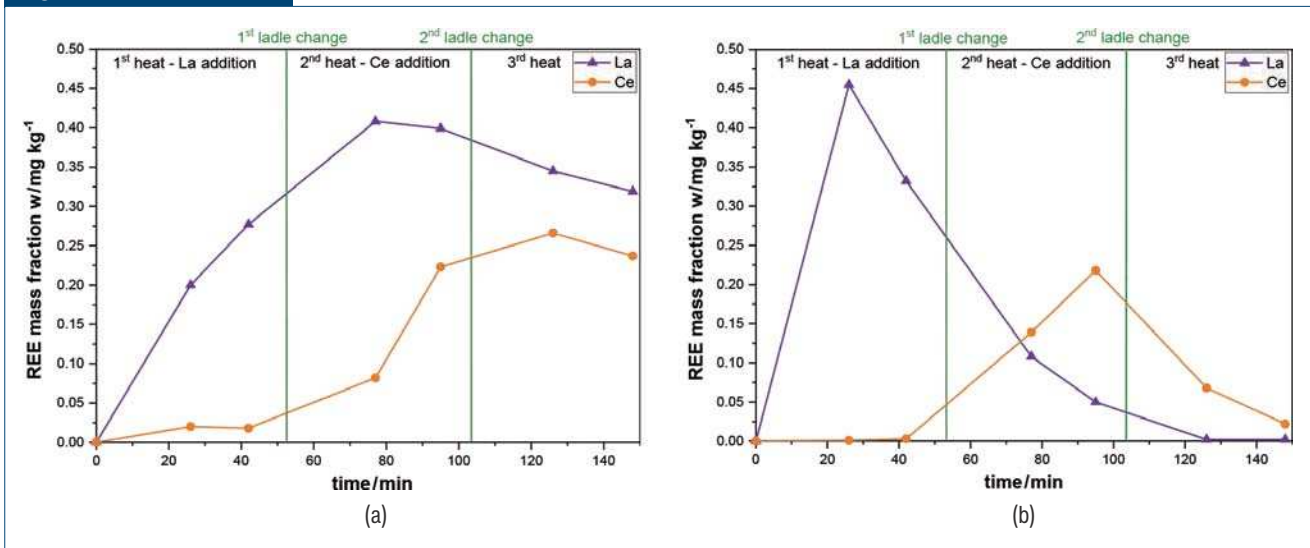
La and Ce content change in the tundish slag (a) and the mold slag (b) over time.

$$2Al_2O_3 + 2La \quad La_2O_3 \square Al_2O_3 + 2Al$$

(Eq. 1)

Fig. 1 illustrates the industrial process route for Ti-ULC steel production and indicates the alloying and sampling steps performed during the tracer experiment. The REE were added after the aluminum deoxidation in metallic form in the Ruhrstahl Heraeus (RH) degasser. The first heat was traced with La, the second heat with Ce, and the third heat was a standard one without addition. After the third heat, the SEN was replaced. Steel samples were taken before and after the alloying in the ladle, in the tundish, and finally in the slab. The chemical composition was analyzed by optical emission spectrometry (OES) and inductively coupled plasma mass spectrometry (ICP-MS). Slag samples were taken every 30 minutes from the tundish and mold. Slag samples were analyzed using x-ray fluorescence analysis (XRF) and wet chemistry. The close-meshed sampling in steel and slag allows the observation of REE distribution over the process time.

The development of La and Ce content from their addition after deoxidation until the slab sample is illustrated in Fig. 2. The theoretical REE content w was about 40 mg kg^{-1}, but the real measured content in the steel was less than 20 mg kg^{-1} due to combustion. Figs. 3a and 3b demonstrate the La and Ce distribution in the tundish and mold slag. Comparing the La and Ce distribution in steel and slag, a clear interaction between the two phases is determined: While both La and Ce continuously decrease in the steel, their content increases in the slag samples over time (for heat 1 and 2) and decreases again for heat 3 where no REE had been added.

Figure 4
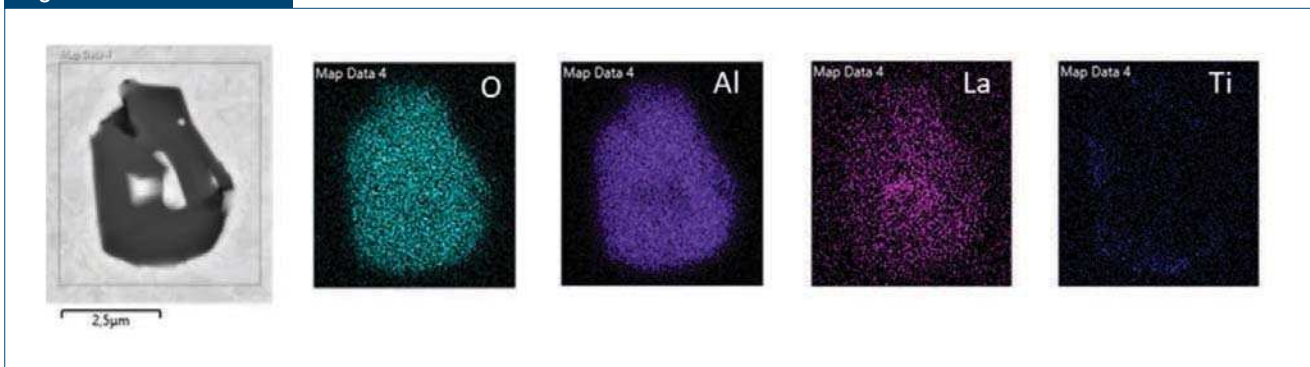
Scanning electron microscope (SEM) image and elemental mapping of a La-traced non-metallic inclusion.

Figure 5
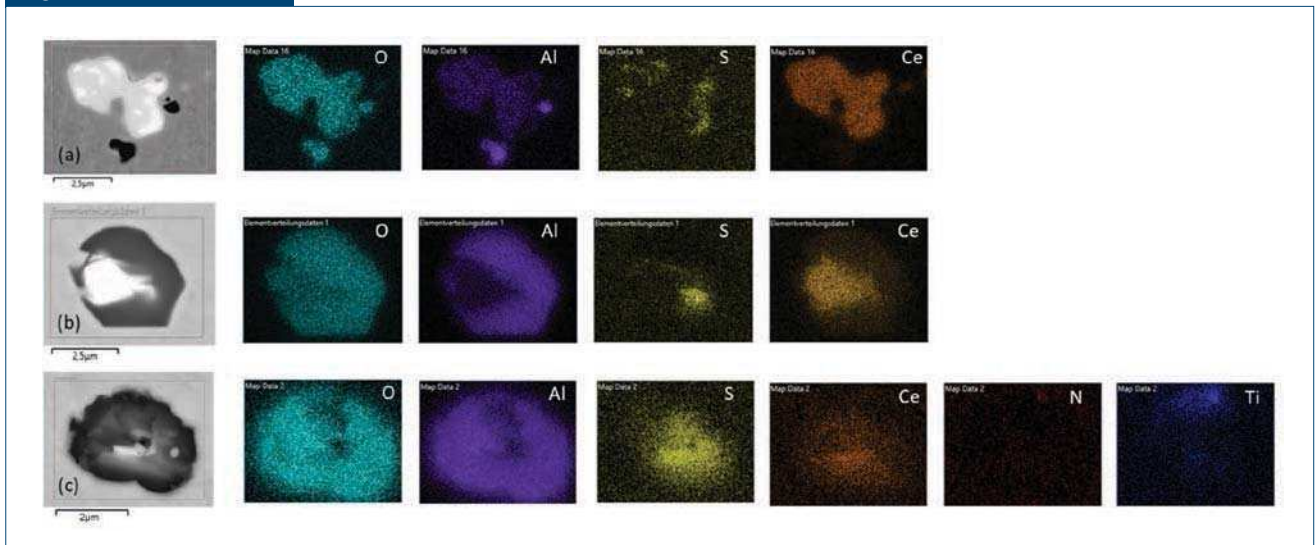
SEM images and elemental mappings of Ce-traced non-metallic inclusions at different stages: after REE addition (a), last ladle sample (b), and slab sample (c).

Manual and automated scanning electron microscope/energy-dispersive x-ray spectroscope (SEM/EDS) measurements have been done for all steel samples to characterize the non-metallic inclusions. The analyses revealed that a significant amount of deoxidation products were traced with REE in each sample. Most Al_2O_3 inclusions were marked with a small amount of La or Ce. No pure La_2O_3 or Ce_2O_3 were found. Some examples of detected non-metallic inclusions in samples from different process steps are shown in Figs. 4 and 5. Inclusions are mostly microscopic and of heterogeneous nature. Combining the results of chemical analyses and SEM/EDS measurements of inclusions, a clear tendency of inclusion separation from the steel to the slag phase is observed.

After the tracer experiment, the SEN was removed, and the clogging layer was investigated with an SEM/EDS analysis. As the elemental distribution in Fig. 6 shows, Al, La and Ce were found in all parts of the clogging layer from the first deposition until the end of casting. This is a strong indication of the essential

Figure 6
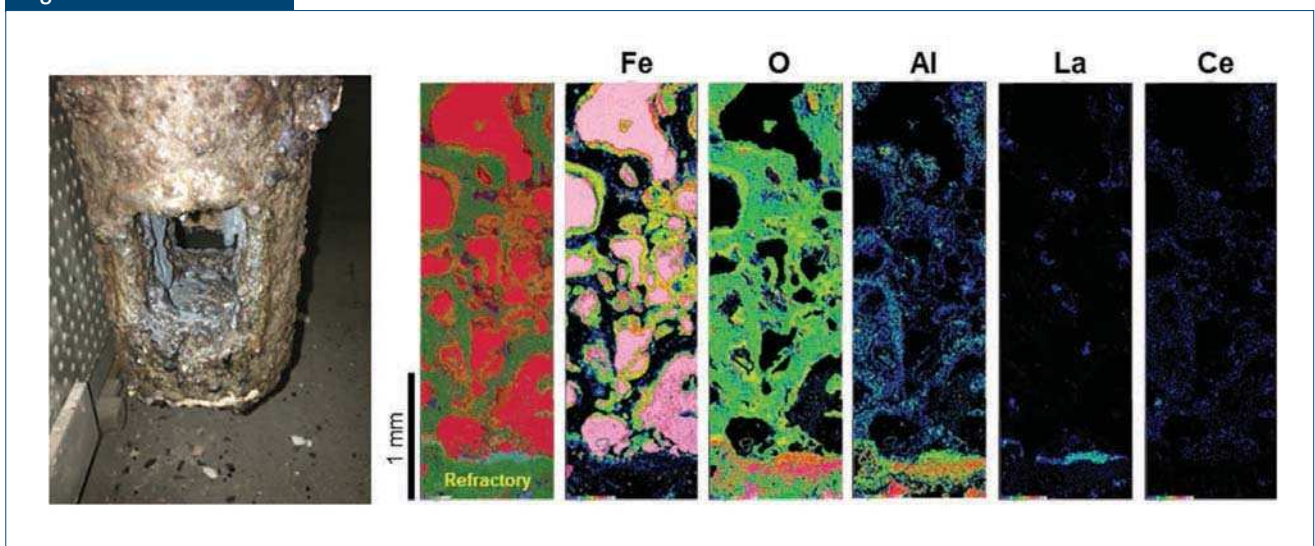
SEN after tracer experiment and energy-dispersive x-ray spectroscope (EDS) mapping of the clogging layer.

Table 1

Summary of Analyzed Samples for Rare Earth Fingerprint Comparison

ID	Sample	Method
1	Clog (SEN sample)	LA ICP-MS (5 line scans at the inner and outer side of the sample each)
2	Auxiliary I (covering agent)	ICP-MS analysis after sinter digestion with Na_2O_2
3	Auxiliary II (sliding gate sand)	ICP-MS analysis after sinter digestion with Na_2O_2
4	Al granules	ICP-MS analysis after sinter digestion with HCl
5	FeTi	ICP-MS analysis after sinter digestion with Na_2O_2
6	FeMn	ICP-MS analysis after sinter digestion with HCl
7	Refractory I	ICP-MS analysis after $LiBO_2$ fusion digestion
8	Refractory II	ICP-MS analysis after $LiBO_2$ fusion digestion
9	Refractory III	ICP-MS analysis after $LiBO_2$ fusion digestion
10	Slag	ICP-MS analysis after $LiBO_2$ fusion digestion
11	Alloying agent (lime)	ICP-MS analysis after $LiBO_2$ fusion digestion

contribution of deoxidation products, especially their agglomeration, in clogging network buildup.

Summing up, the tracer experiment on an industrial scale showed that a significant percentage of deoxidation products was successfully traced. The trials could comprehensively demonstrate the evolution of deoxidation products from their formation over their partial separation to the slag until their deposition in the SEN.

Rare Earth Elements Fingerprint

This approach uses elemental analysis methods, primarily ICP-MS and laser ablation ICP-MS, and relies on noticeable patterns in the distribution of trace elements, such as REE, in the analyzed samples. The REE or lanthanides are composed of the elements La to Lu. Due to their highly similar chemical behavior, the REE are usually analyzed and described as a group. Due to the relative content ratios of the rare earths, a specific pattern is observed for each sample, representing the particular fingerprint of a material. For easier detection of differences in the REE patterns, the REE mass fractions are usually normalized, e.g., to an average earth crust or meteorite composition.[13] This approach can be used as an "indirect tracing" for metallurgical applications. A first study was done by Walkner et al.,[14] trying to connect the appearance of macroscopic inclusions to diverse potential exogenous inclusion sources. The rare earth elemental fingerprint of a clog (SEN sample) is taken as a reference sample for the present study. Secondly, the fingerprints of different alloying elements, auxiliaries and refractory materials are compared to the reference sample. If a similar fingerprint is detected in the samples, this indicates that the respective sample has contributed to the formation of the clog (taking into account that the (trans)formation process did not alter the original pattern). Table 1 summarizes the samples examined in the present study and notes the preparation and analysis method.

Figure 7
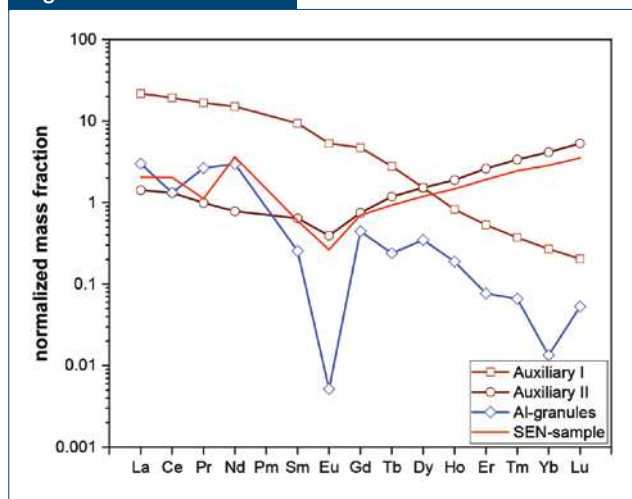
Chondrite normalized REE patterns of different auxiliaries, Al-granules and SEN sample.

Figure 8
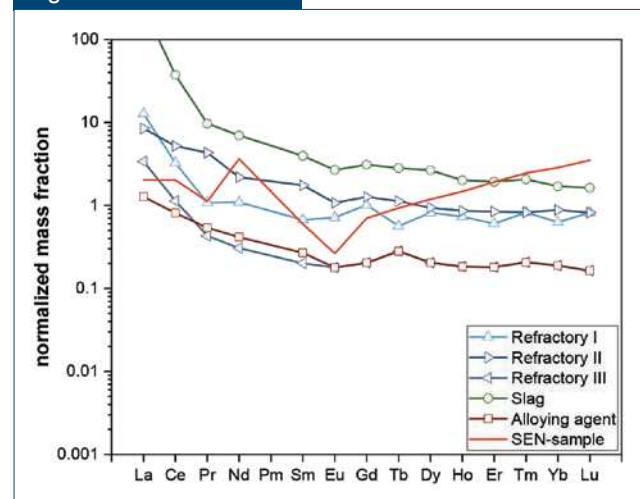
Chrondrite normalized REE patterns of different refractories, slag, alloying agents and SEN sample.

Figs. 7 and 8 summarize the natural REE distribution pattern for the different samples. All values have been normalized to chondrites in the present case.[10,15] The full red line indicates the clog in both diagrams. The clog and Al granules pattern in Fig. 7 show obvious tendencies and anomalies for Eu and Nd in both cases. Additionally, auxiliary II shows an anomaly in Eu, indicating the presence of sliding gate sand in the clog. All distributions in Fig. 8 show inconspicuous trends without any correlation to the clog. The REE contents of FeTi and FeMn were below the detection limits and are therefore not displayed in the diagrams.

Summary and Conclusions

The mechanisms behind the buildup of clogging deposits in Ti-ULC steels are still a matter of ongoing discussion. This article outlines two different tracing approaches to identify potential sources and contributors to the clogging network. First, the classical approach of specific addition of La and Ce to the liquid steel is applied to mark and track inclusion evolution from deoxidation until casting in industrial Ti-ULC production. Second, fingerprints of rare earth elements are compared between the clog and divers alloying elements, auxiliaries and refractories. Both approaches underline a clear correlation between the formed Al_2O_3 as deoxidation products and the clogged network formed inside the SEN. The findings confirm that agglomeration of deoxidation products and their subsequent deposition in the SEN is the main reason for the appearance of clogging in the production of Ti-ULC steels.

Acknowledgments

References

1. J. Lee, S-K. Kim, M-H. Kang and Y-B. Kang, "Interfacial Reaction Between Ultra-Low C Steel and Refractory Material Used for Submerged Entry Nozzle for Continuous Casting," *European Conference on Continuous Casting 9,* 2017, pp. 565–570.

2. S. Michelic, P. Dorrer, G. Kloesch, J. Reiter, A. Paul and C. Bernhard, "Study of Clogging Deposit Build-Up in Al-Killed and Ca-Treated High-Sulfur Steels With Focus," *AISTech 2017 Conference Proceedings,* 2017, pp. 1555–1565.

3. H. Barati, M. Wu, S. Michelic, S. Ilie, A. Kharicha, A. Ludwig and Y-B. Kang, "Mathematical Modeling of the Early Stage of Clogging of the SEN During Continuous Casting of Ti-ULC Steel," *Metallurgical and Materials Transactions B,* Vol. 52, No. 6, 2021, pp. 4167–4178.

4. S.K. Michelic and C. Bernhard, "Significance of Nonmetallic Inclusions for the Clogging Phenomenon in Continuous Casting of Steel — A Review," *Steel Research International,* 2022, p. 2200086.

5. S. Singh, "Mechanism of Alumina Buildup in Tundish Nozzle During Continuous Casting of Aluminium-Killed Steels," *Metall. Trans.,* Vol. 5, 1974, pp. 2165–2178.

6. M. Burty, P. Dunand, J.P. Ritt, H. Soulard, A. Blanchard, G. Jeanne, F. Penet, R. Pluquet and I. Poissonnet, eds., *Control of DWI Steel Cleanness by Lanthanum Tracing of Deoxidation Inclusions, Ladle Slag Treatment and a Methodical Approach,* 1997, pp. 647–653.

7. M.H. Song, M. Nzotta and D. Sichen, "Study of the Formation of Nonmetallic Inclusions by Ladle Glaze and the Effect of Slag on Inclusion Composition Using Tracer Experiments," *Steel Research International,* Vol. 80, No. 10, 2009, pp. 753–760.

8. C. Toulouse, A. Pack, A. Ender and S. Petry, "Stable Oxygen Isotopes for Tracing the Origin of Clogging in Continuous Casting Submerged Entry Nozzles," *Steel Research International,* Vol. 79, No. 2, 2008, pp. 149–155.

9. A. Pack, S. Hoernes, M. Göbbels, R. Bross and A. Buhr, "Stable Oxygen Isotopes — A New Approach for Tracing the Origin of Oxide Inclusions in Steels," *European Journal of Mineralogy,* Vol. 17, No. 3, 2005, pp. 483–493.

10. D. Bandoniene, D. Zettl, T. Meisel and M. Maneiko, "Suitability of Elemental Fingerprinting for Assessing the Geographic Origin of Pumpkin (Cucurbita pepo var. styriaca) Seed Oil," *Food Chemistry,* Vol. 136, No. 3-4, 2013, pp. 1533–1542.

11. D. Bandoniene, C. Walkner, F. Ringdorfer and T. Meisel, "Authentication of Meat and Dairy Products Using Rare Earth Element Labeling and Detection by Solution Based and Laser Ablation ICP-MS," *Food Research International,* Vol. 132, 2020, p. 109106.

12. T. Akagi and K. Edanami, "Sources of Rare Earth Elements in Shells and Soft Tissues of Bivalves From Tokyo Bay," *Marine Chemistry,* Vol. 194, 2017, pp. 55–62.

13. P. Henderson, *Rare Earth Element Geochemistry,* Elsevier, Amsterdam, 1984.

14. C. Walkner, J. Korp, A. Graf, J. Irrgeher, T. Meisel and T. Prohaska, "CSI Steel: Macroscopic Non-Metallic Inclusions in Steels — Identification of Sources and Causes," (in German) *CANAS — Colloquium Analytische Atomspektroskopie,* ed. TU Freiberg, 23.9-26.9.2019, CANAS, 2019.

15. J. Wasson and G. Kellemeyn, "Composition of Chondrites," *Philosophical Transactions of the Royal Society London A,* Vol. 352, 1998, pp. 535–544.

✦

AIST Transactions seeks to publish original research articles focusing on scientific or technical areas relevant to the iron and steel community. All articles are peer-reviewed by Key Reviewers prior to publication.

The scope of the **Transactions** spans all fields of iron and steel manufacturing, from extractive metallurgy to liquid metal processing, casting, thermomechanical processing as well as coating, joining/welding and machining. Articles related to structure and properties, i.e., characterization, phase transition, chemical analysis and testing of creep, corrosion or strength are accepted. In addition, papers on process control, testing and product performance are also encouraged.

The **Transactions** will publish papers on basic scientific work as well as applied industrial research work. Papers discussing issues related to specific products or systems can be considered as long as the structure follows a scientific investigation/discussion, but not for the aim of advertising or for the purpose of introducing a new product. Papers should be no longer than 5,000 words, or 12 pages including figures.

Papers will either be accepted unconditionally, conditionally based on reviewers' comments, or rejected. The review process should be completed in less than two months. Upon acceptance, authors will be asked to complete a form to transfer copyright to AIST.

A PDF proof of the accepted manuscript will be sent electronically to the author(s) approximately one month prior to publication for final approval. Reprints of published manuscripts can be ordered through AIST.

Please contact me with any questions regarding **AIST Transactions.**

P. Chris Pistorius
POSCO Professor of Materials Science and Engineering
Co-Director, Center for Iron and Steelmaking Research
Carnegie Mellon University, 5000 Forbes Ave., Pittsburgh, PA 15213 USA
Phone: +1.412.268.7248
pistorius@cmu.edu

To submit a manuscript for consideration, visit:
aist.org/publications-advertising/iron-steel-technology/aist-transactions/submit-a-manuscript

AIST Transactions are indexed through Chemical Abstracts Service, Columbus, Ohio, USA.

metals

MDPI

Investigating the Origin of Non-Metallic Inclusions in Ti-Stabilized ULC Steels Using Different Tracing Techniques

Kathrin Thiele [1,*], Christoph Truschner [2], Christoph Walkner [3], Thomas C. Meisel [3], Sergiu Ilie [2], Roman Rössler [2] and Susanne K. Michelic [1]

[1] Christian Doppler Laboratory for Inclusion Metallurgy in Advanced Steelmaking, Montanuniversitaet Leoben, Franz Josef–Straße 18, 8700 Leoben, Austria; susanne.michelic@unileoben.ac.at

[2] voestalpine Stahl GmbH, voestalpine-Straße 3, 4020 Linz, Austria; c.truschner@voestalpine.com (C.T.); sergiu.ilie@voestalpine.com (S.I.); roman.roessler@voestalpine.com (R.R.)

[3] Chair of General and Analytical Chemistry, Montanuniversitaet Leoben, Franz Josef–Straße 18, 8700 Leoben, Austria; christoph.walkner@unileoben.ac.at (C.W.); thomas.meisel@unileoben.ac.at (T.C.M.)

[*] Correspondence: kathrin.thiele@unileoben.ac.at; Tel.: +43-3842-402-2243

Abstract: Since steel cleanness comes to the fore of steel producers worldwide, it is necessary to understand the formation mechanism and modification of non-metallic inclusions (NMIs) in more detail. One central point is the identification of the source of especially interfering NMIs to prevent their evolution in the future. The present study applies two approaches to determine the source of NMIs in Ti-stabilized ultra-low carbon (ULC) steels—the active and the passive tracing. Both approaches are applied to an industrial experiment. The active tracing technique is focused on investigating the clogging layer formation in submerged entry nozzles and, hence, the origin of alumina particles. This method adds rare earth elements (REEs) directly to the melt to mark pre-existing deoxidation products at a certain point of the steelmaking process. The main concern of the passive method, the so-called REE fingerprint, is the determination of the source of mesoscopic NMIs. For the REE fingerprint, the pre-existing concentration of REEs in different potential sources and the investigated NMIs are measured by using an inductively coupled plasma mass spectrometer (ICP-MS). The resulting patterns are compared after normalizing the contents to chondrites, and the NMIs' origins are identified. Concerning the EDS analysis and the resulting patterns from the REE fingerprint, the mold slag and, respectively, the casting powder were the sources of the investigated NMIs.

Keywords: non-metallic inclusions; tracing techniques; rare earth elements; rare earth element fingerprint

1. Introduction

Steel cleanness is crucial for a wide spectrum of steel grades and is primarily defined by quantity, size, spatial distribution and the chemical composition of small particles in the steel, so-called non-metallic inclusions (NMIs) [1–3]. NMIs influence the chemical and physical properties of the final product as well as the stability of the steelmaking process [4–6]. One example of their detrimental impact is nozzle clogging during continuous casting at special steel grades, such as Ti-stabilized ultra-low carbon (ULC) steel used in the automotive industry for car body shell parts [7,8]. Of the four main clogging mechanisms, at least one, but in most cases several, always coincides with and contributes to the formation of submerged entry nozzle (SEN) clogging and, consequently, its blockage [9–12]. One of these mechanisms is the agglomeration of deoxidation products and their attachment to the SEN wall due to fluid flow and interfacial tension effects [13]. Another possible cause is reoxidation, which can occur due to air aspiration into the SEN [14]. Phenomena like SEN clogging can be comprehended by understanding how inclusions are formed and modified

during steelmaking. Tracing is a revealing tool for gaining knowledge about inclusions, which allows for marking and tracking the NMI's path throughout the production process.

This publication focuses on two different tracing approaches—active and passive tracing. The active tracing technique is already known in the steel industry [15,16]. In this method, NMIs are partially reduced due to the direct addition of rare earth elements (REEs) [17]. Several studies [18–21] have already managed to track the modification of deoxidation products, such as alumina NMIs, by adding La and Ce to the melt on industrial and laboratory scales. The benefit of this approach is the easy retrieval of REE-marked NMIs during automated scanning electron microscopy with energy dispersive X-ray spectroscopy (SEM/EDS) analysis, since REEs appear brighter than the steel matrix in backscattered electron (BSE) images due to their higher atomic number [22]. However, REEs do not only mark NMIs. They also influence their physical and chemical behaviors, such as wettability or agglomeration tendency [23–25]. Hence, finding another way to identify the origin of NMIs is beneficial.

The second technique, the REE fingerprint, is a novel approach in metallurgy but has already been applied in other research fields, such as archaeology or geo-and food chemistry [26–29]. In the latter, it is mainly utilized to determine the geographical origin of resources used since the soils of origin differ even in the same country [30]. In the REE fingerprint method, the pre-existing concentrations of lanthanoids (La to Lu) are measured by using inductively coupled plasma mass spectrometry (ICP-MS) in the materials to be examined. The concentrations are in the range of a few mg/kg and have to be normalized to a suitable reference dataset in order to facilitate the recognition of patterns. Most frequently, a dataset obtained for chondrites, which are meteoritic rocks, is used [31]. By comparing the patterns with each other, the source of, e.g., an NMI, can be determined. In contrast to active tracing, the NMIs and their properties are not influenced or modified.

Both approaches are applied in the present study to investigate the formation mechanism behind SEN clogging and the origin of mesoscopic NMIs in Ti-stabilized ULC steels. For active tracing, melts are actively marked with La and Ce on an industrial scale. Steel samples are taken at several steps of the production process to study the modification of alumina NMIs using automated SEM/EDS analysis and to identify if pre-existing deoxidation products exist in the final sample or if reoxidation occurs due to FeTi addition. For the second tracing approach, samples with mesoscopic NMIs are prepared from the traced melts. The pre-existing REE concentration of the NMIs and potential sources are measured via laser-ablation (LA) ICP-MS analysis. A match between the REE patterns that results after normalization to chondrites indicates the coherence of, e.g., an NMI and an auxiliary. Both approaches aim to clarify critical topics in steel production.

2. Materials and Methods

2.1. Active Approach

Using the active tracing technique, common NMIs in steel, especially deoxidation products, are marked by REEs to allow us to follow them over the steelmaking process. The direct addition of REEs, mainly La or Ce, after, e.g., the deoxidation of the steel melt, leads to partial reduction of the previously formed inclusions due to the higher oxygen affinity of REEs [17]. During SEM/EDS analysis, the REE-containing parts of the resulting heterogeneous multiphase NMIs appear brighter in the BSE image since REEs have a higher molar mass compared to the surrounding steel matrix. The benefit of the easier tracking of marked NMIs is also connected to the disadvantage of automated SEM/EDS analysis, since a double-threshold scan is necessary to detect not only the particles that are usually darker than the steel matrix but also the brighter ones. The subsequent data evaluation must also be optimized since the REE-containing NMIs are split into their brighter and darker parts and have to be recombined for correct measurement results [32].

2.2. Passive Approach

By using the REE fingerprint, a passive tracing technique, it is possible to analyze the source of, e.g., NMIs or determine the influence of auxiliaries on the clogging layer formation in the SEN. For this approach, the pre-existing REE contents in slags, inclusions, or the clogging layer are measured using ICP-MS or LA-ICP-MS, since only traces of a few mg/kg naturally occur inside these materials. The detected signals are normalized in the following step to achieve a more straightforward and comparable pattern. Therefore, chondrite normalization is used, a standard procedure based on meteoritic rocks, so-called chondrites, due to their similar composition of non-volatile elements to planet Earth. The mass fractions of lanthanoids in the chondrites used for normalization are listed in Table 1. Pm is excluded from the list since it practically does not exist in nature because of its radioactivity and half-life of only 17.7 years [31,33,34].

Table 1. Mass fractions of lanthanoids in chondrites (ng/g) [31].

La	Ce	Pr	Nd	Sm	Eu	Gd	Tb	Dy	Ho	Er	Tm	Yb	Lu
236	616	92.9	457	149	56.0	197	35.5	245	54.7	160	24.7	159	24.5

2.3. Experimental Procedure

2.3.1. Tracer Trial

The industrial tracer trials were performed at the voestalpine Stahl GmbH steel plant in Linz, Austria. Ti-stabilized IF steel was chosen for this experiment due to its susceptibility to clogging. These steels are produced via a basic oxygen furnace route (BOF), followed by ladle furnace treatment, vacuum degassing at the Ruhrstahl–Heraeus (RH) facility and continuous casting using a single-strand slab caster. Figure 1 shows a schematic description of the experimental procedure including the La or Ce alloying after Al deoxidation and the subsequent FeTi addition.
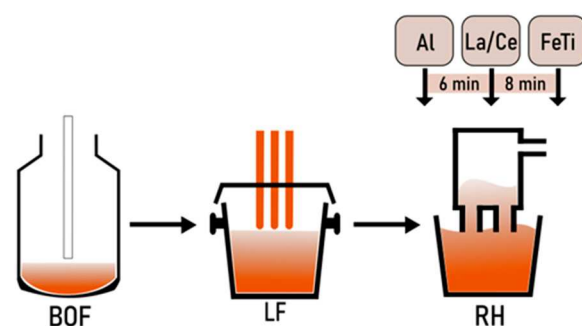
Figure 1. Processing of Ti-IF steel with additional REE treatment during secondary refining.

After crude steel production, 180 tons of steel are tapped into the ladle. Alloy composition and temperature adjustments are performed during ladle furnace treatment. Subsequently, the heat is transferred to the RH facility. Following decarburization, the residual oxygen is killed with Al, and towards the end of the treatment, FeTi is alloyed. A common chemical composition of Ti-IF steel produced in the steel plant of voestalpine Stahl GmbH is presented in Table 2.

Table 2. Chemical composition of a Ti-IF steel sample in g/100 g provided by the voestalpine Stahl GmbH steel plant.

C	Si	Mn	P	S	Al	Ti	N	O_{total}	Fe
0.0011	0.0019	0.1105	0.0091	0.0048	0.0550	0.0549	0.0035	0.0021	Bal.

The tracing experiment involved six Ti-IF heats cast consecutively on the same continuous caster. As shown in Figure 2, the sequence's first and last heats were produced without any tracer addition. The second and fourth were treated with La, while the third and fifth received Ce.
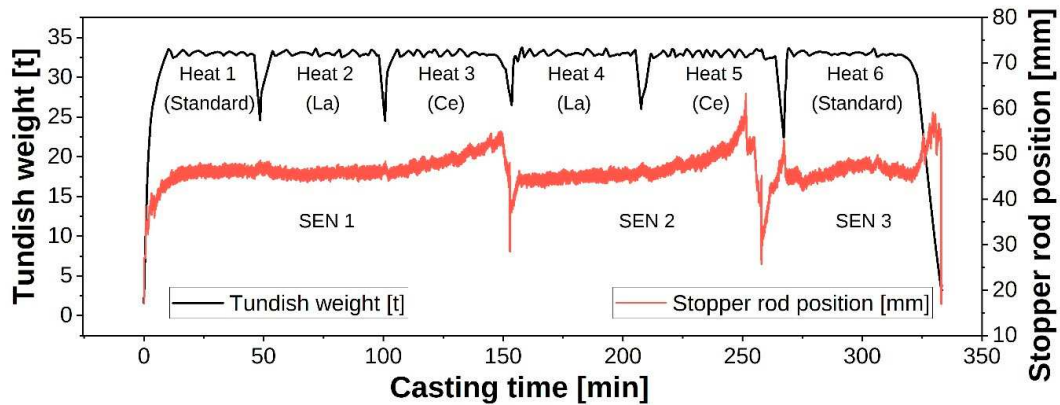

Figure 2. Ti-IF casting sequence of the industrial trial.

The REEs were added to the steel between the Al and FeTi addition, using approximately 40 mg/kg of La or Ce in metallic form. The timing of the tracer addition was purposefully selected to mark the existing inclusion population originating from the deoxidation practice and to distinguish them from later-formed NMIs according to their REE modification. The amount of REEs used was based on successful industrial trials from the literature, to prevent any potential increase in clogging tendency during casting. In the study by Liang et al. [16], 120 kg of a Ce-Fe alloy, with over 10 g/100 g of Ce, was added to 210 t of crude steel resulting in 28 mg/kg Ce in the steel sample from the tundish. Similar relations occurred in the industrial experiment of Gao et al. [35], where 100 kg of a Ce-Fe alloy, with 10 g/100 g of Ce, was alloyed to 250 t and 20 mg/kg Ce was detected in the final product. A third study from Geng et al. [36] added 80 kg of a Ce-Fe alloy, with 10 g/100 g of Ce, to 210 t of liquid iron. The resulting Ce content in the steel sample was about 23 mg/kg. Steel samples and process slag samples were taken in order to investigate the changes in the inclusions' modification and their separation behavior during steel refining and casting. The steel was sampled at the RH facility after Al deoxidation, after REE addition, and finally at the end of vacuum treatment after adding FeTi. Furthermore, steel samples were taken from the tundish to study the modification of NMIs after an extended reaction time. The ladle slag was sampled at the end of secondary refining. Samples of tundish slag were collected at intervals of about 10 min following every ladle exchange. In each case, two mold slag samples were taken per heat in the 20th and 40th minute of casting.

As depicted in Figure 2, three SENs were used during the casting of the Ti-IF sequence. The first SEN (SEN 1) was picked to study the correlation between the formed clogging layer structure, the inclusion specimens, and potential primary materials using the two tracing approaches. For further investigations, the middle section of the SEN was selected and halved. A piece of the inner part of the SEN, mainly consisting of the clogged material, was embedded using a Sn-Bi alloy to stabilize the clogging structure for the following polishing procedure. The investigated area is marked in red in the halved SEN 1 shown in Figure 3. Furthermore, the backscattered electron image of the clogging layer is illustrated.
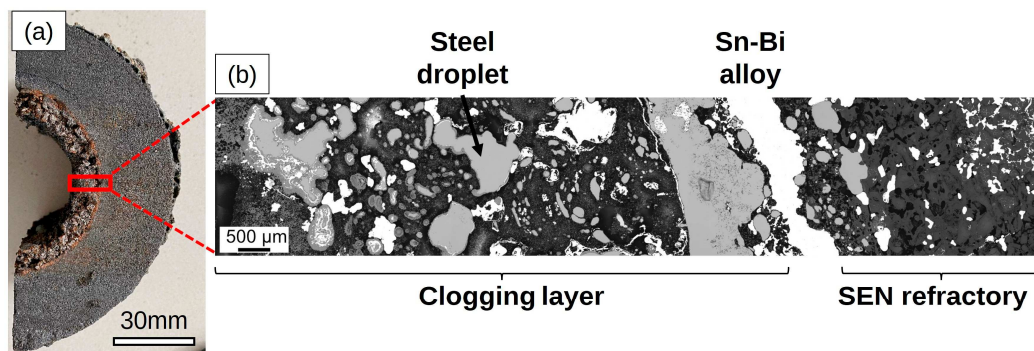
Figure 3. (**a**) Cross-sectional view of the halved SEN 1; (**b**) BSE image: embedded SEN and clogging structure.

2.3.2. Micro-Cleanness Characterization

The method used for the characterization of the REE-traced inclusions in the taken steel samples was the automated SEM/EDS analysis, performed with a JEOL 7200 F field emission SEM (JEOL Germany GmbH, Freising, Germany) equipped with a 100 mm² SDD EDS detector (Oxford Instruments Ultim Max 100; Oxford Instruments GmbH NanoAnalysis, Wiesbaden, Germany) and the AZtec Feature software (AZtec 6.0; Oxford Instruments GmbH NanoAnalysis, Wiesbaden, Germany). The chemical composition of a single particle was detected using area scanning for 1 s at a beam energy of 15 keV, probe current of 13 PC, working distance of 10 mm, and resolution of 1024×1024, with $400\times$ magnification. The first evaluation step with the resulting data was the removal of artifacts, such as scratches or grinding and polishing residues. Next, the heterogeneous multiphase NMIs were recombined to correct the appearing error in the inclusion population, chemical composition, and size due to the detection of more and smaller particles.

2.3.3. Measurements for REE Fingerprint Analysis

Different methods were required to determine the REE concentration in the auxiliaries for the REE fingerprint analysis. The homogeneous investigated materials, such as Al granules or slag formers, had to be digested before ICP-MS analysis. For all auxiliaries, except the Al granules, a $LiBO_2$ fusion digestion was applied. The Al granules were digested by using HCl/HNO_3. The used ICP-MS was an Agilent 7500 (Agilent Technologies, Santa Clara, CA, USA). For the analysis of solid inhomogeneous samples, such as the mesoscopic inclusions or the investigated clogging layer, LA-ICP-MS was utilized to measure the REE concentrations. For this purpose, an Agilent 8800 Triple Quadrupole ICP-MS (Agilent Technologies, Santa Clara, CA, USA) was coupled to an NWR 213 laser ablation system (ESI-NWR, Omaha, NE, USA). In Table 3, the investigated materials and the chosen analyzing methods are listed.

Table 3. Overview of analyzed samples and the analyzing methods used.

Material	Analyzing Method
Al granules	ICP-MS analysis after HCl/HNO_3 digestion
Casting powder	ICP-MS analysis after $LiBO_2$ fusion digestion
Covering agent	ICP-MS analysis after $LiBO_2$ fusion digestion
Sliding gate sand	ICP-MS analysis after $LiBO_2$ fusion digestion
Slag former	ICP-MS analysis after $LiBO_2$ fusion digestion
Mold and tundish slags	ICP-MS analysis after $LiBO_2$ fusion digestion
Clogging layer	ICP-MS analysis after $LiBO_2$ fusion digestion
NMI 1 and 2	LA-ICP-MS (point scans for 180 s)

3. Results

3.1. Active Tracing

3.1.1. NMI Evaluation

The NMI evaluation and the determination of the active tracing success are schematically shown on the samples of the Ce-traced heat cast through the first SEN. The microcleanness evaluation was conducted via automated SEM/EDS analysis, in which the three main types of NMIs were identified after each process step. This is illustrated in Figure 4, where it can be seen that different inclusion types occurred in various stages of the process.
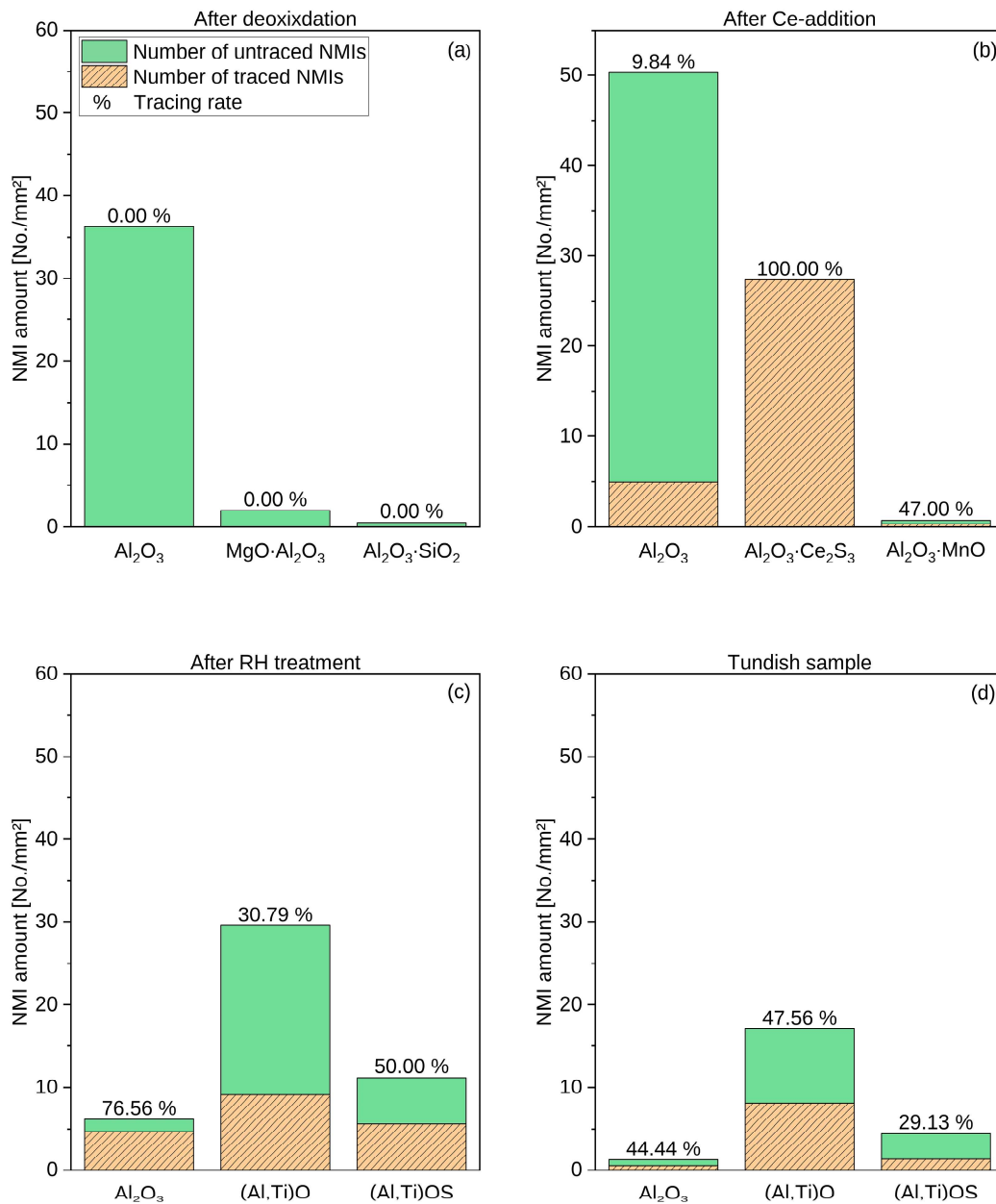

Figure 4. Change in NMI number per mm² over the process in the third melt (Ce-traced): (**a**) after Al deoxidation, (**b**) after Ce addition, (**c**) after RH treatment with the FeTi addition, and (**d**) tundish sample.

The inclusion population of the sample taken after Al deoxidation (Figure 4a) consists of 36.22 No./mm² alumina inclusions and only a few MA spinel and $Al_2O_3 \cdot SiO_2$ inclusions. In the second sample after Ce-addition (Figure 4b), a higher total number of

NMIs was detected (81.05 No./mm²). The main types in the second sample were Al_2O_3 (50.29 No./mm²), $Al_2O_3 \cdot Ce_2S_3$ (27.34 No./mm²), and $Al_2O_3 \cdot MnO$ (0.28 No./mm²). A total of 44.69% of all inclusions (32.62 No./mm²) were Ce-traced Al-containing inclusions in the second sample. After the FeTi addition and RH treatment, the inclusion population in sample three changed to a lower total inclusion density (56.59 No./mm²). The pre-existing inclusion types were also influenced and modified by FeTi. (Al,Ti)-containing oxides and oxide-sulfides existed besides alumina NMIs. The last sample investigated, the tundish sample (Figure 4d), had the same main inclusion types as the previous one but with a decreased total number of NMIs per mm², namely 36.82 No./mm². The total number of NMIs, the three main NMI types, as well as the overall tracing rates of the four investigated samples are listed in Table 4.

Table 4. Total number of NMIs per mm², the three main NMI types per sample, and the associated tracing rates of the samples from the third heat (Ce-traced).

Sample No.	Date of Sampling	Total No. of NMIs (No./mm²)	Three Main NMI Types	Overall Tracing Rate (%)
1	After deoxidation	38.70	Al_2O_3, $MgO \cdot Al_2O_3$, $Al_2O_3 \cdot SiO_2$	-
2	After Ce addition	105.91	Al_2O_3, $Al_2O_3 \cdot Ce_2S_3$, $Al_2O_3 \cdot MnO$	41.26
3	After RH treatment	46.83	Al_2O_3, (Al,Ti)O,·(Al,Ti)OS	38.43
4	Tundish sample	25.06	Al_2O_3, (Al,Ti)O,·(Al,Ti)OS	34.26

The mean equivalent circle diameters (ECDs) and the corresponding standard deviation of the three main NMI types of each sample, categorized into traced and untraced NMIs, are listed in Table 5. In samples 3 and 4, after FeTi addition, the ECDs of the traced NMIs were higher for each inclusion type compared to the untraced ones. The inclusion sizes increased between samples 2 and 4.

Table 5. Mean ECDs in μm of the traced and untraced main NMI types of the Ce-traced samples from the third heat.

Sample No.	NMI Type	Mean ECD Untraced (μm)	Mean ECD Traced (μm)
1	Al_2O_3	2.55 ± 1.66	-
1	$MgO \cdot Al_2O_3$	3.06 ± 1.37	-
1	$Al_2O_3 \cdot SiO_2$	4.43 ± 3.22	-
2	Al_2O_3	1.51 ± 0.53	2.17 ± 1.13
2	$Al_2O_3 \cdot Ce_2S_3$	-	1.48 ± 0.49
2	$Al_2O_3 \cdot MnO$	1.46 ± 0.40	1.34 ± 0.28
3	Al_2O_3	2.24 ± 1.22	3.06 ± 1.50
3	(Al,Ti)O	1.89 ± 1.10	2.72 ±1.07
3	(Al,Ti)OS	1.43 ± 0.46	2.35 ± 1.09
4	Al_2O_3	4.21 ± 1.99	5.23 ± 2.66
4	(Al,Ti)O	2.54 ± 1.39	3.35 ± 1.38
4	(Al,Ti)OS	1.75 ± 0.60	2.15 ± 0.78

Figure 4 also shows the tracing rate for each inclusion type in the four analyzed samples. Besides the Ce-traced Al_2O_3 inclusions, the Al-Ti oxides and oxide-sulfides contained Ce-rich areas as well. The highest total tracing rate in the Al-containing NMIs was found in the second sample after Ce addition at 41.26%, followed by the sample after RH treatment at 38.43%, and the last sample at 34.26%.

The change in inclusion types over the process is shown in Figure 5 with exemplary BSE images and the associated elemental mappings. Figure 5a depicts an example of the

main NMI type, an alumina inclusion after deoxidation. After REE addition, these alumina particles were modified by, e.g., Ce, and NMIs with brighter areas were formed, as shown in Figure 5b. The FeTi addition led to modification in the inclusion landscape, and complex Ce-traced (Al,Ti) oxides were found, as Figure 5c displays. Examples of the two main NMI types in the last sample, traced and untraced (Al,Ti) oxides, are shown in Figure 5d,e.
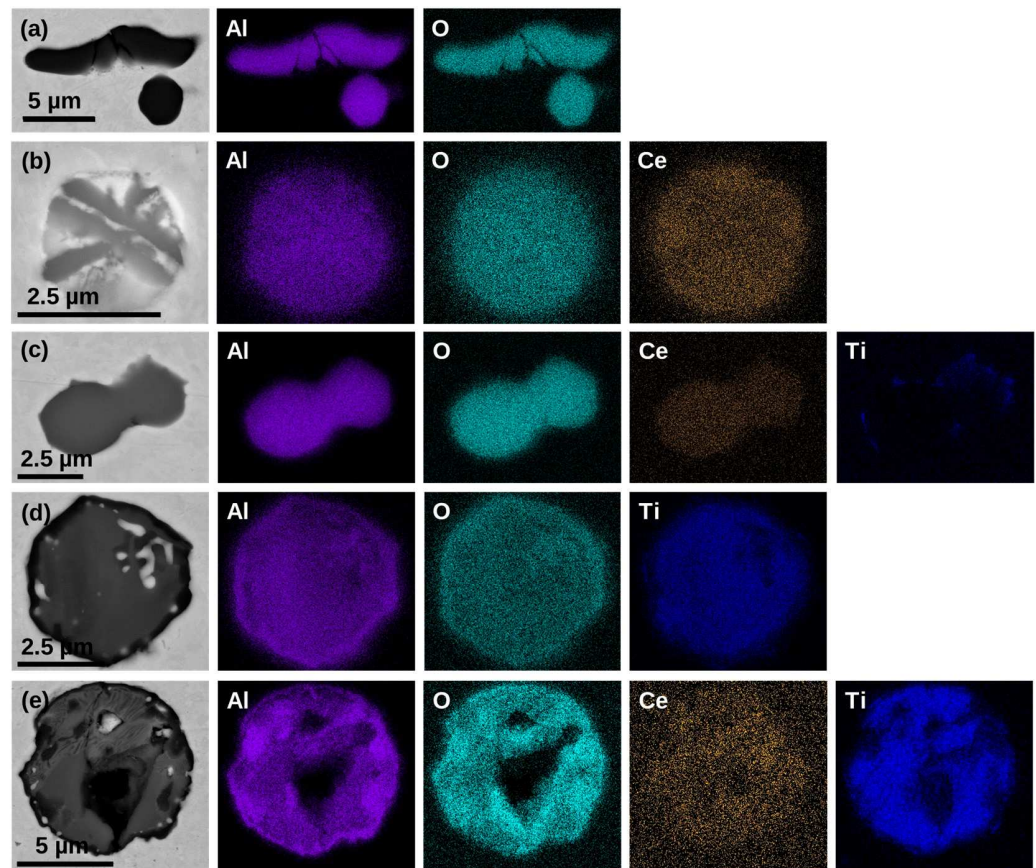

Figure 5. BSE images and elemental mappings of the NMI modification in the Ce-traced melt: (**a**) NMI after Al deoxidation, (**b**) NMI after Ce addition, (**c**) NMI in the sample after FeTi addition, (**d**) traced and (**e**) untraced AT-NMI from the tundish sample.

3.1.2. Clogging Layer Investigation

An SEM/EDS analysis of the clogging layer inside the first SEN was performed to find out if pre-existing, traced alumina inclusions influenced the layer formation. Besides the BSE image and the elemental mappings of the main elements, Al, Fe, and O, the detected concentrations of Ti, La, and Ce are illustrated in Figure 6. Concerning this diagram, the clogging layer can be divided into different parts that can be allocated to the three cast heats. The first part of the clogging layer from the standard heat consisted primarily of a large steel droplet, as seen in the elemental mappings. In the second section, associated with the La-traced heat, an irregular signal of La varying between $w = 0.2$ and 0.9% was detected. The La and Ce signal cannot be assigned to the pre-existing traced aluminum oxide particles with regard to the associated element allocation due to insufficient signal intensity. Similar to La, an irregular signal of Ce appeared in the third part of the clog. The signal of Ti over the whole clogging layer was below $w = 0.2\%$, with no significant peak in the clogged material.
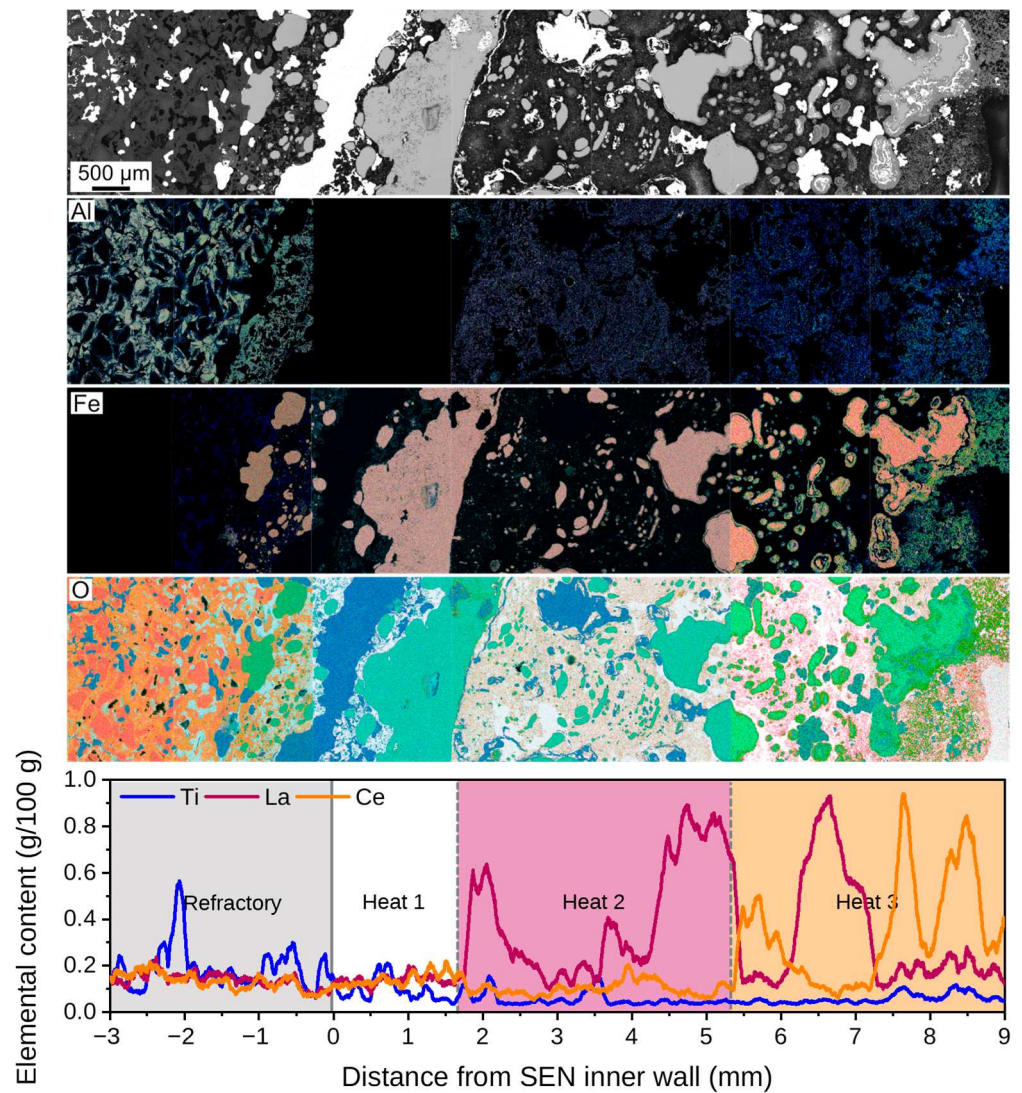
Figure 6. BSE images and the corresponding elemental mappings of the main elements detected in the clogging layer from the investigated SEN; below: EDS-detected elemental content of Ti, La, and Ce over the clogging layer.

3.2. Passive Tracing

The REE concentration in the clogging layer was determined with ICP-MS after a LiBO$_2$ digestion. The averaged mass fraction of the homogenized, digested clogging layer normalized to chondrites is shown as a thick, continuous blue line in Figure 7. Besides the resulting fingerprint of the clogging layer, the patterns of the main influencing auxiliaries, such as slags, casting powder, and Al granules, are illustrated. High mass fractions for La and Ce and a Tb anomaly were detected for the clogging layer. A similar increase in heavy REEs occurs for the patterns of the clogging layer and the sliding gate sand. The other auxiliaries' patterns do not conform with the clogging layer, except for the Tb anomaly of the mold slag from the Ce-traced heat.
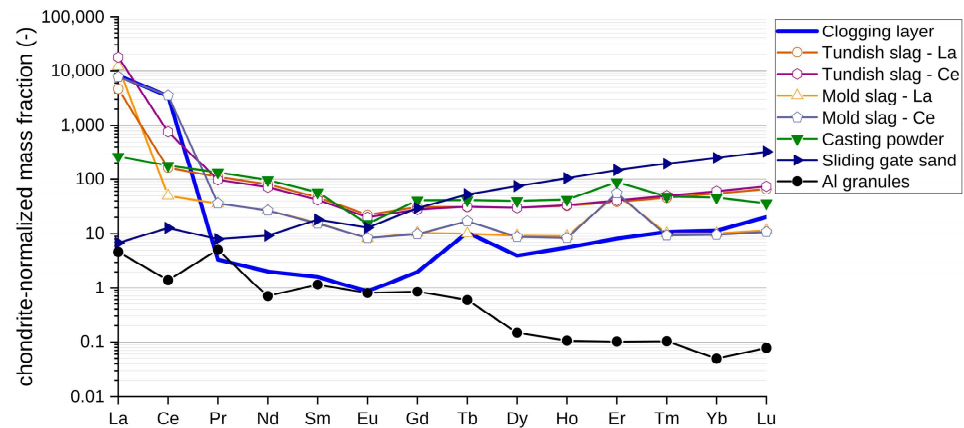
Figure 7. REE fingerprint of mold and tundish slag, casting powder, sliding gate sand, Al granules, and clogging layer.

The REE fingerprint technique was moreover applied to determine the source of mesoscopic NMIs in steel samples from the traced melts. One NMI per melt was investigated via LA-ICP-MS. In Figure 8, the BSE image and the corresponding elemental mappings of the mesoscopic NMI (NMI 1) found in the La-traced melt cast through the first SEN are shown. NMI 1 is a conglomerate primarily consisting of Al-, Ca-, Na-oxides and smaller parts of Zr-, Ti- and La-oxides. The whole conglomerate is surrounded by CaS.
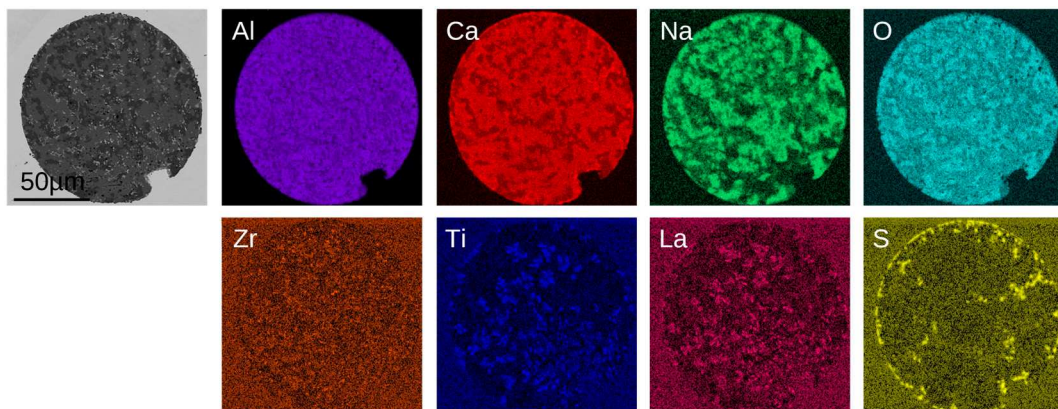
Figure 8. BSE image and elemental mappings of NMI 1.

The detected concentrations are constant over the whole depth of the complex mesoscopic NMI. Figure 9 shows the REE patterns of NMI 1 and all investigated auxiliaries. An Er anomaly occurs in the patterns of NMI 1, the casting powder, and the mold slag. High La mass fractions were detected for NMI 1 and both slags due to the La addition. In the mesoscopic NMI 1 pattern, anomalies for Gd and Yb also occurred. No similarities can be seen between NMI 1 and the other auxiliaries, such as the covering agent, sliding gate sand, slag former, Al granules, and tundish slag of the La-traced heat. The chondrite-normalized mass fraction of the investigated Al granules is significantly lower than those of the slags, the casting powder, and the inclusion. A similarly formed peak for the Er anomaly of the mold slag and mesoscopic NMI 1 can be seen. The Er anomaly is also visible in the casting powder, but with lower intensity.
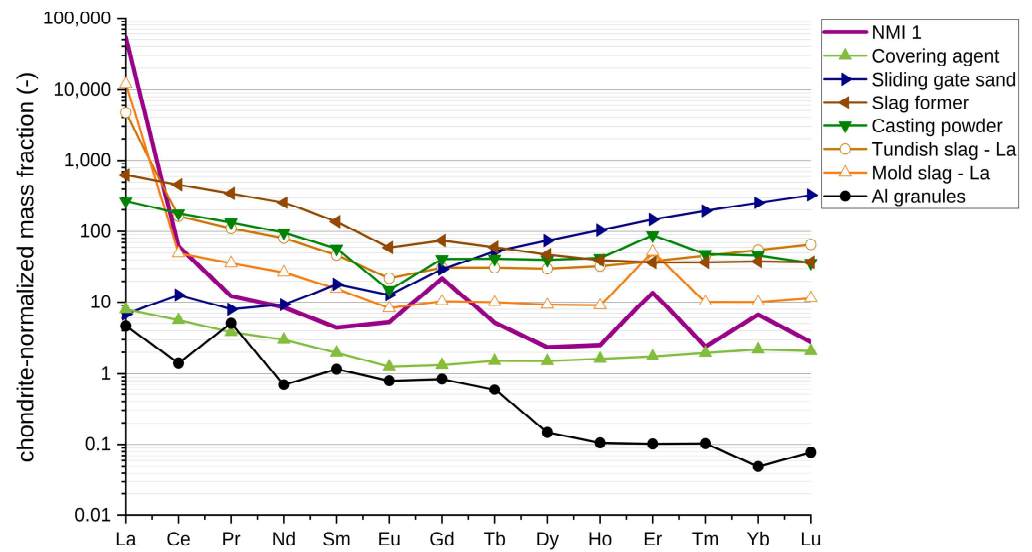
Figure 9. REE fingerprints of all investigated auxiliaries and mesoscopic NMI 1 of La-traced heat.

The second investigated mesoscopic inclusion (NMI 2) is taken from the first Ce-traced heat. The BSE image and the corresponding elemental mappings are illustrated in Figure 10. Similar to NMI 1, this inclusion is a conglomerate consisting of Al-, Ca-, and Na-oxides, with small parts of Zr- and Ti-oxides. Traces of Ce were also detected in conjunction with O and S via manual SEM/EDS analysis.
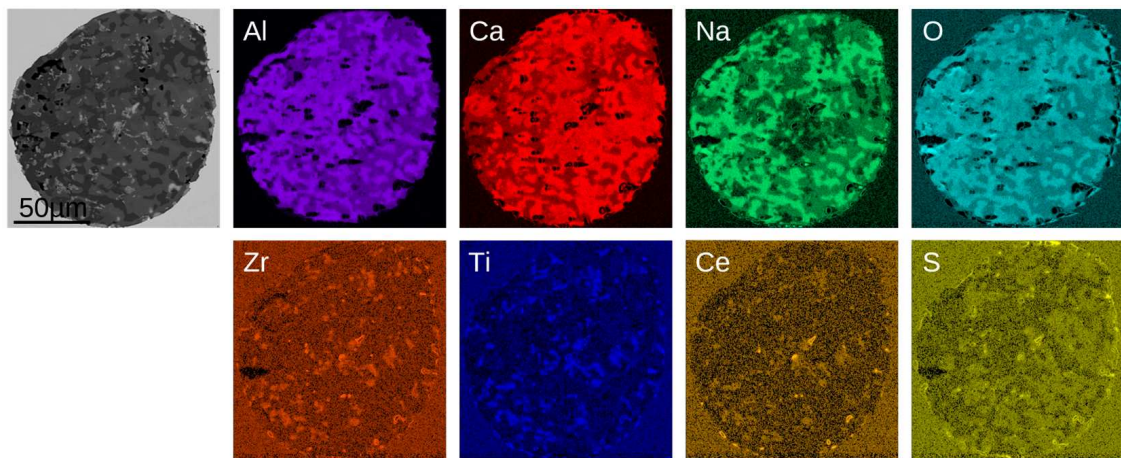
Figure 10. BSE image and elemental mappings of NMI 2.

The REE patterns of NMI 2 and those of the auxiliaries that are the main potential contributors for the formation of NMI 2 (casting powder, Al granules, and both slags of the third heat) are plotted in Figure 11 for better visibility. A coherence can be seen between the patterns of the mold slag and NMI 2. Both lines have high mass fractions of La and Ce as well as Eu, Tb, and Er anomalies. The resulting REE fingerprint of the casting powder also shows Eu and Er anomalies similar to the mold slag and NMI 2. The tundish slag's and Al granules' patterns show no similarity to the other patterns.
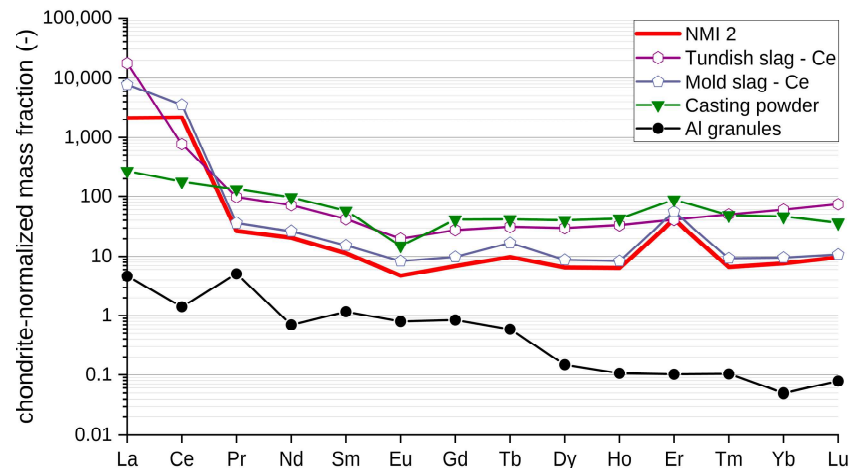
Figure 11. REE fingerprints of mold and tundish slag, casting powder, Al granules, and mesoscopic NMI of Ce-traced heat (NMI 2).

4. Discussion

4.1. Modification of NMIs Using REEs

The aim of applying the active tracing approach to the production of Ti-stabilized IF steels was to determine if an agglomeration of pre-existing alumina inclusions was involved in the clogging layer formation, or if reoxidation and thus newly formed NMIs occurred due to the FeTi addition and subsequently played a role in clogging. The deoxidation products were successfully traced via La or Ce, as was shown in Figure 5 with the example of the Ce-treated heat. Regarding the automated SEM/EDS analysis of the taken samples, it was found that only about 50% of all Al-containing NMIs were marked by REEs. This suggests that the sampling after REE treatment was too fast, and there was too little interaction time between the REEs and the melt. Furthermore, new inclusions occurred after the addition of the REEs.

After RH treatment, fewer inclusions were detected in the automated SEM/EDS analysis due to inclusion separation into the slag. The sample taken after RH treatment consisted primarily of Al- and Ti-containing (AT)-oxides and oxide-sulfides. The tracing rates for FeTi-modified deoxidation products were 30.79% and 50% for oxides and sulfides, respectively. Since already a high number of detected Al_2O_3 NMIs were not marked in the previous sample, it is difficult to determine if the high number of untraced new deoxidation products is due to previous low tracing rates or if inclusions were newly formed after FeTi addition.

After RH treatment, the number of NMIs was reduced further, as the results of the automated SEM/EDS analysis of the tundish sample showed. The inclusion types remained the same as after RH treatment. Concerning the automated SEM/EDS analysis, untraced and traced AT-NMIs occurred simultaneously, leading to the conclusion that, on the one hand, FeTi likely modified pre-existing alumina particles; and, on the other hand, new, smaller NMIs were formed after FeTi addition.

Although active tracing seems to be an easy way to mark and track NMIs over the steelmaking process, this method is also connected to some difficulties since REEs partially reduce pre-existing NMIs. The degree of the reduction depends on the interaction time between the NMIs and REEs. Two potential challenges occur during processing with REEs. While a too-long interaction time leads to a complete reduction of the NMIs to be traced, sampling directly after REE addition results in the problem that not all particles are marked in this stage, as seen with the example of the Ce-traced melt. Furthermore, the examination using automated SEM/EDS analyses of samples containing REE-traced NMIs takes longer due to the required double threshold scan and the subsequent recombination. Last but not least, the wetting and separation behavior of NMIs is influenced by the active tracing technique since the inclusions are modified. Hence, a new tracing approach is demanded.

4.2. Clogging Layer Investigation

The clogging layer was investigated twice. In the first step, it was analyzed via SEM/EDS, and then LA-ICP-MS was used to determine the REE pattern for the fingerprint approach. During SEM/EDS analysis, only a few La- and Ce-traced alumina particles were found in parts of the examined clogging layer. Thus, it can be assumed that pre-existing Al_2O_3 NMIs were involved in the formation of the clogging layer in the SEN. Due to the detection of La and Ce, it is possible to divide the clogged material into three sections for each cast heat through this SEN. The La and Ce signals varied in a low range for amounts between w = 0.2 and 0.9%. The Ti concentration was below w = 0.2% over the whole clogging layer. Hence, in the investigated section of the clog, no Ti-modified Al-NMIs were found. Since only traces of La and Ce were detected with SEM/EDS in the clogging layer, the REE fingerprint approach was applied to confirm the influence of pre-existing deoxidation products on the clogging layer formation.

By using the passive tracing technique, a similar increase in heavy REEs could be observed for the sliding gate sand and the clogging layer. Due to this resemblance, it can be concluded that the sliding gate sand influenced the formation of the clogged SEN. The Al granules showed only low REE concentrations, leading to low mass fractions, which is why a comparison with the resulting pattern is not reasonable. The Tb anomaly that was observed for the clogging layer and the mold slag from the Ce-traced heat was presumably an interference caused by the very high Ce contents. One problem of the REE fingerprint approach concerning the clogging layer is that the signal was averaged. A promising method for more targeted investigations of inhomogeneous materials, such as the clogging layer, would be a spatially resolved analysis of specific parts instead of homogenizing and averaging the detected signal, since the REE concentration varied over the clogging layer. However, dividing the layer into the respective sections and the subsequent spatially resolved analysis is difficult. Further studies to improve the measuring method are required.

While both tracing methods are suitable for the determination of the actual source, they do not provide definitive insights into the underlying mechanism responsible for clogging layer formation. As mentioned in the introduction, the four main mechanisms behind the clogging phenomenon during continuous casting of Ti-stabilized ULC steels coincide in most cases. The FeTi addition is a critical factor for the occurrence of clogging during continuous casting since it influences interfacial tension [37] and further delivers additional oxygen to the melt, leading to the formation of new smaller NMIs [38]. The detection of Ce and La in the SEM/EDS analysis of the clogging layer leads to the conclusion that pre-existing alumina inclusions agglomerated to the nozzle wall, which is one of the most common mechanisms.

4.3. Origin of Mesoscopic NMIs

The SEM/EDS analysis of the mesoscopic NMIs (NMI 1 and 2) led to the result that both particles were conglomerates consisting of different oxides. Al-, Ca-, and Na-oxides were the main oxides in both investigated heterogeneous NMIs. Small parts of Zr-, Ti-, and La-oxides were irregularly distributed in the particles. Due to the high concentration of Ca and Na, as well as the detection of F in the SEM/EDS analysis, the casting powder was identified as one possible source, despite the absence of Si, a major component, in this auxiliary. Applying the REE fingerprint method should clarify if the mesoscopic NMIs originate from the casting powder or if they have another source. Based on the chemical composition of the NMIs, other auxiliaries that may have influenced the inclusions' formation were determined. Similarities between the mold slag and the casting powder occurred in the case of NMI 1 (traced with La). Hence, the main source of the mesoscopic NMIs is likely the casting powder, as was expected after the SEM/EDS analysis, since mold slag is primarily molten casting powder. Although small parts of ZrO_2 were detected during our SEM/EDS analysis, no similarity occurred between the sliding gate sand and the investigated NMIs. Another possible source for ZrO_2 is an absorption of

refractory into the mold slag from the slag zone of the SEN. The presence of ZrO_2 in the mold slag strengthens the assumption that the mold slag is the source of NMI 1. The intensity of the Er anomaly increased more in the REE patterns of the mold slag and the NMIs compared to the sliding gate sand. The Gd and Yb anomalies visible in the pattern of NMI 1 most likely resulted from interferences of $^{139}LaOH^+$ and $^{139}LaO_2^+$ on ^{156}Gd and ^{172}Yb, respectively, occurring due to oxide ion formation in the plasma. The high values for the La mass fraction of NMI 1, tundish, and mold slag are non-natural La concentrations and resulted from the active tracing approach. As a consequence of the La-traced alumina parts occurring in the EDS analysis of NMI 1, the Al granules also influenced the inclusion formation. However, similar to the clogging layer investigation, the REE concentrations in the Al granules being significantly lower than in the other investigated materials made the comparison with the other resulting REE patterns impossible. Thus, the REE fingerprint technique cannot confirm the assumption of the Al influence on the conglomerate after SEM/EDS analysis.

Concerning the manual SEM/EDS analysis, the mesoscopic inclusion of the Ce-traced heat, NMI 2, had origins similar to NMI 1. The resulting elemental pattern after the REE fingerprint investigation differed regarding the occurring anomalies from NMI 1. The pattern of mold slag from the third Ce-traced heat is almost identical to the pattern of NMI 2. Both lines showed anomalies for Eu, Tb, and Er in a similar intensity. In addition to the different intensities for the Eu and Er anomalies, the REE fingerprint differs regarding the higher concentrations for La and Ce and the occurring Tb anomaly. The reason for the significantly higher mass fraction of La and Ce in the mold slag is its contact with the traced melts and carryover slag from the tundish. The Tb anomaly occurred at the clogging layer and NMI 2, but not at NMI 1. Hence, the detected Tb signal seemed to be due to an interference between $^{159}Tb^+$ and $^{142}CeOH^+$. The source of the Ce-traced mesoscopic NMI 2 is similar to that of NMI 1, the mold slag, and thus the casting powder.

5. Conclusions

Active and passive tracing approaches were applied to study the clogging layer formation during the industrial production of Ti-stabilized ULC steels and to further identify the source of mesoscopic NMIs. The following findings were obtained from this study:

1. For the active tracing method, La and Ce were directly alloyed subsequent to Al deoxidation to trace the formed alumina NMIs. The experiment was applied to the production of Ti-stabilized ULC steel on an industrial scale. The micro-cleanness evaluation over this process showed a modification of the formed alumina inclusions after deoxidation to La- or Ce-traced and untraced Al- and Ti-containing oxides in the tundish sample. The occurrence of traced AT-NMIs confirms that alumina particles formed during the deoxidation process exist in the final sample, whereas untraced AT-NMIs led us to the conclusion that new small NMIs were formed after the FeTi addition.

2. The elemental mappings of the SEM/EDS analysis from the clogging layer highlighted only small, traced alumina parts in the clog. The detected concentrations of La and Ce varied in a low range between w = 0.2 and 0.9%, making it possible to divide the clogging layer into three sections corresponding with the three cast heats. Due to the occurrence of traced NMIs in the clog, it can be concluded that pre-existing alumina particles were involved in the layer formation.

3. No similarities between the clog and the investigated Al granules were found during the additional investigation of the clogging layer using the passive tracing approach since the REE concentrations in the Al granules were too low. However, according to the REE fingerprint approach, the sliding gate sand influenced the formation of the clogging layer. The detailed reaction mechanism behind the impact of the sliding gate sand on clogging is not clarified. Hence, further studies need to be conducted to answer this issue.

4.   The two investigated mesoscopic NMIs of La- and Ce-traced heats were conglomerates primarily consisting of Al-, Ca-, and Na-oxides with traces of Zr-, Ti, and La/Ce-oxides. By applying the passive tracing technique, it was determined that the casting powder and the resulting mold slags, respectively, were the sources for both NMIs.

5.   The REE fingerprint technique is a new approach for, e.g., identifying the source of NMIs and learning more about the origin of phenomena such as clogging during steel production. In contrast to the already-applied active tracing method, no additional element, which modifies the existing NMIs and influences their behaviors, is needed for training.

References

1.   Kiessling, R. Clean steel—A debatable concept. *Met. Sci.* **1980**, *14*, 161–172. [CrossRef]
2.   Kaushik, P.; Pielet, H.; Yin, H. Inclusion characterisation—Tool for measurement of steel cleanliness and process control: Part 1. *Ironmak. Steelmak.* **2009**, *36*, 561–571. [CrossRef]
3.   Burty, M.; Louis, C.; Dunand, P.; Osmont, P.; Ruby-Meyer, F.; Nadif, M.; Penet, F.; Isono, T.; Takeuchi, E.; Toh, T. Methodology of steel cleanliness assessment. *Rev. Metall.* **2000**, *97*, 775–782. [CrossRef]
4.   Atkinson, H.V.; Shi, G. Characterization of inclusions in clean steels: A review including the statistics of extremes methods. *Prog. Mater. Sci.* **2003**, *48*, 457–520. [CrossRef]
5.   Thornton, P.A. The influence of non-metallic inclusions on the mechanical properties of steel: A review. *J. Mater. Sci.* **1971**, *6*, 347–356. [CrossRef]
6.   Park, J.H.; Kang, Y. Inclusions in Stainless Steels—A Review. *Steel Res. Int.* **2017**, *88*, 1700130. [CrossRef]
7.   Kaushik, P.; Kruse, D.; Ozgu, M. Assessment of castability issues in interstitial-free (IF) steels. *Rev. Metall.* **2008**, *105*, 92–101. [CrossRef]
8.   Jungreithmeier, A.; Pissenberger, E.; Burgstaller, K.; Mörtl, J. Production of ULC IF Steel Grades at Voestalpine Stahl GmbH, Linz. In Proceedings of the Iron & Steel Society International Technology Conference and Exposition, Indianapolis, IN, USA, 27–30 April 2003.
9.   Rackers, K.G.; Thomas, B.G. Clogging in Continuous Casting Nozzles. In Proceedings of the 78th Steelmaking Conference Proceedings, Iron and Steel Society, Warrendale, PA, USA, 2–5 April 1995; pp. 723–734.
10.   Cui, H.; Bao, Y.P.; Wang, M.; Wu, W. Clogging behavior of submerged entry nozzles for Ti-bearing IF steel. *Int. J. Miner. Metall. Mater.* **2010**, *17*, 154–158. [CrossRef]
11.   Michelic, S.K.; Bernhard, C. Significance of Non-metallic Inclusions for the Clogging Phenomenon in Continuous Casting of Steel—A Review. *Steel Res. Int.* **2022**, *93*, 2200086. [CrossRef]
12.   Singh, S.N. Mechanism of Alumina Buildup in Tundish Nozzle during Continuous Casting of Aluminium-Killed Steels. *Metall. Mater. Trans. B* **1974**, *5*, 2165–2178. [CrossRef]
13.   Nadif, M.; Lehmann, J.; Burty, M.; Domgin, J.-F. Control of steel reoxidation and CC nozzle clogging: An overview. *Metall. Res. Technol.* **2007**, *104*, 493–500. [CrossRef]
14.   Lee, J.-H.; Kang, M.-H.; Kim, S.-K.; Kim, J.; Kim, M.-S.; Kang, Y.-B. Influence of Al/Ti Ratio in Ti-ULC Steel and Refractory Components of Submerged Entry Nozzle on Formation of Clogging Deposits. *ISIJ Int.* **2019**, *59*, 749–758. [CrossRef]
15.   Zhao, B.; Wu, W.; Zhi, J.; Su, C.; Zhang, J. Study on the formation mechanism of clogging layer of rare earth microalloyed Q355 steel's submerged entry nozzle and process optimization. *Ironmak. Steelmak.* **2023**, *50*, 782–793. [CrossRef]
16.   Liang, W.; Li, J.; Lu, B.; Zhi, J.; Zhang, S.; Liu, Y. Analysis on clogging of submerged entry nozzle in continuous casting of high strength steel with rare earth. *J. Iron Steel Res. Int.* **2022**, *29*, 34–43. [CrossRef]

17. Burty, M.; Dunand, P.; Ritt, J.P.; Soulard, H.; Blanchard, A.; Jeanne, G.; Penet, F.; Pluquet, R.; Poissonnet, I. Control of DWI steel cleanness by lanthanum tracing of deoxidation inclusions, ladle slag treatment and a methodical approach. *Ironmak. Conf. Proc.* **1997**, *56*, 711–717.

18. Wang, Y.; Li, C.; Wang, L.; Xiong, X.; Chen, L.; Zhuang, C. Modification of Alumina Inclusions in SWRS82B Steel by Adding Rare Earth Cerium. *Metals* **2020**, *10*, 1696. [CrossRef]

19. Ren, Q.; Zhang, L. Effect of Cerium Content on Inclusions in an Ultra-Low-Carbon Aluminum-Killed Steel. *Metall. Mater. Trans. B* **2020**, *51*, 589–600. [CrossRef]

20. Pan, C.; Hu, X.; Lin, P.; Chou, K. Evolution of Inclusions after Cerium and Titanium Addition in Aluminum Deoxidized Fe-17Cr-9Ni Austenitic Stainless Steel. *ISIJ Int.* **2020**, *60*, 1878–1885. [CrossRef]

21. Li, B.; Zhu, H.; Zhao, J.; Song, M.; Li, J.; Xue, Z. Effect of Rare-Earth La on Inclusion Evolution in High-Al Steel. *Steel Res. Int.* **2021**, *93*, 2100347. [CrossRef]

22. Goldstein, J.I.; Newbury, D.E.; Michael, J.R.; Ritchie, N.W.; Scott, J.H.J.; Joy, D.C. *Scanning Electron Microscopy and X-ray Microanalysis*; Springer: New York, NY, USA, 2018; ISBN 978-1-4939-6674-5.

23. Wang, Y.; Liu, C. Agglomeration Characteristics of Various Oxide Inclusions in Molten Steel Containing Rare Earth Element under Different Deoxidation Conditions. *ISIJ Int.* **2021**, *61*, 1396–1403. [CrossRef]

24. Zhang, L.; Cheng, L.; Ren, Y.; Zhang, J. Effect of cerium on the wettability between 304 stainless steel and MgO–Al2O3-based lining refractory. *Ceram. Int.* **2020**, *46*, 15674–15685. [CrossRef]

25. Wang, H.; Bao, Y.; Zhao, M.; Wang, M.; Yuan, X.; Gao, S. Effect of Ce on the cleanliness, microstructure and mechanical properties of high strength low alloy steel Q690E in industrial production process. *Int. J. Miner. Metall. Mater.* **2019**, *26*, 1372–1384. [CrossRef]

26. Akagi, T.; Edanami, K. Sources of rare earth elements in shells and soft-tissues of bivalves from Tokyo Bay. *Mar. Chem.* **2017**, *194*, 55–62. [CrossRef]

27. Danezis, G.P.; Pappas, A.C.; Zoidis, E.; Papadomichelakis, G.; Hadjigeorgiou, I.; Zhang, P.; Brusic, V.; Georgiou, C.A. Game meat authentication through rare earth elements fingerprinting. *Anal. Chim. Acta* **2017**, *991*, 46–57. [CrossRef] [PubMed]

28. Su, Y.; Yang, M. Combining Rare Earth Element Analysis and Chemometric Method to Determine the Geographical Origin of Nephrite. *Minerals* **2022**, *12*, 1399. [CrossRef]

29. Gallello, G.; Ferro-Vázquez, C.; Chenery, S.; Lang, C.; Thornton-Barnett, S.; Kabora, T.; Hodson, M.E.; Stump, D. The capability of rare earth elements geochemistry to interpret complex archaeological stratigraphy. *Microchem. J.* **2019**, *148*, 691–701. [CrossRef]

30. Cerutti, C.; Sánchez, R.; Sánchez, C.; Ardini, F.; Grotti, M.; Todolí, J.-L. Prospect on Rare Earth Elements and Metals Fingerprint for the Geographical Discrimination of Commercial Spanish Wines. *Molecules* **2020**, *25*, 5602. [CrossRef]

31. Wasson, J.T.; Kallemeyn, G.W. Compositions of chondrites. *Philos. Trans. R. Soc. Lond. Ser. A Math. Phys. Sci.* **1988**, *325*, 535–544. [CrossRef]

32. Thiele, K.; Musi, R.; Ramesh Babu, S.; Michelic, S.K. Optimization of the Two- and Three-Dimensional Characterization of Rare Earth-Traced Deoxidation Products. *Adv. Eng. Mater.* **2023**, *25*, 2201748. [CrossRef]

33. Wibner, S.; Antrekowitsch, H.; Meisel, T.C. Studies on the Formation and Processing of Aluminium Dross with Particular Focus on Special Metals. *Metals* **2021**, *11*, 1108. [CrossRef]

34. Voncken, J. *The Rare Earth Elements*; Springer International Publishing: Cham, Switzerland, 2016; ISBN 978-3-319-26807-1.

35. Gao, S.; Wang, M.; Guo, J.; Wang, H.; Zhi, J.; Bao, Y. Characterization Transformation of Inclusions Using Rare Earth Ce Treatment on Al-Killed Titanium Alloyed Interstitial Free Steel. *Steel Res. Int.* **2019**, *90*, 1900194. [CrossRef]

36. Geng, R.; Li, J.; Shi, C. Evolution of Inclusions with Ce Addition and Ca Treatment in Al-killed Steel during RH Refining Process. *ISIJ Int.* **2021**, *61*, 1506–1513. [CrossRef]

37. Basu, S.; Choudhary, S.K.; Girase, N.U. Nozzle Clogging Behaviour of Ti-bearing Al-killed Ultra Low Carbon Steel. *ISIJ Int.* **2004**, *44*, 1653–1660. [CrossRef]

38. Dorrer, P.; Michelic, S.K.; Bernhard, C.; Penz, A.; Rössler, R. Study on the influence of FeTi-addition on the inclusion population in Ti-stabilized ULC steels and its consequences for SEN-clogging. *Steel Res. Int.* **2019**, *90*, 1800635. [CrossRef]

7.4 Tracing with enriched stable isotopes

Paper VII: <u>K. Thiele</u>, S. Wagner, J. Irrgeher, T. Prohaska and S.K. Michelic, Tracing Non-metallic Inclusions in Steel with Low Levels of Enriched Magnesium Stable Isotopes: A Novel Approach, under review in Metallurgical and Materials Transactions B.

Paper VII deals with tracing by using enriched stable ^{26}Mg isotopes for isotopic modification of the slag. LA-ICP-MS analyses were applied to determine whether the modified slag was the source of Mg-containing NMIs. **Paper VII** is under review in **Metallurgical and Materials Transactions B**.

1 **Tracing Non-metallic Inclusions in Steel with Low Levels of Enriched Magnesium**

2 **Stable Isotopes: A Novel Approach**

3

4 Kathrin Thiele*[1], Stefan Wagner[1,2], Johanna Irrgeher[2], Thomas Prohaska[2] and Susanne K.

5 Michelic[1]

6

7

8 *Corresponding author

9 Dipl.–Ing. Kathrin Thiele[1]

10 Email: kathrin.thiele@unileoben.ac.at

11

12 Dr.nat.techn. Stefan Wagner, MSc[1,2]

13 Email: stefan.wagner@unileoben.ac.at

14

15 Assoc. Prof. Dipl.-Ing. Dr.nat.techn. Johanna Irrgeher[2]

16 Email: johanna.irrgeher@unileoben.ac.at

17

18 Univ.-Prof. Dipl.-Ing. Dr.techn. Thomas Prohaska[2]

19 Email: thomas.prohaska@unileoben.ac.at

20

21 Univ.-Prof Dipl.-Ing. Dr.mont. Susanne K. Michelic[1]

22 Email: susanne.michelic@unileoben.ac.at

23

24 [1]Christian Doppler Laboratory for Inclusion Metallurgy in Advanced Steelmaking,

25 Montanuniversität Leoben, Franz Josef-Straße 18, 8700 Leoben, Austria

26

27 [2]Chair of General and Analytical Chemistry, Montanuniversität Leoben, Franz Josef-Straße

28 18, 8700 Leoben, Austria

29

30 **Abstract**

31

32 Non-metallic inclusions (NMIs) are inevitably formed during steel production, affecting

33 product quality. To investigate the origin of NMIs, active tracing methods by adding specific

34 compounds are state-of-the-art, which, however, influence the NMIs' formation and

35 properties during steel production. Thus, a novel approach has been developed and applied to

36 overcome these drawbacks. The approach uses isotopic tracing where the isotopic pattern of

37 one element of a potential source of NMI is modified by adding small quantities of stable

38 isotope tracers of this element. In this study, slag enriched with ^{26}Mg was prepared and

39 applied in two high-resistance furnace experiments using either MgO or Al_2O_3 crucibles on a

40 laboratory scale. The added amount of ^{26}Mg was 0.6 % and 0.03 % of the total slag and steel

41 mass, respectively, and hence 10-times lower compared to state-of-the-art tracing methods.

42 Analysis of ^{26}Mg/^{24}Mg isotope ratios in potential Mg sources and several multiphase NMIs

43 was conducted by laser ablation inductively coupled plasma mass spectrometry and the

44 amount of spike was computed via isotope pattern deconvolution. This revealed interactions

45 between slag, steel, and refractories that were unambiguously traced back to the ^{26}Mg-

46 enriched slag, confirming the method's effectiveness for assessing NMI origins and

47 modifications.

48

52

53

1. Introduction

The influence of non-metallic inclusions (NMIs) on several physical and chemical properties is well-studied for many steel grades.[1–4] One major topic concerning the impact of NMIs on steel production is the clogging phenomenon, which occurs during continuous casting of, e.g., Ti-stabilized interstitial free steels.[5, 6] The clogging layer formation can be caused by agglomeration of deoxidation products and can result in quality loss of the steel or interruption of the caster sequence, further leading to higher costs.[7–9] So far, several studies have focused on this phenomenon and found potential sources, formation mechanisms, and countermeasures as summarized in the reviews of Ogibayashi[10] and Michelic et al.[11]

Yet, the origin and formation mechanisms of such interfering NMIs are not fully clarified to date. One approach to identifying their source is the active tracing technique. previous tracing studies investigating slag-related NMI formation in steel reported the use of BaO or SrO as slag tracers, which were added in the form of carbonates ($BaCO_3$ or $SrCO_3$).[12, 13] In another approach, rare earth elements (REEs) were directly added to the melt or as a ferroalloy at a specific point in the production process.[14, 15] Due to the partial reduction of deoxidation products by REEs, NMIs are marked, and their modification over the process can be tracked.[16, 17] However, since REEs influence the chemical and physical properties of the marked NMIs,[15, 18–21] a new tracing approach is needed to study the formation and modification of NMIs during steel production. Hence, unwanted changes in the inclusions' properties, such as their agglomeration tendency or wetting behavior, can be avoided.[18, 22]

A promising alternative approach is the use of isotopes as tracers, i.e. isotopic fingerprinting. George de Hevesy and Friedrich Adolf Paneth pioneered the isotopic fingerprinting approach using radioactive isotopes to characterize chemical elements, which was first applied to study the solubility of low-soluble lead compounds.[23] This method was further evolved by using enriched stable (i.e., non-radioactive) isotope tracers with the major advantage that stable isotopes are long lived and nontoxic.[24] In stable isotope tracer experiments, the isotopic composition of an element in the substance under study is modified far beyond natural abundance variations by adding low levels (i.e. small quantities) of at least one selected stable isotope of this element, thus providing an unambiguous extrinsic tag to this element and hence the substance.[25] By determining the isotopic composition using mass spectrometric techniques such as inductively coupled plasma mass spectrometry (ICP-MS), the isotopically

87 tagged substance can then be followed along its pathway from one compartment to another.

88 These unique assets of the enriched stable isotope tracing method have resulted in its

89 widespread application throughout different research fields, above all in ecological and

90 biological,[26–29] as well as clinical and medical studies.[30–33]

91

92 The application of enriched stable isotope experiments for NMI tracing or metallurgical

93 studies in general has not been reported until now. Pack et al.[34] were the first to investigate

94 the origin of oxidic NMIs in the clogging layer of a submerged entry nozzle using natural, i.e.

95 non-enriched natural abundance variations of oxygen (O) isotopes. They showed that by

96 assessing the natural isotopic variations of O in possible NMI sources such as refractories,

97 slags, atmospheric and process O, and comparing them to the isotopic composition of O in

98 NMIs, potential mechanisms of NMI formation and related clogging could be identified.

99 However, precise source apportionment was hampered by the relatively small and often

100 overlapping natural isotopic variation ranging between approximately +10 ‰ and +25 ‰ in

101 the different investigated source materials.[34] Moreover, potential isotopic fractionation

102 between the O source and oxidic NMI may have caused a change of the O isotopic

103 composition during the process, eventually affecting the final conclusions about NMI

104 formation.

105

106 Considering the drawbacks of the above mentioned approaches, the use of low levels of

107 enriched stable isotopes can be advantageous. For this purpose, dedicated data reduction

108 strategies are required. Isotope pattern deconvolution (IPD) has emerged as a preferred

109 method when introducing only minimal amounts of tracer material is crucial, initially in

110 clinical and biological studies. IPD effectively addresses the challenge of analyzing isotopic

111 mixtures composed of both enriched stable isotopes and those at natural-abundance levels. [35,

112 36]

113 A significant advantage of this mathematical tool is its capacity to determine the individual

114 contributions (referred to as molar fractions) of each input source to a mixture of the natural

115 isotope source and the introduced, isotopically enriched tracer. This functionality is crucial in

116 the deconvolution of interconverting analytes. Additionally, IPD enhances this process by

117 enabling the deduction of even smaller amounts of tracer and reducing the uncertainty

118 surrounding the molar fraction of the tracer, particularly when it is uncertain how much tracer

119 is assimilated during a process.

120 The use of isotopically enriched stable isotopes in combination with isotopic analysis by mass
121 spectrometry and subsequent IPD has proven to be an important tool for studying elemental
122 pathways. For example, Draxler et al.[31] used isotopically enriched magnesium (Mg) to
123 monitor elemental migration during biological degradation of a metallic Mg-based bone
124 implant highly enriched in ^{26}Mg (>99 %) in an animal model. The authors demonstrated the
125 unique potential of the approach for precise source apportionment, especially when combined
126 with spatially resolved isotopic analysis by laser ablation (LA-)ICP-MS, which opens the
127 extension to NMI studies in metallurgical applications. Given its frequent occurrence in NMIs
128 as well as many possible sources of NMI formation such as slags and refractories, Mg with its
129 three stable isotopes (i.e. ^{24}Mg, ^{25}Mg, ^{26}Mg) may be particularly relevant for identifying
130 potential interactions between the phases in the steel/slag/refractory system.
131
132 In the present study, the isotopic fingerprint approach using ^{26}Mg stable isotope as tracer was
133 applied for the first time in an NMI tracing experiment on a laboratory scale. It was
134 hypothesized that by using a slag enriched with low levels of ^{26}Mg stable isotope tracer,
135 possible interactions between the slag, refractories, and NMIs leading to the formation of Mg-
136 containing NMIs in steel could be identified.

2. Materials and methods

2.1. Experimental design

An overview of the experimental design is provided in Table 1. In summary, a MgO-containing slag enriched with ^{26}Mg was prepared and applied in two Tammann-type furnace experiments conducted on a laboratory scale. The two experiments differed in the used refractories and potential Mg sources contributing to NMI formation to assess the method's capability for source tracing of NMIs under different conditions. The first experiment (experiment MG) had two possible Mg sources: the ^{26}Mg-enriched slag and a MgO crucible with natural Mg isotopic composition. In the second experiment (experiment AL), the crucible was dense Al$_2$O$_3$. Sources of Mg in this experiment were the ^{26}Mg-enriched slag as for experiment MG, as well as pre-existing magnesium aluminate (MA)-spinel NMIs with natural Mg isotopic composition from the input material.

Table 1. Summary of the experimental design (details on Mg sources and refractories are provided in the following sections).

Experiment	Refractory	Mg source 1 – Stable isotope tracer	Mg source 2 – Natural isotopic composition
MG	MgO crucible	^{26}Mg-enriched slag	MgO crucible
AL	Al$_2$O$_3$ crucible	^{26}Mg-enriched slag	Pre-existing MA-spinel

2.2. Design of ^{26}Mg-enriched slag

The design of the target Mg isotopic composition for the slag in NMI tracing experiments considered the enriched stable isotope Mg material available commercially, the anticipated natural Mg levels in the input sources, and the expected uncertainty associated with the analytical methods to be used for characterization, particularly LA-ICP-MS. Details of the slag preparation and IPD calculation are provided in sections 2.3 and 2.7.2, respectively.

Figure 1a shows the natural isotopic composition of Mg as reported by the Commission on Isotopic Abundances and Atomic Weights (CIAAW) of the International Union of Pure and Applied Chemistry (IUPAC),[37] as well as the isotopic composition of the ^{26}Mg spike and the resulting ^{26}Mg-enriched slag. The ^{26}Mg spike was pure Mg metal with an ^{26}Mg-enrichment >99 %. The natural background levels of Mg in steel, including potential Mg-containing inclusions in the starting material, as well as the overall uncertainty of Mg isotope ratio data

166   derived from LA-ICP-MS, conservatively estimated to be 20 %, were considered in designing

167   the target enrichment of ^{26}Mg in the slag. Natural isotope abundance variations of Mg,

168   expressed using $\delta^{26/24}$Mg values, are confined to a maximum range between -6 ‰ and 1 ‰

169   (i.e., $\delta^{26/24}$Mg = [-6 ‰, 1‰]; Figure 1b) as compiled in Coplen and Shrestha.[38]

170   Consequently, attaining an uncertainty ≤0.1 ‰ is desirable for the precise measurement of

171   these minute natural isotopic variations.[39]

172

173   To accommodate the aforementioned factors and to achieve raw measurement ratios markedly

174   different from natural Mg isotope ratios, the target mixture ratio between the ^{26}Mg spike and

175   natural Mg in the slag was set to yield a contribution of the ^{26}Mg spike of 20 % and natural

176   Mg of 80 % (molar fraction). This alters the isotopic abundances to 63.29 %, 8.03 %, and

177   28.68 % for ^{24}Mg, ^{25}Mg, and ^{26}Mg, respectively (Figure 1a), resulting in a theoretical $\delta^{26/24}$Mg

178   of 2256 ‰ in the ^{26}Mg-enriched slag as calculated by IPD and shown in Figure 1b. This

179   adjustment significantly surpasses natural levels (Figure 1a and b) and aims for a conservative

180   target relative bias within the possible natural isotopic variation range of Mg. Thereby,

181   identification of potential contributions of the ^{26}Mg-enriched slag to the total Mg in NMIs is

182   achievable even amid substantial uncertainties (up to 50 %, resulting in a variation of

183     $\delta^{26/24}$Mg of approximately ±1000 ‰) in the measured isotope ratios resulting from the applied

184   LA-ICP-MS characterization method.

185
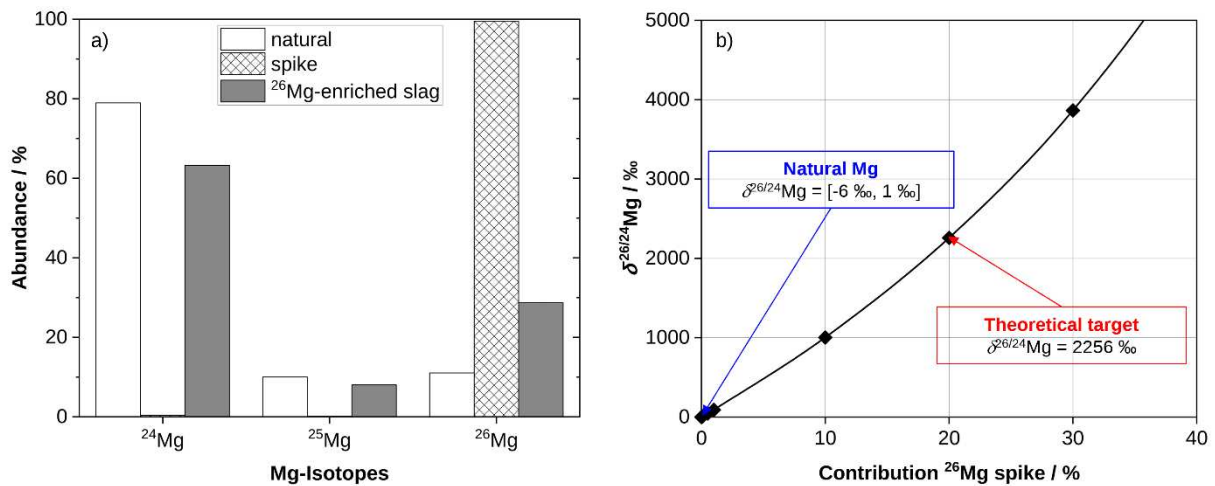
Figure 1. a) Isotopic composition of natural Mg,[37] ^{26}Mg spike, and theoretical isotopic composition of ^{26}Mg-
enriched slag. b) Theoretical $\delta^{26/24}$Mg at different contributions of the ^{26}Mg spike calculated by IPD. Natural Mg
corresponds to a defined $\delta^{26/24}$Mg = [-6 ‰, 1‰], the position is marked by the blue arrow. The black line shows
the theoretical increase of $\delta^{26/24}$Mg with increasing contribution of the ^{26}Mg spike. The theoretical target
$\delta^{26/24}$Mg = [2256 ‰], in the enriched slag is marked by the red arrow.

191

2.3. Preparation of [26]Mg-enriched slag

A schematic of the workflow to prepare [26]Mg-enriched slag is provided in Figure 2.
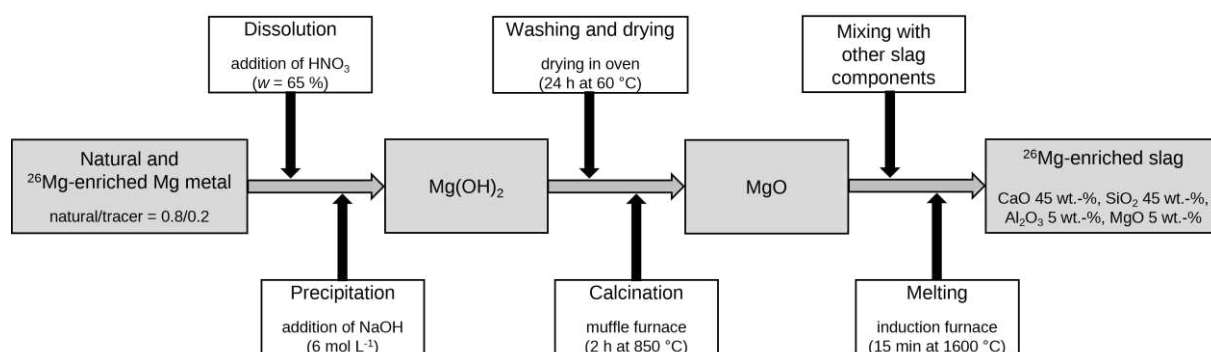
Figure 2. Workflow for the preparation of [26]Mg-enriched slag.

Isotopically enriched elemental Mg with an isotopic composition of 0.37 %, 0.12 %, and 99.51 ± 0.05 % for [24]Mg, [25]Mg, and [26]Mg, respectively, was obtained from Trace Sciences International (Richmond Hill, Ontario, CA, USA). The certificate of analysis and the elemental composition of the material is compiled in Figures S1 and S2 in the Supporting Information. The [26]Mg-enriched metal spike ($m = 90$ mg) was mixed with fine Mg metal chips ($m = 360$ mg; Chair of Nonferrous Metallurgy, Montanuniversität Leoben, Leoben, AT) with natural isotopic composition of 78.99 %, 10.00 %, and 11.01 % for [24]Mg, [25]Mg, and [26]Mg, respectively (Figure 1a), in an acid-cleaned perfluoroalkoxy-polymer (PFA) vial. The applied mixture ratio resulted in the previously mentioned theoretical spike/natural molar fraction of 25. The Mg metal mixture was dissolved in 7 mL of HNO_3 ($w = 65$ %; p.a., Carl Roth GmbH, Karlsruhe, Germany; further purified by sub-boiling distillation), diluted with 10 mL of laboratory water type 1 ($\sigma = 0.055$ µS cm^{-1}; MilliQ IQ 7000, Merck-Millipore, Darmstadt, Germany), and vigorously shaken by hand. The Mg solution was then transferred into an acid-cleaned centrifugation vial and topped up to a total volume of 20 mL using laboratory water type 1, giving a final Mg^{2+} concentration of 0.82 mol L^{-1}. Subsequently, 20 mL of NaOH ($c = 6$ mol L^{-1}; p.a., Carl Roth GmbH, Karlsruhe, Germany) was added drop-wise to fully convert the dissolved Mg^{2+} to $Mg(OH)_2$. The supernatant was discarded, and the obtained $Mg(OH)_2$ precipitate was thoroughly washed using laboratory water type 1 and centrifugation to remove impurities. The washed $Mg(OH)_2$ was then transferred onto a poly(tetrafluoroethylene) (PTFE) foil and dried in a drying cabinet (UF 110, Memmert GmbH + Co. KG, Schwabach, Germany) at 60 °C for 24 h. The dry $Mg(OH)_2$ powder was calcined in a laboratory chamber furnace (Economy, Carbolite Gero GmbH & Co. KG, Neuhausen, Germany) at 850 °C for two hours to produce MgO powder.[40] Finally, the [26]Mg-enriched MgO powder was mixed with the three other slag components, CaO, SiO_2 and Al_2O_3, in a

8

221   carbon crucible and subsequently melted in an induction furnace (MU-900, Indutherm

222   Erwärmungsanlagen GmbH, Walzbachtal/Wössingen, Germany) to obtain the ^{26}Mg-enriched

223   slag with a target composition of 45 g/100g CaO, 45 g/100g SiO$_2$, 5 g/100g of MgO and

224   5 g/100g of Al$_2$O$_3$. The final ^{26}Mg mass fraction in the slag was 0.6 %. The amount of slag

225   required corresponds to 5 % of the total mass of the melt. In the experiments planned in this

226   study, the mass ratio of steel and slag equates to 220 g steel to 11 g slag. Thus, the ^{26}Mg mass

227   fraction over the entire experiment was only 0.04 %. The purities of the slag components are

228   compiled in Table S1 in the Supporting Information. The electrical power for the slag heating

229   was 15 kW. The furnace was flushed with N$_2$ during the entire slag production process. After

230   reaching 1600 °C, the temperature was maintained for 15 min before cooling started.

231

232   The complete method of preparing ^{26}Mg-enriched slag was repeated twice on different days to

233   assess the procedural reproducibility. The major element mass fractions of the ^{26}Mg-enriched

234   slag were determined with a wavelength dispersive XRF (Axios, Malvern Panalytical, UK)

235   using certified and uncertified geological reference material for external calibration. Regular

236   participation in proficiency test program GeoPT (International Association of Geoanalysts)

237   corroborates the data quality.[41]

238   **2.4. Preparation of pre-melt**

239   To produce a consistent pre-melt for both experiments MG and AL, 250 g of pure iron with

240   an O content of 126 µg/g and low concentrations of other alloying elements were heated

241   together with 8 g of an O-rich master alloy with an O content of nearly 0.2 g/100 g in a

242   resistance-heated Tammann-type furnace (Ruhstrat HRTK 32 Sond., Ruhstrat Power

243   Techology GmbH, Bovenden, Germany). The O-rich master alloy was produced by melting

244   chips of electrolytic iron in a high-temperature furnace (HT 64/1, Nabertherm GmbH,

245   Lilienthal, Germany) inside an Al$_2$O$_3$ crucible resulting in an alloy with an O content close to

246   the solubility limit of O in liquid steel at 1600 °C. The starting O content of this pre-melt was

247   approximately 300 µg/g before Al deoxidation to obtain conditions similar to those in

248   industry. The primary goal of producing this Al-deoxidized pre-melt for the trial in MgO

249   crucible was to achieve an inclusion population consisting mainly of Al$_2$O$_3$. The pure iron

250   used for experiment AL already contained traces of Mg, which resulted in the formation of

251   MA-spinel additional to Al$_2$O$_3$ during melting and deoxidation of the iron and the O-rich

252   master alloy in the Tammann-type furnace. The elemental composition of the input materials

253   for both experiments is listed in Table 2.

Sample	C	Si	Mn	Al	O	Fe
	% (g/100 g)					
Experiment MG	0.0015	0.0030	0.0270	0.0010	0.0126	Balance
Experiment AL	0.0040	0.0020	0.0145	0.0033	0.0034	Balance
Master alloy	0.0015	0.0278	0.0268	0.0005	~ 0.2	Balance

254 **Table 2.** Elemental composition of the pure iron used for both trials and the O-rich master alloy.

255

2.5. Melting experiment

A resistance-heated Tammann-type furnace (Ruhstrat HRTK 32 Sond., Ruhstrat Power Technology GmbH, Bovenden, Germany) was chosen as aggregate for the experiments since melting takes place under an inert atmosphere by Ar flushing at 1600 °C. Further, this furnace allows to alloy as well as to take samples during the melting process and thus to track changes in the inclusion population over the process time. Previous publications described this furnace's structure, operating mode and sampling in detail.[42, 43] A schematic illustration of the experimental setup is shown in Figure 3.
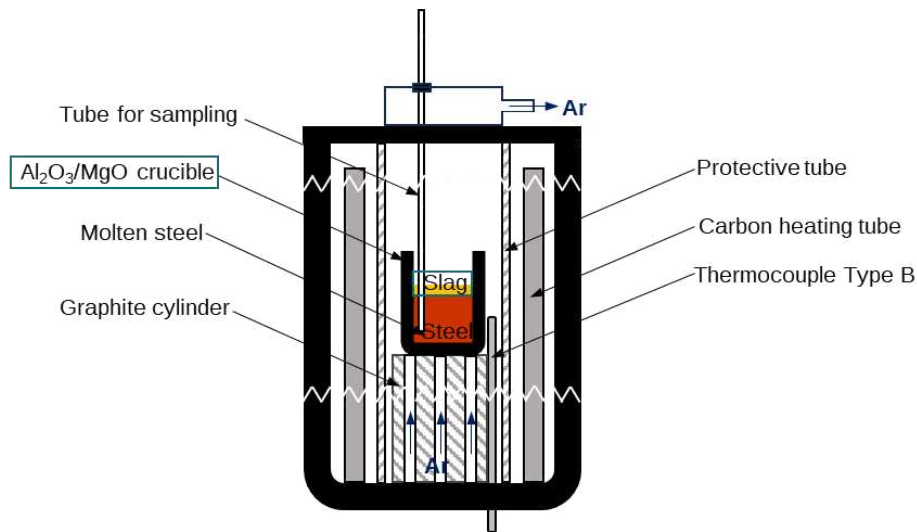
Figure 3. Schematic illustration of the resistance-heated Tammann-type furnace with MgO crucible for experiment MG and with Al₂O₃ crucible for experiment AL. Modified from Truschner et al.[14]

Figure 4 illustrates the timeline of both experiments MG and AL, including the timepoints of slag addition, sampling steel samples (P1-P7) during the melting process, the start of cooling, and the removal of the remaining melt (RM) from the experimental setup.

First, 220 g of the previously produced pre-melt was heated to 1600 °C in the furnace. A quartz rod was used for stirring in the beginning, to increase the interaction area of slag and steel since this furnace has nearly no bath movement otherwise. The first sample (P1) was taken from the untreated pre-melt immediately before adding 11 g of the [26]Mg-enriched slag.

10

275 After slag addition, samples (P2-P7) were taken every five minutes for half an hour before

276 cooling started. An E235 steel tube with an attached Peleus ball was used for sampling.

277 Finally, the remaining melts were cooled inside the furnace to room temperature.
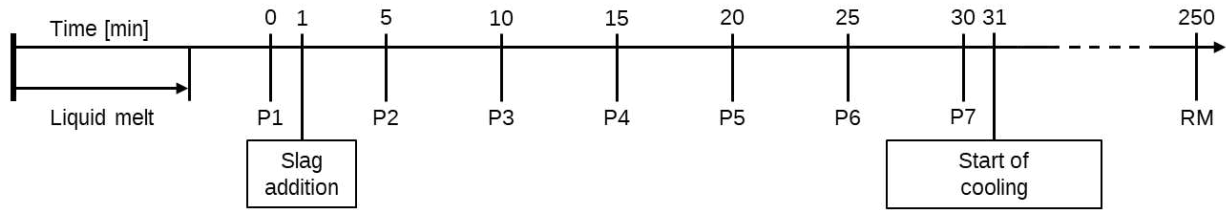
278

279 **Figure 4.** Timeline of both experiments MG and AL marking the sampling and slag addition.

280 **2.6. Analytical methods**

281 **2.6.1. Sample preparation**

282 The high porosity of samples P1-P7 after cutting them out of the steel tube necessitated their

283 compressing by hydraulic pressing. This cold work step was carried out via a hydraulic press

284 (Hydraulische Werkstattpresse 10T, ERBA GmbH, Wien, Austria) with a force equivalent to

285 eight metric tons. These compressed specimens, as well as a disk of the remaining melt from

286 both trials were conductively embedded, ground with silicon carbide (SiC) paper, and

287 polished with diamond suspension with a grain size of 9 µm, 3 µm, and 1 µm. These

288 metallographic sections were used for automated SEM/EDS analysis of NMIs (see details in

289 section 2.6.2). For LA-ICP-MS analysis (see details in section 2.6.3). The sections used for

290 SEM/EDS were further cut to a height of 5 mm to fit into the sample chamber of the LA

291 system. Additionally, the NMIs in the steel samples of experiment AL were marked by using

292 the focused ion beam (FIB) technique,[44][45] given the observed difficulty in the first

293 experiment MG to distinguish them from surface alterations using the light optical

294 microscope (LOM) installed in the LA system. To this end, first an SEM/EDS investigation of

295 the NMIs was implemented to assess their chemical composition before four FIB-markers

296 were applied around the identified Mg-containing NMIs at a distance of 100 µm each. For

297 LA-ICP-MS of the refractories, parts of the new and used crucibles were cold embedded in

298 epoxy resin and ground as the steel samples described above. In case of the used crucibles, the

299 focus was on the investigation of the potential penetration by the slag. For LA-ICP-MS of the

300 slags, droplets of the slags were directly placed into the sample chamber without any prior

301 sample preparation.

2.6.2. SEM/EDS

SEM/EDS is applied to determine the chemical composition, morphology parameters, and spatial distribution of NMIs in the steel samples. At the automated SEM/EDS investigation, all particles with a darker grayscale in the backscattered electron image (BSE) compared to the surrounding steel matrix are detected. An area scan is used to gather the EDS spectra. In this study, automated SEM/EDS investigation was used to determine the relation between Mg-containing NMIs and non-Mg-containing NMIs, as well as the changes of Mg-containing inclusions over the process. The instrument used for this analysis was a field-emitting SEM (JEOL 7200 F; JEOL Germany GmbH, Freising, Germany) equipped with a 100 mm^2 silicon-drift detector (SDD) (Oxford Instruments Ultim Max 100; Oxford Instruments GmbH NanoAnalysis, Wiesbaden, Germany) for EDS analysis. The AZtec Feature software (AZtec 6.0, Oxford Instruments GmbH NanoAnalysis, Wiesbaden, Germany) was applied for automated measurement. The beam energy was 15 keV with a probe current of 13 and a working distance of 10 mm. The resolution was set to 1024 pixels × 960 pixels, and the magnification was 400x. The minimum particle size was 9 pixels with a minimum equivalent circular diameter (ECD) of 1 µm. A single particle was measured for 1 s.

2.6.3. LA-ICP-MS

LA-ICP-MS was used to assess $^{26}Mg/^{24}Mg$ isotope ratios in the ^{26}Mg-enriched slag, new and used MgO and Al_2O_3 crucibles, and NMIs. Two different laser ablation systems were used, including (1) a 213 nm solid-state Nd:YAG laser ablation system (NWR213, Elemental Scientific Lasers, Bozeman, MT, USA) equipped with a TwoVol2 ablation chamber connected to a customized Liebig type quartz gas mixer, and (2) a 193 nm exciplex ArF laser ablation system (imageGeo193, Elemental Scientific Lasers, Bozeman, MT, USA) equipped with a TwoVol3 ablation chamber with an analytical cup connected to a dual concentric injector (DCI). The latter system allows for fast washout and is therefore beneficial to investigate the lateral distribution of elemental and isotopic patterns in micro-sized structures such as NMIs. Both laser ablation systems were coupled to a quadrupole ICP-MS (NexION 2000, Perkin Elmer, Waltham, MA, USA) set to record count rates for m/z 24, 25, and 26 (as well as 13, 27, 29, 43, 57, 60, and 208 for selected analyses) with a total acquisition time of 0.1-0.3 s per data point. Instrument sensitivity was optimized daily using glass SRM 610 (NIST, Gaithersburg, MD, USA), which also served as standard for instrumental isotopic fractionation (IIF) correction of Mg isotopes (see details in section 2.7.2). The samples were analyzed in line-scan mode with a laser beam spot size of 5-50 µm, scan speed of 5-10 µm s^{-1},

335 energy of 20-40 %, pulse repetition rate of 10-40 Hz, and line length up to 5 mm. Helium was

336 used as carrier gas at a flow rate of 0.8-0.9 L min^{-1}. The applied instrumental setups and

337 parameters for all analyses are compiled in the Supporting Information (Table S2).

338 **2.7. Data processing**

339 **2.7.1. SEM/EDS**

340 Apart from NMIs, scratches, pores and grinding residues were detected at the automated

341 SEM/EDS measurement of samples P1-P7 and RM due to their darker appearance compared

342 to the steel matrix in BSE images. Hence, an adjustment of the received data was required.

343 Detected particles with an ECD greater than 15 µm were removed since the evaluation

344 focused on microscopic NMIs. After this correction, particles with no non-metallic bonding

345 partners were deleted. Furthermore, particles with a chemical composition similar to that of

346 the steel matrix were removed from the data set. In the last step, the NMIs were grouped into

347 different types concerning their chemical composition. A detailed description of the manual

348 steel cleanness evaluation can be found in Thiele et al. [46]

349 **2.7.2. LA-ICP-MS**

350 Processing of LA-ICP-MS data was conducted in Microsoft Excel®. First, raw intensities

351 (counts) of each m/z were blank corrected by subtracting the average gas blank intensity (n =

352 50) recorded before each line. Blank-corrected $^{26}Mg/^{24}Mg$ ratios were calculated point-by-

353 point and then further corrected for IIF by applying Russell's law [47] (Eq. 1a). The

354 fractionation factor, f, was calculated using SRM 610 (NIST, USA) as standard, assuming a

355 true, natural $^{26}Mg/^{24}Mg$ ratio of 0.1394 [31] (Eq. 1b). For ^{26}Mg-enriched slag and crucibles,

356 $^{26}Mg/^{24}Mg$ of SRM 610 was analyzed directly before or after the respective sample with

357 congruent LA-ICP-MS parameters. For analysis of NMIs, the daily average $^{26}Mg/^{24}Mg$ of

358 SRM 610 analyzed using a laser spot size of 50 µm was used due to inadequate signal-to-

359 noise separation during SRM 610 analysis when using a spot size of only 10 µm applied for

360 NMI analysis to resolve Mg features at the microscale. Finally, IIF-corrected $^{26}Mg/^{24}Mg$

361 ratios in samples were converted to delta (δ, in ‰) values (Eq. 1c).

$$\left(^{26}Mg/^{24}Mg\right)_{corr} = \left(^{26}Mg/^{24}Mg\right)_{meas} \times \left(\frac{M(^{26}Mg)}{M(^{24}Mg)}\right)^{f} \qquad \textbf{(Eq. 1a)}$$

$$f = \ln\left(\frac{(^{26}Mg/^{24}Mg)_{true}}{(^{26}Mg/^{24}Mg)_{meas}}\right)\Big/\ln\left(\frac{M(^{26}Mg)}{M(^{24}Mg)}\right) \qquad \text{(Eq. 1b)}$$

$$\delta^{26/24}Mg = \frac{(^{26}Mg/^{24}Mg)_{corr}}{(^{26}Mg/^{24}Mg)_{nat}} - 1 \qquad \text{(Eq. 1c)}$$

362   where $M(^{26}Mg)$ and $M(^{24}Mg)$ denote the atomic weights as provided by CIAAW.[37]

363   Isotope pattern deconvolution (IPD) using multiple linear regression was applied to assess the

364   molar fraction (in %) of ^{26}Mg derived from the ^{26}Mg spike to the total Mg content in ^{26}Mg-

365   enriched slag, crucibles, and NMIs.[31, 48] The model allows to deconvolute the contribution of

366   up to three sources (x_{source}) to the total amount of Mg following calculation of the individual

367   isotopic abundances of all Mg stable isotopes according to Eqs. 2a-b:

$$A^{i}_{spl} = \frac{R^{i}_{corr}}{\sum_{i=1}^{n} R^{i}_{corr}} \qquad \text{(Eq. 2a)}$$

$$\begin{bmatrix} A^{24}_{spl} \\ A^{25}_{spl} \\ A^{26}_{spl} \end{bmatrix} = \begin{bmatrix} A^{24}_{source\,1} & A^{24}_{source\,2} & A^{24}_{source\,3} \\ A^{25}_{source\,1} & A^{25}_{source\,2} & A^{25}_{source\,3} \\ A^{26}_{source\,1} & A^{26}_{source\,2} & A^{26}_{source\,3} \end{bmatrix} \times \begin{bmatrix} x_{source\,1} \\ x_{source\,2} \\ x_{source\,3} \end{bmatrix} + \begin{bmatrix} e^{24} \\ e^{25} \\ e^{26} \end{bmatrix} \qquad \text{(Eq. 2b)}$$

368

369   where A^{i}_{spl} denotes the isotopic abundance of a single Mg isotope (i) in the sample (spl) and

370   R^{i}_{corr} denotes the IIF-corrected Mg isotope ratios. Because there are more knowns (isotopic

371   abundances) than unknowns (molar fractions of two sources, including (1) ^{26}Mg spike and (2)

372   natural Mg) in the matrix model, an error vector is included.[30, 48]

373

374   For final data plotting, values smaller than the instrumental limit of quantification (LOQ = 10

375   × standard deviation (s) of ^{24}Mg in the gas blank before and after each line) were set to zero.

376   For the ^{26}Mg-enriched slag and crucibles, i.e., samples with a relatively homogeneous Mg

377   distribution, the moving average (n = 10) was calculated for signal smoothing,[49] and outliers

378   were removed based on a $2s$ (95 % confidence interval) criterion.[48] For NMIs, i.e. samples

379   with a highly heterogeneous Mg distribution at the microscale, the central moving average

380   (n = 3) was calculated for signal smoothing, and no direct outlier correction was performed

381   due to the small sample size ranging between only 10-25 individual data points per NMI.

382   However, values with unrealistically low (<0 %) or high (>100 %) contributions of the ^{26}Mg-

383   enriched spike or natural Mg were excluded to account for instrumental bias. Unless stated

384   otherwise, errors on average $\delta^{26/24}Mg$ values reported in text are expressed as combined

385   uncertainties (u_c; k = 1) including the between- and within-line variability, considering at least

386   three individual lines.

3. Results

3.1. Characterization of ^{26}Mg-enriched slag

The developed method for preparing ^{26}Mg-enriched slag was evaluated by assessing the slags' chemical characteristics. First, the elemental mass balance of two individual trials conducted on two different days for preparation of the ^{26}Mg-enriched slag for experiments MG and AL was assessed. Overall, the metallic Mg, including the ^{26}Mg-enriched spike and Mg metal chips, was converted to dry ^{26}Mg-enriched MgO powder with an average recovery of 108 % ± 9 % (mean ± s), demonstrating a quantitative reaction. Subsequently, the prepared ^{26}Mg-enriched MgO was melted together with CaO, SiO$_2$, and Al$_2$O$_2$, producing ^{26}Mg-enriched slag with an elemental composition in agreement with the theoretical target values as confirmed by XRF analysis (Table 3).

Table 3. Target and experimental elemental and isotopic composition of the ^{26}Mg-enriched slag.

Sample	CaO	SiO$_2$	Al$_2$O$_3$	MgO	Others [a]	$\delta^{26/24}$Mg
	% (g/100 g)					‰
Slag – theoretical	45.0	45.0	5.0	5.0	–	2256
Slag – experimental	44.9	45.5	4.5	4.5	0.6	1925 ± 148

[a] Mainly Na$_2$O (w = 0.3 %) with trace amounts of TiO$_2$ (w = 0.06 %), Fe$_2$O$_3$ (w = 0.04 %), P$_2$O$_5$ (w = 0.02 %), SO$_3$ (w = 0.02 %), K$_2$O (w = 0.02 %), and SrO (w = 0.01 %).

In addition to the elemental characteristics, the ^{26}Mg-enriched slags produced for experiments MG and AL were assessed for their ^{26}Mg/^{24}Mg ratios, expressed as $\delta^{26/24}$Mg values (Eq. 1c), using LA-ICP-MS. The average measured $\delta^{26/24}$Mg was 1820 ‰ ± 95 ‰ for experiment MG and 2030 ‰ ± 83 ‰ for experiment AL, resulting in an average $\delta^{26/24}$Mg of 1925 ‰ ± 148 ‰ (mean ± s) for both slags (Table 3). This value was close to the theoretical target $\delta^{26/24}$Mg of 2256 ‰ predicted by IPD (Figure 1b) and indicated a contribution of 18 % (equating to a molar fraction of 21 %) of ^{26}Mg derived from the ^{26}Mg spike to the total Mg content in the slag. Results of all line-scan analyses, including ^{24}Mg intensities, $\delta^{26/24}$Mg values, as well as individual contributions of the ^{26}Mg spike and natural Mg are compiled in Table S3 in the Supporting Information.

15

3.2. Experiment MG (MgO crucible)

After melting in the Tammann-type furnace, the samples P1-P7 and the remaining melt were first investigated for their micro cleanness by automated SEM/EDS analysis. Figure 5 shows that the proportion of Mg-containing NMIs over all detected NMIs increased over the process. Sample P1, which was taken before slag addition, had a low proportion of Mg-containing NMIs with 2.78 %. Over the process, the proportion of Mg-containing NMIs showed a general rising, albeit varying trend. The remaining melt had the highest proportion of Mg-containing NMIs with 66.04 %.
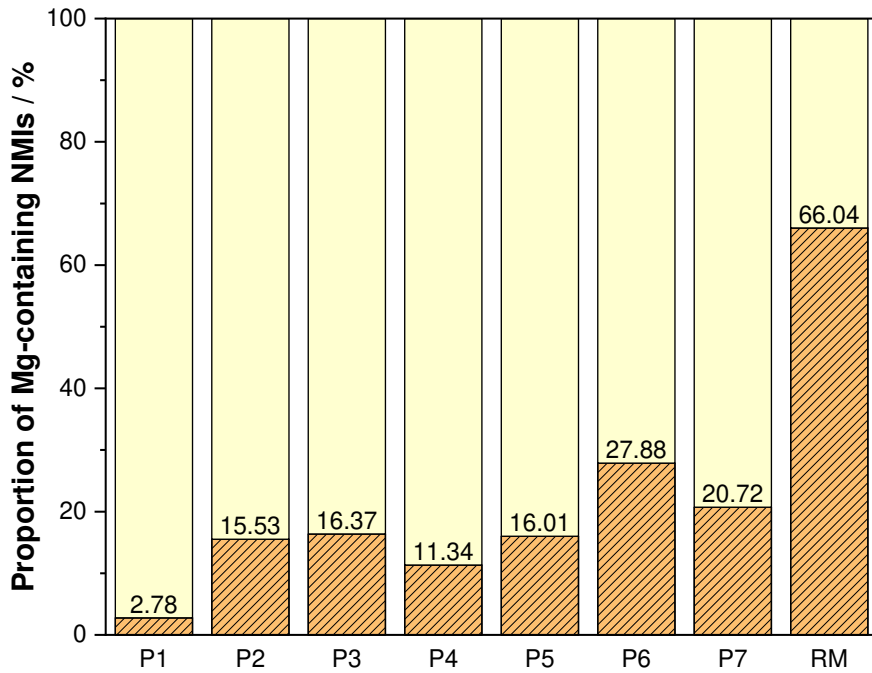
Figure 5. Change in the proportion of Mg-containing NMIs over the process time for samples P1-P7 and the remaining melt (RM) in experiment MG.

Table 4 lists the mean ECDs and the associated standard deviation of all detected NMIs and all Mg-containing NMIs in the pre-melt, samples P1-P7, and the remaining melt. The size of the Mg-containing NMIs in samples P1-P7 varied between 2.23 µm ± 1.08 µm (P6) and 2.76 µm ± 1.14 µm (P1). The mean ECD of the detected particles increased over the process and reached its maximum in the remaining melt with 3.22 µm ± 1.74 µm for Mg-containing NMIs and 3.02 µm ± 1.87 µm for all NMIs.

16

Table 4. Mean ECDs and standard deviation (*s*) of all detected NMIs and of all Mg-containing NMIs in µm for the pre-melt, samples P1-P7, and the remaining melt (RM) of experiment MG

Sample	Mean ECD of all NMIs [µm]	Mean ECD of Mg-containing NMIs [µm]
Pre-melt	2.46 ± 1.65	4.22 ± 1.85
P1	1.39 ± 0.57	2.76 ± 1.14
P2	1.54 ± 0.78	2.29 ± 1.16
P3	1.56 ± 0.82	2.28 ± 1.22
P4	1.52 ± 0.63	2.40 ± 1.04
P5	1.61 ± 0.68	2.49 ± 1.16
P6	1.64 ± 0.82	2.23 ± 1.08
P7	1.63 ± 0.78	2.41 ± 1.12
RM	3.02 ± 1.87	3.22 ± 1.74

The main inclusion type in the pre-melt with an area fraction of 94.39 % of all detected NMIs was Al_2O_3, followed by MA-spinel with 1.82 %. The remaining detected NMIs were SiO_2 and multiphase NMIs such as $Al_2O_3 \cdot SiO_2$. In samples P1-P7 and in the remaining melt, the main NMI types were MA-spinel, complex multiphase NMIs consisting of MA-spinel surrounded by a (Ca, Si, Al, Mg) oxide, as well as Al_2O_3. In the remaining melt the proportion of these three main NMI types were MA-spinel, MA-spinel surrounded by a (Ca, Si, Al, Mg) oxide, and Al_2O_3, accounting for 42.1 %, 23.4 %, and 6.3 %, respectively, of all detected NMIs. Exemplary BSE images as well as the elemental mappings of the two main NMI types in samples P1-P7 and the remaining melt are shown in Figure 6.
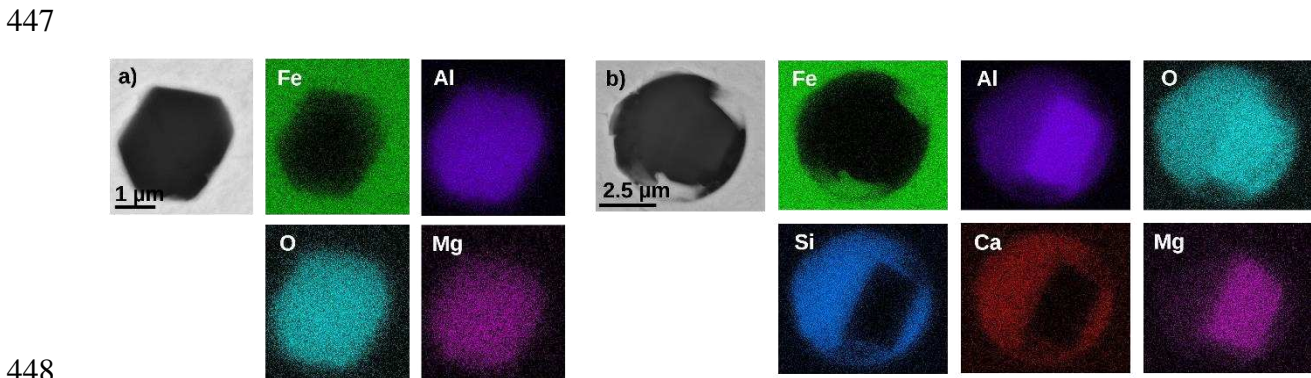
Figure 6. BSE-image and corresponding elemental mapping of a) an MA-spinel of P3, and b) a multiphase NMI of remaining melt formed by steel/slag interactions in experiment MG. Color scales in element maps correspond to relative elemental contents from low (dark) to high (bright).

After the micro cleanness investigation, LA-ICP-MS was conducted on randomly selected NMIs as well as the new and used MgO crucible. The LOM image, ^{24}Mg intensities, and $\delta^{26/24}$Mg isotope ratios of the line-scan analyses across two exemplary NMIs in the remaining

456   melt are presented in Figure 7. Results of all line-scan analyses of the new and used MgO
457   crucible are compiled in Table S4 in the Supporting Information.

458
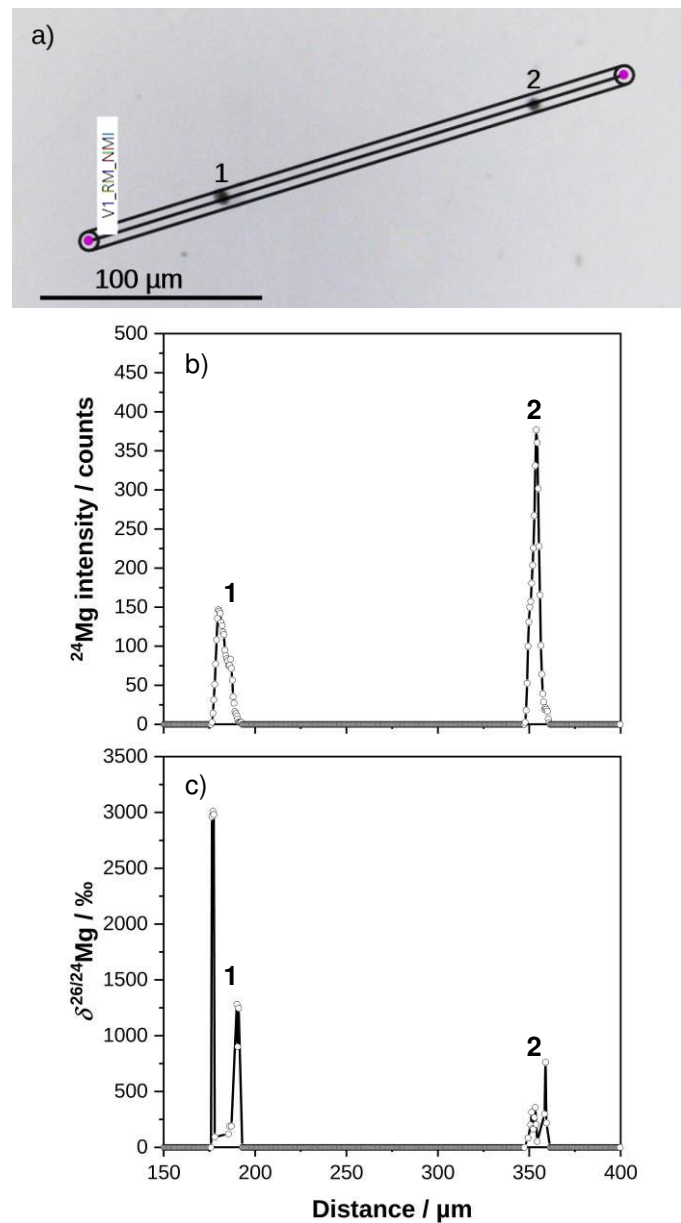
Figure 7. a) LOM image, b) ^{24}Mg intensity, and c) $\delta^{26/24}$Mg isotope ratio across Mg-containing NMIs in the
remaining melt of experiment MG. Lines connecting data points in b) and c) are guides to the eye.

462   The line-scan analyses across the two investigated NMIs in the remaining melt, denoted as
463   NMI-1 and NMI-2 in Figure 7, showed comparable patterns of the ^{24}Mg intensity and
464    $\delta^{26/24}$Mg isotope ratios. While the ^{24}Mg intensity was consistently below the LOQ in the steel
465   matrix, a substantial increase to a maximum of 147 counts and 377 counts was observed when
466   scanning across NMI-1 and NMI-2, respectively (Figure 7b). This confirms the presence of
467   Mg in these NMIs as shown in the Mg maps of the MA-spinel and multiphase NMIs in the
468   remaining melt obtained by SEM/EDS (Figure 6). However, while the maximum ^{24}Mg

18

469   intensity was observed in the center area for both NMI-1 and NMI-2 (Figure 7b), maximum

470      $\delta^{26/24}$Mg values of up to 3008 ‰ (NMI-1) and 762 ‰ (NMI-2) were observed in the outer

471   area of these NMIs (Figure 7c). Accordingly, the IPD-calculated contribution of the ^{26}Mg

472   spike was dependent on the lateral positioning across the NMIs, showing minimum

473   contribution of the ^{26}Mg spike down to 1.07 % (NMI-1) and 0.71 % (NMI-2) in the center

474   area, framed by maximum contributions up to 16.6 % (NMI-1) and 7.50 % (NMI-2) in the

475   outer areas. This results in a contribution of Mg from the slag in the analyzed NMIs of up to

476   approximately 90 %.

477

478   For the new and used MgO crucible, substantial within-line variability of the ^{24}Mg intensity

479   up to 53 % relative standard deviation was observed (Table S4), reflecting the high porosity

480   of the material. The average $\delta^{26/24}$Mg isotope ratio of the new MgO crucible was 152 ‰ ±

481   140 ‰ (Table S4) and hence not different from natural Mg (Figure 1) with respect to the

482   combined uncertainty. However, a substantial difference compared to the ^{26}Mg-enriched slag

483   used in this experiment ($\delta^{26/24}$Mg = 1820 ‰ ± 95 ‰; Table S3) was observed. The average

484      $\delta^{26/24}$Mg isotope ratio of the used MgO crucible, i.e. after the melting experiment, was

485   50 ‰ ± 26 ‰ (Table S4). Thus, there is no evidence of ^{26}Mg spike from the slag in the used

486   crucible, as also shown by the negligible contribution of the ^{26}Mg spike of 0.48 % ± 0.21 %

487   (Table S4) to the total Mg calculated via IPD.

488   **3.3. Experiment AL (Al$_2$O$_3$-crucible)**

489   Figure 8 illustrates the change in the proportion of Mg-containing NMIs over the process time

490   for experiment AL. Sample P1 taken before slag addition had a high proportion of Mg-

491   containing NMIs with 45.85 %. After slag addition, the proportion varied considerably

492   between 15.40 % (P7) and 36.82 % (P5). The highest proportion of Mg-containing NMIs was

493   detected in the remaining melt with 66.70 %. No steady increase over time was observed in

494   contrast to experiment MG.
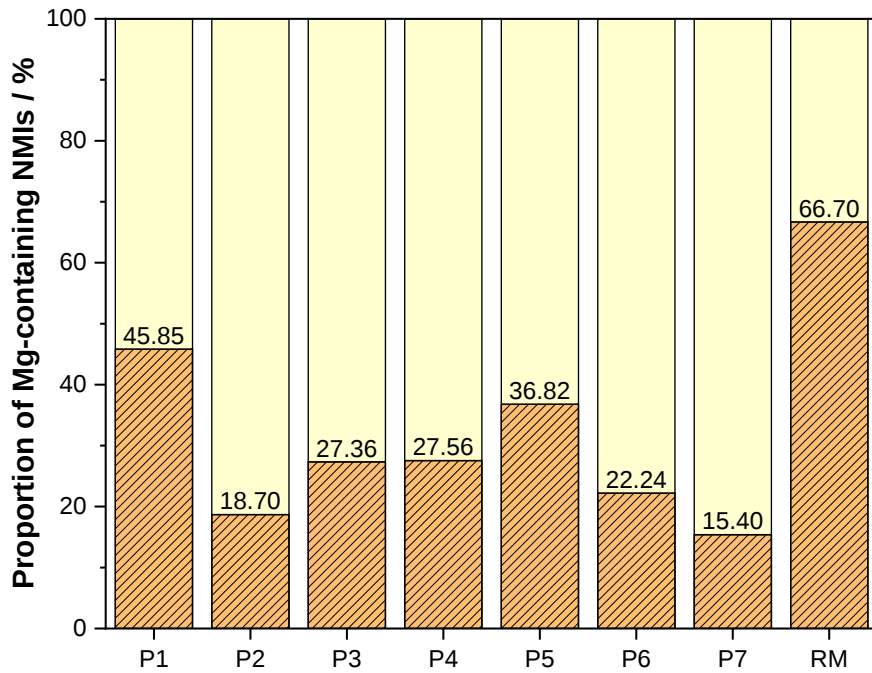
Figure 8. Change in the proportion of Mg-containing NMIs over the process time for samples P1-P7 and the remaining melt (RM) in experiment AL.

The main inclusion types in the pre-melt were MA-spinel and Al_2O_3 with an area fraction of 72.85 % and 24.41 %, respectively, of all detected NMIs. The mean ECDs of all detected NMIs and all Mg-containing NMIs for the pre-melt, samples P1-P7, and remaining melt are listed in Table 5. For Mg-containing NMIs, the mean ECD shows minimal variation, ranging from 2.60 μm ± 1.02 μm (P5) to 2.99 μm ± 1.28 μm (P2) throughout the process, indicating a stable trend with no discernible increase or decrease over time. In comparison, the mean size of all detected particles in samples P1-P7 decreased over the process from 3.23 μm ± 1.55 μm (P2) to 1.87 μm ± 1.12 μm (P7). As for experiment MG, the mean ECD increased for the detected NMIs and the Mg-containing NMIs in the remaining melt. The main NMI types in the remaining melt were MA-spinel, multiphase NMIs consisting of MA-spinel and a (Ca, Si, Al, Mg) oxide, and Al_2O_3, accounting for 51.0 %, 20.8 %, and 8.5 %, respectively, of all detected NMIs.

Table 5. Mean ECDs and standard deviation of all detected NMIs and of all Mg-containing NMIs in μm for the pre-melt, samples P1-P7, and the remaining melt (RM) of experiment AL

Sample	Mean ECD of all NMIs [μm]	Mean ECD of Mg-containing NMIs [μm]
Pre-melt	3.37 ± 1.85	2.76 ± 1.15
P1	3.00 ± 1.88	2.75 ± 1.23
P2	3.23 ± 1.55	2.99 ± 1.28
P3	3.00 ± 2.06	2.76 ± 1.32
P4	2.55 ± 2.05	2.64 ± 1.11
P5	2.38 ± 1.66	2.60 ± 1.02
P6	2.11 ± 1.25	2.65 ± 0.85
P7	1.87 ± 1.12	2.75 ± 1.12
RM	3.58 ± 1.93	3.57 ± 1.50

The modification of NMIs by the slag is shown in Figure 9 on the example of an MA-spinel. In Figure 9a, a natural homogeneous pre-existing MA-spinel in sample P1 is shown. In comparison, Figure 9b shows a modified MA-spinel in the remaining melt consisting of an MA-spinel in the center area surrounded by a (Ca, Si, Al, Mg) oxide.
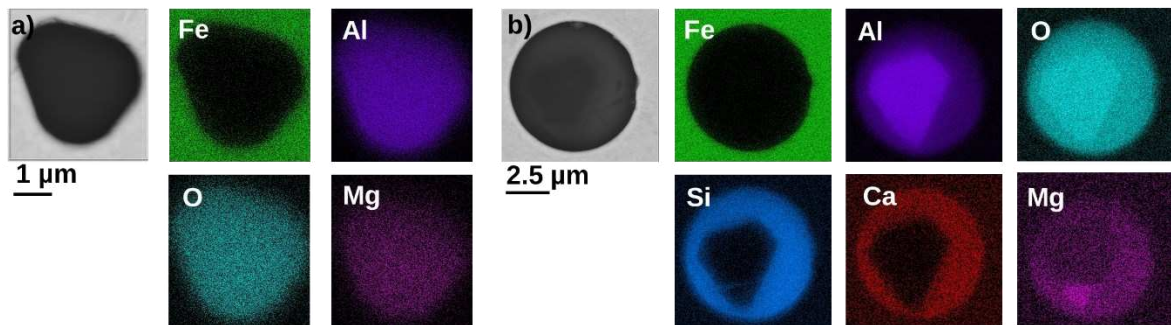
Figure 9. BSE-image and corresponding elemental mapping of a) an MA-spinel of P1, b) a multiphase NMI of remaining melt formed by steel/slag interactions in experiment AL. Color scales in element maps correspond to relative elemental contents from low (dark) to high (bright).

As for experiment MG, NMIs were analyzed by LA-ICP-MS. However, in experiment AL, the NMIs were also marked by FIB, which facilitated the retrieval of the exact same NMI as previously analyzed by SEM/EDS using the LOM installed in the laser ablation system. Figure 10 shows a BSE-image of an examplary FIB-marked heterogenous NMI and the corresponding elemental mappings. The illustrated NMI represents a MA-spinel surrounded by a complex (Ca, Si, Al, Mg) oxide found in the remaining melt.

539   Figure 10 shows a BSE-image of an examplary FIB-marked heterogenous NMI and the

540   corresponding elemental mappings. The illustrated NMI represents a MA-spinel surrounded

541   by a complex (Ca, Si, Al, Mg) oxide found in the remaining melt.
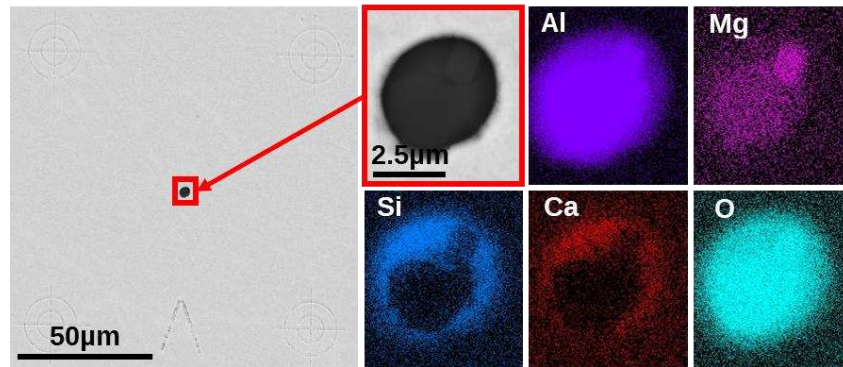
542

543   **Figure 10.** BSE image and elemental mapping of a FIB-marked multiphase NMI found in the remaining melt of
544   experiment AL. Color scales in element maps correspond to relative elemental contents from low (dark) to high
545   (bright).

546

547   The LOM images, ^{24}Mg intensities, and $\delta^{26/24}$Mg isotope values of the LA-ICP-MS line-scan

548   analyses across two exemplary, FIB-marked NMIs in the remaining melt of experiment AL

549   are presented in Figure 11. Results of all line-scan analyses of the new and used Al_2O_3

550   crucible are compiled in Table S4 in the Supporting Information.

551
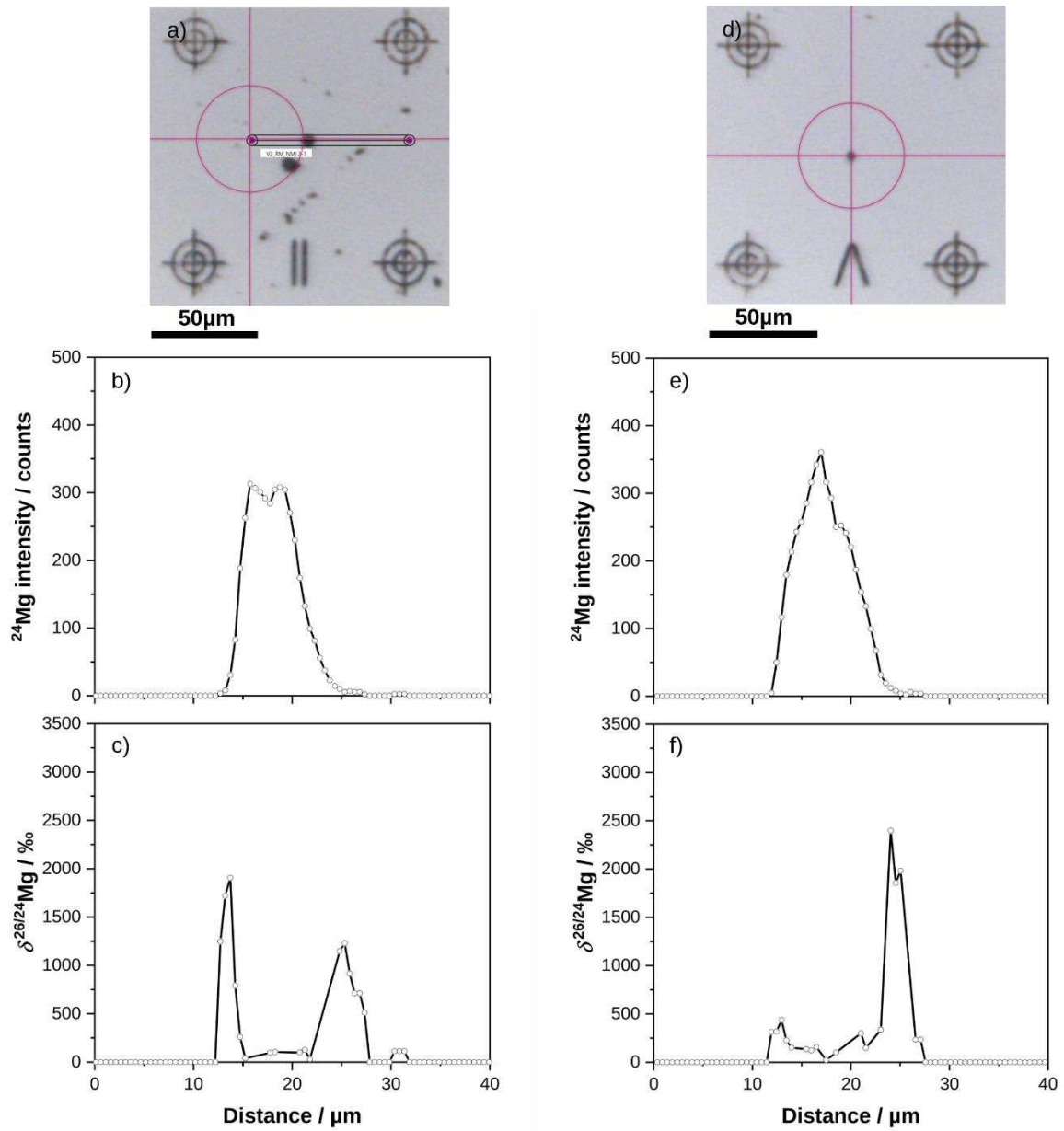
Figure 11. a) and b) LOM images, b) and e) ^{24}Mg intensities, and c) and f) $\delta^{26/24}$Mg isotope ratios across Mg-containing NMIs in the remaining melt of experiment AL. Lines connecting data points in b), c), e), and f) are guides to the eye.

23

555 For both shown NMIs, comparable patterns of the ^{24}Mg intensities and $\delta^{26/24}$Mg isotope

556 values, were observed (Figure 11), which resembled those found in experiment MG (Figure 7).

557 The ^{24}Mg intensity was below the LOQ in the steel matrix but increased substantially to a

558 maximum of 313 counts and 361 counts for NMI-1 and NMI-2 (Figure 11b andFigure 11e),

559 again confirming the presence of Mg in these NMIs as shown by elemental mappings of the

560 SEM/EDS analysis (Figure 9 and Figure 10). The maximum ^{24}Mg intensity was observed in

561 the center area for both NMI-1 and NMI-2 (Figure 11b and 11e), whereas maximum $\delta^{26/24}$Mg

562 values of up to 1907 ‰ (NMI-1) and 2027 ‰ (NMI-2) were observed in the outer area of

563 these NMIs (Figure 11c and 11f). Therefore, also the IPD-calculated contribution of the ^{26}Mg

564 spike was as in experiment MG dependent on the lateral positioning across the NMIs,

565 showing minimum contributions down to 0.39 % (NMI-1) and 0.05 % (NMI 2) in the center

566 area, surrounded by maximum contributions up to 14.8 % (NMI-1) and 11.0 % (NMI 2) in the

567 outer areas. This results in a contribution of Mg from the slag in the analyzed NMIs of up to

568 approximately 80 %.

569

570 Analysis of the new and used Al_2O_3 crucible on the same measurement day and using the

571 same LA-ICP-MS parameters (Table S2), thus ensuring direct comparability of the recorded

572 ^{24}Mg intensity data, showed an increase of the average ^{24}Mg intensity by approximately one

573 order of magnitude in the used crucible after the melting experiment (Table S4). The average

574 $\delta^{26/24}$Mg isotope ratio of the new Al_2O_3 crucible was 4 ‰ ± 100 ‰ (Table S4) and hence in

575 agreement with natural Mg (Figure 1) but substantially different to the ^{26}Mg-enriched slag

576 used in this experiment ($\delta^{26/24}$Mg = 2030 ‰ ± 83 ‰; Table S3). For the used Al_2O_3 crucible,

577 the average $\delta^{26/24}$Mg isotope ratio increased to 1471 ‰ ± 522 ‰ (Table S4).

578

579 In addition to bulk analysis of randomly selected parts of the used Al_2O_3 crucible, the

580 interaction zone between the crucible and the slag was investigated by LA-ICP-MS. Results

581 are shown in Figure 12. The ^{24}Mg intensity increased from about 200 counts at the starting

582 point of the line-scan (marked as 0 µm in Figure 12a) in the crucible to about 20000 counts at

583 the end point (marked as 1500 µm in Figure 12a) in the adherent slag residue (Figure 12b).

584 The $\delta^{26/24}$Mg isotope ratio increased from about 200 ‰ to 2000 ‰ from start to end along the

585 line, showing a linear trend of increased ^{26}Mg spike contribution from about 2 % to 10 %

586 within the crucible (distance 0-800 µm), until reaching a stable plateau of about 18 % when

587 on the slag (Figure 12c). The average $\delta^{26/24}$Mg isotope ratio of the used slag, obtained by

588 analyzing three individual line-scans across different pieces of the residual (i.e. used) slag,

24

589 was 1969 ‰ ± 96 ‰, indicating a contribution of the ^{26}Mg spike of 18.2 % ± 0.7 % (Table

590 S3). This corresponds to the original isotopic composition of the slag (Table 3).

591
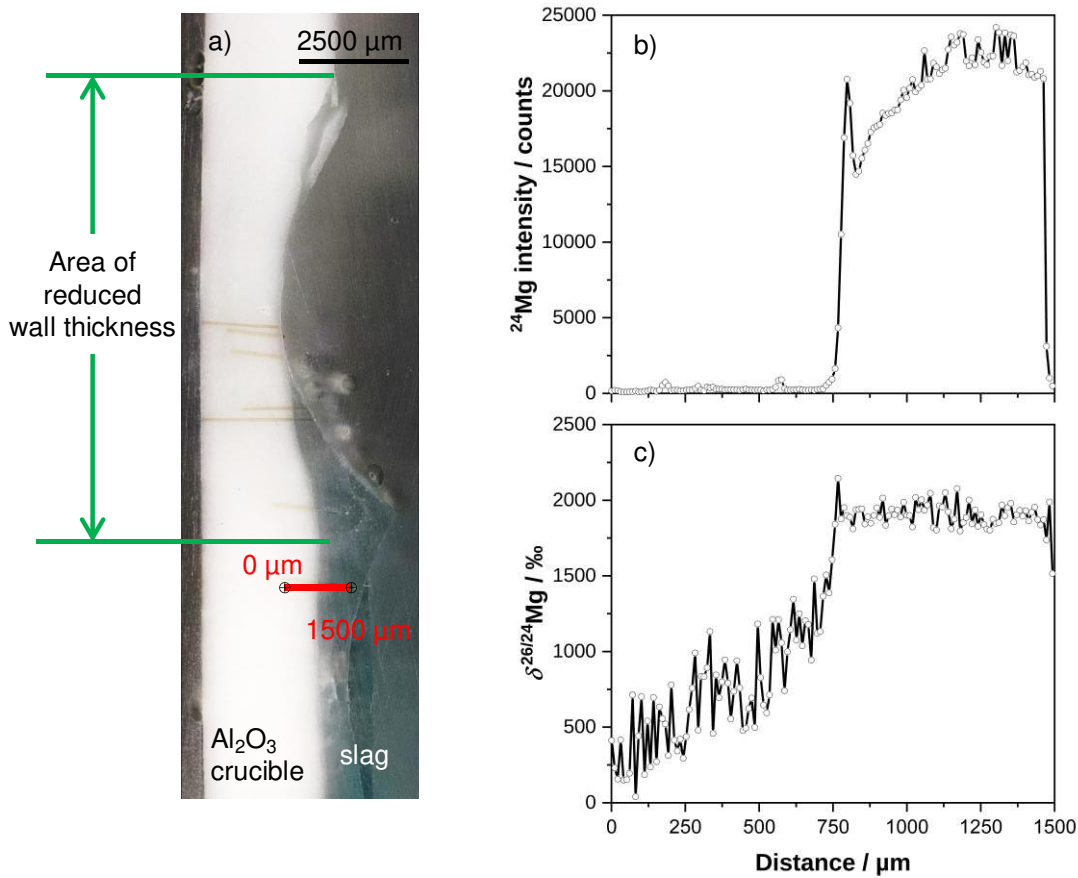
Figure 12. a) LOM image, b) ^{24}Mg intensity, and c) $\delta^{26/24}$Mg isotope ratio at the phase interface between Al$_2$O$_3$ crucible and ^{26}Mg-enriched slag in experiment AL. Lines connecting data points in b) and c) are guides to the eye.

4. Discussion

4.1. Comparison of micro cleanness in both experiments

597 The SEM/EDS evaluation of the NMI distribution over the course of the melting experiment

598 revealed distinct differences between experiments MG and AL. The proportion of Mg-

599 containing NMIs over all NMIs as well as the change of the number of NMIs per mm²

600 between the pre-melt and the remaining melt are shown in Figure 13.

25
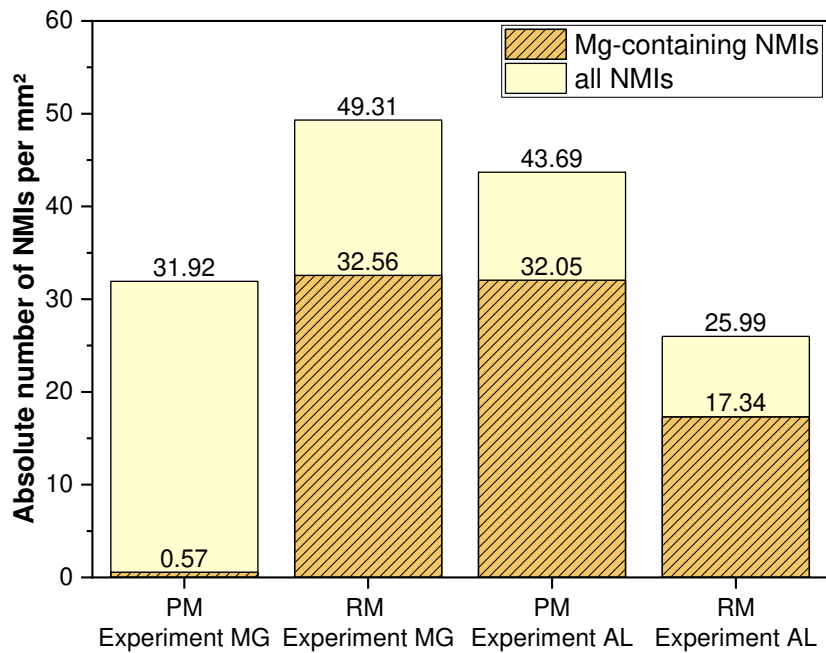
Figure 13. Comparison of NMI distribution in the pre-melts (PM) and remaining melts (RM) of experiments MG and AL.

The pre-melt of experiment MG contained mainly Al_2O_3 NMIs, while the prevailing NMI type detected in the pre-melt of experiment AL was an MA-spinel with an area fraction of 72.85 %. Thus, the number of Mg-containing NMIs was already higher for samples P1-P7 in experiment AL as compared to experiment MG.

Regarding the NMI distribution, another distinction between the two trials occurred. The number of detected Mg-containing NMIs increased nearly steadily over the process time in experiment MG (Figure 5). In comparison no trend was observed in experiment AL (Figure 8). About 66 % of all detected NMIs contained Mg in the remaining melts of both experiments.

The two experiments differed especially in the number of NMIs per square millimeter of steel (Figure 12). In experiment MG, the number of NMIs per mm² increased from 31.92 NMI/mm² in the pre-melt to 49.31 NMI/mm² in the remaining melt, while it was reduced from 43.69 NMI/mm² to 25.99 NMI/mm² in experiment AL. This clear difference between the two experiments was caused by three reasons: First, no slag was found after cooling in experiment MG, leading to the conclusion that the slag was absorbed over the process time by the not-densely sintered MgO crucible, hindering separation of NMIs into the slag. In experiment AL, the steel was in contact with the slag over the whole process time and hence approximately 40 % of NMIs were absorbed by the slag due steel/slag interactions that

26

occurred despite the low bath movement. Second, the NMIs in experiment MG had a long contact time with the MgO crucible, resulting in a higher number of Mg-containing NMIs. Third, the number of NMIs per mm² in the pre-melt of experiment AL was more than 25 % higher compared to experiment MG, and furthermore, it already contained of MA-spinel NMIs with a proportion of >70 %.

The mean ECD in experiment MG slightly increased over time in samples P1-P7 and reached its maximum value in the remaining melt. Compared to that, the mean ECD decreased over time in experiment AL. The decrease in the mean ECD can be caused by interaction with the slag. In the case of experiment MG, the values of the ECDs and the related standard deviations were lower than in experiment AL for non-Mg-containing NMIs in samples P1-P7. However, the values of the mean ECDs and the related standard deviations were almost similar in the remaining melt for both experiments, likely due to the slow cooling inside the furnace and related grain growth.

4.2. Stability and interactions of the ^{26}Mg-enriched slag with NMIs and refractories

The slag residues retrieved in experiment AL enabled the analysis of the slags' ^{26}Mg-enrichment stability over the melting process. No differences in the $\delta^{26/24}$Mg isotope ratio between the slag residues and the new slag used in this experiment were found with respect to the uncertainty (Figure 14), indicating that the ^{26}Mg-enrichment is fully conserved and stable throughout the high-temperature melting process and subsequent cooling of the melt in the Tammann-type furnace. This high process stability without significant isotopic fractionation is crucial for further interpretation of potential slag interactions with refractories and NMIs, as measured patterns of distinct ^{26}Mg enrichment in these potential sinks will now truly reflect slag-derived Mg inputs.

Consequently, each NMI originating from slag interactions will exhibit an isotopic composition of Mg which is markedly different than those originating from natural Mg sources, irrespective of the process. Although no slag residues were retrieved in experiment MG, a similar process stability can be presumed for the ^{26}Mg-enriched slag used in this experiment given the overall identical process parameters.
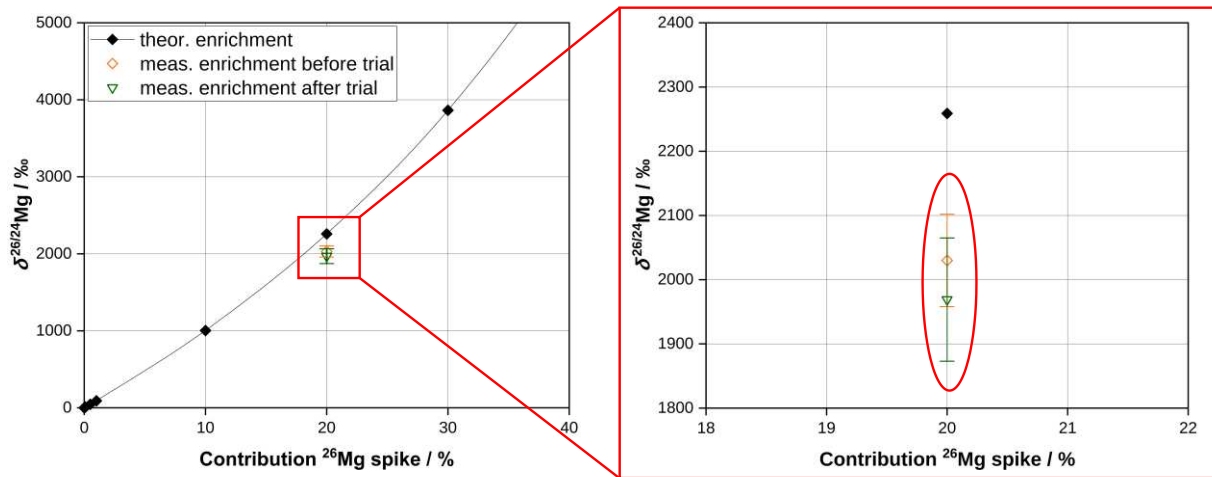
Figure 14. Theoretical $\delta^{26/24}$Mg isotope ratio of the enriched slag and the measured ratio of the slag before and after Experiment AL. Error bars show the u_c of the measured enrichments.

The automated SEM/EDS analysis of steel samples from both experiments MG and AL showed that similar NMI types were formed, indicating similar process conditions. In particular, the presence of multiphase NMIs consisting of MA-spinel surrounded by a (Ca, Si, Al, Mg) oxide in both experiments points towards steel/slag interactions during the process. [50] This indication is further corroborated by the spatially resolved $\delta^{26/24}$Mg isotope ratio data obtained by LA-ICP-MS and further evaluated by IPD, where clear patterns of ^{26}Mg enrichment were consistently observed especially in the outer areas of the investigated NMIs corresponding to the surrounding (Ca, Si, Al, Mg) oxide. Here, contributions of the ^{26}Mg spike up to 16.6 % were measured. The determination of these elevated contributions of the ^{26}Mg spike within the complex oxide segment of the multiphase NMI points out that this specific area is a consequence of interactions with the ^{26}Mg-enriched slag. The center of the complex NMIs consisted of an MA-spinel where the Mg originates predominantly from a natural source, as confirmed by the low to negligible contribution of the ^{26}Mg spike within these areas. Therefore, together with the results from SEM/EDS, it can be concluded that steel/slag interactions took place in both experiments, causing modification of NMIs during the process.

Interactions between slag and refractories were particularly evident in experiment AL. Here, the slag was found adhering to the inner wall of the Al_2O_3 crucible and a discernible reduction in the crucible wall thickness within the slag zone was observed (Figure 12a). The slag residues were found below the primary slag zone, which is attributable to the shrinking of the steel sample during cooling. In the investigated part of the crucible, several LA-ICP-MS line-scans were performed to determine the lateral distribution of the $\delta^{26/24}$Mg isotope ratio and

28

682   associated IPD-calculated contribution of the ^{26}Mg spike across the crucible/slag interface.
683   The observed steady increase of the contribution of the ^{26}Mg spike from deeper parts of the
684   crucible towards the slag-facing interface signifies slag diffusion into the Al$_2$O$_3$ crucible,
685   which was not directly evident from the ^{24}Mg intensity reflecting the overall Mg content. In
686   the case of experiment MG, the not-densely sintered MgO crucible must have fully absorbed
687   the slag during the melting process since no slag residues were found on its inner or outer wall.
688   Moreover, although several pieces of the used crucible were investigated, no indication of any
689   contribution of the ^{26}Mg spike was detected.

4.3. Tracing NMIs in steel using enriched stable isotopes – methodological perspectives and challenges

692   Isotopic fingerprinting using enriched stable isotope tracers in combination with spatially
693   resolved isotopic analysis by LA-ICP-MS and data reduction by IPD is a novel passive
694   tracing approach in metallurgy that allows for identifying sources and mechanisms of NMI
695   formation in steel. Both aspects are of critical importance for the optimization and control of
696   production processes and product quality in steel production. By using enriched stable
697   isotopes for NMI tracing, the inherent process modification induced by established (active)
698   NMI tracing methods is effectively overcome and the properties and behavior of the traced
699   NMIs remain unchanged. Hence, the formation of NMIs could be studied without any tracer-
700   dependent impact for the first time.

701

702   The described method to produce isotopically enriched slag is simple, features high
703   procedural reproducibility, and can be easily adapted for different applications. Mg was used
704   as an exemplary stable isotope system due to its well-known occurrence in NMIs. However,
705   the approach can also be extended to trace different elements with multiple stable isotopes
706   that are potentially involved in NMI formation such as Ca, Si, and Ti. Moreover, the applied
707   absolute amount of tracer addition is very low, accounting for only 0.6 % of the slags' mass
708   and 0.03 % of the total mass of the melt in the presented laboratory experiments.

709

710   Active slag tracing techniques typically require much higher tracer additions to ensure
711   successful experiments. For instance, previous tracing studies investigating slag-related NMI
712   formation in steel reported the use of BaO or SrO as slag tracers, which were added in the
713   form of carbonates (BaCO$_3$ or SrCO$_3$) at mass fractions accounting for 5-15 % of the slag's

714 mass.[12, 13] During the melting experiment, no significant melting losses of the alkaline earth

715 oxides were reported. [13] In contrast, melting losses are a critical factor when using REEs for

716 NMI tracing, despite the lower amounts required compared to the alkaline earth oxides. [21, 51]

717 Thereby, there exists a substantial risk of experiment failure, which is especially detrimental

718 when resource-intensive experiments are conducted on an industrial scale.

719

720 In contrast to these drawbacks of the active tracing techniques, the present study showed that

721 low levels of ^{26}Mg spike were sufficient to modify the Mg isotopic composition of the slag

722 significantly. The level of ^{26}Mg-enrichment in the slag, defined by the molar fraction of the

723 ^{26}Mg spike of 25 % ($\delta^{26/24}$Mg = 2256 ‰), was conservatively designed to ensure distinct

724 differences as compared to natural Mg sources within the relatively high uncertainty on

725 $\delta^{26/24}$Mg values of about 100 ‰ of the used LA-ICP-MS instrumentation and operating

726 parameters for high-resolution analysis. Thereby, an unambiguous extrinsic tag was added to

727 the slag, which was not affected by the melting process, and later found in distinct areas of

728 complex multiphase NMIs with a spatial expansion of a few µm only, with the additional

729 benefit of using instrumentation that is widely available in analytical laboratories.

730

731 However, commercial costs for enriched stable isotope materials are currently relatively high.

732 For example, the cost for the ^{26}Mg spike with an enrichment of >99 % used in this study was

733 18.65 €/mg. At the applied ^{26}Mg spike molar fraction of 25 % in the slag, this accounts for a

734 total cost of approximately 6500 € per kg of steel melt under the experimental conditions.

735 Therefore, it would be highly beneficial to further reduce the absolute amount of spike

736 addition, especially when aiming at a potential scale-up of the approach to industrial steel

737 production. Auspiciously, the molar fraction of ^{26}Mg spike in the slag could be substantially

738 reduced to levels as low as 0.1 % ($\delta^{26/24}$Mg = 9 ‰) when using advanced high-precision

739 instrumental setups such as femtosecond laser ablation systems coupled to multi-collector

740 ICP-MS, where measurement uncertainties on $\delta^{26/24}$Mg values below 1 ‰ are attainable.[52]

741 This would result in mass fractions of the ^{26}Mg spike of ≤0.003 % of the slags' mass and

742 ≤0.0002 % of the total mass of the melt, potentially reducing experimental costs for the

743 enriched stable isotope material by a factor of 200, resulting in approximately 30 € per kg of

744 steel melt, thus making large-scale laboratory setups feasible.

5. Conclusion

This study proved the potential of isotopic fingerprinting using low levels of enriched stable isotope tracers to identify the origin and modification of NMIs in steel. Following main findings can be drawn from the application of this novel tracing technique:

1. Isotopic fingerprinting was used for the first time in the field of metallurgy. The approach enabled the accurate assessment of the origin, modification, and material interaction of NMIs without changing their properties and behavior. Thereby, the drawbacks of state-of-the-art NMI tracing methods characterized by an inherent process modification through the active addition of specific elements has been effectively overcome.

2. Only low levels of the enriched stable isotope tracer were required to significantly change the isotopic ratio of the NMI-source under study, i.e. slag, which can be prepared following routine laboratory procedures. The amount of tracer addition was about 10-times lower as compared to established slag-tracing methods, and could be further reduced in future applications, potentially reducing experimental costs.

3. For the isotopic system under study, Mg, no significant isotopic fractionation was observed over the melting process taking into account the measurement uncertainty. This proves the suitability as effective slag tracer in steel production, as the isotopic signature of the isotopically tagged source material remains unaltered.

4. The Mg-containing multiphase NMIs had a similar composition and structure irrespective of the applied refractory (i.e. MgO or Al_2O_3 crucible). The two trials differed in their NMI types in the pre-melt. While experiment AL consisted-primarily of MA spinel inclusions, the main NMI type in experiment MG was Al_2O_3.-The NMIs consisted of a MA-spinel in the center surrounded by a ring of (Ca, Si, Al, Mg) oxide. Isotopic fingerprinting in combination with spatially resolved isotopic analysis by LA-ICP-MS revealed that the MA-spinel originated from a source with natural Mg isotopic composition such as the crucible or pre-existing NMIs, whereas the adjoining oxidic ring originated from interactions with the ^{26}Mg-enriched slag.

5. Distinct interactions between slag and refractories were found, including the observation of slag diffusion up to approximately 1 mm into a densely sintered Al_2O_3 crucible.

777 The successful development and application of a novel stable isotope tracing technique in this
778 study have marked a significant advancement in the field of metallurgy. By enabling the
779 precise tracing of NMIs in steel without altering their properties or behaviors, this technique
780 not only offers a more refined method of source identification but also minimizes the potential
781 interference observed with traditional methods. The implications of these findings allow for
782 enhanced quality control and traceability in steel manufacturing processes.
783

6. References

1. P. A. Thornton: *J Mater Sci*, 1971, vol. 6, pp. 347–56. https://doi.org/ 10.1007/BF02403103.
2. N. Ånmark, A. Karasev, and P. G. Jönsson: *Steel Res. Int.*, 2017, vol. 88, p. 1600111. https://doi.org/ 10.1002/srin.201600111.
3. R. QI, M. JIN, X. LIU, and B. GUO: *J. Iron Steel Res. Int.*, 2016, vol. 23, pp. 531–38. https://doi.org/ 10.1016/S1006-706X(16)30084-X.
4. H. Tervo, A. Kaijalainen, T. Pikkarainen, S. Mehtonen, and D. Porter: *Mater. Sci. Eng. A*, 2017, vol. 697, pp. 184–93. https://doi.org/ 10.1016/j.msea.2017.05.013.
5. H. Cui, Y. P. Bao, M. Wang, and W. Wu: *INT J MIN MET MATER*, 2010, vol. 17, pp. 154–58. https://doi.org/ 10.1007/s12613-010-0206-y.
6. S. Basu, S. K. Choudhary, and N. U. Girase: *ISIJ Int.*, 2004, vol. 44, pp. 1653–60. https://doi.org/ 10.2355/isijinternational.44.1653.
7. G. C. Duderstadt, R. K. Iyengar, and J. M. Matesa: *JOM*, 1968, vol. 20, pp. 89–94. https://doi.org/ 10.1007/BF03378699.
8. Fukuda Y, Ueshima Y and Mizoguchi S: *ISIJ Int.*, 1992, vol. 32, pp. 164–68. https://doi.org/ 10.2355/isijinternational.32.164.
9. M. Burty, L. Peeters, E. Perrin, S. Münzer, P. Colucci, D. Salvadori, F. Schadow, J.-M. Valcarcel, and J. Claes: *Rev. Metall. / Cah. Inf. Tech.*, 2005, vol. 102, pp. 745–51. https://doi.org/ 10.1051/metal:2005106.
10. S. Ogibayashi: *Taikabutsu Overseas*, 1995, vol. 15, pp. 3–14.
11. S. K. Michelic and C. Bernhard: *Steel Res. Int.*, 2022, vol. 93, pp. 1–18. https://doi.org/ 10.1002/srin.202200086.
12. C. Liu, X. Gao, S. Ueda, M. Guo, and S. Kitamura: *ISIJ Int.*, 2020, vol. 60, pp. 1835–48. https://doi.org/ 10.2355/isijinternational.ISIJINT-2019-695.
13. F. Fuhr, G. Torga, F. Medina, and C. Cicutti: *Ironmaking Steelmaking*, 2007, vol. 34, pp. 463–70. https://doi.org/ 10.1179/174328107X174609.
14. C. Truschner, K. Thiele, S. Ilie, R. Rössler, A. Jungreithmeier, and S. K. Michelic: *Steel Res. Int.*, 2023, pp. 1–15. https://doi.org/ 10.1002/srin.202300665.
15. H. Wang, Y. Bao, J. Zhi, C. Duan, S. Gao, and M. Wang: *ISIJ Int.*, 2020, vol. 61, pp. 657–66. https://doi.org/ 10.2355/isijinternational.ISIJINT-2020-053.
16. M. Burty, P. Dunand, J. P. Ritt, H. Soulard, A. Blanchard, G. Jeanne, F. Penet, R. Pluquet, and I. Poissonnet: *Steelmaking Conference Proceedings Chicago*, 1997, pp. 647–53.
17. M. Nadif, M. Burty, H. Soulard, M. Boher, C. Pusse, J. Lehmann, and F. Meyer: *Metall. Res. Technol.*, 2007, pp. 493–500. https://doi.org/ 10.1051/metal:2007209.
18. Y. Wang and C. Liu: *ISIJ Int.*, 2021, vol. 61, pp. 1396–403. https://doi.org/ 10.2355/isijinternational.ISIJINT-2020-684.
19. W. Cheng, B. SONG, Z. Yang, and J. Mao: *Trans. Indian Inst. Met.*, 2022, vol. 75, pp. 2837–46. https://doi.org/ 10.1007/s12666-022-02612-7.
20. J. Zhang, L. Zhang, Q. Ren, and J. Hu: *ISIJ Int.*, 2023, vol. 63, pp. 779–90. https://doi.org/ 10.2355/isijinternational.ISIJINT-2022-333.
21. R. Geng, J. Li, and C. Shi: *J. Iron Steel Res. Int.*, 2022, vol. 29, pp. 1659–68. https://doi.org/ 10.1007/s42243-022-00751-1.
22. X. Wang, Z. Wu, B. Li, W. Chen, J. Zhang, and J. Mao: *J. Rare Earths*, 2024, vol. 42, pp. 431–45. https://doi.org/ 10.1016/j.jre.2023.04.015.
23. George de Hevesy: *Some applications of isotopic indicators*, 1944.
24. S. Stürup, H. R. Hansen, and B. Gammelgaard: *Anal. Bioanal. Chem.*, 2008, vol. 390, pp. 541–54. https://doi.org/ 10.1007/s00216-007-1638-8.
25. J. Irrgeher and T. Prohaska: *Anal. Bioanal. Chem.*, 2016, vol. 408, pp. 369–85. https://doi.org/ 10.1007/s00216-015-9025-3.

834 26. A. Zitek, J. Irrgeher, M. Kletzl, T. Weismann, and T. Prohaska: *Fish. Manage. Ecol.*, 2013,
835   vol. 20, pp. 354–61. https://doi.org/ 10.1111/fme.12018.
836 27. T. E. Dawson, S. Mambelli, A. H. Plamboeck, P. H. Templer, and K. P. Tu: *Annu. Rev.
837   Ecol. Evol. Syst.*, 2002, vol. 33, pp. 507–59. https://doi.org/
838   10.1146/annurev.ecolsys.33.020602.095451.
839 28. F. Dang, Y.-Z. Chen, Y.-N. Huang, H. Hintelmann, Y.-B. Si, and D.-M. Zhou: *Environ.
840   Sci. Technol.*, 2019, vol. 53, pp. 3802–10. https://doi.org/ 10.1021/acs.est.8b06135.
841 29. H. Shen, F. Pang, S. Jiang, M. He, K. Dong, L. Dou, Y. Pang, X. Yang, X. Ruan, M. Liu,
842   and C. Xia: *Nucl. Instrum. Methods Phys. Res., Sect. B*, 2015, vol. 361, pp. 643–48.
843   https://doi.org/ 10.1016/j.nimb.2015.05.034.
844 30. J. Irrgeher, T. Berger, A. Tchaikovsky, C. Tschegg, G. Gouya, P. Lechner, A. Retzmann,
845   C. Opper, C. Firbas, M. Freissmuth, K. Peschel-Credner, K. Anderle, C. Meisslitzer, M.
846   Wolzt, and T. Prohaska: *Anal. Bioanal. Chem.*, 2023, vol. 415, pp. 255–68. https://doi.org/
847   10.1007/s00216-022-04311-0.
848 31. J. Draxler, E. Martinelli, A. M. Weinberg, A. Zitek, J. Irrgeher, M. Meischel, S. E. Stanzl-
849   Tschegg, B. Mingler, and T. Prohaska: *Acta Biomater.*, 2017, vol. 51, pp. 526–36.
850   https://doi.org/ 10.1016/j.actbio.2017.01.054.
851 32. K. Samekova, C. Firbas, J. Irrgeher, C. Opper, T. Prohaska, A. Retzmann, C. Tschegg, C.
852   Meisslitzer, A. Tchaikovsky, G. Gouya, M. Freissmuth, and M. Wolzt: *Sci. Rep.*, 2021,
853   vol. 11, p. 14796. https://doi.org/ 10.1038/s41598-021-94245-x.
854 33. J. A. Rodríguez-Castrillón, M. Moldovan, J. I. García Alonso, J. J. Lucena, M. L. García-
855   Tomé, and L. Hernández-Apaolaza: *Anal. Bioanal. Chem.*, 2008, vol. 390, pp. 579–90.
856   https://doi.org/ 10.1007/s00216-007-1716-y.
857 34. A. Pack, S. Hoernes, M. Göbbels, R. Bross, and A. Buhr: *Eur. J. Mineral.*, 2005, vol. 17,
858   pp. 483–93. https://doi.org/ 10.1127/0935-1221/2005/0017-0483.
859 35. J. Meija: *Anal. Bioanal. Chem.*, 2006, vol. 385, pp. 486–99. https://doi.org/
860   10.1007/s00216-006-0298-4.
861 36. J. Meija, L. Yang, J. A. Caruso, and Z. Mester: *J. Anal. At. Spectrom.*, 2006, vol. 21, pp.
862   1294–97. https://doi.org/ 10.1039/b607823k.
863 37. CIAAW Commission on isotopic abundances and atomic weights: Atomic Weight of
864   Magnesium | Commission on Isotopic Abundances and Atomic Weights (05.11.2021),
865   https://ciaaw.org/magnesium.htm. Accessed 10 November 2023
866 38. T. B. Coplen and Y. Shrestha: *Pure Appl. Chem.*, 2016, vol. 88, pp. 1203–24.
867   https://doi.org/ 10.1515/pac-2016-0302.
868 39. W. A. Brand, T. B. Coplen, J. Vogl, M. Rosner, and T. Prohaska: *Pure Appl. Chem.*, 2014,
869   vol. 86, pp. 425–67. https://doi.org/ 10.1515/pac-2013-1023.
870 40. G. Kastiukas, X. Zhou, B. Neyazi, and K. T. Wan: *J. Mater. Civ. Eng.*, 2019, vol. 31,
871   04019110. https://doi.org/ 10.1061/(ASCE)MT.1943-5533.0002786.
872 41. A. Hakim, F. Melcher, W. Prochaska, and T. C. Meisel: *J. Asian Earth Sci.*, 2022, vol. 227,
873   p. 105095. https://doi.org/ 10.1016/j.jseaes.2022.105095.
874 42. S. K. Michelic and C. Bernhard: *Scanning*, 2017, p. 2326750. https://doi.org/
875   10.1155/2017/2326750.
876 43. P. Dorrer, S. K. Michelic, C. Bernhard, A. Penz, and R. Rössler: *Steel Res. Int.*, 2019, vol.
877   90, p. 1800635. https://doi.org/ 10.1002/srin.201800635.
878 44. J. Melngailis: *J. Vac. Sci. Technol., B*, 1987, vol. 5, pp. 469–95. https://doi.org/
879   10.1116/1.583937.
880 45. L. A. Giannuzzi and F. A. Stevie: *Micron*, 1999, vol. 30, pp. 197–204. https://doi.org/
881   10.1016/S0968-4328(99)00005-0.
882 46. K. Thiele, R. Musi, T. Prohaska, J. Irrgeher, and S. K. Michelic: *J. Mater. Res. Technol.*,
883   2024, vol. 28, pp. 2247–57. https://doi.org/ 10.1016/j.jmrt.2023.12.172.

884   47. W. A. Russell, D. A. Papanastassiou, and T. A. Tombrello: *Geochim. Cosmochim. Acta*,
885   1978, pp. 1075–90. https://doi.org/ 10.1016/0016-7037(78)90105-9.
886   48. J. Irrgeher, A. Zitek, M. Cervicek, and T. Prohaska: *J. Anal. At. Spectrom.*, 2014, vol. 29,
887   pp. 193–200. https://doi.org/ 10.1039/C3JA50212K.
888   49. J. Draxler, A. Zitek, M. Meischel, S. E. Stranzl-Tschegg, B. Mingler, E. Martinelli, A. M.
889   Weinberg, and T. Prohaska: *J. Anal. At. Spectrom.*, 2015, vol. 30, pp. 2459–68.
890   https://doi.org/ 10.1039/C5JA00354G.
891   50. M. Jiang, X. H. Wang, and W. J. Wang: *steel research int.*, 2010, vol. 81, pp. 759–65.
892   https://doi.org/ 10.1002/srin.201000065.
893   51. S. Gao, M. Wang, J. Guo, H. Wang, J. Zhi, and Y. Bao: *Steel Res. Int.*, 2019, vol. 90, p.
894   1900194. https://doi.org/ 10.1002/srin.201900194.
895   52. M. Oeser, I. Horn, R. Dohmen, and S. Weyer: *Eur. J. Mineral.*, 2023, vol. 35, pp. 813–30.
896   https://doi.org/ 10.5194/ejm-35-813-2023.
897

Author contributions

Kathrin Thiele: conceptualization, methodology, validation, formal analysis, investigation, data curation, writing – original draft, writing – review and editing, visualization

Stefan Wagner: conceptualization, methodology, validation, formal analysis, investigation, data curation, writing – original draft, writing – review and editing

Johanna Irrgeher: conceptualization, methodology, validation, writing – original draft, writing – review and editing

Thomas Prohaska: conceptualization, methodology, writing – review and editing

Susanne K. Michelic: conceptualization, methodology, writing – review and editing, supervision, funding acquisition, project administration

Data availability

The datasets generated during the current study are available from the corresponding author on reasonable request.

Conflict of interest statement

The authors declare no competing interests.

8 Summary and Conclusion

The present thesis and the associated research aim to enhance the state-of-the-art technique and develop new approaches to trace NMIs in steel. Modern analytical techniques were included to implement these novel tracing methods in metallurgy. Hence, this work connected the application-oriented research of ferrous metallurgy with the fundamental science of chemistry. Concerning the state-of-the-art technique, a active tracing method, especially the characterization, must be edited for correct evaluations. For this purpose, the AI-assisted data analyses were implemented as a supporting tool. Since the active tracing approach by using REEs is linked to high melting losses and further influences the behavior of NMIs, the main topic of this research was the development of novel tracing approaches in metallurgy to identify the origin of NMIs without influencing them.

The first task was to determine a suitable alloying concept for active tracing on a laboratory scale since REEs have an even higher oxygen affinity than deoxidizers, such as Al. For this study, a high-frequency remelting furnace was selected to evaluate the potential of three different alloying concepts (**Paper I** [61]; **Chapter 7.1**). The most effective alloying method to minimize oxidation of REEs was the usage of a ferroalloy of the REEs, followed by the addition of REEs wrapped in Al-foil. Besides that, the most important prevention of oxidation is to shorten the time between preparation and melting and, consequently, the contact time with the atmosphere. However, the achieved recovery rates are closely linked to the experimental setup. The study points out how the recovery rate of REEs at laboratory trials can be increased where the losses are significantly higher compared to industrial experiments.

The second issue of this thesis deals with the optimization of characterization techniques for a more accurate evaluation of REE-traced NMIs in micro-cleanness. The focus was on the most common two-dimensional technique, the automated SEM/EDS analysis, and the

sequential chemical extraction, a three-dimensional method. The occurring problem at automated SEM/EDS analysis is the erroneous split of heterogeneous, REE-traced, multiphase NMIs. The errors arising from this characterization method can be diminished by implementing a MATLAB tool that recombines single phases of complex NMIs. The three-dimensional characterization method enabled the investigation of the morphology of REE-traced NMIs since the dissolution of unstable NMIs was prevented due to the usage of the sequential technique. A detailed description of the methodologies, the results and the main outcomes of this topic can be found in the study published in **Paper II** [86] (**Chapter 7.2**). Due to the implementation of the recombination tool, this study makes a major contribution to the characterization of REE-containing NMIs.

As the integration of AI-based solutions is increasing in all sections, it was important to adapt AI-assisted tools to characterize steel cleanness for an accelerated evaluation. The first step was to use image-based characterization by AI for a binary distinction between NMI and non-NMI due to the analysis of BSE images. Since this approach resulted in an accuracy of over 95 %, a 4-class model was utilized to further differentiate between traced and untraced NMIs that can be homogeneous or heterogeneous (**Paper III** [101]; **Chapter 7.2**). Although the dataset was limited, AI-support is promising for prospective steel cleanness characterization.

For more application-orientated research, active tracing trials were performed on industrial and laboratory scales by adding La and Ce (**Paper IV** [73]; **Chapter 7.1**). The micro-cleanness was compared concerning occurring NMIs and their modification over the process. In both setups, the REE addition led to a decrease in the NMI size. Regarding the NMI types, traced and untraced (Al, Ti) oxides were detected in the remaining melt. Concluding this finding, reoxidation after the addition of FeTi occurred. In addition, the clogging layer and the slags were investigated in the industrial experiment. Regarding the former, it was found that REE-traced deoxidation products contributed to the clogging layer formation. As for the latter, a steady increase of the REE content in the slags was measured, indicating a separation tendency of these NMIs into the slag. The study is essential for understanding active tracing since it shows the similarities as well as the differences between tracing experiments on industrial and laboratory scale.

Since tracing with REEs is linked to several challenges, the key issue of the present thesis was the development of alternative approaches to identifying the source of NMIs. For this purpose, two tracing techniques were implemented – the elemental fingerprint and the isotopic spiking. The elemental fingerprint is based on the natural concentration of REEs in materials, which are unique for each substance. In the first study, where this technique was implemented (**Paper V** [149]; **Chapter 7.3**), the clogging layer of an SEN was investigated together with

several auxiliaries, alloying elements and refractories. The resulting patterns showed that the sliding gate sand and Al granules contributed to the clogging layer formation. In the second publication (**Paper VI** [150]; **Chapter 7.3**) about this passive tracing technique, the source of mesoscopic NMIs was investigated, together with the determination of the contributing auxiliaries on the clogging layer formation. Compared to the former study, no unambiguous assignment between the analyzed auxiliaries and the clogging layer was found. However, the mesoscopic NMIs originated from the mold slag and, consequently, from the casting powder. In both studies, the findings of the elemental fingerprint were confirmed by the active tracing with La and Ce since the samples came from industrial tracing experiments on ULC steels. The elemental fingerprint is a novel and promising technique for metallurgical issues. As the two studies showed, the origin of NMIs and clogging layers can be investigated without alloying an additional tracer.

Besides the elemental fingerprint, the second novel tracing approach was the isotopic spiking. This technique is based on modifying the isotopic pattern of one potential source by adding enriched stable isotopes. The method was tested on a laboratory scale by isotopically modifying the slag by adding ^{26}Mg. The analysis of the NMIs in the steel samples made it possible to distinguish between NMIs formed or modified by the slag and other natural sources according to the measured isotopic ratio. The methodology of the isotopic spiking applied to metallurgical issues is described in **Paper VII** (**Chapter 7.4**). Similar to the elemental fingerprint, this method does not influence the properties of NMIs. Furthermore, these modified NMIs cannot visibly distinguished at common characterization methods from untraced NMIs compared to the NMIs formed at the active tracing method using REEs.

This thesis focused on developing, implementing, and optimizing methodologies to trace NMIs during steel production. The work includes the improvement of the state-of-the-art active tracing method concerning laboratory trials and characterization. Further, two novel tracing approaches were implemented, representing a significant advancement for metallurgical aspects. The following points contain the activities carried out in this thesis:

- The common active tracing technique was improved, particularly the alloying concept on a laboratory scale, to increase the recovery rate.
- The characterization of REE-containing NMIs was optimized. The developed recombination tool is an important instrument for a less error-prone validation regarding NMI size, spatial distribution and chemical composition of multiphase NMIs.
- The implementation of an AI-assisted tool to support the automated SEM analysis was a major point for a reduction of the determination time of traced NMIs. However,

more data is required for an adequate and more precise usage of image-based characterization by AI-support.

- Comparisons between industrial and laboratory active tracing trials were performed. Although similar NMI types and modifications occurred, further experiments in the industry are required since identical conditions cannot be experimentally simulated.

- The implementation of the two novel tracing techniques in metallurgy enabled alternative methods to identify the source of NMIs or the contributing auxiliaries on the clogging layer formation.

- Elemental fingerprinting and isotopic spiking require high-resolution analysis by ICP-MS to determine the low concentrations of REEs or the isotopic distribution of only a few µg/g.

- Isotopic spiking is based on modifying one potential source by adding enriched stable isotopes.

- The great benefit of elemental fingerprinting and isotopic spiking techniques are that the properties and behavior of NMIs and, consequently, the steel are not influenced compared to the active one with REEs.

The research provides information on the impact of NMIs, especially deoxidation products, on the clogging layer formation during continuous casting of Ti-stabilized ULC steels. All active tracing studies using REEs demonstrated that reoxidation and, subsequently, the formation of new deoxidation products occurred. The industrial trials and relating thereto the investigation of the clogging layer showed that pre-existing deoxidation products contribute to its formation. The comparison of active tracing with REEs and the elemental fingerprint results in **Paper V** [149] (**Chapter 7.3**) confirmed that Al granules played an essential role in clogging.

NMIs influence the chemical and mechanical properties of steel and thereby lower its quality. Furthermore, NMIs can influence the production of specific steel grades. One major topic in this context is clogging during continuous casting of, e.g., Ti-stabilized IF-steel. The occurrence of clogging leads to losses in steel quality, longer process times, and, therefore, higher production costs if interruptions of the casting sequence occur. Hence, it is important to identify the source of NMIs and track their path over the process. In this work, the focus was on tracking NMIs in a clogging-sensitive steel grade, Ti-stabilized IF-steels, by applying different tracing methods. Thus, the impact of NMIs on the clogging layer formation can be studied since the agglomeration of deoxidation products at the steel/refractory interface on the SEN is one possible mechanism for clogging. Beyond that, the appearance of reoxidation can also be identified.

In the case of elemental fingerprinting and isotopic spiking, the applied methods to trace NMIs or the clogging layer formation were implemented for the first time in ferrous metallurgy. As the results of these approaches showed in **Papers V** to **VII**, both techniques are suitable for determining the source of NMIs and tracking their modification over the process. Compared to active tracing using REEs, the state-of-the-art method, the novel methods do not influence the properties of NMIs.

9 Outlook

Although this work was specialized in clogging-sensitive ULC steel, the tracing methods can be applied to other steel grades to clarify the origin of phenomena that occur during steelmaking. Furthermore, these techniques can contribute to understanding the formation, origin and modification of NMIs and, subsequently, the properties of the final product.

Since REEs are not only used as tracers of NMIs, but also as grain refiner, their application in metallurgy will increase over the next years. Hence, the recombination tool will further on be an important program for a less error-prone evaluation of the steel cleanness in REE-containing steels.

It is expected that the implementation of AI-assistance will increase in the next decades since the support of AI can fast-track the evaluation process. Currently, there are several approaches to implementing AI in metallurgy and steel cleanness evaluation. Besides the need for more data to achieve precise assistance of AI-driven tools, it is inevitable to sensitize humans on how to implement AI.

The REE-Fingerprint has the potential to identify connections between auxiliaries, refractories and the formation of NMIs or clogging. At the moment, several potential sources for NMIs in steelmaking are characterized concerning their elemental fingerprint to create a database. Since the REE-Fingerprint is sensitive concerning the origin of the materials tested, it is required to identify the REE concentration for several different suppliers. However, the method is limited by the lateral resolution of the laser. Hence, only mesoscopic NMIs can be investigated without a too high influence of the signal from the surrounding matrix. Furthermore, not all auxiliaries contain a sufficient concentration of REEs, limiting the implementation of the REE-Fingerprint method.

Besides elemental fingerprinting, isotopic spiking also has great potential as a tracing technique. Similar to the REE-Fingerprint, the behavior of NMIs is not influenced. Concerning industrial trials, there are several possibilities to implement this technique. One option is modifying the isotopic ratio of Ti in FeTi, which enables the study of the impact and behavior of FeTi on nozzle clogging and pre-existing deoxidation products. Another possibility is the change of the isotopic ratio of one component in the slag to be analyzed, as shown in the experiments in **Paper VII** (**Chapter 7.4**). This isotopic modification enables the investigation of whether NMIs originate or are influenced by the slag or other auxiliaries. The difficulty of the limited lateral resolution can be countervailed by applying the quantification method, isotope pattern deconvolution. However, since this method is not trivial, there are currently approaches to use other analyzing techniques. On the one hand, atom probe tomography (APT) is used for spatially resolved measurement. On the other hand, there are trials to measure the isotopic composition of microscopic NMIs by using time-of-flight secondary ion mass spectrometry (ToF-SIMS). Compared to LA-ICP-MS and APT, it is possible to analyze the whole NMI and measure the different phases at multiphase NMIs without completely destroying the NMIs using the latter method. Since the preparation for ToF-SIMS enables a faster analysis with a lower effort, the special focus is on implementing this method.

As the iron and steel industry is in a transformation process towards lower greenhouse gas emissions, new aggregates and processes will be implemented in the future. Relating thereto, the inclusion metallurgy will be faced with new challenges due to changes in chemical composition and, thereby, the occurrence of different inclusion populations. Hence, tracing techniques will be important tools to determine the origin of the newly formed NMIs as well as to track their modification over the process. In particular, the two novel approaches, REE-Fingerprint and isotopic spiking, are of great interest since no change of the NMI's behavior occurs.

A. Appendix

A.1 Acronyms

AI	Artificial Intelligence
APT	Atom Probe Tomography
ICP-MS	Inductively Coupled Plasma – Mass Spectrometer
ICP-OES	Inductively Coupled Plasma – Optical Emission Spectroscopy
ICP-QMS	Inductively Coupled Plasma – Quadrupole Mass Spectrometer
IF	Interstitial Free
IPD	Isotope Pattern Deconvolution
LA-ICP-MS	Laser Ablation – Inductively Coupled Plasma – Mass Spectrometer
NME	Nichtmetallischer Einschluss
NMI	Non-Metallic Inclusion
RH	Ruhrstahl Heraeus
REE	Rare Earth Element
REM/EDX	Rasterelektronen¬mikroskopie mit energiedispersiver Röntgenspektro-skopie
SE	Seltene Erden
SEM/EDS	Scanning Electron Microscopy with Energy Dispersive Spectroscopy

SEN	Submerged Entry Nozzle
Spark-OES	Spark – Optical Emission Spectroscopy
ToF-SIMS	Time-of-Flight Secondary Ion Mass Spectrometry
ULC	Ultra-Low Carbon
XRF	X-Ray Fluorescence

A.2 List of figures

A.3 List of tables

A.4 Authorship contributions

The description of the contributor roles according to the Contributor Roles Taxonomy (CRediT) by Brand et al. [180] is described in **Table A-I**. The authorship contributions are listed in **Table A-II**.

Table A-I: CRediT – contributor role taxonomy [180].

Contributor role	Definition
Conceptualization	Ideas; formulation or evolution of overarching research goals and aims
Methodology	Development or design of methodology; creation of models
Software	Programming, software development; designing computer programs; implementation of the computer code and supporting algorithms; testing of existing code components
Validation	Verification, whether as a part of the activity or separate, of the overall replication/ reproducibility of results/experiments and other research outputs
Formal Analysis	Application of statistical, mathematical, computational, or other formal techniques to analyze or synthesize study data
Investigation	Conducting a research and investigation process, specifically performing the experiments or data/evidence collection

Resources	Provision of study materials, reagents, materials, patients, laboratory samples, animals, instrumentation, computing resources, or other analysis tools
Data curation	Management activities to annotate (produce metadata), scrub data, and maintain research data (including software code, where it is necessary for interpreting the data itself) for initial use and later reuse
Writing – Original Draft	Preparation, creation and/or presentation of the published work, specifically writing the initial draft (including substantive translation)
Writing – Review & Editing	Preparation, creation and/or presentation of the published work by those from the original research group, specifically critical review, commentary or revision – including pre- or post-publication stages
Visualization	Preparation, creation and/or presentation of the published work, specifically visualization/data presentation
Supervision	Oversight and leadership responsibility for the research activity planning and execution, including mentorship external to the core team
Project Administration	Management and coordination responsibility for the research activity planning and execution
Funding Acquisition	Acquisition of the financial support for the project leading to this publication

Table A-II: Authorship contribution – K. Thiele.

No.	Publications	Contributor role of K. Thiele
Paper I	Thiele, K.; Presoly, P.; Ernst, D.; Babu, S. R.; Michelic, S. K. Evaluation of different alloying concepts to trace non-metallic inclusions by adding rare earths on a laboratory scale. *Ironmaking and Steelmaking.Vol.32* **2023**, *50*, 507–516. DOI: 10.1080/03019233.2022.2124816.	Conceptualization, Methodology, Validation, Formal Analysis, Investigation, Resources, Data curation, Writing – Original Draft, Writing – Review & Editing, Visualization, Project Administration
Paper II	Thiele, K.; Musi, R.; Ramesh Babu, S.; Michelic, S. K. Optimization of the Two- and Three-Dimensional Characterization of Rare Earth-Traced Deoxidation Products. *Adv Eng Mater* **2023**, 2201748. DOI: 10.1002/adem.202201748.	Conceptualization, Methodology, Validation, Formal Analysis, Investigation, Resources, Data curation, Writing – Original Draft, Writing – Review & Editing, Visualization, Project Administration
Paper III	Thiele, K.; Musi, R.; Prohaska, T.; Irrgeher, J.; Michelic, S. K. AI assisted steel cleanness evaluation: Predicting the morphology of La-traced non-metallic inclusions using backscattered-electron images. *Journal of Materials Research and Technology* **2024**, *28*, 2247–2257. DOI: 10.1016/j.jmrt.2023.12.172.	Conceptualization, Methodology, Validation, Formal Analysis, Investigation, Resources, Data curation, Writing – Original Draft, Writing – Review & Editing, Visualization, Project Administration
Paper IV	Truschner, C.; Thiele, K.; Ilie, S.; Rössler, R.; Jungreithmeier, A.; Michelic, S. K. Tracing of Deoxidation Products in Ti-Stabilized Interstitial Free Steels by La and Ce on an Industrial and Laboratory Scale. *steel research int.* **2023**. DOI: 10.1002/srin.202300665.	Conceptualization, Methodology, Software, Formal analysis, Investigation, Resources, Data curation, Writing – Original Draft, Visualization, Project Administration

Paper V	Thiele, K.; Ilie, S.; Rössler, R.; Walkner, C.; Meisel, T.; Prohaska, T.; Michelic, S. Different Approaches to Trace the Source of Non-Metallic Inclusions in Steel. *Iron & Steel Technology.Vol.3* **2023**, *20*. DOI: 10.33313/TR/0723.	Methodology, Validation, Formal Analysis, Investigation, Resources, Data curation, Writing – Original Draft, Visualization
Paper VI	Thiele, K.; Truschner, C.; Walkner, C.; Meisel, T. C.; Ilie, S.; Rössler, R.; Michelic, S. K. Investigating the Origin of Non-Metallic Inclusions in Ti-Stabilized ULC Steels Using Different Tracing Techniques. *Metals* **2024**, *14*, 103. DOI: 10.3390/met14010103.	Conceptualization, Methodology, Validation, Investigation, Resources, Data curation, Writing – Original Draft, Visualization
Paper VII	Thiele, K.; Wagner, S.; Irrgeher, J.; Prohaska, T.; Michelic, S. K. Tracing Non-metallic Inclusions in Steel with Low Levels of Enriched Magnesium Stable Isotopes: A Novel Approach, under review in Metallurgical and Materials Transactions B	Conceptualization, Methodology, Validation, Formal Analysis, Investigation, Data curation, Writing – Original Draft, Writing – Review & Editing, Visualization

A.5 Declaration of the use of AI-based tools

Table A-III summarizes the AI-based tools used in this thesis together with the amount, type and purpose.

Table A-III: Summary of the used AI-based tools.

Purpose	Amount in %	Tool / Version	Note
Improvement of linguistic readability and grammar check	10	Grammarly 6.8.261	Word Add-In

A.6 Bibliography

[1] R. Kiessling, Clean steel - a debatable concept. Metal Science 14 (1980), 4, pp. 161–172. doi:10.1080/02670836.2020.12097372

[2] L. Zhang and B.G. Thomas, State of the art in evaluation and control of steel cleanliness, Review. ISIJ Int. 43 (2003), 3, pp. 271–291. doi:10.2355/isijinternational.43.271

[3] A.L.V. Da Costa e Silva, Non-metallic inclusions in steels – origin and control. J. Mater. Res. Technol. 7 (2018), 3, pp. 283–299. doi:10.1016/j.jmrt.2018.04.003

[4] N. Ånmark, A. Karasev and P.G. Jönsson, The Influence of Microstructure and Non-Metallic Inclusions on the Machinability of Clean Steels. Steel Res. Int. 88 (2017), 1, pp. 1600111. doi:10.1002/srin.201600111

[5] Y. Murakami, S. Kodama and S. Konuma, Quantitative evaluation of effects of non-metallic inclusions on fatigue strength of high strength steels. I: Basic fatigue mechanism and evaluation of correlation between the fatigue fracture stress and the size and location of non-metallic inclusions. Int.J.Fatigue 11 (1989), 5, pp. 291–298. doi:10.1016/0142-1123(89)90054-6

[6] P.A. Thornton, The Influence of Nonmetallic Inclusions on the Mechanical Properties of Steel: A Review. J Mater Sci 6 (1971), 4, pp. 347–356. doi:10.1007/BF02403103

[7] L. Wang, J. Xin, L. Cheng, K. Zhao, B. Sun, J. Li, X. Wang and Z. Cui, Influence of inclusions on initiation of pitting corrosion and stress corrosion cracking of X70 steel in near-neutral pH environment. Corrosion Science (2019), 147, pp. 108–127. doi:10.1016/j.corsci.2018.11.007

[8] A.L.V. Da Costa e Silva, The effects of non-metallic inclusions on properties relevant to the performance of steel in structural and mechanical applications. J. Mater. Res. Technol. 8 (2019), 2, pp. 2408–2422. doi:10.1016/j.jmrt.2019.01.009

[9] M. Li, H. Wu and Y. Sun, Influence of Non-metallic Inclusions on Corrosive Properties of Polar Steel. Front. Mater. 25 (2021), 8. doi:10.3389/fmats.2021.602851

[10] J. Velázquez, J. Hernández-Huerta, M. Diaz-Cruz, E. Hernández-Sánchez, A. Cervantes-Tobón, S. Capula-Colindres and R. Cabrera-Sierra, Study on the Influence of Non-Metallic Inclusions on the Pitting Corrosion of API 5L X60 Steel. Coatings 13 (2023), 6, pp. 1040. doi:10.3390/coatings13061040

[11] H. Chen, G. Ma, L. Lu, Y. Huang and X. Li, Unraveling the effect of Al2O3-MnS complex inclusion on the pitting corrosion behavior of dual phase steel. Corrosion Science (2024), 230, pp. 111938. doi:10.1016/j.corsci.2024.111938

[12] M. Schickbichler, S. Ramesh Babu, M. Hafok, C. Turk, G. Schneeberger, A. Fölzer and S.K. Michelic, Comparison of methods for characterising the steel cleanness in powder metallurgical high-speed steels. Powder Metallurgy 66 (2023), 4, pp. 316–332. doi:10.1080/00325899.2023.2170848

[13] F. Klocke, O. Dambon and B. Behrens, Analysis of defect mechanisms in polishing of tool steels. Prod. Eng. Res. Devel. 5 (2011), 5, pp. 475–483. doi:10.1007/s11740-011-0301-6

[14] S. Basu, S.K. Choudhary and N.U. Girase, Nozzle Clogging Behaviour of Ti-bearing Al-killed Ultra Low Carbon Steel. ISIJ Int. 44 (2004), 10, pp. 1653–1660. doi:10.2355/isijinternational.44.1653

[15] H. Barati, M. Wu, S. Michelic, S. Ilie, A. Kharicha, A. Ludwig and Y.-B. Kang, Mathematical Modeling of the Early Stage of Clogging of the SEN During Continuous Casting of Ti-ULC Steel. Metall. Mater. Trans. B 52 (2021), 6, pp. 4167–4178. doi:10.1007/s11663-021-02336-x

[16] L. Zhang, Y. Wang and X. Zuo, Flow Transport and Inclusion Motion in Steel Continuous-Casting Mold under Submerged Entry Nozzle Clogging Condition. Metall. Mater. Trans. B 39 (2008), 4, pp. 534–550. doi:10.1007/s11663-008-9154-6

[17] G. Li, C. Lu, M. Gan, Q. Wang and S. He, Influence of Submerged Entry Nozzle Clogging on the Flow Field and Slag Entrainment in the Continuous Casting Mold by the Physical Model. Metall. Mater. Trans. B 53 (2022), 3, pp. 1436–1445. doi:10.1007/s11663-022-02451-3

[18] C. Bernhard, G. Xia, M. Egger, A. Pissenberger and S.K. Michelic, Experimental investigation into the influence of Ti on the clogging of ULC steels in continuous casting. AISTech Proceedings, pp. 2191–2200, Atlanta, USA (2012), AIST—Association for Iron & Steel Technology.

[19] S.K. Michelic and C. Bernhard, Significance of Nonmetallic Inclusions for the Clogging Phenomenon in Continuous Casting of Steel—A Review. Steel Res. Int. 93 (2022), 7, pp. 2200086. doi:10.1002/srin.202200086

[20] B.G. Thomas and H. Bai, Tundish nozzle clogging- Application of computational models, in: 18th Process Technology Division Conference Proceedings. pp. 895–912 .

[21] S.N. Singh, Mechanism of Alumina Buildup in Tundish Nozzle during Continuous Casting of Aluminium-Killed Steels. Metall.Trans. 5 (1974), pp. 2165–2178.

[22] K.G. Rackers and B.G. Thomas, Clogging in Continuous Casting Nozzles, in: 78th Steelmaking Conference Proceedings. pp. 723–734 .

[23] S. Ogibayashi, Mechanism and Countermeasure of Alumina Buildup on Submerged Nozzle in Continuous Casting. Taikabutsu Overseas 15 (1995), 1, pp. 3–14.

[24] T.B. Braun, J.F. Elliott and M.C. Flemings, The clustering of alumina inclusions. Metall. Mater. Trans. B 10 (1979), 2, pp. 171–184. doi:10.1007/BF02652461

[25] M. Nadif, J. Lehmann, M. Burty and J.-F. Domgin, Control of steel reoxidation and CC nozzle clogging: an overview. Rev. Metall. / Cah. Inf. Tech. 104 (2007), 10, pp. 493–500. doi:10.1051/metal:2007209

[26] Fukuda Y, Ueshima Y and Mizoguchi S, Mechanism of alumina deposition on alumina graphite immersion in continuous caster. ISIJ Int. 32 (1992), 1, pp. 164–168. doi:10.2355/isijinternational.32.164

[27] W. Yang, L. Zhang, Y. Ren, W. Chen and F. Liu, Formation and Prevention of Nozzle Clogging during the Continuous Casting of Steels: A Review. ISIJ Int. 64 (2024), 1, pp. 1–20. doi:10.2355/isijinternational.ISIJINT-2023-376

[28] M. Suzuki, Y. Yamaoka, N. Kubo and M. Suzuki, Oxidation of Molten Steel by the Air Permeated through a Refractory Tube. ISIJ Int. 42 (2002), 3, pp. 248–256. doi:10.2355/isijinternational.42.248

[29] R. Tuttle, K.D. Peaslee and J.D. Smith, Effect of Nozzle Permeability on Clogging, in: AISTech 2004 Proceedings - Volume II .

[30] H. Barati, M. Wu, A. Kharicha and A. Ludwig, Role of Solidification in Submerged Entry Nozzle Clogging During Continuous Casting of Steel. Steel Research International 91 (2020), 12, pp. 2000230. doi:10.1002/srin.202070121

[31] K. Thiele, S. Wagner, C. Walkner, T.C. Meisel, J. Irrgeher, T. Prohaska and Susanne K. Michelic, Tracing the origin of non-metallic inclusions by elemental and isotopic fingerprints. JAF - Junganalytiker*innenforum, Leoben (2023).

[32] J.-H. Lee, M.-H. Kang, S.-K. Kim, J. Kim, M.-S. Kim and Y.-B. Kang, Influence of Al/Ti Ratio in Ti-ULC Steel and Refractory Components of Submerged Entry Nozzle on Formation of Clogging Deposits. ISIJ Int. 59 (2019), 5, pp. 749–758. doi:10.2355/isijinternational.ISIJINT-2018-672

[33] P. Dorrer, S.K. Michelic, C. Bernhard, A. Penz and R. Rössler, Study on the influence of FeTi-addition on the inclusion population in Ti-stabilized ULC steels and its consequences for SEN-clogging. Steel Res. Int. 90 (2019), 7, pp. 1800635. doi:10.1002/srin.201800635

[34] P. Kaushik, D. Kruse and M. Ozgu, Assessment of castability issues in interstitial-free (IF) steels. Rev. Metall. / Cah. Inf. Tech. 105 (2008), 2, pp. 92–101. doi:10.1051/metal:2008020

[35] Y.-J. Park, W.-Y. Kim and Y.-B. Kang, Phase equilibria of Al2O3–TiO system under various oxygen partial pressure: Emphasis on stability of Al2TiO5–Ti3O5 pseudobrookite solid solution. Journal of the European Ceramic Society 41 (2021), 14, pp. 7362–7374. doi:10.1016/j.jeurceramsoc.2021.06.052

[36] H. Matsuura, C. Wang, G. Wen and S. Sridhar, The Transient Stages of Inclusion Evolution During Al and/or Ti Additions to Molten Iron. ISIJ Int. 47 (2007), 9, pp. 1265–1274. doi:10.2355/isijinternational.47.1265

[37] C. Wang, N.T. Nuhfer and S. Sridhar, Transient Behavior of Inclusion Chemistry, Shape, and Structure in Fe-Al-Ti-O Melts: Effect of Gradual Increase in Ti. Metall. Mater. Trans. B 41 (2010), 5, pp. 1084–1094. doi:10.1007/s11663-010-9397-x

[38] U. Diéguez-Salgado, P. Dorrer, S.K. Michelic and C. Bernhard, Experimental investigation of the system nonmetallic inclusion-molten steel-refractory system at high temperatures. Journal of Materials Engineering and Performance 27 (2018), 10, pp. 4983–4988. doi:10.1007/s11665-018-3468-6

[39] C. Hua, Y. Bao and M. Wang, A Transient Nozzle Clog Formation and Peeling Model. Metall. Mater. Trans. B 53 (2022), 6, pp. 3757–3764. doi:10.1007/s11663-022-02638-8

[40] J.-H. Lee, M.-H. Kang, S.-K. Kim and Y.-B. Kang, Oxidation of Ti Added ULC Steel by CO Gas Simulating Interfacial Reaction between the Steel and SEN during Continuous Casting. ISIJ Int. 58 (2018), 7, pp. 1257–1266. doi:10.2355/isijinternational.ISIJINT-2018-164

[41] M.G. González-Solórzano and R.D. Morales, Physical Modeling and Mathematical Modeling Using the Scale-Adaptive Simulation Model of Nozzle Design Effects on the Flow Structure in a Slab Mold. Steel Res. Int. 93 (2022), 11, pp. 2200395. doi:10.1002/srin.202200395

[42] R. Chaudhary, B.T. Rietow and B.G. Thomas, Differences between Physical Water Models and Steel Continuous Casters: A Theoretical Evaluation, in: Materials Science and Technology MS&T 2009. pp. 1090–1101 .

[43] P. Kaushik, J. Lehmann and M. Nadif, State of the Art in Control of Inclusions, Their Characterization, and Future Requirements. Metall. Mater. Trans. B 43 (2012), 4, pp. 710–725. doi:10.1007/s11663-012-9646-2

[44] C.E. Cicutti, J. Madias and J.C. Gonzelz, Control of microinclusions in calcium treated aluminium killed steels. Ironmaking Steelmaking 24 (1997), 2, pp. 155–159.

[45] H.V. Atkinson and G. Shi, Characterization of inclusions in clean steels: a review including the statistics of extremes methods. Progress in Materials Science 48 (2003), 5, pp. 457–520. doi:10.1016/S0079-6425(02)00014-2

[46] L. Zhang and B. Thomas, State of the Art in Evaluation and Control of Steel Cleanliness. ISIJ Int. 43 (2003), 3, pp. 271–291. doi:10.2355/isijinternational.43.271

[47] L.F. Zhang, Indirect Methods of Detecting and Evaluating Inclusions in Steel-A Review. Journal of Iron and Steel Research International 13 (2006), 4, pp. 1–8. doi:10.1016/S1006-706X(06)60067-8

[48] P. Kaushik, H. Pielet and H. Yin, Inclusion characterisation - tool for measurement of steel cleanliness and process control: Part 1. Ironmaking Steelmaking 36 (2009), 8, pp. 561–571. doi:10.1179/030192309X12492910938131

[49] S.K. Michelic, G. Wieser and C. Bernhard, On the representativeness of automated SEM/EDS analyses for inclusion characterisation with special regard to the measured sample area. ISIJ Int. 51 (2011), 5, pp. 769–775. doi:10.2355/isijinternational.51.769

[50] A. Mayerhofer, Enhanced characterization of non-metallic inclusions for (sub) micro steel cleanness evaluations. Ph.D thesis, Leoben, Austria (2021).

[51] Y. Wang and C. Liu, Agglomeration Characteristics of Various Oxide Inclusions in Molten Steel Containing Rare Earth Element under Different Deoxidation Conditions. ISIJ Int. 61 (2021), 5, pp. 1396–1403. doi:10.2355/isijinternational.ISIJINT-2020-684

[52] J. Collins, V. Calkins and J. McGurty, Applications of rare earths to ferrous and non-ferrous alloys. US Atomic Energy Commission (AEC), US Air Force, General Electric Co. Aircraft Nuclear Propulsion Dept., Cincinnati, OH (United States) (1959).

[53] K. Baumgartner, C. Bernhard, P. Presoly, M. Hafok and H. Leitner, The potential for grain refinement of a super austenitic stainless steel with a cerium grain refiner. ESSC and DUPLEX 2017 - 9th European Stainless Steel Conference - Science and Market and

5th European Duplex Stainless Steel Conference and Exhibition, Bergamo, Italy (2017), Associazione Italiana di Metallurgia.

[54] Y. Ji, M.-X. Zhang and H. Ren, Roles of Lanthanum and Cerium in Grain Refinement of Steels during Solidification. Metals 8 (2018), 11, pp. 884. doi:10.3390/met8110884

[55] H. Wang, Y. Bao, J. Zhi, C. Duan, S. Gao and M. Wang, Effect of Rare Earth Ce on the Morphology and Distribution of Al_2O_3 Inclusions in High Strength IF Steel Containing Phosphorus during Continuous Casting and Rolling Process. ISIJ Int. 61 (2020), 3, pp. 657–666. doi:10.2355/isijinternational.ISIJINT-2020-053

[56] Y. Wang, C. Li, L. Wang, X. Xiong, L. Chen and C. Zhuang, Modification of Alumina Inclusions in SWRS82B Steel by Adding Rare Earth Cerium. Metals 10 (2020), 12, pp. 1696. doi:10.3390/met10121696

[57] H. Li, Y. Yu, X. Ren, S. Zhang and S. Wang, Evolution of Al_2O_3 inclusions by cerium treatment in low carbon high manganese steel. J. Iron Steel Res. Int. 24 (2017), 9, pp. 925–934. doi:10.1016/S1006-706X(17)30135-8

[58] N. Mao, W. Yang, D. Chen, W. Lu, X. Zhang, S. Chen, M. Xu, B. Pan, L. Han, X. Zhang and Z. Wang, Effect of Lanthanum Addition on Formation Behaviors of Inclusions in Q355B Weathering Steel. Materials 15 (2022), 22. doi:10.3390/ma15227952

[59] G. Cai and C. Li, Effects of Ce on Inclusions, Microstructure, Mechanical Properties, and Corrosion Behavior of AISI 202 Stainless Steel. J. of Materi Eng and Perform 24 (2015), 10, pp. 3989–4009. doi:10.1007/s11665-015-1651-6

[60] Z. Ning, C. Li, J. Wang, Y. Zhai, X. Xiong and L. Chen, Refinement and Modification of Al_2O_3 Inclusions in High-Carbon Hard Wire Steel via Rare Earth Lanthanum. Materials 16 (2023), 14. doi:10.3390/ma16145070

[61] K. Thiele, P. Presoly, D. Ernst, S.R. Babu and S.K. Michelic, Evaluation of different alloying concepts to trace non-metallic inclusions by adding rare earths on a laboratory scale. Ironmaking and Steelmaking 50 (2023), 5, pp. 507–516. doi:10.1080/03019233.2022.2124816

[62] B. Li, H. Zhu, J. Zhao, M. Song, J. Li and Z. Xue, Effect of Rare-Earth La on Inclusion Evolution in High-Al Steel. Steel Res. Int. 93 (2021), 2, pp. 2100347. doi:10.1002/srin.202100347

[63] S. Luo, Z. Shen, Z. Yu, W. Wang and M. Zhu, Effect of Ce Addition on Inclusions and Grain Structure in Gear Steel 20CrNiMo. Steel Res. Int. 92 (2021), 3, pp. 2000394. doi:10.1002/srin.202000394

[64] J.I. Goldstein, D.E. Newbury, J.R. Michael, N.W. Ritchie, J.H.J. Scott and D.C. Joy, Scanning Electron Microscopy and X-Ray Microanalysis. 4. Edition, New York, NY (2018), Springer New York.

[65] ThermoFisher, SEM working principle: the detection of backscattered electrons. https://www.thermofisher.com/at/en/home/global/forms/industrial/backscattered-electrons-sem.html, Accessed: 22.03.2024

[66] R. Geng, J. Li and C. Shi, Evolution of Inclusions with Ce Addition and Ca Treatment in Al-killed Steel during RH Refining Process. ISIJ Int. 61 (2021), 5, pp. 1506–1513. doi:10.2355/isijinternational.ISIJINT-2020-672

[67] W. Liang, J. Li, B. Lu, J. Zhi, S. Zhang and Y. Liu, Analysis on clogging of submerged entry nozzle in continuous casting of high strength steel with rare earth. J. Iron Steel Res. Int. 29 (2022), 1, pp. 34–43. doi:10.1007/s42243-021-00637-8

[68] S. Gao, M. Wang, J. Guo, H. Wang, J. Zhi and Y. Bao, Characterization Transformation of Inclusions Using Rare Earth Ce Treatment on Al-Killed Titanium Alloyed Interstitial Free Steel. Steel Res. Int. 90 (2019), 10, pp. 1900194. doi:10.1002/srin.201900194

[69] J. Zhang, Y. Ren, Q. Ren and L. Zhang, Transient Evolution of Nonmetallic Inclusions in a Si–Mn-Killed Stainless Steel with Cerium Addition. Steel Res. Int. 93 (2022), 7, pp. 2100773. doi:10.1002/srin.202100773

[70] N. Yadav and G.G. Roy, Evolution of Inclusions and Their Statistics in Low-Carbon Aluminum-Killed (LCAK) Steel Treated with Mischmetal. Metall. Mater. Trans. B 55 (2024), pp. 1601–1618. doi:10.1007/s11663-024-03052-y

[71] J. Wang, L. Wang, C. Chen, X. Wang and F. Zhao, Effect of rare earth on primary carbides in H13 die steel and their addition method: a review. J. Iron Steel Res. Int. 31 (2024), 3, pp. 531–551. doi:10.1007/s42243-023-01149-3

[72] X. Wang, G. Li, Y. Chen, Q. Wang and Y. Liu, Industrial Trials on Preparation of Cerium-Treated H13 Steel by Electroslag Remelting with Cerium-Oxide Containing Slag. Steel Res. Int. 94 (2023), 6, pp. 2200786. doi:10.1002/srin.202200786

[73] C. Truschner, K. Thiele, S. Ilie, R. Rössler, A. Jungreithmeier and S.K. Michelic, Tracing of Deoxidation Products in Ti-Stabilized Interstitial Free Steels by La and Ce on an Industrial and Laboratory Scale. Steel Res. Int. 95 (2023), 3, pp. 2300665. doi:10.1002/srin.202300665

[74] C. Pan, X. Hu, P. Lin and K. Chou, Evolution of Inclusions after Cerium and Titanium Addition in Aluminum Deoxidized Fe-17Cr-9Ni Austenitic Stainless Steel. ISIJ Int. 60 (2020), 9, pp. 1878–1885. doi:10.2355/isijinternational.ISIJINT-2020-028

[75] Q. Ren, Z. Hu, L. Cheng, X. Kang, Y. Cheng and L. Zhang, Modification Mechanism of Lanthanum on Alumina Inclusions in a Nonoriented Electrical Steel. Steel Res. Int. 93 (2022), 10, pp. 2200212. doi:10.1002/srin.202200212

[76] M. Wang, S. Gao, X. Li, G. Wu, L. Xing, H. Wang, J. Zhi and Y. Bao, Reaction Behaviour between Cerium Ferroalloy and Molten Steel during Rare Earth Treatment in the Ultra-low Carbon Al-killed Steel. ISIJ Int. 61 (2021), 5, pp. 1524–1531. doi:10.2355/isijinternational.ISIJINT-2020-678

[77] Q. Ren and L. Zhang, Effect of Cerium Content on Inclusions in an Ultra-Low-Carbon Aluminum-Killed Steel. Metall. Mater. Trans. B 51 (2020), 2, pp. 589–600. doi:10.1007/s11663-020-01779-y

[78] Z. Adabavazeh, W.S. Hwang and Y.H. Su, Effect of Adding Cerium on Microstructure and Morphology of Ce-Based Inclusions Formed in Low-Carbon Steel. Sci. Rep. 7 (2017), pp. 46503. doi:10.1038/srep46503

[79] Y. Li, T. Zhang, Y. Feng, C. Liu and M. Jiang, Liquid Regions of Lanthanum-Bearing Aluminosilicates. Materials 13 (2020), 2, pp. 450. doi:10.3390/ma13020450

[80] C. Bernhard, G. Xia, M. Egger, A. Pissenberger and S.K. Michelic, Experimental investigation into the influence of Ti on the clogging of ULC steels in continuous casting. AISTech Proceedings, pp. 2191–2200, Atlanta, USA (2012), AIST—Association for Iron & Steel Technology.

[81] G.M. Faulring, J.W. Farrell and D.C. Hilty, Steel flow through nozzles: influence of calcium. Iron Steelmaker 7 (1980), 2, pp. 57–66.

[82] M. Burty, P. Dunand, J.P. Ritt, H. Soulard, A. Blanchard, G. Jeanne, F. Penet, R. Pluquet and I. Poissonnet, Control of DWI steel cleanness by lanthanum tracing of deoxidation inclusions, ladle slag treatment and a methodical approach, in: Steelmaking Conference Proceedings Chicago. pp. 647–653 (1997).

[83] A. Katsumata and H. Todoroki, Effect of Rare Earth Metal on Inclusion Composition in Molten Stainless Steel. Iron & Steelmaker 29 (2002), 7, pp. 51–59.

[84] B. Zhao, W. Wu, J. Zhi, C. Su and J. Zhang, Study on the formation mechanism of clogging layer of rare earth microalloyed Q355 steel's submerged entry nozzle and

process optimization. Ironmaking Steelmaking 50 (2023), 7, pp. 782–793. doi:10.1080/03019233.2023.2185738

[85] Y. Xie, M. Song, B. Wang, H. Zhu, Z. Xue, A. Mayerhofer, S.K. Michelic, C. Bernhard and J.L. Schenk, Statistical Analysis of the Inclusions in Rare Earth-M (M = Ca and Ti) Treated Steel. Metall. Mater. Trans. B 52 (2021), pp. 2101–2110. doi:10.1007/s11663-021-02163-0

[86] K. Thiele, R. Musi, S. Ramesh Babu and S.K. Michelic, Optimization of the Two- and Three-Dimensional Characterization of Rare Earth-Traced Deoxidation Products. Adv Eng Mater 25 (2023), 11, pp. 2201748. doi:10.1002/adem.202201748

[87] Y. Meng, C. Yan, X. Yang and X. Ju, A Statistical Analysis on the Complex Inclusions in Rare Earth Element Treated Steel. ISIJ Int. 60 (2020), 3, pp. 534–538. doi:10.2355/isijinternational.ISIJINT-2019-428

[88] A.V. Muntin, P.Y. Zhikharev, A.G. Ziniagin and D.A. Brayko, Artificial Intelligence and Machine Learning in Metallurgy. Part 1. Methods and Algorithms. Metallurgist 67 (2023), 5-6, pp. 886–894. doi:10.1007/s11015-023-01576-3

[89] P.Y. Zhikharev, A.V. Muntin, D.A. Brayko and M.O. Kryuchkova, Artificial Intelligence and Machine Learning In Metallurgy. Part 2. Application Examples. Metallurgist 67 (2024), 9-10, pp. 1545–1560. doi:10.1007/s11015-024-01648-y

[90] R. Zhang and J. Yang, State of the art in applications of machine learning in steelmaking process modeling. INT J MIN MET MATER 30 (2023), 11, pp. 2055–2075. doi:10.1007/s12613-023-2646-1

[91] D. Kriesel, A Brief Introduction to Neural Networks. http://www.dkriesel.com, Accessed: 28.04.2024

[92] S. Guo, J. Yu, X. Liu, C. Wang and Q. Jiang, A predicting model for properties of steel using the industrial big data based on machine learning. Comput.Mater.Sci. (2019), 160, pp. 95–104. doi:10.1016/j.commatsci.2018.12.056

[93] Q. Xie, M. Suvarna, J. Li, X. Zhu, J. Cai and X. Wang, Online prediction of mechanical properties of hot rolled steel plate using machine learning. Materials & Design (2021), 197, pp. 109201. doi:10.1016/j.matdes.2020.109201

[94] W. Zhao, F. Chen, H. Huang, D. Li and W. Cheng, A New Steel Defect Detection Algorithm Based on Deep Learning. Computational Intelligence and Neuroscience (2021), pp. 5592878. doi:10.1155/2021/5592878

[95] I. Konovalenko, P. Maruschak, V. Brevus and O. Prentkovskis, Recognition of Scratches and Abrasions on Metal Surfaces Using a Classifier Based on a Convolutional Neural Network. Metals 11 (2021), 4, pp. 549. doi:10.3390/met11040549

[96] L.S. Carlsson, P.B. Samuelsson and P.G. Jönsson, Interpretable Machine Learning—Tools to Interpret the Predictions of a Machine Learning Model Predicting the Electrical Energy Consumption of an Electric Arc Furnace. Steel Res. Int. 91 (2020), 11, pp. 2000053. doi:10.1002/srin.202000053

[97] M. Abdulsalam and B. Webler, Machine Learning Approaches for the Analysis of Non-Metallic Inclusion Data Sets, in: 2019 AISTech Conference Proceedings. pp. 2667–2674 .

[98] M. Abdulsalam, M. Jacobs and B.A. Webler, Automated Detection of Non-metallic Inclusion Clusters in Aluminum-deoxidized Steel. Metall. Mater. Trans. B 52 (2021), 6, pp. 3970–3985. doi:10.1007/s11663-021-02312-5

[99] M. Abdulsalam, N. Gao, B.A. Webler and E.A. Holm, Prediction of Inclusion Types From BSE Images: RF vs. CNN. Front. Mater. 8 (2021), pp. 754089. doi:10.3389/fmats.2021.754089

[100] S. Ramesh Babu, R. Musi, K. Thiele and S.K. Michelic, Classification of Nonmetallic Inclusions in Steel by Data-Driven Machine Learning Methods. Steel Res. Int. 94 (2023), 1, pp. 2200617. doi:10.1002/srin.202200617

[101] K. Thiele, R. Musi, T. Prohaska, J. Irrgeher and S.K. Michelic, AI assisted steel cleanness evaluation: Predicting the morphology of La-traced non-metallic inclusions using backscattered-electron images. J. Mater. Res. Technol. 28 (2024), pp. 2247–2257. doi:10.1016/j.jmrt.2023.12.172

[102] D. Janis, R. Inoue, A. Karasev and P.G. Jönsson, Application of Different Extraction Methods for Investigation of Nonmetallic Inclusions and Clusters in Steels and Alloys. Advances in Materials Science and Engineering (2014), pp. 210486. doi:10.1155/2014/210486

[103] H. Doostmohammadi, A. Karasev and P.G. Jönsson, A Comparison of a Two-Dimensional and a Three-Dimensional Method for Inclusion Determinations in Tool Steel. Steel Res. Int. 81 (2010), 5, pp. 398–406. doi:10.1002/srin.200900149

[104] X. Zhang, L. Zhang, W. Yang, Y. Zhang, Y. Ren and Y. Dong, Comparison of 2D and 3D morphology of non-metallic inclusions in steel using different methods. Metall. Res. Technol. 114 (2017), 1, pp. 113. doi:10.1051/metal/2016056

[105] S. Ramesh Babu and S.K. Michelic, Overview of application of automated SEM/EDS measurements for inclusion characterization in steelmaking. MetalMat (2024). doi:10.1002/metm.18

[106] K. Thiele, S. Ilie, R. Roessler and S. Michelic, Characterization of Rare-Earth-Elements-Traced Non-Metallic Inclusions by Different Methods, in: 8th International Congress on the Science and Technology of Steelmaking 2022. pp. 80–87 .

[107] A.V. Karasev and H. Suito, Quantitative evaluation of inclusion in deoxidation of Fe-10 mass% Ni alloy with Si, T, Al, Zr, and Ce. Metall. Mater. Trans. B 30 (1999), pp. 249–257.

[108] D. Janis, A. Karasev, R. Inoue and P.G. Jönsson, A Study of Cluster Characteristics in Liquid Stainless Steel and in a Clogged Nozzle. Steel Res. Int. 86 (2015), 11, pp. 1271–1278. doi:10.1002/srin.201400316

[109] Y. Bi, A.V. Karasev and P.G. Jönsson, Three Dimensional Evaluations of REM Clusters in Stainless Steel. ISIJ Int. 54 (2014), 6, pp. 1266–1273. doi:10.2355/isijinternational.54.1266

[110] M. Nabeel, A. Karasev and P.G. Jönsson, Formation and Growth Mechanism of Clusters in Liquid REM-alloyed Stainless Steels. ISIJ Int. 55 (2015), 11, pp. 2358–2364. doi:10.2355/isijinternational.ISIJINT-2015-293

[111] A.V. Karasev and H. Suito, Analysis of Size Distribution of Inclusions in Metal by Using Single-particle Optical Sensing Method. ISIJ Int. 41 (2001), 11, pp. 1357–1365. doi:10.2355/isijinternational.41.1357

[112] D.J. Swinden and J.H. Woodhead, Kinetics of the nucleation and growth of proeutectoid ferrite in some Fe-C-Cr alloys. J Iron Steel Inst 209.11 209 (1971), 11, pp. 883–899.

[113] M. Schickbichler, K. Thiele and S.K. Michelic, Evaluierung der Unterschiede zwischen sequenzieller chemischer und elektrolytischer Extraktion anhand von Seltene Erden (SE)-haltigen Einschlüssen. BHM (Berg- und Hüttenmännische Montanhefte) 169 (2024), 3, pp. 119–123. doi:10.1007/s00501-024-01435-x

[114] D.A. Atwood, The Rare Earth Elements: Fundamentals and Applications (2012), Wiley.

[115] H.-G. Stosch, Geochemie der Seltenen Erden. https://www.agw.kit.edu/downloads/Studiengang/Geochemie%20der%20Seltenen%20Erden%20(Stosch,%208%20MB).pdf, Accessed: 26.04.2024

[116] Rare Element Resources, Rare Earth Elements. https://www.rareelementresources.com/rare-earth-elements, Accessed: 07.03.2024

[117] V. Balaram, Rare earth elements: A review of applications, occurrence, exploration, analysis, recycling, and environmental impact. Geoscience Frontiers 10 (2019), 4, pp. 1285–1303. doi:10.1016/j.gsf.2018.12.005

[118] M. Adeel, J.Y. Lee, M. Zain, M. Rizwan, A. Nawab, M.A. Ahmad, M. Shafiq, H. Yi, G. Jilani, R. Javed, R. Horton, Y. Rui, D.C.W. Tsang and B. Xing, Cryptic footprints of rare earth elements on natural resources and living organisms. Environment international (2019), 127, pp. 785–800. doi:10.1016/j.envint.2019.03.022

[119] I. Wysocka, Determination of rare earth elements concentrations in natural waters - A review of ICP-MS measurement approaches. Talanta (2021), 221, pp. 121636. doi:10.1016/j.talanta.2020.121636

[120] A.M. Dobney, A.J. Mank, K.H. Grobecker, P. Conneely and C.G. de Koster, Laser ablation inductively coupled plasma mass spectrometry as a tool for studying heterogeneity within polymers. Analytica chimica acta 423 (2000), 1, pp. 9–19. doi:10.1016/S0003-2670(00)01047-3

[121] S. Ashoka, B.M. Peake, G. Bremner, K.J. Hageman and M.R. Reid, Comparison of digestion methods for ICP-MS determination of trace elements in fish tissues. Analytica chimica acta 653 (2009), 2, pp. 191–199. doi:10.1016/j.aca.2009.09.025

[122] T. Prohaska, J. Irrgeher, A. Zitek and N. Jakubowski, Sector field mass spectrometry for elemental and isotopic analysis. Cambridge (2015), Royal Society of Chemistry.

[123] M. Sanborn and K. Telmer, The spatial resolution of LA-ICP-MS line scans across heterogeneous materials such as fish otoliths and zoned minerals. J. Anal. At. Spectrom. 18 (2003), 10, pp. 1231. doi:10.1039/b302513f

[124] Y. Ke, W. Guo, L. Jin, L. Qiao, H. Yang and S. Hu, Direct quantitative determination of rare earth elements in REE-rich mineral powders by LA-ICP-MS. Chem. Res. Chin. Univ. 33 (2017), 3, pp. 360–364. doi:10.1007/s40242-017-6399-0

[125] Y. Ke, Y. Sun, P. Lin, J. Zhou, Z. Xu, C. Cao, Y. Yang and S. Hu, Quantitative determination of rare earth elements in scheelite via LA-ICP-MS using REE-doped tungstate single crystals as calibration standards. Microchemical Journal (2019), 145, pp. 642–647. doi:10.1016/j.microc.2018.11.016

[126] D.V.M. Sousa, A.T. Abreu, G.M.S. Sampaio, C.C. Lana, D.A.S. Rodrigues and H.A. Nalini, Determination of rare earth elements in Fe-minerals using external calibration by LA-ICP-MS and application on Cauê Iron Formation (Brazil). Talanta (2020), 219, pp. 121239. doi:10.1016/j.talanta.2020.121239

[127] J. T. Wasson and G. W. Kallemeyn, Compositions of chondrites. Phil. Trans. R. Soc. Lond. A 325 (1988), 1587, pp. 535–544. doi:10.1098/rsta.1988.0066

[128] J. Voncken, The Rare Earth Elements: An Introduction. Delft, NL (2016), Springer International Publishing.

[129] A.C. Kerr, Rare-earth-element (REE) behaviour in the strange lake intrusion, Labrador: resource estimation using predictive methods, Newfoundland and Labrador Department of Natural Resources (2013).

[130] S. Wibner, H. Antrekowitsch and T.C. Meisel, Studies on the Formation and Processing of Aluminium Dross with Particular Focus on Special Metals. Metals 11 (2021), 7, pp. 1108. doi:10.3390/met11071108

[131] L.A. Haskin, M.A. Haskin, F.A. Frey and T.R. Wildeman, Relative and Absolute Terrestrial Abundances of the Rare Earths, in: Origin and Distribution of the Elements. pp. 889–912 (1968), Elsevier.

[132] P. Möller and G.K. Muecke, Significance of Europium anomalies in silicate melts and crystal-melt equilibria: a re-evaluation. Contr. Mineral. and Petrol. 87 (1984), 3, pp. 242–250. doi:10.1007/BF00373057

[133] C. Walkner, Korp, Jörg, C., A. Graf, J. Irrgeher, T. Meisel and T. Prohaska, CSI Stahl: Makroskopische nichtmetallische Einschlüsse in Stählen – Ermittlung von Quellen und Ursachen. CANAS, Freiberg, Deutschland (2019).

[134] F.F. Fu, T. Akagi, Y. Suzuki, K. Watanabe and S. Yabuki, Rare earth element distribution in the acetic acid soluble fraction of combusted coals: Its implication as a proxy for the original coal-forming plants. Geochem. J. 38 (2004), 4, pp. 333–343. doi:10.2343/geochemj.38.333

[135] F.F. Fu, T. Akagi, S. Yabuki, M. Iwaki and N. Ogura, Distribution of rare earth elements in seaweed: implication of two different sources of rare earth elements and silicon in seaweed. Journal of Phycology 36 (2000), 1, pp. 62–70. doi:10.1046/j.1529-8817.2000.99022.x

[136] T. Akagi and K. Edanami, Sources of rare earth elements in shells and soft-tissues of bivalves from Tokyo Bay. Marine Chemistry (2017), 194, pp. 55–62. doi:10.1016/j.marchem.2017.02.009

[137] R.W. Kay and P.W. Gast, The Rare Earth Content and Origin of Alkali-Rich Basalts. The Journal of Geology 81 (1973), 6, pp. 653–682. doi:10.1086/627919

[138] G.P. Danezis, A.C. Pappas, E. Zoidis, G. Papadomichelakis, I. Hadjigeorgiou, P. Zhang, V. Brusic and C.A. Georgiou, Game meat authentication through rare earth elements fingerprinting. Analytica chimica acta (2017), 991, pp. 46–57. doi:10.1016/j.aca.2017.09.013

[139] C. Cerutti, R. Sánchez, C. Sánchez, F. Ardini, M. Grotti and J.-L. Todolí, Prospect on Rare Earth Elements and Metals Fingerprint for the Geographical Discrimination of Commercial Spanish Wines. Molecules 25 (2020), 23, pp. 5602. doi:10.3390/molecules25235602

[140] G. Gallello, C. Ferro-Vázquez, S. Chenery, C. Lang, S. Thornton-Barnett, T. Kabora, M.E. Hodson and D. Stump, The capability of rare earth elements geochemistry to interpret complex archaeological stratigraphy. Microchemical Journal (2019), 148, pp. 691–701. doi:10.1016/j.microc.2019.05.050

[141] Y. Su and M. Yang, Combining Rare Earth Element Analysis and Chemometric Method to Determine the Geographical Origin of Nephrite. Minerals 12 (2022), 11, pp. 1399. doi:10.3390/min12111399

[142] B.S. Kamber, Geochemical fingerprinting: 40 years of analytical development and real world applications. Applied Geochemistry 24 (2009), 6, pp. 1074–1086. doi:10.1016/j.apgeochem.2009.02.012

[143] R. Hark and R.S. Harmon, Geochemical Fingerprinting Using LIBS, in: S. Musazzi, U. Perini (Eds.), Laser-induced breakdown spectroscopy: Theory and applications. pp. 309–348, Berlin, New York (2014), Springer.

[144] Ž. Šmit, K. Janssens, E. Bulska, B. Wagner, M. Kos and I. Lazar, Trace element fingerprinting of façon-de-Venise glass. Nucl. Instrum. Methods Phys. Res., Sect. B 239 (2005), 1-2, pp. 94–99. doi:10.1016/j.nimb.2005.06.182

[145] C. D'Antone, R. Punturo and C. Vaccaro, Rare earth elements distribution in grapevine varieties grown on volcanic soils: an example from Mount Etna (Sicily, Italy). Environmental monitoring and assessment (2017), 189, pp. 160. doi:10.1007/s10661-017-5878-6

[146] D. Joebstl, D. Bandoniene, T. Meisel and S. Chatzistathis, Identification of the geographical origin of pumpkin seed oil by the use of rare earth elements and discriminant analysis. Food chemistry 123 (2010), 4, pp. 1303–1309. doi:10.1016/j.foodchem.2010.06.009

[147] D. Bandoniene, D. Zettl, T. Meisel and M. Maneiko, Suitability of elemental fingerprinting for assessing the geographic origin of pumpkin (Cucurbita pepo var. styriaca) seed oil. Food chemistry 136 (2013), 3-4, pp. 1533–1542. doi:10.1016/j.foodchem.2012.06.040

[148] D. Bandoniene, T. Meisel, A. Rachetti and C. Walkner, A tool to assure the geographical origin of local food products (glasshouse tomatoes) using labeling with rare earth elements. Journal of the science of food and agriculture 98 (2018), 12, pp. 4769–4777. doi:10.1002/jsfa.9124

[149] K. Thiele, S. Ilie, R. Rössler, C. Walkner, T. Meisel, T. Prohaska and S.K. Michelic, Different Approaches to Trace the Source of Non-Metallic Inclusions in Steel. Iron & Steel Technology 20 (2023), 7. doi:10.33313/TR/0723

[150] K. Thiele, C. Truschner, C. Walkner, T.C. Meisel, S. Ilie, R. Rössler and S.K. Michelic, Investigating the Origin of Non-Metallic Inclusions in Ti-Stabilized ULC Steels Using Different Tracing Techniques. Metals 14 (2024), 1, pp. 103. doi:10.3390/met14010103

[151] N. Jakubowski, R. Brandt, D. Stuewer, H.R. Eschnauer and S. Görtges, Analysis of wines by ICP-MS: Is the pattern of the rare earth elements a reliable fingerprint for the provenance? Fresenius' Journal of Analytical Chemistry 364 (1999), 5, pp. 424–428. doi:10.1007/s002160051361

[152] T.E. Dawson, S. Mambelli, A.H. Plamboeck, P.H. Templer and K.P. Tu, Stable Isotopes in Plant Ecology. Annu. Rev. Ecol. Evol. Syst. 33 (2002), 1, pp. 507–559. doi:10.1146/annurev.ecolsys.33.020602.095451

[153] J. Irrgeher and T. Prohaska, Application of non-traditional stable isotopes in analytical ecogeochemistry assessed by MC ICP-MS--A critical review. Anal. Bioanal. Chem. 408 (2016), 2, pp. 369–385. doi:10.1007/s00216-015-9025-3

[154] George de Hevesy, Some applications of isotopic indicators (December 12, 1944).

[155] G. Treglia, E. Giovannini, D. Di Franco, M.L. Calcagni, V. Rufini, M. Picchio and A. Giordano, The role of positron emission tomography using carbon-11 and fluorine-18 choline in tumors other than prostate cancer: a systematic review. Annals of nuclear medicine 26 (2012), 6, pp. 451–461. doi:10.1007/s12149-012-0602-7

[156] W.A. Brand and T.B. Coplen, Stable isotope deltas: tiny, yet robust signatures in nature. Isotopes in Environmental and Health Studies 48 (2012), 3, pp. 393–409. doi:10.1080/10256016.2012.666977

[157] J. Flagg and E. Wiig, Tracer Isotopes in Analytical Chemistry. Ind. Eng. Chem. Anal. Ed. 13 (1941), 5, pp. 341–345. doi:10.1021/i560093a021

[158] A.V. Tikhomirov, Centrifugal enrichment of stable isotopes and modern physical experiments. Czechoslovak Journal of Physics 50 (2000), 4, pp. 577–580.

[159] N.G. Basov, É.M. Belenov, V.A. Isakov, E.P. Markin, A.N. Oraevskiĭ and V.I. Romanenko, New methods of isotope separation. Sov. Phys. Usp. 20 (1977), 3, pp. 209–225. doi:10.1070/PU1977v020n03ABEH005343

[160] S. Stürup, H.R. Hansen and B. Gammelgaard, Application of enriched stable isotopes as tracers in biological systems: a critical review. Anal. Bioanal. Chem. 390 (2008), 2, pp. 541–554. doi:10.1007/s00216-007-1638-8

[161] H. Shen, F. Pang, S. Jiang, M. He, K. Dong, L. Dou, Y. Pang, X. Yang, X. Ruan, M. Liu and C. Xia, Study on 41Ca-AMS for diagnosis and assessment of cancer bone metastasis in rats. Nucl. Instrum. Methods Phys. Res., Sect. B (2015), 361, pp. 643–648. doi:10.1016/j.nimb.2015.05.034

[162] K. Samekova, C. Firbas, J. Irrgeher, C. Opper, T. Prohaska, A. Retzmann, C. Tschegg, C. Meisslitzer, A. Tchaikovsky, G. Gouya, M. Freissmuth and M. Wolzt, Concomitant oral intake of purified clinoptilolite tuff (G-PUR) reduces enteral lead uptake in healthy humans. Sci. Rep. 11 (2021), 1, pp. 14796. doi:10.1038/s41598-021-94245-x

[163] A. Zitek, J. Irrgeher, M. Kletzl, T. Weismann and T. Prohaska, Transgenerational marking of brown trout Salmo trutta f.f., using an 84 Sr spike. Fish. Manage. Ecol. 20 (2013), 4, pp. 354–361. doi:10.1111/fme.12018

[164] F. Dang, Y.-Z. Chen, Y.-N. Huang, H. Hintelmann, Y.-B. Si and D.-M. Zhou, Discerning the Sources of Silver Nanoparticle in a Terrestrial Food Chain by Stable Isotope Tracer Technique. Environ. Sci. Technol. 53 (2019), 7, pp. 3802–3810. doi:10.1021/acs.est.8b06135

[165] I.-Y. Kim, S.-H. Suh, I.-K. Lee and R.R. Wolfe, Applications of stable, nonradioactive isotope tracers in in vivo human metabolic research. Experimental & molecular medicine 48 (2016), 1, e203. doi:10.1038/emm.2015.97

[166] P. Bonaventura, A. Lamboux, F. Albarède and P. Miossec, A Feedback Loop between Inflammation and Zn Uptake. PloS one 11 (2016), 2, e0147146. doi:10.1371/journal.pone.0147146

[167] J. Draxler, E. Martinelli, A.M. Weinberg, A. Zitek, J. Irrgeher, M. Meischel, S.E. Stanzl-Tschegg, B. Mingler and T. Prohaska, The potential of isotopically enriched magnesium

to study bone implant degradation in vivo. Acta Biomater. (2017), 51, pp. 526–536. doi:10.1016/j.actbio.2017.01.054

[168] A. Pack, C. Toulouse and R. Przybilla, Determination of oxygen triple isotope ratios of silicates without cryogenic separation of NF3- technique with application to analyses of technical O2 gas and meteorite classification. Rapid communications in mass spectrometry RCM 21 (2007), 22, pp. 3721–3728. doi:10.1002/rcm.3269

[169] S. Stürup, The use of ICPMS for stable isotope tracer studies in humans: a review. Analytical and Bioanalytical chemistry 378 (2004), 2, pp. 273–282. doi:10.1007/s00216-003-2195-4

[170] A. Tchaikovsky, J. Irrgeher, A. Zitek and T. Prohaska, Isotope pattern deconvolution of different sources of stable strontium isotopes in natural systems. J. Anal. At. Spectrom. 32 (2017), 11, pp. 2300–2307. doi:10.1039/C7JA00251C

[171] J. Irrgeher, A. Zitek, M. Cervicek and T. Prohaska, Analytical factors to be considered for the application of enriched strontium spikes to monitor biological systems. J. Anal. At. Spectrom. 29 (2014), 1, pp. 193–200. doi:10.1039/C3JA50212K

[172] J. Meija, L. Yang, J.A. Caruso and Z. Mester, Calculations of double spike isotope dilution results revisited. J. Anal. At. Spectrom. 21 (2006), 11, pp. 1294–1297. doi:10.1039/b607823k

[173] J. Meija, Mathematical tools in analytical mass spectrometry. Anal. Bioanal. Chem. 385 (2006), 3, pp. 486–499. doi:10.1007/s00216-006-0298-4

[174] J. Irrgeher, T. Berger, A. Tchaikovsky, C. Tschegg, G. Gouya, P. Lechner, A. Retzmann, C. Opper, C. Firbas, M. Freissmuth, K. Peschel-Credner, K. Anderle, C. Meisslitzer, M. Wolzt and T. Prohaska, Enriched stable 204Pb as tracer at ultra-low levels in clinical investigations. Anal. Bioanal. Chem. 415 (2023), 2, pp. 255–268. doi:10.1007/s00216-022-04311-0

[175] C. Rodrigues, C. Máguas and T. Prohaska, Strontium and oxygen isotope fingerprinting of green coffee beans and its potential to proof authenticity of coffee. Eur Food Res Technol 232 (2011), 2, pp. 361–373. doi:10.1007/s00217-010-1362-z

[176] C. Toulouse, A. Pack, A. Ender and S. Petry, Stable Oxygen Isotopes for Tracing the Origin of Clogging in Continuous Casting Submerged Entry Nozzles. Steel Res. Int. 79 (2008), 2, pp. 149–155. doi:10.1002/srin.200806330

[177] M. Dole, G.A. Lane, D.P. Rudd and D.A. Zaukelies, Isotopic composition of atmospheric oxygen and nitrogen. Geochim. Cosmochim. Acta 6 (1954), 2-3, pp. 65–78. doi:10.1016/0016-7037(54)90016-2

[178] C. Toulouse, Sauerstoffisotope zur Klärung der Herkunft nichtmetallischer Ausscheidungen (Clogging) beim Stranggießen von Stahl. PhD thesis, Göttingen (2007).

[179] F. Fuhr, G. Torga, F. Medina and C. Cicutti, Application of slag tracers to investigate source of non-metallic inclusions. Ironmaking Steelmaking 34 (2007), 6, pp. 463–470. doi:10.1179/174328107X174609

[180] A. Brand, L. Allen, M. Altman, M. Hlava and J. Scott, Beyond authorship: attribution, contribution, collaboration, and credit. Learned Publishing 28 (2015), 2, pp. 151–155. doi:10.1087/20150211